# Developing epitaxial graphene for the purpose of nanoelectronics

Andrew James Strudwick
Department of Physics and Astronomy
University of Leeds

A thesis submitted for the degree of

*Doctor of Philosophy*

May 3rd 2012

# Intellectual Property Statement

The candidate confirms that the work submitted is his own, except where work which has formed part of jointly-authored publications has been included. The contribution of the candidate and the other authors to this work has been explicitly indicated below. The candidate confirms that appropriate credit has been given within the thesis where reference has been made to the work of others.

**Joint Publication 1**. **Title**:‘Probing residual strain in epitaxial graphene layers on 4H-SiC($000\bar{1}$) with Raman spectroscopy’. **Published**: Applied Physics Letters, 98, 051910, 2011. **Authors**: A. J. Strudwick (myself, AJS), G. L. Creeth (GLC), N. A. B. Johansson (NABJ) and C H Marrows (CHM). **My Contribution (AJS)**: Design of the experiment, contributed to the growth of the graphene samples, wrote the majority of the final paper, analyzed the data used, took the majority of the data used. **Contribution of others**: GLC - Discussion about data analysis, growth of some of the graphene samples used. NABJ - Took some of the Raman data used as part of a summer project. CHM - Supervisory role, aided with discussion of results, contributed to the editing of the final paper. **Use of the publication in this thesis**: The work from this publication is used within Chapter 5 of this thesis.

**Joint Publication 2**. **Title**:'Surface morphology and transport studies of epitaxial graphene on SiC($000\bar{1}$)'. **Published**: Physical Review B, 83, 195440, 2011. **Authors**: G. L. Creeth (GLC), A. J. Strudwick (myself, AJS), J. T. Sadowski (JTS) and C H Marrows (CHM). **My Contribution (AJS)**: Contributed to the growth of some of the graphene samples, took the majority of the atomic force microscopy data used, analyzed the atomic force microscopy data used, was present during the taking of the low energy electron microscopy data taken to aid in the discussion of the results, experimental procedure and analysis. **Contribution of others**: GLC - The main author of the paper, wrote the main paper, took the electronic transport data and carried out the fitting and analysis of that data, growth of some of the graphene samples used, performed most of the low energy electron microscopy data analysis. JTS - Scientist at Brookhaven National Lab responsible for the taking of the low energy electron microscopy data, contributed ideas towards the experiment design and data analysis CHM - Supervisory role, aided with discussion of results. **Use of the publication in this thesis**: The work from this publication is used within Chapter 4 of this thesis.

# Acknowledgements

I would like to thank both Prof Chris Marrows and Dr Graham Creeth for their guidance over the past four years. Chris's help and insights during the writing up of this thesis and the papers surrounding made the process much less painful. Graham's help with ideas and discussions over the years as well as the direct work carried out with electrical transport measurements and LEEM data that contributed to Chapter 4 has been invaluable. Thank you to Intel Ireland, especially Dr Bernie Capraro for his/their help and funding throughout the project.

Thanks to the workshop staff, Mr John Turton and Mr Phil Cale for putting up with my never ending requests. Mr Leigh Harris, Mr Bryan Gibbs and Mr Richard Oliver for putting the furnace system together. Mr Stuart Weston and Dr Mannan Ali for helping sort out the masses of documentation required. Thanks to collaborators Dr Steve Tear, Dr Vlado Lazarov and Dr Andrew Vick at the University of York for the STM and TEM images shown, Dr Jurek Sadowski from Brookhaven National Lab for support with taking LEEM and LEED data and Dr Alex Walton in Leeds for his help at patience with the Nanoprobe.

To everyone around the department, it really has been a nice environment to work in for the last 4 years and I will miss it. My friends, for being around when a distraction from physics was required be it in the pub, playing sport or traveling around the world to watch england play cricket.

Finally to my family, we have had another roller coaster 12 months but as always have celebrated the good times together and pulled each other through the bad as you should. The support of my Aunties, Uncles, my brother Chris (+ Nat and the boys) and my Dad has been immense throughout, I could not have done this without them. My mum always said I'd be a doctor...

# Abstract

Work presented here has been centered around the growth of epitaxial graphene via the thermal decomposition of 4H silicon carbide wafers. Improvements to ultra high vacuum growth procedures used within the research group have been made via the optimization of annealing times and temperatures. The optimization involved the use of surface science techniques such as low energy electron diffraction, atomic force microscopy, low energy electron microscopy and Raman spectroscopy amongst others to monitor changes in surface reconstructions, lateral grain sizes of graphene domains and graphene coverage on the surface as the growth parameters were varied.

Improvements observed via the surface science techniques such as increasing the lateral domain grain sizes from 10s nm to 100s nm and increasing the graphene film coverage were linked to the betterment of the electronic properties of the graphene films (electronic measurements carried out by Graham Creeth), this linking lead to published work. The mechanical properties of these films were also measured via the use of Raman spectroscopy to probe the formation of strains within the graphene and compare growth carried out on the silicon carbide $(000\bar{1})$ face to literature work carried out on the (0001) face to show evidence of graphene-substrate decoupling within the films grown here, this work also lead to a publication.

Alternate growth procedures have also been investigated. This involved carrying out annealing processes in inert argon gas atmospheres. Atomically terraced substrates were produced via annealing in argon gas atmospheres at temperatures of ~1500°C. These terraced

substrates where then subsequently graphitised by increasing the annealing temperature to ~1600°C allowing for a single stage substrate preparation and graphitisation process. A result not published elsewhere.

A Nanoprobe system has been used to manipulate the graphene films grown under argon atmosphere and make 4-probe electrical transport measurements allowing sheet resistance measurements to be made.

# Contents

# Chapter 1

# Introduction

## 1.1 Introduction

Since it was first isolated experimentally in 2004 (1) there has been a huge surge in research activity into graphene, with over a thousand graphene related publications each year.(2) Graphene is a truly two-dimensional material, it consists of a single layer of carbon atoms arranged in a honeycomb lattice. It has been shown to have remarkable mechanical and electrical properties, including high tensile strength,(3) room temperature quantum Hall effect (4) and high carrier mobilities. (5) Graphene also promises room temperature ballistic transport (6) and the low spin-orbit (7) interactions in graphene should allow for long spin diffusion lengths. These properties make graphene a strong candidate for future electronic and spintronic device applications (8), with work already carried out to show graphene based transistors,(9) flexible electronics (10) and even full wafer scale graphene integrated circuits.(11)

To fully integrate graphene into electronic device applications a way of producing wafer-scale good quality graphene is required. The original scotch-tape (1) or micro-mechanical cleavage method of producing graphene leads to the production of graphene flakes that are scattered on a substrate and is not really scalable for industrial fabrication purposes. Chemical vapor deposition (CVD) growth of graphene onto metal substrates (10; 12; 13) shows promise in producing large scale graphene sheets, however for device fabrication these sheets require transferring on an insulating substrate. Recent research has shown improvement in these transfer techniques (10; 14; 15; 16) with particular promise for the fabrication of flexible graphene electronic devices.

Work here has concentrated on the production of so called epitaxial graphene via the thermal decomposition of silicon carbide, a process which has long been touted for producing graphene for electronic applications.(17) This process involves heating a silicon carbide wafer to high temperatures in either a vacuum (17; 18; 19; 20; 21; 22; 23; 24; 25) or in an inert gas atmosphere.(24; 25; 26; 27) At these temperatures the silicon within the silicon carbide, evaporates away preferentially to the carbon. This leaves behind a carbon rich surface which at these high temperatures is mobile enough to reconstruct and form sp$^2$ bonded graphene.

Detailed reviews of the key results in graphene technology and epitaxial graphene will be presented in chapter 2 of this thesis with particular emphasis on the different methods for graphene production, the key advances in epitaxial graphene production and the properties of graphene that make it desirable for electronic applications.

### 1.1.1 Aims and Details of this Work

The aim of this project has been to understand and improve the growth of epitaxial graphene on silicon carbide, with a view to providing a consistent method for producing high quality, large scale graphene films that can be integrated into electronic devices.(28) The growth of epitaxial graphene on silicon carbide is controlled by a number of key parameters, these are the growth temperature, the duration of the growth anneal and the pressure at which the process is carried out. Also important to the final quality of the grown graphene films is the quality of the initial silicon carbide substrate used. Typically as purchased silicon carbide wafers are marred by scratches due to a mechanical polishing step during production, this can lead uneven graphene growth on the surfaces. Different sample preparation techniques such as chemical etching,(27) hydrogen annealing (26; 29) and extra polishing stages (30) can be used to remove these polishing scratches to produce flat, atomically stepped silicon carbide substrates.

Initial growth processes were carried out in ultra high vacuum (UHV) at a base pressure of $\sim10^{-10}$ mbar. Silicon carbide is a polar wafer and consists of a silicon terminated and a carbon terminated face, the graphene growth on each of these faces being different.(18; 19; 21; 24) It has been shown that the growth of graphene on the carbon terminated face produces material that has better electrical properties than that of the silicon terminated face.(31) For this reason, samples grown in UHV during this work mainly concentrated on the carbon terminated face. Samples were then produced at varying growth temperatures and times and analyzed via a number of various surface science techniques such as Raman microscopy, low energy electron diffraction, atomic force microscopy and low energy electron microscopy. These techniques allow for material properties such as lateral grain size, graphene coverage on the substrate and graphene thickness to be determined. Trends in how growth conditions effect these properties can then be seen and the growth procedure changed to further improve the graphene quality. This led to key improvements in graphene film quality, most notably with increased graphene coverage on the substrate surfaces leading to the formation of complete graphene films and with the increasing of the lateral grain size present within the graphene films from 10s nm to 100s nm.

Strains are observed to build up during the growth of epitaxial graphene. These have been explained elsewhere for graphene grown on the silicon terminated face of silicon carbide to be due to the difference in thermal expansion coefficients between the graphene and silicon carbide.(32) Here (33), these strains were measured for samples with varying annealing times at a growth temperature of 1400° grown on the carbon terminated face. The strain values obtained were less than those seen on the silicon terminated face, indicating that there is a strain relief mechanism due to the extra decoupling between graphene layers and the substrate on the carbon terminated face.

Whilst carrying out this project, it became apparent from work carried out elsewhere (24; 25; 26; 27) that varying the pressure at which the graphene growth is carried out is important. Here, initially this was done by introducing a confined geometry above the silicon carbide during growth (34) in UHV, thus increasing the partial pressure of silicon carbide above the surface. Latterly this was done by annealing in an argon gas atmosphere in a tube furnace system.

During argon annealing runs carried out within the tube furnace system at a temperature of 1500°C showed the silicon carbide substrates previously marred by polishing scratches form atomic terraces thus removing the damage caused by the scratches. This type of terrace is usually achieved via the use of a hydrogen etching treatment which involves high temperature annealing of silicon carbide wafers in a flammable hydrogen rich atmosphere, a process which leads to safety issues.(26; 29) The formation of terraces via annealing in just an inert gas atmosphere alleviates the need for high temperature annealing in a flammable atmosphere and allows for the potential of a single stage annealing process to both prepare the silicon carbide substrates and subsequently graphitise these substrates.

The graphitisation of these atomically terraced substrates was achieved by raising the annealing temperature to 1600°C and work was then carried out to vary both the growth times and temperatures and analyze samples with a view to improving the graphene film quality. Initial graphene films were seen to be ‘island-like’ and sparsely populated on the surface as well as containing rips and folds. Varying growth times and temperatures led to the final sample grown during this process to be annealed for 120 minutes at 1650°C demonstrating 100$\mu$ms areas of uniform graphene growth. It has been seen that the furnace temperature is too low to growth graphene on the carbon terminated face as observed elsewhere (35), so graphene samples from the furnace have been grown on the silicon terminated face.

Graphene films grown via annealing in argon atmosphere have been locally contacted and manipulated using a Nanoprobe STM system. The graphene films have been cut into shapes using the STM tips then contacted to allow 4-probe electrical measurements to be taken on these cut shapes to allow sheet resistances within the graphene films to be found. The measurement geometries cut into the graphene films can be cut in such away as to align in a parallel or perpendicular direction to the underlying silicon carbide substrate terraces. This allows for anisotropies in resistance observed elsewhere, (36; 37) thought to be due to the presence of substrate steps, to be investigated.(38)

# Chapter 2

# Graphene Theory and Literature Review

## 2.1 Graphene

### 2.1.1 General Properties and Band Theory of Graphene

Graphene is a truly two-dimensional material. It consists of single sheet of carbon atoms arranged in a honeycomb lattice, a kind of carbon nano-mesh that is often likened to chicken wire in structure. Graphene can be folded, stacked and rolled to form other carbon allotropes such as buckyballs, graphite and carbon nanotubes respectively. Although only experimentally isolated for the first time in 2004 (1), graphene has been used as a model theoretical system for many decades (39) in order to explain the properties of the materials mentioned above. Since the first, Nobel prize winning experiments on isolated graphene flakes (1), there has been a huge surge in research in this field with over a thousand papers a year now being produced on graphene and ten thousand overall.(2)

Graphene has been dubbed a new 'wonder material' with possible uses in a wide-range of applications such as transistor technology, (9) spintronic applications (8), gas-sensing technology (40) and transparent flexible electronics.(10)

Key to all of these uses are the properties possessed by graphene. To begin with, as graphene is a two-dimensional material, it is in effect 'all surface' this makes it very sensitive to adsorbates that form on the surface. This along with the strong affect adsorbates have on the electronic properties of graphene make it useful as a gas sensor. Measured high carrier mobilities ( 200,000 $\text{cm}^2$/ V s) and ballistic transport ($\mu$m device scale) in graphene films(5) have lead graphene to be touted as a potential more than Moore material for future post-CMOS (complementary metal-oxide semiconductor) transistor technology.

As carbon is a relatively light element, with atomic number 6, the spin orbit-coupling in graphene is small (7), when compared to heavier elements such as silicon which has atomic number 14. This makes graphene interesting for use in spintronic devices, where the electron spin is used to transfer information as opposed to the charge.(41) Despite being only one layer thick, the in-plane bonds within graphene systems are strong, this leads to a graphene film having a high Young's modulus value of 1.0 terapascals .(3) This allows for standard top-down patterning of graphene films into device structures to be possible, along with the broadband high transmittance of graphene makes graphene a viable material for use in flexible transparent electronic applications.(42)

As previously mentioned, the electronic band structure of graphene has been understood for many years.(39) The chicken wire structure of graphene is produced by $\text{sp}^2$ bonded carbon atoms. This means that each carbon atom forms covalent bonds ($\sigma$ bonds) to three others, thus leaving each carbon atom one electron to contribute for conduction ($\pi$ bonds). The honeycomb structure has two atoms per unit cell, as each electron in the unit cell is inequivalent, the band structure of graphene consists of two bands. Each of these bands has a cosine dependence of the electron energy with respect to the wave vector $k$. The band structure of graphene is drawn in Figure 2.1 following the tight-binding model proposed by Wallace.(39)

The two bands touch at six points on the edge of the first Brillouin zone, this makes graphene a zero band-gap semiconductor. At these six points, named the Dirac points, the band structure appears to be conical, meaning that the dispersion relation is linear as

$$E = \hbar \cdot v_{\mathrm{F}} \cdot k \tag{2.1}$$

This is the Dirac-Weyl equation, where $k$ is the momentum of the carrier and $V_{\mathrm{f}}$ is the Fermi velocity. This linear dispersion relation is unlike the usual parabolic

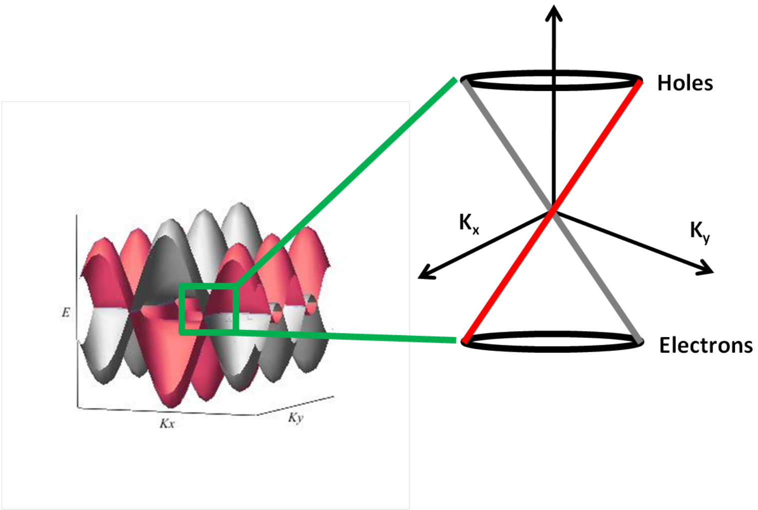

Figure 2.1: Band structure of graphene produced following the tight-binding model shown in (39). Area around the Dirac point is enlarged to show the conical form of the band structure.

dispersion relationship observed for charge carriers in semiconductors.(43) The linear nature of the dispersion relation found in graphene (Figure 2.1) around the Dirac points leads to the electrons and holes having a zero effective mass. Though classically the effective mass is given by

$$\frac{1}{m_*} \propto \frac{d^2E}{dK^2}$$

suggesting an infinite effective mass it is the successful description of the carriers behavior by equation 2.1 that allows them to be described as massless in the region close to the Dirac points.

As mentioned earlier, the band structure of graphene consists of two degenerate subbands. As a result, charge carriers exhibit a psuedospin which is linked to the particular sublattice that they belong to. This pseudospin can be observed in the half-integer quantum Hall behaviour of graphene sheets (see section 2.1.3). As an electron traverses a closed path in the graphene lattice, the valley degeneracy that gives pseudospin leads to the electron picking up a phase change of $\pi$, known as a Berry's phase (6; 7; 31; 44), this then alters the conventional quantum Hall effect in graphene systems.(4; 45; 46; 47; 48; 49)

This is the idealised scenario for an isolated graphene sheet for picturing the graphene band structure. In practice this band structure is modified depending on the experimental conditions, such as the presence of a substrate or other graphene layers. In the case of mulitlayer graphene, the band structure is modified in a way that is dependent on the stacking present between the graphene layers. In AB stacked, known as Bernal stacked, graphene (as commonly found in highly ordered pyrolytic graphite) is stacked with the corner of the hexagon on the second sheet placed above the central gap on the first. For Bernal stacked graphene the intervalley degeneracy is lifted due to interlayer coupling. Practically, this means that less ordered stacking, such as stacking with rotational disorder as seen in epitaxial graphene grown on silicon carbide ($000\bar{1}$) does not lift the intervalley scattering and leads to multilayer systems maintaining the preferential electronic properties of single layer graphene.(50)

The substrate on which the graphene sits can have an effect on the graphene band structure. Strains induced by graphene substrate interactions can affect the band structure, with strain proposed as a possible route for opening up a band gap within graphene films for transistor applications (see section 2.4.3). The substrate can also inadvertently dope the graphene. In an isolated graphene sheet, the charge carrier concentration tends towards zero as the Fermi level sits at the Dirac points, this can be shifted in the presence of substrate doping.(6; 7; 31)

### 2.1.2 Shubnikov-de-Haas (SdH) Oscillations in Graphene

Magnetoconductance measurements are regularly used to probe the electronic properties of two-dimensional electron gas (2DEG) systems in general. In general this involves applying a magnetic field perpendicular to the graphene film (or other 2DEG) plane. In the presence of this magnetic field ($\vec{B}$) the electrons on graphene undergo a Lorentz force ($\vec{F}$),

$$\vec{F} = e\vec{v} \times \vec{B} = m\vec{v}\vec{\omega_c} \tag{2.2}$$

where $e$ is the charge of the electron, $\vec{v}$ is the electron velocity, $\vec{\omega_c}$ is the cyclotron frequency and $m$ is the electron mass. The electrons behave as simple harmonic oscillators (43) and the electrons now follow circular paths. This leads to quantisation of electrons in the conduction plane. The electron energy spectrum is now quantised and consists of Landau levels. These energy levels are separated by equidistant gaps proportional to the cyclotron frequency (Equation 2.3a). The energy levels of this system are then given by Equation 2.3b where $L$ is the Landau level number.

$$\vec{\omega_c} = \frac{e\vec{B}}{m} \tag{2.3a}$$

$$E_L = (L + 1/2)\hbar\omega_c \tag{2.3b}$$

As the magnetic field is varied the Landau levels pass periodically through the Fermi energy. This causes an oscillation in the population of electrons at the Fermi energy, this then causes quantum oscillations in the thermodynamic and transport properties of a metal (43), these oscillations are known as Shubnikov-de-Hass (SdH) oscillations.

These oscillations are more pronounced in conductors that have charge carriers with long mean free paths as their is less blurring of the energy levels from scattering events. Graphene is one such material and as such, SdH oscillations have been observed in graphene.(17; 31; 51; 52) As mentioned earlier the electrons in graphene can be treated as massless Dirac fermions. This causes the Landau level spacings in graphene to not be equidistant, this manifests itself in the periodicity of the SdH oscillations observed in graphene.(7; 53)

### 2.1.3 Quantum Hall Effect in Graphene

The quantum Hall effect (QHE) has lead to the award of two Nobel prizes, the first to Klaus von Klitzing (54) for the original experimental discovery of the QHE and then jointly to Tsui and Stormer (55) for the experimental discovery of the fractional quantum Hall effect and Laughlin (56) for providing the theoretical model to explain these findings.

Again, to observe the QHE a magnetic field must be applied perpendicular to the 2DEG conduction plane. As described earlier, this causes Landau level quantization to occur. In an ideal system, the Landau levels would be Dirac delta functions, however the presence of disorder within practical systems causes broadening of the Landau levels. This gives areas of localized and extended states within each Landau level, with the localised regions near the edge of the levels.(57) This leads to plateaux being observed in the Hall conductance $\sigma_{xy}$ when the Fermi level lies within one of these regions of localised states due to the absence of available states. If a gate voltage is applied to allow sweeping of the Fermi level, these plateaux occur in a regular sequence given by $\sigma_{xy} = (4e^2/h)N$ where $N$ is any integer.

As mentioned earlier, the presence of a Berry's phase in graphene leads to a different QHE in graphene (as shown in Figure 2.2), the QHE is referred to as the half-integer quantum Hall effect, the first Landau level is populated by both electrons and holes and conductance plateaux occur at $\sigma_{xy} = \pm(2e^2/h)$ for the first level with each subsequent spacing occurring with at a regularity of $\sigma_{xy} = (4e^2/h)(N + 1/2)$, this effect is not seen in bilayer graphene and the traditional integer quantum Hall effect is recovered. The QHE was observed in graphene produced via micro-mechanical cleavage(51; 52) including room temperature QHE (4) before it was observed in epitaxial graphene(47; 58; 59). This was due to production issues in epitaxial graphene such as control of sample thickness on the SiC(000$\bar{1}$) face and doping effects on the SiC(0001) face.

### 2.1.4 Quantum Confinement in Graphene

A key aim for research directed at integrating graphene into semiconductor devices for conventional transistor applications is the requirement for an energy band-gap to be introduced into the naturally gapless graphene.(9) One such method that has shown success is the confinement of graphene into nanoribbons (GNRs). The graphene is cut into thin strips (less than 100s nm), this introduces quantum confinement conditions into the graphene band structure, much like those observed in carbon nanotubes.(60) It has been shown that the size of the band-gap induced depends inversely on the width of the GNRs.(61; 62) As the size of the band-gap is dependent on the width of the GNR, accurate control of the width along the length of a GNR device is important for performance.(62) Also important is the determination and understanding of the edge type present as the mechanisms for band-gap formation are different between armchair and

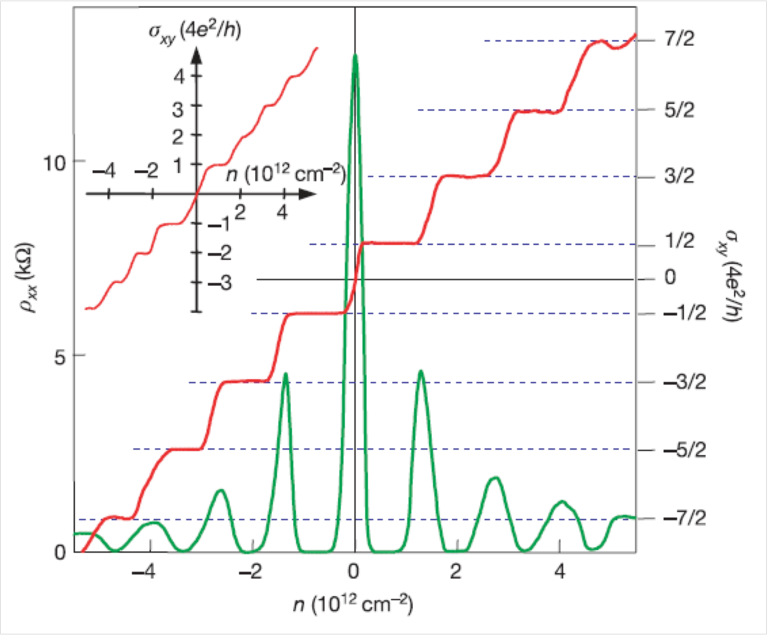

Figure 2.2: Quantum Hall effect observed in monolayer graphene and bilayer graphene [inset]. The magnetic field is held constant whilst the carrier concentration is varied via a gate voltage. The Hall conductance $\sigma_{xy}$ (red lines) and the longitudinal conductance $\sigma_{xx}$ (green lines) are then measured. (51)

zig-zag edges. Armchair edges produce gaps via confinement effects and because the hopping integral increases as slight atomic bond-length increases occur.(62) Band-gaps occur in zig-zag edges due to a staggered sublattice potential from magnetic ordering.(62)

There have been various methods suggested and tested for the production of GNRs. The nanocutting of graphene films via the use of transition metal nanoparticles has been shown (63; 64; 65) to produce very clean edges.(66) Chemical etching procedures have also been used to produce GNRs, again high quality edges are possible by this method.(62) Standard lithographic methods were used to pattern the first graphene nanoribbons experimentally.(61) Templated growth of epitaxial graphene has also been used to produce graphene nanoribbons and pattern transistors onto the surface, this shows promise for large scale production and electronic contacting of GNRs.(67). Chemical bottom-up methods for the fabrication of graphene nanoribbons have also been suggested (68) as has the catalytic etching or ‘unzipping’ of carbon nanotubes.(69)

## 2.2 Epitaxial Graphene

### 2.2.1 Introduction to Epitaxial Graphene

Around the same time (17) of the discovery of isolated graphene flakes via the micro-mechanical cleavage method work was being carried out to make electronic devices out of ‘ultra thin graphite’ via the high temperature annealing of silicon carbide wafers. The idea was to use the silicon carbide wafer to produce large areas of few layer graphitic material, preferably on the wafer-scale to allow the material to be used for large scale production of electronic components. Silicon carbide is preferential to be used as a substrate, it can be produced to be semi-insulating which allows for standard direct top-down lithographic patterning techniques to be used to form electronic devices of graphene, without the need to transfer the grown graphene onto a different substrate, a process that can often damage the graphene films. Silicon carbide has been used for many years in high power electronics applications (70), so procedures for producing top quality, large scale wafers (up to 3 inches (71)) are known, as are the procedures for polishing and flattening these surfaces,(29; 30) useful for producing the best quality graphene.

The silicon carbide polytype used in this work is 4H, this means that the layers are ABCA stacked with the H denoting the hexagonal symmetry in the lattice structure.(72) Silicon carbide is also polar in nature and the (0001) and $(000\bar{1})$ planes are terminated with silicon and carbon atoms respectively, this has important effects on the quality and nature of graphene produced on each of these faces

In this section, the main production methods for epitaxial graphene will be discussed and the benefits and limitations of each addressed.

### 2.2.2 Ultra High Vacuum Growth of Epitaxial Graphene

Carbon growth on silicon carbide wafers via annealing at high temperatures has a long history.(18) Although graphene was seen as a contaminant that appeared during the investigation of high temperature surface reconstructions, (18) the idea to use this carbon layer for electronic applications came in 2004.(17) The growth process of epitaxial graphene involves heating silicon carbide wafers to high temperatures, typically around 1100°C, at these high temperatures the surface of silicon carbide begins to break apart as it becomes unstable. Chemical bonds begin to break, leaving free atoms that are mobile enough to leave the surface. Silicon atoms evaporate away preferentially to the carbon atoms, thus leaving behind a carbon rich surface. Once three layers worth of silicon have evaporated from the surface, the carbon atom density on the surface (73; 74) is high enough such that the mobile atoms can rearrange and reconstruct to form an $sp^2$ bonded graphene layer.(17; 19; 21; 27; 75; 76; 77; 78; 79)

As the silicon desorption occurs preferentially at certain nucleation sites, the nature of the graphene formed depends on the specific nucleation site. For example, on stepped graphene surfaces, it is energetically favorable for the silicon atoms at the step edge to leave the surface (73; 80), here the graphene growth proceeds outwards from the step edge and growing ‘carpet-like’ over other steps. If on the other hand the silicon evaporates from a screw dislocation, then the graphitisation occurs outwards from the dislocation, with the graphene forming along the walls of the depression up to the level of the substrate.(35) Substrate scratches, originating from the polishing processes can also act as nucleation points for growth (81), thicker graphene layers with smaller grains can be seen around these features. As discussed in greater detail in a later section (section 3.4.4) these kind of growth processes can make it difficult to measure graphene thicknesses with scanning probe techniques as it is not always obvious which layer is the silicon carbide substrate when attempting to measure relative height changes.

As substrate defects are so important in terms of nucleating the growth of graphene, various pre-growth treatments of the surface are used to limit such things as substrate scratches and dislocations. This can include extra polishing of the surfaces to provide near scratch-free substrates, such as the wafers used in this work that were polished by Novasic, a company that specialises in wafering and wafer polishing.(30) During the growth of epitaxial graphene in ultra high vacuum (UHV) a flux of silicon has been used to form surface reconstructions that are preferential for graphene growth.(82) Annealing silicon carbide wafers at high temperatures in hydrogen gas rich atmospheres is also used, this yields a well ordered and atomically stepped substrate that leads to subsequent, better graphene growth.(29)

The original process for epitaxial graphene growth involved the high temperature annealing process to be carried out in ultra high vacuum.(17; 77) As the silicon carbide is heated, various surface reconstructions take place on each of the polar faces (19; 78; 83) until finally a carbon rich surface is achieved. These surface reconstructions will be addressed in further detail in a later section (section 3.5.3). The diffraction patterns observed from each of these carbon rich surfaces varies significantly from one polar face to the other, indicating differences in the graphene growth processes between the two faces.

Initial work on epitaxial graphene films carried out during this work concentrated on growth on the silicon terminated (0001) face. In general the graphene growth process on the silicon-terminated face has a slower silicon evaporation rate than that of growth on the carbon-terminated face (23; 24; 26; 34; 77). The first carbon rich layer is also strongly bound to the silicon carbide substrate via its $\pi$ electrons, forming a so-called ‘buffer layer’.(21; 23; 24; 34; 50; 77; 84) The subsequent graphene grows in good order to this buffer layer, with each layer Bernal stacked to the last. This can be seen in the low energy electron diffraction images from graphene growth on this face.(19; 21; 78; 83) Graphene formation on the silicon-terminated face is widely accepted to be a self-limiting process,(34; 77) meaning that growing single or few layer graphene is a simpler process.

The silicon evaporation rate on the carbon-terminated face is quicker and does not have a buffer layer between the first carbon-rich layer and the silicon carbide substrate. This leads to less of an interaction between the silicon carbide substrate and the graphene layer(s), subsequent graphene layer growth has a rotational disorder (34; 50; 77) which can also be seen as dashed rings in the low energy electron diffraction (19; 21; 78). In general, the morphology of graphene grown on the silicon-terminated face, consists of domains (grains) of graphene with larger lateral size than those on the carbon-terminated face, with a much narrower variation of layer thicknesses seen on the silicon-terminated face (24). Although large scale production of single layer graphene is more difficult on the carbon-terminated face (34; 77), the decoupling present between the graphene layers allows multilayer graphene to maintain the electronic properties of single layer graphene.(50) This leads to higher electrical conductivities (up to 30,000 $\mathrm{cm^2V^{-1}s^{-1}}$) on the carbon-terminated face, compared to the silicon face (up to 2,000 $\mathrm{cm^2V^{-1}s^{-1}}$).(34; 77)

The growth process has many interlinked factors that contribute to the overall quality of the resulting graphene films. The absence of the need for of an external carbon source removes some variables usually associated with this kind of growth process, there is no need to consider source flow rates and flux for example. The factors that do control the growth are the annealing temperature, annealing duration and the pressure at which the process is carried out. If an external gas is used to control the pressure of the growth process it is important that an inert gas is used which will not react with the graphene. These factors are linked, which can mean that optimizing one parameter can adversely effect one of the others. On a simplistic level, the growth process is dependent on two key factors, the net evaporation rate of silicon from the surface, and then the lateral progression of graphene domains on the surface once they have formed. External fluxes of both silicon (82) and carbon sources (85) have been used to control the net silicon evaporation rates, though they are not essential and it has been shown that increasing the pressure can control this, some of these methods will be discussed in the following sections (2.2.3 and 2.2.4) and their effect on growth conditions discussed.

### 2.2.3 Confined Geometry Growth of Epitaxial Graphene

A mentioned in the previous section 2.2.2, the growth of epitaxial graphene depends on a number of interlinked parameters. Controlling these parameters is key to producing high quality epitaxial graphene. Epitaxial graphene grown in ultra high vacuum can be somewhat defected, (24) owing to the high silicon evaporation rates from the surface and the relatively low temperatures often used for the growth process. The low growth temperature (∼1200°C) is close to the temperature at which a number of surface reconstructions take place on the silicon carbide surface, thus the substrate is not at equilibrium when graphene growth takes place. This leads to the defected graphene observed via UHV growth. Increasing the growth temperature allows for some coalescence of grain boundaries to occur (28) and leads to improved graphene growth but the evaporation rates remain high, making controlled layer growth difficult.

One method suggested to improve the control of the silicon evaporation rate is to carry out the annealing process whilst confining the space around the silicon carbide wafer.(34; 86) The silicon carbide is placed within a graphite enclosure that contains a small leak.(34) Annealing can then be carried out in either UHV or insert gas atmospheres and good quality graphene layers produced in a controlled manner on both the (0001) and $(000\bar{1})$ faces. The silicon evaporation rate can be tuned with changing the size of the 'leak' in the system and by introducing an inert gas into the enclosed volume. Growth of graphene in this manner has been shown to produce high quality graphene as can be seen in a number of papers which demonstrate such things as the quantum Hall effect (47) and high electron mobilities .(87) Work here has used this principle to help control growth in both UHV and argon gas atmospheres.

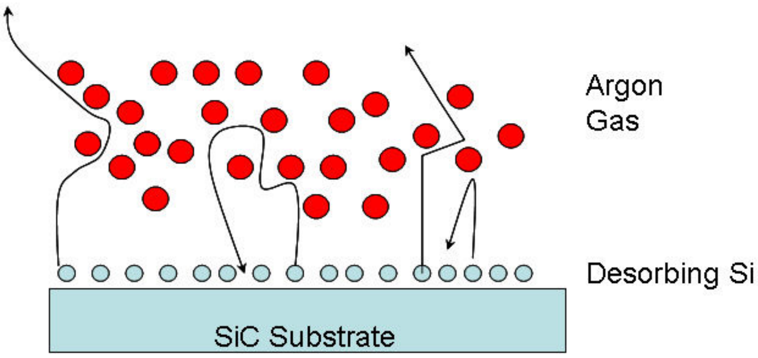

Figure 2.3: Schematic of the effect of argon gas in the growth process. The now finite possibility of silicon atoms being backscattered and returning to the substrate surface is shown.

### 2.2.4 Inert Gas Atmosphere Growth of Epitaxial Graphene

Another method suggested for increasing the quality of epitaxial graphene growth is to carry out the procedure in an inert argon gas atmosphere.(26; 27) In a process similar to that used to increase the lifetime of lightbulbs, the argon gas present gives a silicon atom escaping the silicon carbide substrate a finite chance of being scattered back onto the sample surface as shown in Figure 2.3. This slows down the rate of silicon evaporation, leading to an increase in onset temperature of graphene growth. The graphene growth now begins at a temperature above the surface reconstructions of silicon carbide, this stabler and equilibrated surface leads to better graphene growth. It can be seen that this method leads to layer-by-layer growth on the (0001) face that contains very large graphene domain sizes (10s $\mu$m) when compared to growth in UHV (100s nm) (25; 26; 27) with improved electron mobilities.(26) This method leads to somewhat uneven growth on the $(000\bar{1})$ face with even evidence for the formation of an interface layer between the graphene and the substrate when the silicon gas pressure is raised.(24; 35) Work here has been carried out on the growth of epitaxial graphene via this method.

### 2.2.5 Epitaxial Graphene as a Resistance Standard

The quantum Hall effect (QHE) allows resistance to be described in terms of the fundamental constants of the electron charge $e$ and planks constant $h$ as the Hall resistance in two-dimensional systems is quantised in fractions of $R_{\mathrm{K}} = h/e^2 = 25,812.807557(18)\Omega$. $R_{\mathrm{K}}$ is the resistance quantum, as such the QHE is used as the international standard for measuring resistance. Fairly recent developments have led to the measurement of the QHE on epitaxial graphene grown on both SiC(000$\bar{1}$) (47) and SiC(0001). (58; 59) The results obtained by Tzalenchuk et al (59) of the QHE in large area epitaxial graphene grown on SiC(0001) show the Hall quantisation to be accurately measured to a few parts per billion at a temperature of 300 mK.

Several devices were also measured at a temperature of 4.2 K to an accuracy of some tens in the $10^9$ which shows the robustness of the QHE in graphene grown epitaxially on SiC(0001). The accuracy of this measurement is an improvement of four orders of magnitude over the best previous results obtained on micromechanically exfoliated graphene flakes and are comparable to those obtained in established semiconductor resistance standards.(59)

The main transport measurements from this work are shown in Figure 2.4 insets a) and b). Data from inset a) is taken from a small Hall bar with dimensions (11 $\mu$m × 2 $\mu$m) and b) from a larger Hall bar with dimensions (160 $\mu$m × 35 $\mu$m) respectively, both of which exhibit the quantum Hall effect. Figure 2.5 inset a) shows the mean deviation of the $R^0_{\mathrm{xy}}$ value from a large Hall bar away from the $R_{\mathrm{K}}/2$ value as function of bias current through the sample. The accurate values of $R_{\mathrm{xy}}$ were taken at a point where $R_{\mathrm{xx}}$ is virtually zero and the accuracy of the Hall resistance measurement is determined by the use of a cryogenic current comparator bridge.

It can be seen that the most accurate value for $R^0_{\mathrm{xy}}$ was taken at 11.6 $\mu$A and was taken over an 11 hour period. Inset b) of Figure 2.5 shows the Allan deviation of $R^0_{\mathrm{xy}}$ away from $R_{\mathrm{K}}/2$ as a function of the measurement time $\tau$. The $1 \setminus \tau^{1/2}$ dependence of this deviation is a signature that the noise present is white noise.(88) There are suggestions for improving the accuracy of these findings still further. These include increasing the breakdown current by using

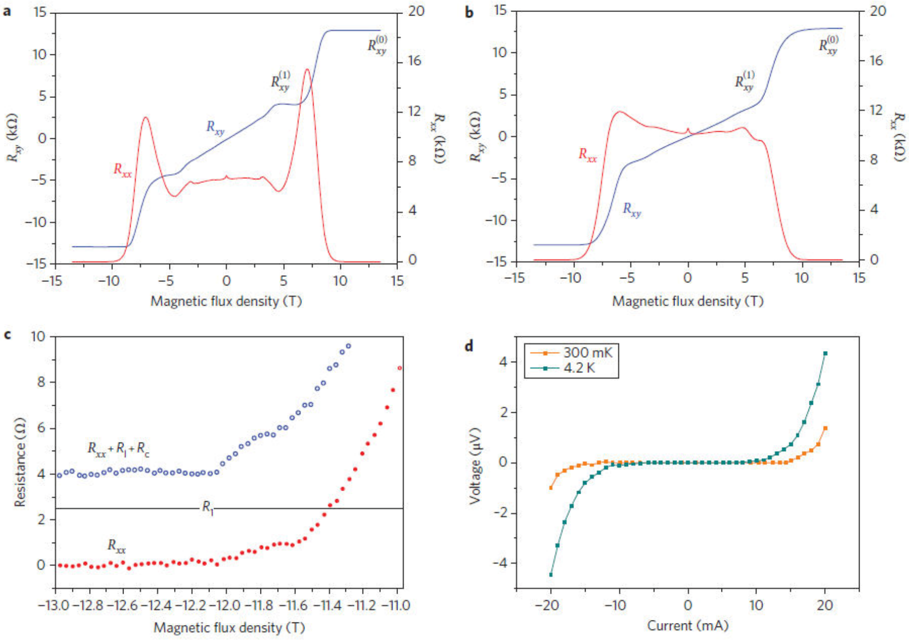

Figure 2.4: QHE in epitaxial graphene. **a**, Transverse ($R_{xy}$) and longitudinal ($R_{xx}$) resistance of the 11.6 $\mu$m × 2 $\mu$m device measured at $T = 4.2$ K with 1 $\mu$A current. $R_{xy}^{(0)}$ and $R_{xy}^{(1)}$ represent Hall resistance plateaus at filling factors $\nu = 2$ and $\nu = 6$ respectively. The carrier density $n_s = 6.5 \times 10^{11}$ cm$^{-2}$ was obtained from SdHOs. **b**, Transverse ($R_{xy}$) and longitudinal ($R_{xx}$) resistance of the 160 $\mu$m × 35 $\mu$m device measured at $T = 4.2$ K with 1 $\mu$A current. The carrier density $n_s$ was obtained from SdHOs. **c**, Measurements of the longitudinal resistance $R_{xx}$ performed in a four-point configuration (filled red circles), which excludes contact resistances, and in a three-point configuration (open blue circles), which, as well as $R_{xx}$, includes the contact resistance $R_c$ and the resistance of the leads from room-temperature electronics down to the sample $R_l = 2.5$ Ω On the plateau, $R_{xx}$ is very nearly zero and $R_c$ is $\sim 1.5$ Ω for all measured contacts. These measurements were performed while sweeping the magnetic field; hence there is a relatively large spread. **d**, Determination of the breakdown current $I_{max}$ of non-dissipative transport from measurement of the current-voltage characteristic in the longitudinal direction at 14 T: $I_{max} \approx 13$ $\mu$A at 300 mK and $I_{max} \approx 5$ $\mu$A at 4.2 K. The residual longitudinal resistance was confirmed as $R_{xx} < 0.2$ mΩ at 300 mK measured with $I_{sd} = 12$ $\mu$A, and $R_{xx} < 2.4$ mΩ at 4.2 K measured with $I_{sd} = 2.5$ $\mu$A.(59)

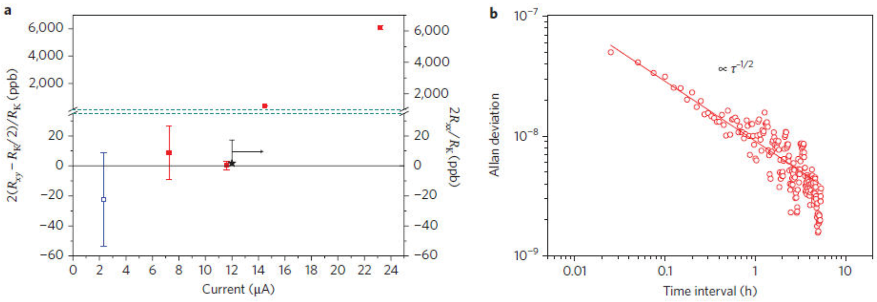

Figure 2.5: Determination of Hall resistance quantisation accuracy. **a**, Mean relative deviation of $R_{xy}^{(0)}$ from $R_K/2$ at different bias currents (ppb, parts per billion). The value at the smallest current was measured at 4.2 K (open blue squares), and all other values at 300 mK (filled red squares). The most accurate measurement with an 11.6 $\mu$A source-drain current at 14 T and 300 mK was performed over ∼11 hours. The value of $R_{xx}/R_K$ determined in the same conditions is also shown (black star) together with the measurement uncertainty. **b**, Allan deviation of $R_{xy}^{(0)}$ from $R_K/2$ versus measurement time $\tau$. The square root dependence indicates purely white noise.(59)

the flexibility of device design offered by large area epitaxial graphene on silicon carbide wafers, optimization of contact geometry and the use of multiple parallel Hall bar devices.(59)

## 2.3 Other Graphene Production Methods

### 2.3.1 Micro-mechanical Cleavage Method

Perhaps one reason for the initial success and attention to graphene as a material, was the novel and relatively simple way in producing it. Graphene was originally isolated in a process often referred to as the 'scotch-tape method'.(1) This method involves the use of adhesive tape to cleave layers off good quality graphite crystals. When the cleaving process is repeated enough times, the debris produced on the tape is then pressed down onto a silicon wafer topped with either a 100 or 300 nm silicon oxide layer. These two layer thicknesses of oxide layer allow monolayer graphene to be distinguishable from other thicknesses of multi layer graphene or bulk graphite via differences in light absorption caused by additional graphene layers.

The method produces isolated graphene flakes, typically 10s to 100s $\mu$m in size that are irregularly scattered across the substrate. These can then be located and contacted electronically and have been used to probe very interesting physical properties such as the quantum Hall effect.(4; 51; 52) This method of graphene production is relatively cheap and provides a basis for probing fundamental properties of graphene films. However it suffers from a lack of scalability as each flake has its own unique shape and position on a substrate, thus hindering the use of mass production techniques to pattern graphene based devices.

### 2.3.2 Chemical Vapour Deposition (CVD) Growth

Graphene growth on metal substrates has been observed to produce large areas of graphene. Initially graphene was observed from the annealing of ruthenium in UHV with the source of carbon coming from carbon introduced into the bulk metal.(89) Other methods have seen chemical vapour deposition (CVD) used to

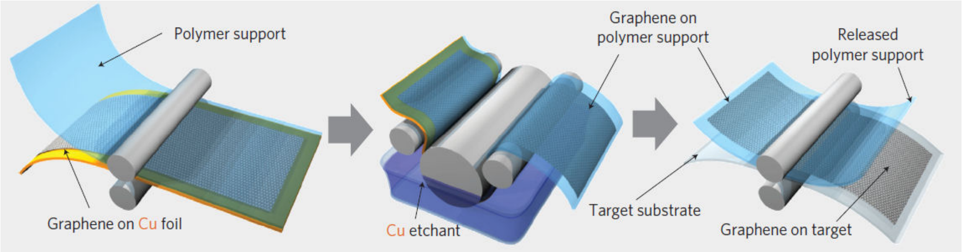

Figure 2.6: A schematic of the roll-to-roll method for transferring graphene films from a copper substrate to a PET film.(10)

form graphene layers on rigid nickel substrates.(13) However, in order to study the electrical properties of graphene formed in this way it must be transferred onto an insulating substrate before it can be electrically contacted. The transfer process often damaged the graphene film and led to limited scalability in terms of film size. A breakthrough was made by Li et al (90) by successfully growing graphene films on thin, flexible, copper foil substrates. This graphene could then be transferred onto silicon or glass substrates with a method similar to that developed by Reina et al.(16) This method successfully transfered graphene flakes produced by the micro-mechanical cleavage method from one oxidised silicon substrate to a second via the use of a poly(methyl methacrylate) (PMMA) layer which is subsequently dissolved using acetone.

This idea was then progressed by Bae et al (10) by using a 30-inch copper foil substrate. The foil is rolled into a tube and inserted into a CVD chamber for growth. Then a roll-to-roll method (10) as depicted in Figure 2.6 is used to transfer the graphene substrate and onto a target substrate. This roll-to-roll method has three main steps (1) successful adhesion of polymer supports to the graphene on the copper foil; (2) etching away of the copper layers; and (3) the release of graphene layers and their transfer onto target substrates. This has led to the successful transfer of very large areas of graphene onto PET substrates for subsequent use in touch screen devices, as shown in Figure 2.7. The transferred graphene was shown to be of high quality and defect free via the use of Raman microscopy and was shown to exhibit the half-integer QHE, an indication of the quality of the electrical properties.

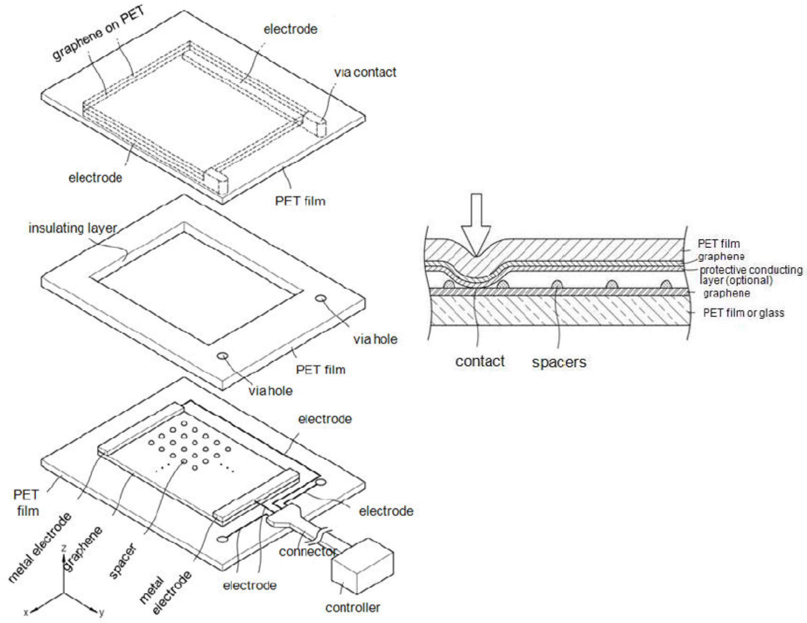

Figure 2.7: A schematic of the production of a touchscreen device made from graphene .(10)

### 2.3.3 Other Graphene Production Methods

There have been many production methods for graphene suggested and the following section in no way provides an exhaustive list. A promising area for graphene usage is in the area of graphene composite materials. Graphene can be used in a similar way to carbon nanotubes and carbon fibers to strengthen plastics and also allow for conductive plastic materials.(91; 92) Graphene can be made into solutions via a dispersion technique (often graphene oxide is dissolved in solution)(91; 92) these can then be used to make these composite materials. Also the dispersions can be used in a number of other ways, such as to integrate with other two-dimensional materials to make up layered structures with engineered qualities via the choice of materials.(93; 94)

Alternative methods for graphene production involve the unzipping of carbon nanotubes via transition metal nanoparticles to form graphene nanoribbons,(69) and even via the use of carbon based waste materials in a CVD-like process.(95)

## 2.4 Strain effects in graphene

### 2.4.1 Causes of strain in Graphene

As a truly two-dimensional material, applied strains can have a large effect on the properties of graphene films. This can include the modification of the electronic properties of the material, such as the introduction of an energy band-gap (96) and the physical properties of the material, with the introduction of ripples and wrinkles into the graphene.(97) It is therefore important to understand the causes of strains in graphene films, such that strains can be reduced or increased, dependent on the objective.

During the production of graphene flakes by micro mechanical cleavage of graphite, folds and wrinkles can be induced in the graphene films during the transfer process, these cause strains to develop and have been shown to effect the properties of the films.(98) Flake graphene has also been used in experiments to probe the strain response of graphene by creating devices to purposefully strain the graphene in a controlled manner whilst monitoring changes in properties such as Raman peak positioning.(99; 100; 101)

Graphene films are very sensitive to interactions with the substrate, with shifts in wavenumber seen for graphene flakes deposited on different substrates, and even the observation of Raman G-band splitting, an indicator of strain, seen for graphene on glass substrates.(102)

In epitaxial graphene films, the cooling process from the high growth temperatures can induce strains within the graphene films. As the film cools, it expands (103) whilst the underlying silicon carbide contracts,(104) thus leading to the formation of a compressive strain.(32; 33) In epitaxial graphene films scanning probe techniques show the formation of wrinkle-like structures. The nature of these features has lead to some debate, with the origin possibly being due to the formation of nanotube-like structures (105) or strain induced wrinkles.(106) N'Diaye et al (97) looked at strains in graphene films grown via CVD on platinum (111) and iridium (111) substrates to observe the in-situ formation of wrinkles and lend support to the strain-induced wrinkle model for the features observed with scanning probe techniques in other epitaxial graphene materials.

### 2.4.2 Measurement of Strains in Graphene

There are a number of techniques that have been used to measure the effects of strains in graphene films. One technique that has proven very useful for this is Raman microscopy, the details of which can be found in chapter 5. There have been a number of experiments carried out on the external straining of flake graphene materials using flexible substrates whilst monitoring the Raman response of the flakes.(99; 100; 101) This has allowed for the experimental measurement of the Grüneisen parameter in graphene for the main Raman bands.(100; 101)

The use of Raman information along with scanning probe microscopy techniques is very useful in understanding how topological features in the graphene films correspond to shifts in Raman peak positions, and ultimately strains. This is particularly important in understanding the strain mechanisms in epitaxial graphene films and how features in the underlying silicon carbide substrate can effect the graphene growth.(32; 33) Scanning probe techniques can also be used to image the size of wrinkles and folds that form within graphene films, with scanning tunneling microscopy very useful in showing that the graphene films remain continuous over these wrinkle structures.(106)

Electron diffraction (micro-low energy electron diffraction) and electron microscopy (LEEM) techniques have also been shown to be useful in monitoring strains within graphene films and can allow for in-situ measurements of strain relaxation and wrinkle formation to be observed.(97) Strain effects have also been linked to electrical measurements with Hall bar devices patterned within regions of uniform strain, having higher mobilities than those patterned within regions having a large amount of strain variation.(107)

### 2.4.3 Band-Gap Engineering with Strains

For the use of graphene in post-CMOS transistor technology, an energy band-gap is necessary to allow the transistor to be fully switched-off and thus conserve power.(9) Strains have been touted as a way of producing such a band-gap in graphene films.(96) If a uniaxial strain is applied to a graphene film, the graphene lattice becomes distorted. This leads to the breaking of sub-lattice symmetries within the graphene sheet as shown in Figure 2.8, this symmetry breaking can be shown to introduce a band-gap.(96)

As Figure 2.9 shows, this band-gap can in theory be up to 300 meV for a 1% strain in the graphene films. The use of strains to induce band-gaps in graphene films can be shown to be beneficial to other forms of band-gap engineering in graphene. Firstly, the size of the band-gap is somewhat tuneable allowing for size control within a device prepared say on a piezo-electric substrate and much more control than band-gaps induced by substrate interactions in epitaxial graphene samples. The band-gap opening via this method is also more efficient than methods such as molecular absorption and the electric field tuning of bilayer graphene samples.(96)

### 2.4.4 Pseudo-Magnetic Fields Produced by Strains

As well as band-gap engineering, non-uniform strains in graphene systems can also lead to other, very interesting effects. One such effect is the creation of so-called ‘pseudo-magnetic fields’ with effective magnetic field strengths in the

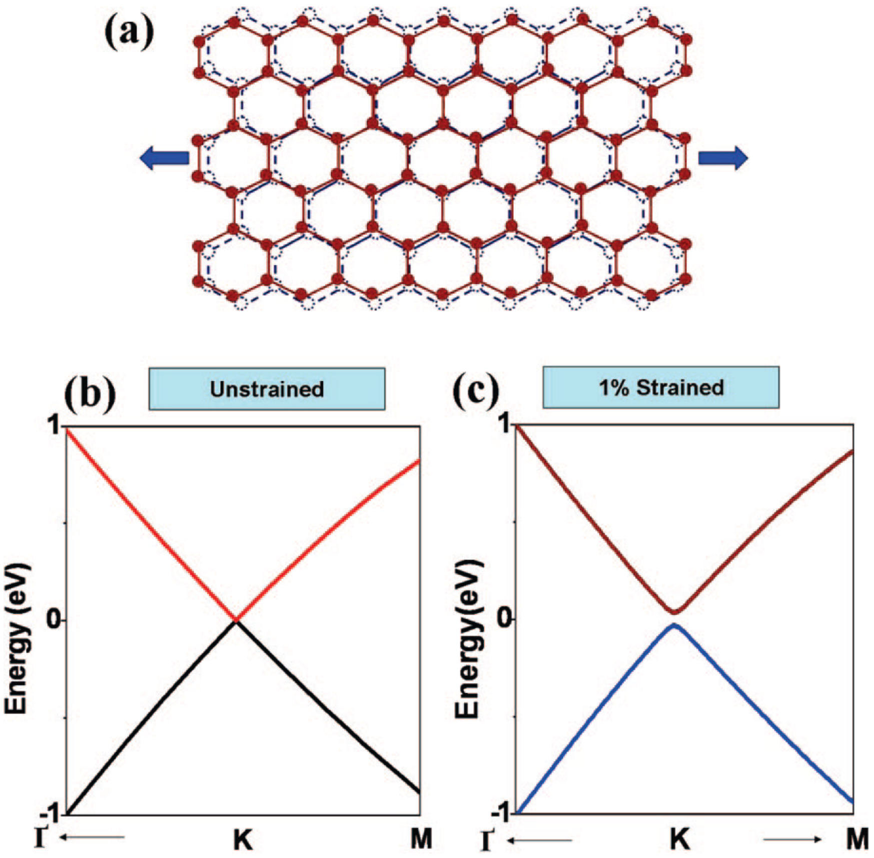

Figure 2.8: a) Schematic representation of the effect of uniaxial tensile stress on a graphene supercell. The dashed (solid) lattices indicate the unstrained (strained) graphene. Calculated band structure of unstrained (b) and 1% tensile strained (c) graphene. A band gap is clearly seen on the band structure of strained graphene. Arrows in b) and c) indicate the strain direction.(96)

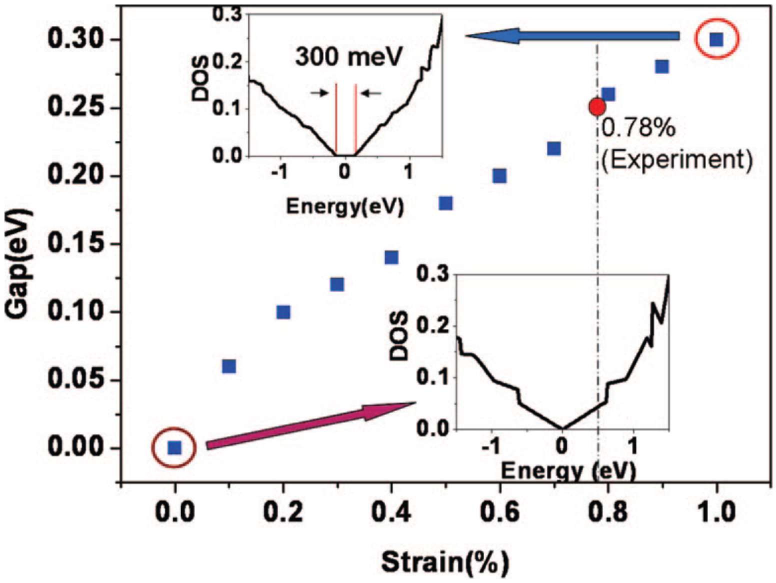

Figure 2.9: Band gap of strained graphene with the increase of uniaxial tensile strain on graphene. The magnitude of the gap is determined by the gap opening of the density of states. The insets show the calculated density of states (DOS) of unstrained and 1% tensile strained graphene. The dashed line and red solid dot indicate the calculated band gap of graphene under the highest strain (0.78%) in our experiment.(96)

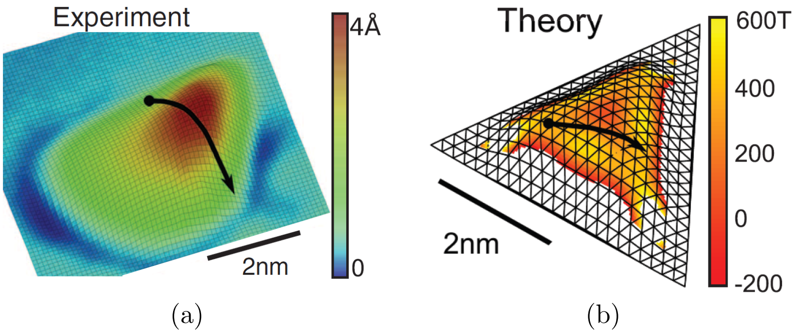

(a) (b)

Figure 2.10: a) STM topography of a graphene nanobubble. b) Simulated effective magnetic field strength of a graphene nanobubble.(108)

order of 100s Tesla. The application of a non uniform strain on a graphene film leads to breaking of sub-lattice symmetries,(108) this leads to a modification of the electron-hopping potential between atoms, this leads to an effective vector potential. This gauge field then acts on the charge carriers in the system, much in the same way as a magnetic field would, causing them to go into cyclotron motion and thus inducing Landau levels within the system.(108; 109)

This effect has been realised experimentally via the growth of graphene ‘nanobubbles’ on Pt(111) substrates. The typical shape of a graphene nanobubble is shown in Figure 2.10(a), the strain is brought about due to the difference in thermal expansion coefficients between the Pt(111) substrate and the graphene during the cooling process after growth.(108) The compression occurs in a trigonal manner due to the nature of the graphene-substrate interaction, this kind of symmetry is seen to be preferential for creating large pseudo-magnetic fields and leads to fields as shown in Figure 2.10(b). These nanobubbles were then probed with scanning tunneling spectroscopy to reveal the Landau level formation and to measure the size of the effective magnetic fields created. The fields produced are in the 100s Tesla range as shown in Figure 2.10(b). This technique could be used to probe the effects of extremely high magnetic fields at room temperature in the fraction of the cost of producing a facility to do this with conventional magnets.(108)

## 2.5 Graphene Based electronic devices

### 2.5.1 Graphene Based Transistors

The favorable electronic properties of graphene have resulted in it being a material being strongly considered for post-CMOS transistor technology advancements. It is therefore important to see where the current research stands on developing graphene for this purpose and what challenges remain in this field. A review paper by Schwierz (9) highlights the progress made in developing graphene materials for post-CMOS use and the key problems that still need to be addressed.

A major problem in the integration of graphene into logic-gate transistor devices is the absence of a band-gap in graphene, this leads to large power consumptions as the transistor can never be fully switched off. As mentioned earlier there are a number of methods being investigated for the creation of a band-gap in graphene, such as confinement into graphene nanoribbons,(60; 61; 62) the use of uniaxial strains (96) and the use of bilayer graphene systems.(20) All of these processes for creating band-gaps also lead to modification of the other graphene electronic properties which is detrimental to the materials use in devices, for example the cutting of graphene into nanoribbons leads to a decrease in electron mobilities.(9)

The lack of a band-gap is less important in the production of RF transistors and the high saturation velocities and carrier mobilities make graphene well suited for this purpose. RF transistors made from graphene with intrinsic cut-off frequencies in the 100 GHz range have been produced out of epitaxial graphene on silicon carbide,(110) CVD grown graphene (90) and mechanically cleaved graphene flakes.(111; 112) Still there are issues with graphene in RF transistor applications, such as the lack of satisfactory saturation, which impacts adversely on the cut-off frequencies in devices.(9)

It also important in the development of graphene transistor technology is the ability to create full integrated circuits out of graphene. There are some key issues with graphene compared to other semi conducting materials that need to be addressed in the formation of graphene-based integrated circuits such as the different ohmic contact formation mechanisms, the difficulties in contacting graphene (poor adhesion) to metals and oxides and the issues surrounding graphene's susceptibility to being damaged during plasma processing.(11) Despite this, recent advancements have seen integrated circuits produced from graphene.(11) Also demonstrated is the ability to selectively grown epitaxial graphene along step edges in order to produce large arrays of transistors.(113)

It is important to note that although there are still real problems to be addressed and resolved before graphene can become widely used in the transistor technology industry, the progress made to date in such a short time has been great shows promise to suggesting that the existing problems can be overcome to achieve graphene based transistor devices.(9) A recent development has seen the production of graphene transistors on a diamond-like substrate.(114) The CVD process used to produce the graphene on the diamond like substrates in this work could be beneficial for the final integration of graphene into industrial scale transistor production.(114; 115)

### 2.5.2 Graphene Based Transparent Flexible Electronics

The high electrical conductivities and optical transparencies offered by graphene make it an ideal candidate for use in transparent conducting electrodes.(42) The production of large area graphene on flexible substrates via either dispersal from solution (91; 92) or by roll-to-roll (10) methods from CVD grown graphene has allowed graphene to be used in the production of prototype flexible electronic devices.

This has included the use of graphene in photo-voltaic solar cell devices,(116) light emitting diodes,(117) and touchscreen devices.(10) Graphene offers advantages over the current standard indium tin oxide transparent conductor devices. Most notably is the ability to use graphene on substrates other than glass, this allows the devices to be flexible and less susceptible to damage and allows for wider integration possibilities for devices. Another important factor is the rising cost and falling availability of indium, making graphene a cheaper and more readily available material to use.

A recent review paper provides a very good summary of graphene-based flexible electronic applications, along with the photonic and optoelectronic properties

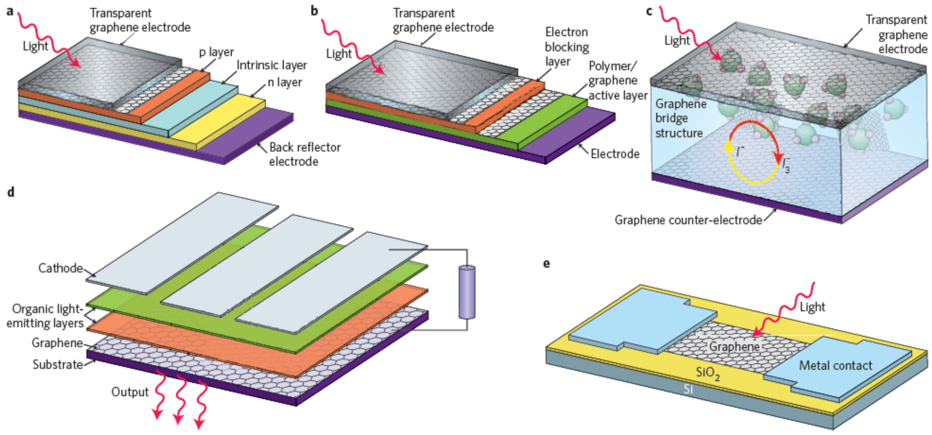

Figure 2.11: Graphene-based optoelectronic devices. **a** − **c** Schematics of inorganic (**a**), organic (**b**) and dye-sensitized (**c**) solar cells. **d**, **e** Schematics of an organic LED (**d**) and a photo detector (**e**). The cylinder in **d** represents an applied voltage. Image taken from (42).

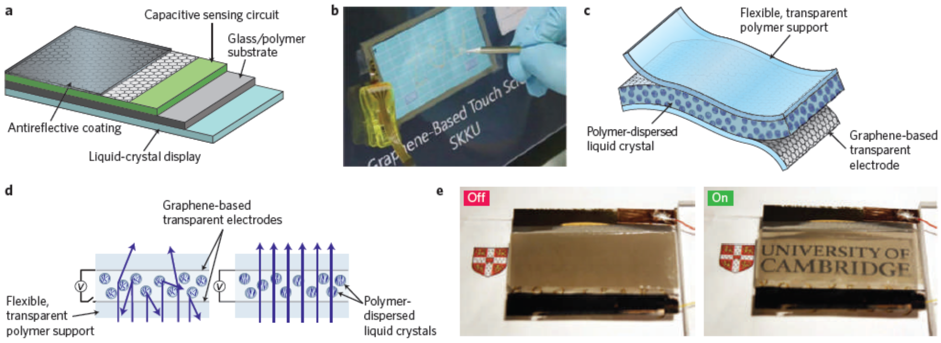

Figure 2.12: Graphene touch screen and smart window devices. **a**, schematic of a capacitive touch screen. **b**, Resistive graphene-based touch screen. **c** Schematic of a PDLC smart window using a GTCF. **d**, With no voltage, the liquid-crystal molecules are not aligned, making the window opaque. **e**, Graphene/nanotube based smart window in either an off (left) or on (right) state. Image taken from (42).

of graphene.(42) Figures 2.11 and 2.12 are adapted from this review paper and shows the possible structure of a number of graphene-based devices including already made graphene-based touch screens (10) and smart window prototypes. Key properties of graphene leave it strongly placed for wide-scale use in this area of device manufacture, with graphene promising low-cost and highly flexible transparent electrodes for the use in a number of different devices.

### 2.5.3 Graphene Based Spintronic Devices

Graphene has shown promise in the field of spintronic applications. In spintronics, the spin of the electron is used to carry information as well as the charge, leading to advanced approaches to memory storage and processing. The ability to inject spins into a semiconducting channel and transform the spin information into a significant output signal is a key issue in spintronics. The understanding of these concepts are also key in developing spin transistors.(118) The low spin-orbit and hyperfine interactions in graphene make it an ideal candidate for spintronic devices, with large spin coherence lengths predicted for graphene materials.(6; 7) The high electron velocities are also favorable in graphene-based spin transistors and leads to smaller dwell times when compared to other semiconductor materials.(119) This allows for spin transport with significant output signals comparable to other semiconducting materials in graphene and carbon nanotube spin transistors even when the spin injection efficiency is comparably lower.(119; 120)

Spin transport measurements have been carried out in graphene.(121; 122; 123; 124; 125; 126; 127) The largest non-local magneto resistance measurement in any material was reported for single layer graphene flakes, where previous issues involving spin injection efficiency (122) were rectified and a tunnel barrier between the graphene film and the ferromagnetic electrodes achieved.

# Chapter 3

# Experimental Methods Used

## 3.1 Graphene Growth in Ultra High Vacuum (UHV)

The history and theory of the growth of epitaxial graphene is discussed in detail in section 2.2, where the main factors that control the growth of epitaxial graphene are introduced and discussed. This section will concentrate on the experimental conditions used within this work for the production of epitaxial graphene under ultra high vacuum conditions.

### 3.1.1 Details of the Processes Carried out in this Work

In this work, the graphene growth carried out in ultra high vacuum was conducted in a molecular beam epitaxy (MBE) machine. This machine has a base pressure of typically $10^{-10}$ mbar at the growth temperatures used. The heating is carried out using a carbon filament heater, which is used to radiatively heat the sample to a maximum possible temperature of 1550°C, this temperature is measured via a thermocouple connected to the sample manipulator, this thermocouple had previously been calibrated using optical pyrometry. For annealing purposes the silicon carbide wafers, that are typically 3-inch diameter, semi-insulating wafers from Cree and are for the most part diced into 5 mm × 10 mm chips (some chips are larger/smaller than this, all fit within the 10 mm × 10 mm size range), these chips are then mounted into a molybdenum plate sample holder as shown in Figure 3.1(a) for annealing. During the annealing process, both the carbon-terminated and silicon-terminated faces will undergo graphitisation.

In-situ low energy electron diffraction can then be used to determine whether graphitisation has taken place and the sample is either removed for further examination or annealed again for further growth. As shown in Figure 3.1(a) the edges of the silicon carbide chip are in contact with the molybdenum sample holder, whereas the central regions are open to the ultra high vacuum. Therefore it was been observed (33) that a temperature gradient exists over a typical 5 mm × 10 mm sample such that more graphene growth occurs at the hotter edge regions than at the cooler central regions.

As discussed earlier in section 2.2.3, it has been shown that by confining the space above the silicon carbide during the annealing process (34) the rate of silicon desorption from the surface is slowed down, resulting in the production of better quality graphene. In our system, the face of silicon carbide pointing towards the heating element is somewhat confined already as shown in Figure 3.1(b), and a difference is observed between graphene films grown pointing towards the heater and away from the heater. Further confinement was introduced via the use of a sapphire cap placed above the sample during annealing as shown in Figure 3.1(c).(28; 33) So it is therefore important to decide which sample face is the target face before carrying out the annealing process.

## 3.2 High Temperature Tube Furnace

It has been shown that high temperature annealing processes, conducted in either inert gas atmospheres or in active gas mixtures, can be used to improve the quality of epitaxially grown graphene. This can include improving the quality of the silicon carbide surface prior to graphene growth via processes such as hydrogen etching,(29; 128; 129) or the graphene growth process itself can be carried out in inert gas conditions with beneficial results.(25; 26; 27) Post-graphene growth processes, such as preferential track etching with metallic nanoparticles have also been carried out in furnace systems under active (hydrogen) gas atmospheres.(63; 65) With these findings in mind, it was decided that in order to progress in improving the quality of our graphene films and to investigate possible band-gap

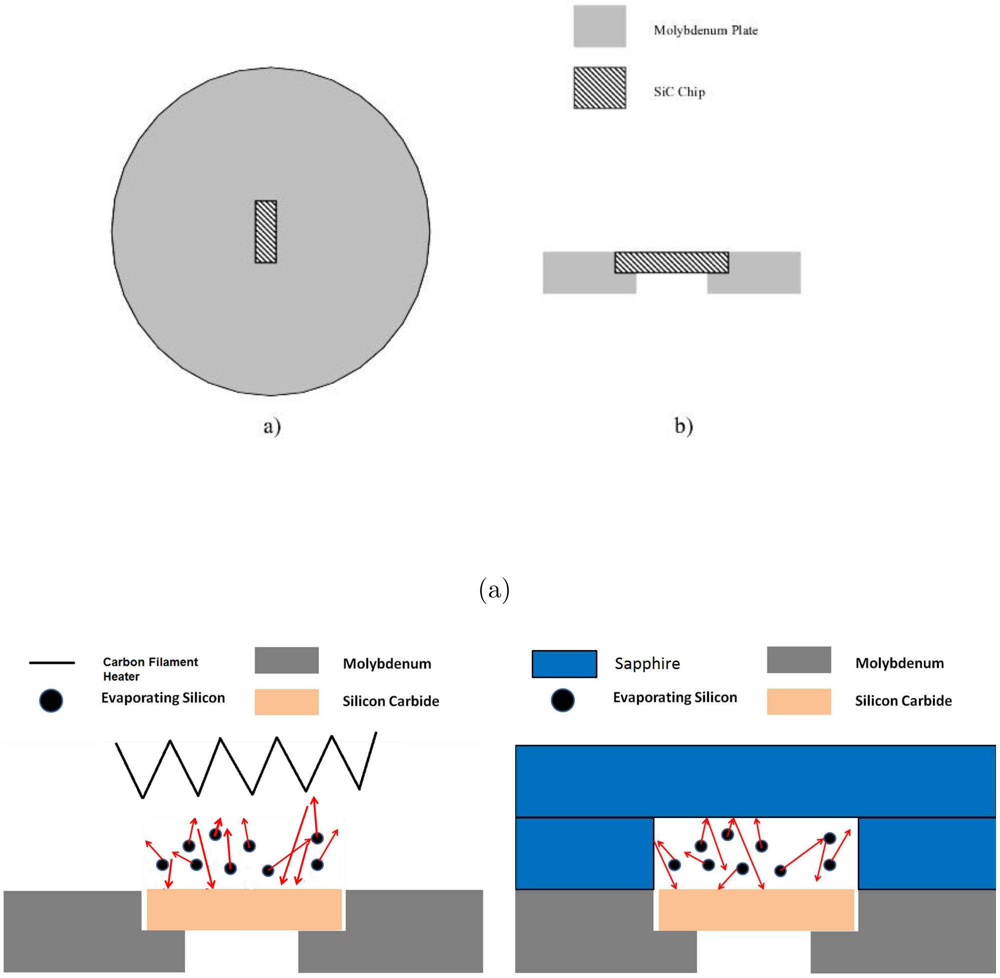

(a)

(b)

(c)

Figure 3.1: a) Schematic of the MBE (UHV) molybdenum sample holder. b) Schematic of the confinement under the carbon filament heater. c) Schematic of the confinement under the sapphire cap.

engineering via graphene nanoribbon production, a high temperature furnace system with gas flowing capabilities would be required.

### 3.2.1 System Design

The furnace system would have to be designed in such a way to allow all the processes mentioned above to be carried out. Some key points taken into consideration were:

- Top temperature of at least 1600°C (high enough to allow sample graphitisation and hydrogen etching)
- The ability to flow hydrogen gas through the system (to allow hydrogen etching procedures to be carried out)
- A dedicated argon gas line for the system (to allow graphene growth under inert gases)
- Ability to measure the gas flow (for control purposes)
- Ability to measure the pressure (for safety and control purposes)

With these taken into consideration along with various health and safety protocols the plan shown in Figure 3.2 was drawn up and constructed. The design of the gas lines was carried out by myself and the installation of these lines carried out by workshop technicians withing the department. The tube furnace itself is a MTIXTL-GSL-1700X-80 furnace.(130) The furnace has a top operating temperature of 1700°C and the tube is made out of high purity alumina (99.8 percent purity).(130) Alumina of this grade is very stable within the operating temperatures of the furnace system, however in order to stop the tube shattering, the maximum ramp rate in temperature allowed with the furnace is 5 °C/minute. It has been seen that slow ramp rates, especially during the cooling process can be beneficial (131) to hydrogen etching silicon carbide, though most graphene growth processes carried out in inert atmospheres elsewhere have fast ramping rates both up to and down from the chosen growth temperature.(26)

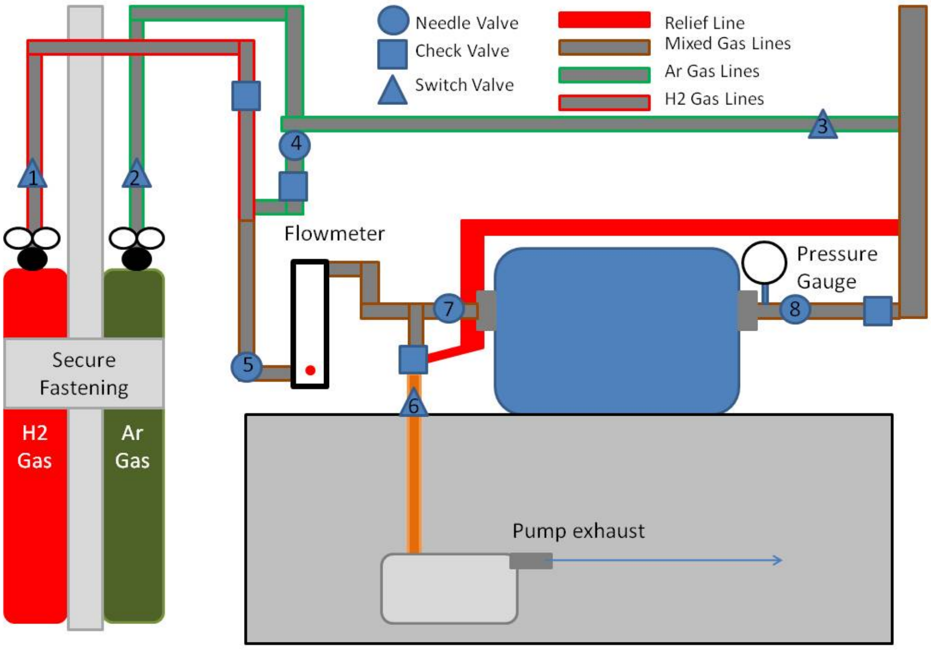

Figure 3.2: Schematic of the furnace set-up.

The system is fitted with a mechanical rotary pump to allow flush and pump purging of the tube prior to annealing runs. Annealing in vacuum conditions is not possible as it leads to warping and bending of the tube, which can ultimately lead to a tube fracture/failure. It has been found that a flush and pump with 10 repeats is sufficient to limit contamination during annealing procedures. The gas used during the flush and pump is always grade N6.0 argon as provided by BOC gases. It was found that using lesser grades of argon lead to oxidation of the silicon carbide wafers during annealing above temperatures of ∼1200°C.

To further protect the samples from oxidation and contamination during annealing, a graphite sample holder was designed as shown in Figure 3.3(a) and 3.3(b). The carbon sample holder allows the sample to be annealed within a gas flow whilst maintaining a confined space around the sample, a technique which has been used elsewhere to grow high quality epitaxial graphene.(34) The holder is cut into the dimensions shown in Figures 3.3(a) and 3.3(b) from a block of high quality graphite from Olmec Advanced Materials LTD with a maximum impu-

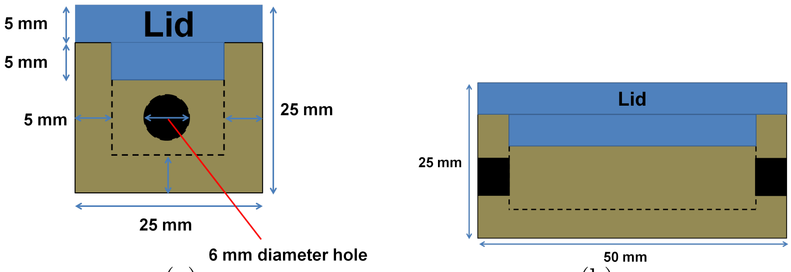

(a)

(b)

Figure 3.3: a) Schematic of the furnace graphite sample holder (front on view). b) Schematic of the furnace graphite sample holder (side on view).

rity level of 200 ppm. Previous to using the carbon sample holders, open alumina ceramic boats were used. Switching to the carbon sample holders resulted in a great improvement in sample quality. With a switch between obtaining highly contaminated (notably oxidation) samples to samples showing expected and desired morphologies.

## 3.2.2 Furnace processes

### 3.2.2.1 Argon annealing

It has been shown (25; 26; 27) that annealing silicon carbide in inert gas atmospheres as opposed to ultra high vacuum can lead to improvements in the quality of the graphene produced. The principle is similar to the use of inert gases to extend the lifetime of lightbulb filaments. With the gas present, the silicon evaporating away from the surface of the silicon carbide has a finite possibility of being scattered back towards the surface as shown in Figure 2.3. This effectively slows down the rate of silicon desorption from the surface and hence raises the temperature at which graphene formation begins. Silicon carbide undergoes a number of surface reconstructions at temperatures between 800°C and 1200°C,(18) in ultra high vacuum the onset of graphene growth typically occurs around 1100°C meaning that growth occurs at the same time as surface reconstructions, this leads to poorer graphene growth.(26) The presence of argon gas raises the graphene growth onset temperature to around 1500°C, thus decoupling the graphene growth process from the surface reconstructions of silicon carbide, hence leading to better quality graphene growth.

When carrying out argon annealing processes the system is again flushed and pumped ten times with argon gas to avoid sample oxidation and contamination. A flow of argon is then maintained throughout the annealing procedure, with a flow rate of typically 1.5 slm (standard liters per minute). This ensures that all the gas within the tube is replaced roughly every 3 minutes. It was found that sample oxidation and contamination could be further reduced by the use of a carbon sample holder as shown in Figures 3.3(a) and 3.3(b). The samples are placed into the sample holder then the holder placed into the center of the furnace. The samples are then heated to a pre-programmed schedule, typical annealing temperatures are between 1000°C and 1700°C with final annealing times between 5 and 60 minutes. To avoid shattering the ceramic tube, a slow heating and cooling rate of 5°C per minute is maintained. During cooling, when the temperature falls to around 700°C the flow of argon is stopped and the sample is left to cool in a slight over-pressure of argon gas. Once cooled, the samples can then be removed for analysis.

As described earlier within the furnace design section 3.2.1 the furnace system is capable of high temperature anneals under hydrogen rich atmospheres. However, due to results discussed within Chapter 6, where beneficial substrate preparation was obtained via annealing processes carried out under argon gas, work on annealing in hydrogen gas has yet to be carried out.

## 3.3 Raman Microscopy

### 3.3.1 Basic Raman Theory

Raman microscopy has been shown to be a very powerful tool in the analysis of carbon based materials including carbon nanotubes,(60; 132) bulk graphite materials, (133; 134) and graphene.(60; 101; 135; 136) Raman microscopy is used to probe excitations present within a chosen sample, these excitations can include vibrational, rotational and electronic excitations if these excitations result in a change of polarizability of the electron cloud.

During the procedure a laser is shone on a sample, this incident light can then interact with excitations present within the sample. These interactions cause a shift in energy level of the incident photons, this shift either up or down in energy level then gives information about the nature of the excitations in the sample. This information is gained by analyzing the wavenumber shifts between the incident photon energy and those of the inelastically scattered photons.

The scattering of a photon to a higher energy state is called Stokes scattering and scattering into a lower energy state is anti-Stokes scattering, the energy level diagrams for these processes can be seen in Figure 3.4. As anti-Stokes scattering requires the vibrational states to be out of the low energy states, anti-Stokes scattering is much less likely to occur than Stokes scattering. The population levels of the vibrational states can be calculated using a Boltzmann distribution,(137) this means that the relative intensities between Stokes and anti-Stokes peaks in Raman spectra will be dependent on the temperature and the differences in intensity between the Stokes and anti-Stokes scattering can be used to measure the temperature of a system.(137)

Although the Stokes scattering is more intense and generally more widely used in Raman spectroscopy than the anti-Stokes scattering, there are occasions when measuring the anti-Stokes side of the Raman spectrum is beneficial. For example if the sample under observation fluoresces at a frequency that affects the Stokes spectrum, then the anti-Stokes spectrum can be used to avoid this interference.(137) Both Stokes and anti-Stokes scattering is much less intense than the elastic process of Rayleigh scattering. For this reason a key component of any Raman system is the filtering out of the Rayleigh scattered light.

The inelastic scattering processes occur when the vibrational mode excited results in a change in molecular polarizability,(137) this causes an energy transfer to occur between the incident photon and the molecular vibration, and therefore an inelastic scattering process. This is the 'basic selection rule' for Raman scattering processes and it suggests on a simplistic level that symmetric vibrations will produce the most intense Raman bands as in general they alter the molecular polarizability.(137)

Another important feature of Raman spectroscopy which also plays a key role in the understanding of graphene Raman spectra is the process of resonance

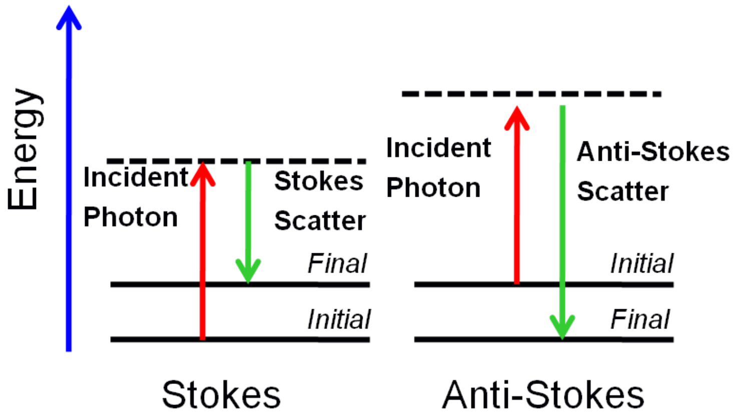

Figure 3.4: Schematic of the energy level changes involved in Stokes and anti-Stokes scattering. The dashed line indicates the virtual state. Adapted from (137).

Raman scattering.(135; 136) Resonant Raman scattering occurs when the laser frequency used is the same energy as an electronic transition, scattering enhancements in the range of $10^6$ are possible. The resonance scattering process is shown in Figure 3.5.

To obtain resonance Raman scattering, a laser beam is chosen which has an energy close to that of an electronic transition. Ideally this would be carried out using a tuneable laser and the laser frequency would be purposefully chosen to correspond to the energy difference between the ground vibrational state and the first or second vibronic state of the excitation state (shown in Figure 3.5). It is fortunate that the maximum resonance scattering is not required for some enhancement to be observed, and practically it is simpler to use a laser line already available in the laboratory to carry out the experiments, as long as this laser frequency is close to the resonance frequency then some enhancement will be seen.

A simplified schematic of a typical Raman spectrometer setup can be seen in Figure 3.6. A monochromatic light source, typically a laser light anywhere in the range of near infra-red light to ultra violet light, is focused onto a sample via a series of mirrors and microscope lenses. This light then is scattered, both

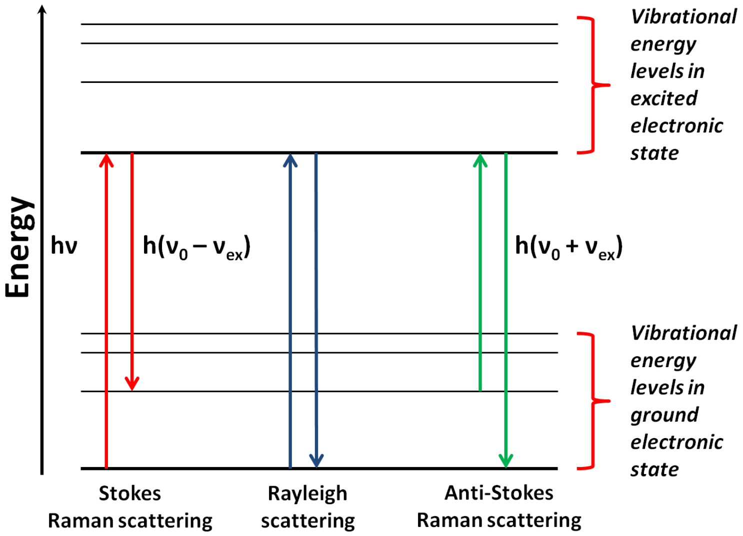

Figure 3.5: Schematic of the energy level changes involved resonance Raman scattering. $\nu_0$ is the frequency of the laser light. Adapted from (137).

inelastically and elastically by the sample. This scattered light (green arrows in Figure 3.6) is then sent via a series of mirrors, to a 2 way mirror where it is then split away from the incident laser beam. The scattered light is then filtered via the use of notch and edge filters, to remove the Rayleigh scattered light. The inelastically scattered light is then split into its constituent wavelengths using a diffraction grating and a charge coupled detector (CCD) is used to measure the wavenumber shifts and intensity of the scattered light, this information then forms the Raman spectrum of the sample.

### 3.3.2 The Raman Spectrum of Graphene

In graphene there are three key Raman bands as shown in Figure 3.7 and Figure 3.8. These are the D band, the G band and the 2D band. The G band is linked to the stretching of C-C chains (101) as shown in Figure 3.9(a), the D band is associated with the breathing mode vibration of a benzene ring as shown in Figure 3.9(b) with the 2D band being the 2nd overture of this vibration.(101) The D band is not present in pristine graphene, the mechanism requires the presence of

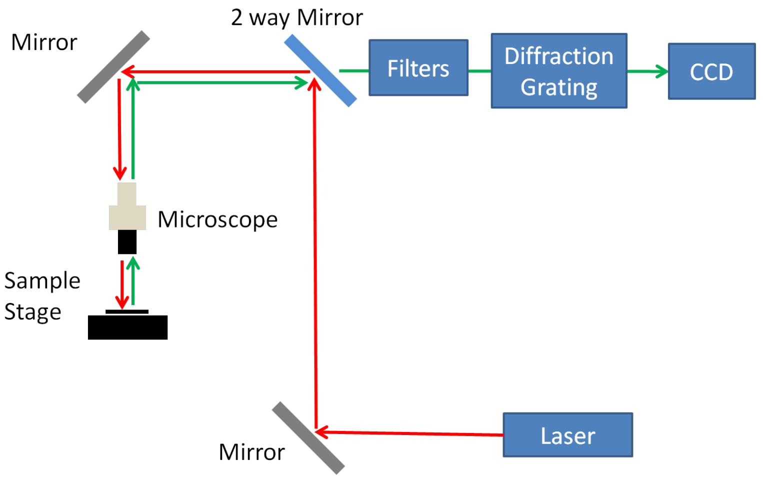

Figure 3.6: Schematic diagram of a Raman system setup. Adapted from (137).

a defect in order for energy and momentum to be successfully conserved during the process. The D band is a double resonant Raman process and consists of 4 steps. (i) A laser induced generation of an electron-hole pair, (ii) Electron-phonon scattering with an exchanged momentum q $\sim$ K, (iii) Electron scattering from a defect. The recoil from this interaction absorbs the momentum of the electron-hole pair, (iv) Electron-hole recombination. So without the presence of a defect, step (iii) would be absent and energy and momentum would not be conserved, and the D band would be absent. The 2D band is present in the absence of defects as the process involves two phonons with opposite momentum so momentum is always conserved, even in the absence of defects.(135; 136)

### 3.3.3 Using Raman Microscopy to Measure Grain Size in Graphene

The dependence of the D band on the presence of defects allows this band to provide a measure of the quality of graphene present. Tuinstra and Koenig (134) showed in graphite samples that the D band was absent in defect free graphite, and that the ratio in intensity of the D band peak compared to the G band peak was inversely proportional to the lateral grain size of the graphite crystals ($L_\alpha$)

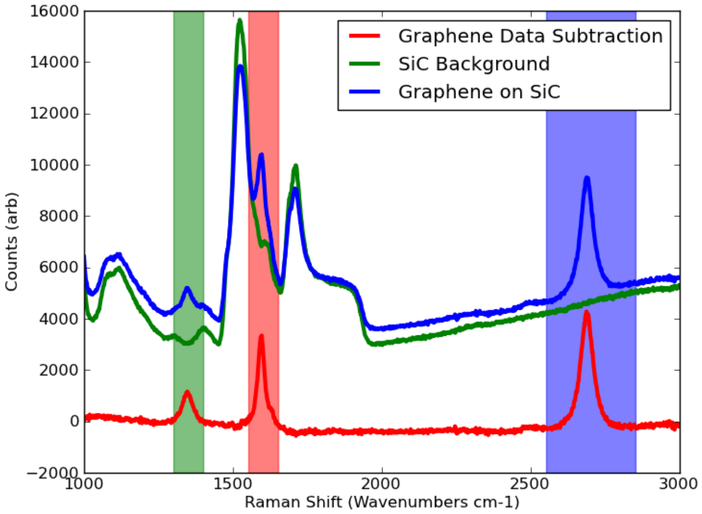

Figure 3.7: Raman data from: a sample annealed at 1450°C for 20 minutes in ultra high vacuum (Graphene on SiC), an unannealed SiC wafer (SiC Background) and the subtraction of the previous two sets of data (Graphene Data Subtraction). The shaded areas correspond to the positions of the main graphene Raman bands: D band (Green), G Band (Red) and 2D Band (Blue).

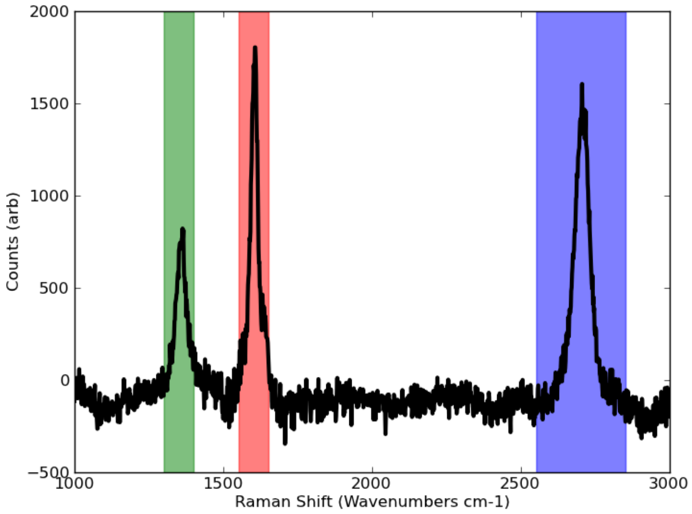

Figure 3.8: Raman data from: a sample annealed at 1450°C for 20 minutes in ultra high vacuum. All data is 'Graphene Data Subtraction' datae. The shaded areas correspond to the positions of the main graphene Raman bands: D band (Green), G Band (Red) and 2D Band (Blue).

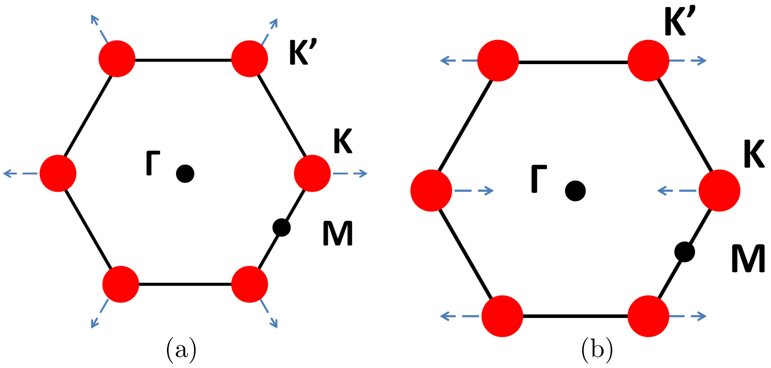

Figure 3.9: a) Schematic of the vibrational mode corresponding to the Raman G band in graphene. b) Schematic of the vibrational mode corresponding to the Raman D band in graphene. Adapted from (101).

within the graphite films.(134)

This corresponds to the amount of edge or boundary present within the films, this makes Raman very useful in measuring the grain sizes present within epitaxial graphene samples on silicon carbide (138; 139), the grain size is given by,

$$L_\alpha(\mathrm{nm}) = (2.4 \times 10^{-10})\lambda_i^4(I_D/I_G)^{-1} \tag{3.1}$$

where $\lambda_i$ is the wavelength of the incident laser light, $I_\mathrm{D}$ and $I_\mathrm{G}$ are the integrated intensities of the D and G bands respectively.(138; 139) The larger the lateral grain size, the better quality of graphene is present, as such Raman can be used as a check of sample quality in epitaxial graphene films.

It is also important to note that as shown in Figure 3.7 that the second order silicon carbide peaks mask the underlying graphene G and D bands, meaning that a subtraction of a blank silicon carbide reference spectrum is required to obtain the graphene data, and this can often affect the graphene peak data.

### 3.3.4 Using Raman Microscopy to Measure Strains Within Graphene Sheets

The theory of how Raman microscopy can be used to measure strain values will be described in great detail within Chapter 5. As a quick summary, a compressive strain acting in-plane on a graphene film will cause phonon hardening of the in-plane 2D breathing mode, this means that the vibration requires more energy to occur, thus causing the position of this Raman band to shift to higher wavenumbers. Typical Raman spectra taken during this work are shown in Figures 3.7 and 3.8, the silicon carbide substrate spectrum overlaps and somewhat dwarfs the graphene spectrum in the wavenumber range containing the graphene G and D bands, however the Raman 2D band in graphene is relatively unaffected by the silicon carbide substrate spectrum. For this reason, the position of the 2D band was used during this work.

### 3.3.5 Raman G Band Splitting

During the taking of Raman spectra from epitaxial graphene samples grown under argon gas atmospheres (section 7.2.1.2) a splitting of the G band is observed. An

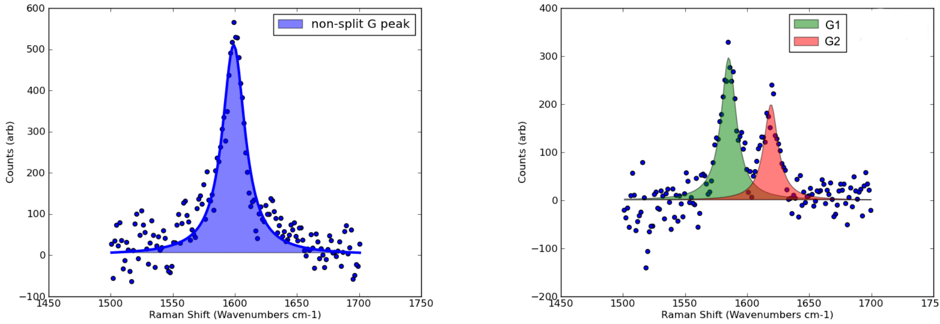

(a) (b)

Figure 3.10: a) Data from epitaxial graphene grown on SiC(0001) in ultra high vacuum showing no G peak split.(b) Data from epitaxial graphene grown on SiC(0001) in an argon atmosphere showing evidence of G peak splitting.

example of G peak splitting can be seen in Figure 3.10 which shows G peak data from epitaxial graphene grown under different growth conditions. These samples show differing G peak spectra. For the sample grown in ultra high vacuum (Figure 3.10(a)) there is no evidence of G peak splitting, as expected for a pristine graphene sample and the data is fitted with a single Lorentzian function. However for the sample grown under an argon atmosphere (Figure 3.10(b)) the G peak is split into two distinct components and now needs to be fitted by a double Lorentzian function.

As mentioned earlier, the C-C stretching mode is responsible for the G peak ($\Gamma$ - $E_{2g}$ phonon). The $E_{2g}$ consists of 2 modes, the transverse optical mode (TO) and the longitudinal optical (LO) mode. In pristine graphene these modes have the same vibrational frequency (132) thus resulting in a single peak. As will be discussed in great detail during section 7.2.1.2, external effects such as strains, (99; 100) confinement (132) and curvature (132) have been observed elsewhere to contribute to the TO and LO phonons having differing frequencies and therefore causing a split in the G band.

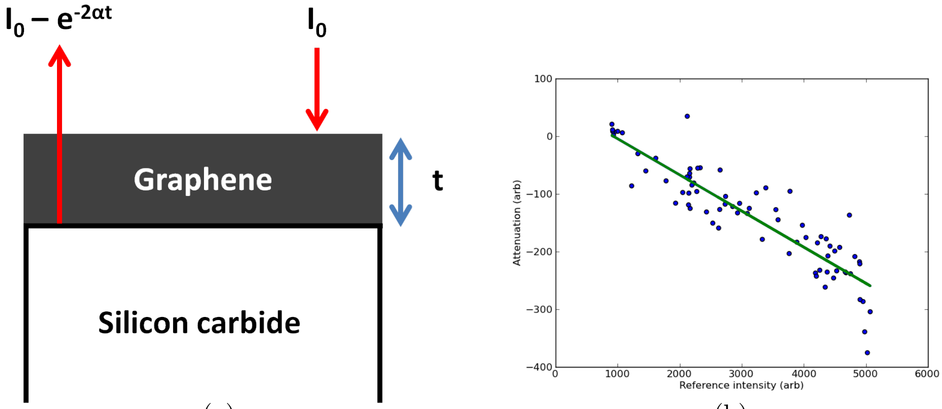

(a) (b)

Figure 3.11: a) Schematic diagram showing how the silicon carbide signal is attenuated by graphene overlayers, adapted from (140). b) Example plot of the attenuation of silicon carbide signal from a sample with graphene over layers against the intensity of the silicon carbide reference spectrum in order to extract a thickness value.

### 3.3.6 Using Raman Microscopy to Measure Thickness of Graphene Films

When producing epitaxial graphene films it is important to know the thickness of graphene present. Raman microscopy has been shown to be able to provide estimates on these thickness values that are comparable to those obtained by other techniques.(140) One method, utilizes the Beer-Lambert law to compare the intensity of an un-attenuated silicon carbide reference spectrum ($I_{\mathrm{ref}}$) to that of an attenuated silicon carbide signal from a sample with graphene on top ($I_{\mathrm{sample}}$) as shown in Figure 3.11(a). The incident laser intensity ($I_0$) is attenuated by a factor of $e^{-2\alpha t}$ as it passes through the graphene film of thickness, $t$. $\alpha$ is the absorption coefficient ($\alpha \sim 0.02$) for graphene and the factor of 2 comes from the beam passing through the graphene film twice.

Experimentally, a reference silicon carbide spectrum is taken from the same wafer that graphene growth has taken place on (ideally this could be the same chip as the growth, after plasma etching to remove the graphene), an annealed sample, that has undergone graphitisation is then analysed. A subtraction of the sample spectrum from the reference spectrum is then made ($I_{\text{ref}} - I_{\text{sample}}$). It can then be shown that

$$\frac{I_{\text{sample}}}{I_{\text{ref}}} = \exp(-2\alpha t) \tag{3.2a}$$

$$\frac{I_{\text{ref}} - I_{\text{sample}}}{I_{\text{ref}}} = -2\alpha t \tag{3.2b}$$

Equation 3.2b shows that plotting $I_{\text{ref}} - I_{\text{sample}}$ against $I_{\text{ref}}$ should produce a straight line graph as shown in Figure 3.11(b) and a value for the thickness ($t$) can be obtained from the gradient of this line. The data for this plot is typically taken around a peak feature in the silicon carbide spectrum to increase the attenuation affect.(140) As the laser light penetrates deeper than say, electrons used in Auger spectroscopy, and elastic electrons emitted during x-ray photoelectron spectroscopy, the use of Raman microscopy for thickness estimates is particularly useful for thick graphene samples (10+ layers).(140)

There are other methods for estimating graphene thicknesses with Raman. These include tracking the number of peaks used to fit the Raman 2D peak (135) and tracking the width of the 2D peak fit. Both these methods are somewhat dependent on the substrate present and are not directly applicable to all epitaxial graphene samples, so work here on thickness estimates with Raman microscopy has concentrated on the attenuation method described here.

### 3.3.7 Details of the Raman Systems Used in This Work

In this work, the Raman microscopy has been carried out on two main systems. The majority of Raman data has been taken using a Renishaw microspectrometer with the sample excited using a 633 nm HeNe laser. The laser power was typically 4 mW with a spot size of ~4 $\mu$m, which was focused with a 50× lens. The spectral resolution in this system can be estimated to be ~6 cm$^{-1}$ based on the full width at half maximum of a silicon 520 cm$^{-1}$ peak. For probing sample uniformity, this system is equipped with a coarse XY stage, which allows different areas of a typical 5×10 mm sample to be examined. The second system is an Horiba microspectrometer. This system is equipped with both a 633 nm red laser as well as a 532 nm green laser. This system has a smaller spot size of ~1 $\mu$m owing to a confocal microscope with 50× microscope. For probing sample uniformity, this system also possesses a manual XY stage for taking course measurements across samples. The system can also take Raman map data with a maximum scan size of 40 $\mu$m × 40 $\mu$m, allowing for Raman data comparisons to be made with other microscopy techniques, such as atomic force microscopy and low energy electron microscopy that have similar scan ranges.

Scan times and ranges varied on the aim of the particular experiment and on the specific conditions at the time. Samples if deemed too 'dirty' or contaminated can be cleaned with acetone and isoproponol prior to scanning. Regular calibrations of the systems are carried out using inbuilt procedures and reference samples, such as silicon, to ensure that experimental runs remain consistent.

## 3.4 Atomic Force Microscopy (AFM)

### 3.4.1 AM-AFM Experimental Setup and Feedback Control

In amplitude modulated atomic force microscopy (AM-AFM), a sharp probe (ideally one atom radius) is oscillated above, but very close to, a sample surface. This probe, often referred to as a tip, is situated at the end of a microcantilever. This microcantilever is mechanically excited at a fixed frequency, at or close to the first flexural resonant frequency. As the tip is close to the sample, there are tip-surface interaction forces, these forces cause the amplitude of the oscillation to be reduced from its free value. The observables from an AM-AFM experiment are the amplitude of the microcantilever oscillation and the phase difference (lag) between the microcantilever external excitation and the actual tip motion.

The main components of an AFM system are shown in Figure 3.12. In general there are five main components to any general AFM system. They are the cantilever-tip system, a detection system, a tip-sample motion system, the feedback controller and finally the image processing and display system. The first three of these components are usually housed in a single unit, usually named the microscope base.(141)

As the name suggests, the modulation of the free amplitude of the microcantilever is used as a feedback parameter in order to map out the topography of

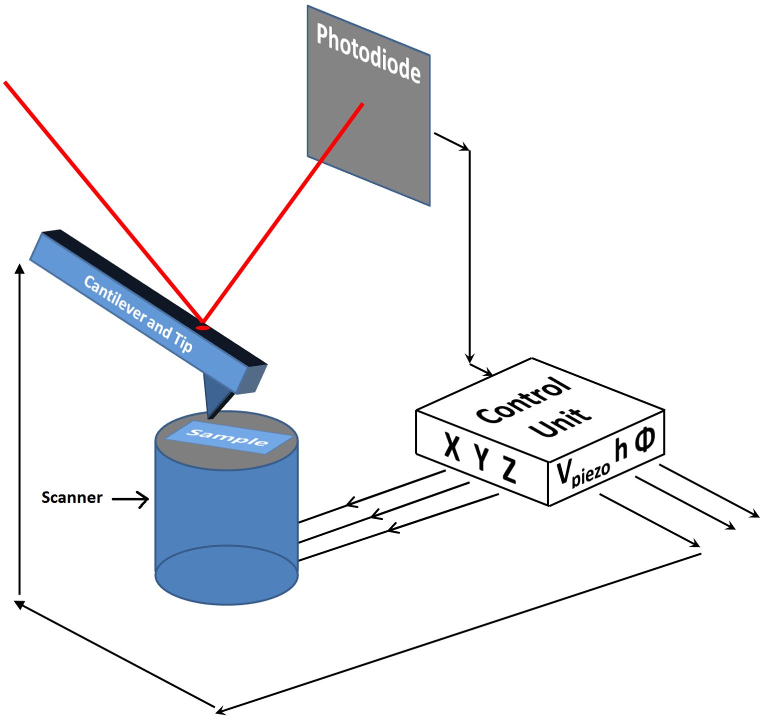

Figure 3.12: Schematic of the basic components of an amplitude modulation atomic force microscope. Adapted from (141).

the surface. In AM-AFM there are two different imaging regimes, the attractive and repulsive regimes. The attractive (repulsive) regime is defined as when the force between tip and sample surface negative (positive). Assuming the chemical composition of the tip-sample interface remains constant, the force exerted by the tip on the sample depends on several key factors. These include the free amplitude of the cantilever oscillation, the radius of the tip, the chosen value for the amplitude to run the feedback and the imaging regime.

The feedback controller in AM-AFM maintains the free amplitude at a fixed value whilst the tip is either held at a fixed position on the sample surface or is scanned across the sample.The circuitry used in an AM-AFM feedback controller can be seen in Figure 3.13. A lock-in detector returns a signal related to the detection amplitude and phase of the input at the chosen excitation frequency or its harmonics. The process for maintaining a constant amplitude involves comparing the instantaneous values of the amplitude $\mathrm{A_i}$ to a reference, or set-point amplitude value ($\mathrm{A_{sp}}$). The aim of the feedback loop is to keep the error signal $\mathrm{A_{sp}}$ - $\mathrm{A_i}$ as small as possible. This is done by feeding the error signal through the proportional-integral-differential system. The output from this sends a signal to the z-piezo scanner, this causes the z-piezo to either approach or withdraw the tip in order to minimise the difference between $\mathrm{A_{sp}}$ and $\mathrm{A_i}$. The maximum scan speed for an AFM system is set by its feedback loop, frequency loops in the MHz range are now available.(142)

The bending of the tip-cantilever system caused by the tip-surface forces is most-commonly detected with the use of an optical beam deflection method.(141) In this method, a laser light is shone onto the back of the tip-cantilever system, the reflection of this beam is then monitored by a position sensitive photodetector consisting of several photodiodes, this process is shown in Figure 3.12. The photo-currents produced by the detectors are fed into a differential amplifier, this generates an output signal in volts. Normal and lateral forces can be detected by the use of four-segmented photodiodes.(141)

In order to perform an AM-AFM scan, both the cantilever-tip system and tip-sample system need to be in motion. To excite the cantilever oscillation a dither piezo is used, that is glued at the clamped end of the cantilever. For tip-sample motion, the most common method is to use a tube scanner. This is a hollow,

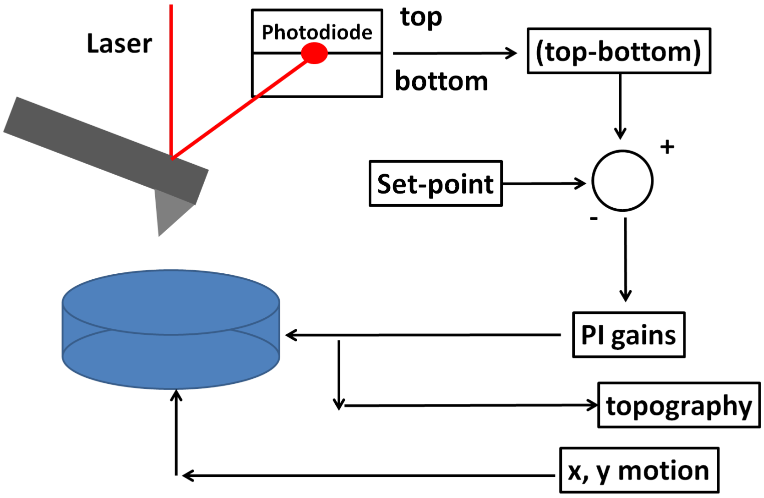

Figure 3.13: Schematic of the basic components used in the feedback circuitry used in amplitude modulated atomic force microscope. Adapted from (141).

segmented tube that allows motion in the x,y and z planes. It can be situated either above or underneath the sample surface. Piezoelectric actuators provide high accuracy in positioning with subangstrom precision. Piezoelectric actuators do have drawbacks. The relationship between applied voltage and displacement is not linear. Problems such as creep, aging, hysteresis and thermal drift also affect the accuracy of the piezoelectrics. Software based corrections and regular calibrations help to improve the accuaracy of the piezoelectrics.(141)

### 3.4.2 Topological and Phase imaging

To understand the dynamics of the tip-surface interaction, there are a number of models, a good review of these models can be found in a book by Garcia (141). Here I will concentrate on the model which describes the tip-cantilever system as a driven simple harmonic oscillator and the tip-surface interactions as perturbations on this harmonic oscillator behavior. This is by no means an exhaustive explanation of the tip-cantilever and tip-surface interactions and more in-depth explanations can be found here (141; 143).

The solutions of the equation of a driven simple harmonic oscillator provide many explanations and concepts needed to describe the processes involved in dynamic AFM.(141; 143) The motion of a driven simple harmonic oscillator is described by

$$m\ddot{z} = -kz - \frac{m\omega_0}{Q}\dot{z} + F_0 \cos \omega t, \tag{3.3}$$

where $\mathrm{F}_0$ and $\omega$ are the amplitude and frequency of the driving force respectively; m,Q,$\omega_0$, and k are, respectively, the effective mass, quality factor, angular natural frequency (undamped), and the force constant of the free cantilever.

At low driving frequencies with respect to the free resonant frequency, the response is then controlled by the stiffness of the spring. The oscillator moves in step with the driving force, with an amplitude close to $F_0/k$. At high driving frequencies that are very large with respect to $\omega_0$, the term $kz$ is small compared to $\ddot{z}$, here the response is controlled by inertia. In this case, a relatively small oscillation amplitude should be expected with a phase shift of 180° between the acceleration of the harmonic oscillator and the displacement.

If damping is introduced to the driven simple harmonic oscillator, there are 3 distinct regimes. (141; 143) The most relevant of these regimes to understanding and modeling dynamic AFM is the underdamped regime. Here $\frac{1}{2}Q < 1$, and the solution in the underdamped regime has a transient term and a steady motion and is described by

$$z = B \exp(-\frac{\alpha}{2}t) \cos(\omega_r t - \beta) + A \cos(\omega t - \phi), \tag{3.4}$$

where $\alpha = \omega_0/Q$.

Initially, both the transient and steady motion are prominent; however the transient term is reduced by a factor of $1/e$ after a time $2Q/\omega_0$. The steady motion is a sinusoidal function (harmonic) that oscillates with the excitation frequency $\omega$ and has a phase lag with respect to the driving force. The transient term oscillates with a frequency $\omega_r$, this should be considered the new resonant frequency. The damping ($\alpha$) modifies the resonant frequency of the harmonic oscillator.

The damping of the oscillator introduces a phase lag ($\phi$), the behavior of which with differing drive frequencies and cantilever Q factors is shown in Figure 3.14(b). The behavior of the amplitude of the damped oscillator with varying

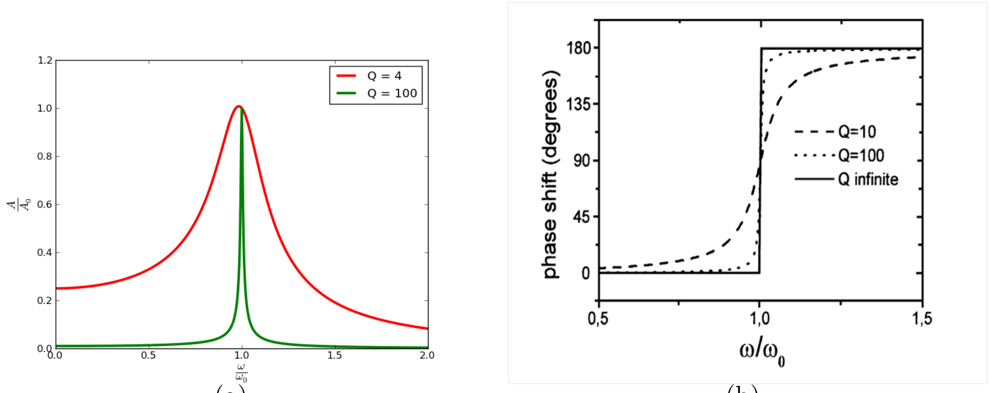

(a) (b)

Figure 3.14: a) Dependence of the amplitude as a function of excitation frequency for a forced harmonic oscillator with damping. Adapted from (141). b) Dependence of the phase shift as a function of excitation frequency for a forced harmonic oscillator with damping, taken from (143). Curves for different Q factors shown.

drive frequency and cantilever Q factor is shown in Figure 3.14(a). During imaging surface with AM-AFM it is common to acquire three types of image, these are related to the phase, amplitude and height of the cantilever as it is scanned across the surface. In this work, height (topography) and phase images are used. In order to produce height (topography) images, the height of the cantilever from the surface is tracked whilst the amplitude remains fixed. Phase images are produced by plotting the phase shift of the oscillation whilst tracking the surface topography at a fixed amplitude. The phase shift image is acquired simultaneously to the height (topography) image.

The amplitude of the cantilever depends on the sample topography and sample composition.(141) However the phase shift signal depends on the energy transferred from the tip to the sample surface and also on the strength of the interactions. In heterogeneous samples, it has been shown (141) that the phase shifts observed depend on energy dissipation in those regions. Phase imaging can therefore provide a good way of distinguishing areas of differing composition, that may not be always resolvable in height images.(73) It has been suggested that the phase contrast between the silicon carbide substrate and graphene layers comes from differing adsorbate levels on the two materials.(73) This can be very

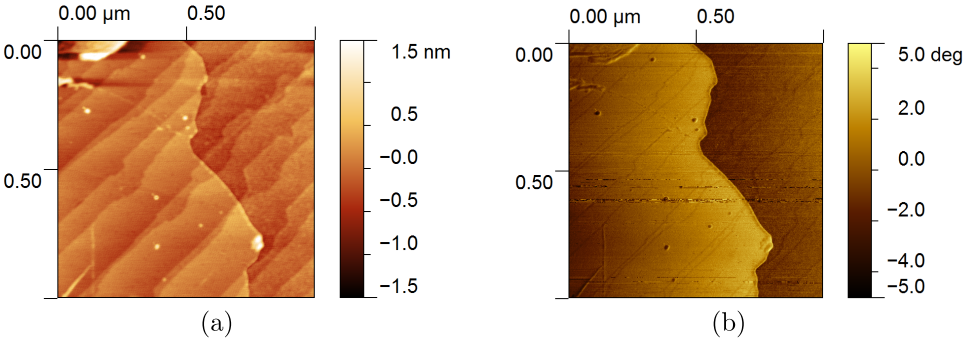

(a)

(b)

Figure 3.15: a) AM-AFM height image of a graphene sheet on a terraced SiC(0001) substrate b) AM-phase height image of a graphene sheet on a terraced SiC(0001) substrate. Large contrast can be observed between the graphene sheet (light) and silicon carbide substrate (dark) in the phase image due to differences in the tip-sample interactions on the two surfaces.

useful when imaging epitaxial graphene samples as the growth mechanism makes absolute height measurements of step heights between the graphene and silicon carbide substrate difficult to measure, making graphene identification difficult, whereas using AFM phase imaging can help distinguish graphene rich areas from bare silicon carbide substrate.(73)

An example of a topographic AFM image of a graphene sheet on a terraced silicon carbide (0001) surface can be seen in Figure 3.15(a). The terraces on the silicon carbide terraces can be seen, and there is a difference in height between the silicon carbide and the graphene sheet, and folds and ripples can be seen in the graphene film (left of image). Figure 3.15(b) shows the phase image of the same region. Now the regions of graphene and silicon carbide show a large contrast with the graphene area on the left looking much brighter (higher phase) than the silicon carbide region on the left.

### 3.4.3 Limitations of AM-AFM

In order to determine the usefulness of a technique for the process it is being used for, its limitations must be understood. In AFM there are a number of different limiting factors that control the overall quality and reliability of the AFM data.

The resolution of an AFM is closely linked to the noise present in the system. For example the overall resolution of an AFM is governed by the noise in the cantilever deflection. Key limitations to understand for results presented in this work are the vertical resolution and the lateral resolution of the system. These are important as they can limit the ability to measure quantities such as lateral grain size and step heights in epitaxial graphene samples.

#### 3.4.3.1 Spatial Resolution

There are a number of factors that contribute to the overall resolution and accuracy of AFM topographic images. A topographic image is mathmatically expressed as a function of height variation $h(x, y)$ on the spatial coordinates $x$ and $y$. So for a good AFM image, the microscope must be able to distinguish between both lateral and vertical resolutions. The effects that can contribute to and limit this resolution such as the electrical and mechanical noise within the system, the apex size of the tip, the tip-surface forces decay length and the surface compliance. AFM imaging is also non-linear, this means that unlike lens-based microscopes, the image of a surface is not the sum of the individual images of the features on the surface. This non-linear nature of the imaging affects the spatial resolution.

The vertical resolution of an AFM image can be thought of as the minimum step height that can be measured on the surface. The vertical resolution ($\delta h_n$) is limited by the noise in the imaging signal ($\delta A$) (amplitude). The vertical noise can therefore be defined as the ratio between the noise in the amplitude signal and the gradient of the amplitude with respect to the average tip-surface distance ($dA/dz_c$),

$$\delta h_n = \frac{\delta A}{|dA/dz_c|}, \tag{3.5}$$

$dA/dz$ varies with differing surface stiffness. For a hard (stiff) surface $dA/dz$ is nearly 1 and the vertical noise is given by the amplitude noise $\delta A$ (or the deflection noise $\delta z_c$). For soft samples $dA/dz$ is in the range $0.2 - 0.5$, as such $\delta h_n$ lies between $2\delta A$ and $5\delta A$. The deflection noise has two major components. These are the thermal noise ($\delta z_{th}$) of the cantilever and the overall detector noise

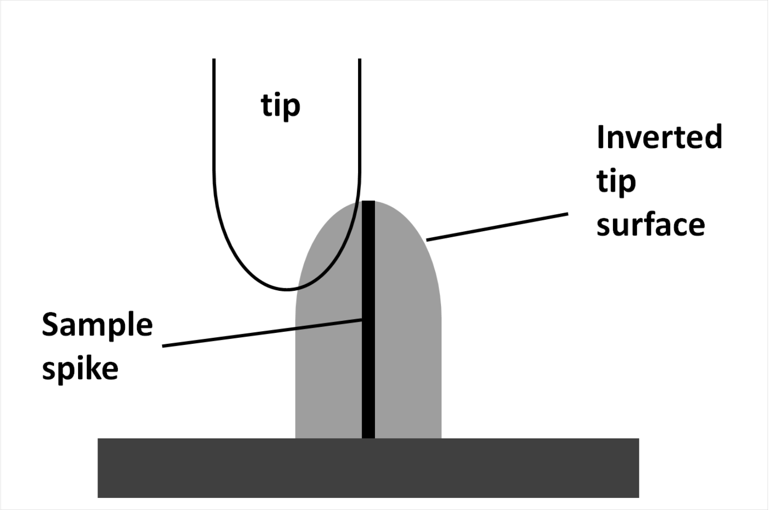

Figure 3.16: Schematic of the distortion caused by the finite tip size when imaging a sharp feature. The observed (apparent) image is the inverted tip surface. Adapted from (141)

($\delta z_{det}$) in the system. As these two sources of noise are statistically independent, they can be added as,

$$\delta A \approx \delta z = \sqrt{\delta z_{th}^2 + \delta z_{det}^2}. \tag{3.6}$$

The optical detector noise is the limiting factor in the overall detector noise ($\delta z_{det}$), if the system is successfully shielded from electromagnetic and acoustic noise then this is the major source of noise. The thermal noise is commonly much smaller than the detector noise.

The total thermal noise can be shown to be,

$$\delta z_{th}(total) = \sqrt{\frac{k_B T}{k}}. \tag{3.7}$$

Where $k$ is the cantilever spring constant. It is important to note that the thermal noise depends on the both the cantilever geometry and the surrounding environment. For example, using cantilevers with a high resonant frequency and a large force constant will lead to decreased noise.

Schematic diagrams to describe the lateral resolution in AFM is shown in Figure 3.16 and 3.17, a definition for the lateral resolution taking into account

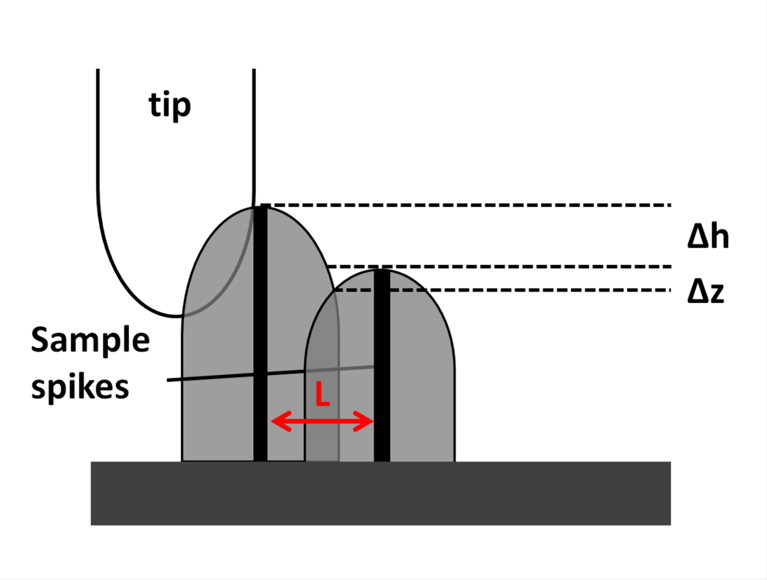

Figure 3.17: Schematic of the AFM imaging process by a tip of finite radius R over two sharp spike features. The minimum resolvable lateral separation between the spikes depends on the height difference between the features (Δh). This height difference and the tip radius R define the dimple depth (Δz). Δz must be greater than the noise to be resolvable. Adapted from (141) and (144)

the finite tip size has been proposed by Bustamante and Keller (144). Here, both the tip and the surface are assumed to be undeformable objects (Figure 3.16). The lateral resolution $l$ is then defined to be the minimum lateral separation at which a dimple depth of $\Delta z$ that occurs due to the intersection of the individual images of two sample features is larger than the noise (Figure 3.17). This definition therefore states that the lateral seperation $l$ between two sharp features that are imaged by a parabolic tip, with an end radius (tip apex) $R$ depends on both the height difference between the two adjacent features $\delta h$, and the vertical resolution $\delta h_r$ such that,

$$l = \sqrt{2R}(\sqrt{\delta h_r}\sqrt{\delta h_r + \delta h}). \tag{3.8}$$

Equation 3.8 illustrates the nonlinear nature of the image formation in AFM. The lateral resolution is shown to be a function of the height difference between adjacent features, therefore, this must be determined separately for each feature in the image. This definition of lateral resolution can be considered to be the AFM analogue of the Rayleigh criterion for resolution in optical microscopy. It is important to note that atomic scale imaging requires very sharp tip apexes (sub 1 nm). The height difference must also be below 0.5 nm for atomic and molecular imaging.

Another factor determining the ultimate lateral resolution of a system is the number of pixels used in the data recording process. If the number of pixels used is taken to be $N_{\mathrm{p}}$, then it follows that for a scan of lateral size $\Delta x$ the lateral resolution in the image can be no better than $\Delta$ x / $\mathrm{N_p}$. So for a 5 $\mu$m scan with 512 pixels (a typical scan parameter used here) the best lateral resolution observable is ∼10 nm.

#### 3.4.3.2 Image Distortion and Surface Reconstruction

Figures 3.16 and 3.17 show how AFM images of non flat surfaces are highly influenced by the finite tip apex size. Distortions induced by the tip are important whenever the surface has features with aspect ratios that are comparable to or sharper than those of the tip apex size.(141) This problem in AFM is known as dilation. When confronted with these issues, most AFM users will either ensure their AFM tip is sharper than the known feature size, or will give all measured width values in terms of the full width at half maximum (FWHM) of the measured width value. Alternatively there are a number of mathematical algorithms for reconstructing true images from data, once the tip geometry is known, a comprehensive list of these algorithms can be found in the reference (141).

Figure 3.18 illustrates the dilation process in AFM. the convolution occurs because the tips apparent and true imaging points are different. The image is formed by the trace of the tip end. The images process assumes that the physical end of the tip is always the closest point to the surface. This is not true when the surface has features that are sharper than the tip apex. Also, when the curvature of a sample feature is greater than the tip curvature, there will be regions where the tip contacts the surface in two positions simultaneously. This is shown in Figure 3.18 and has been shown that these double contact points lead to the

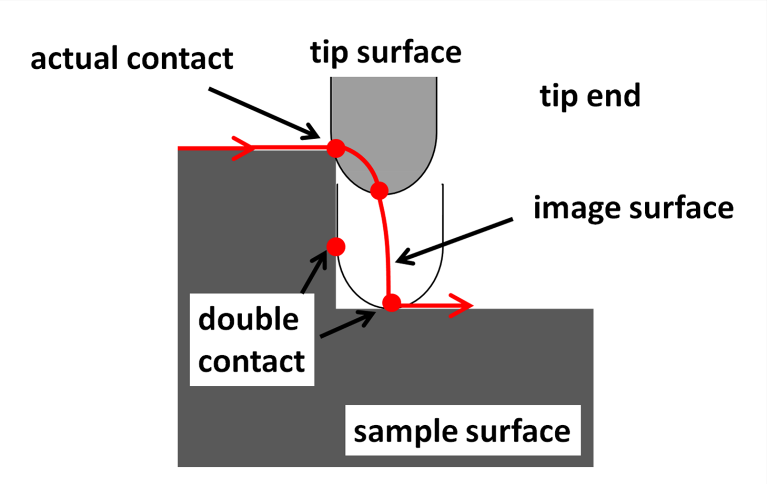

Figure 3.18: Schematic of AFM imaging a step. An image is formed by the trace of the tip end. In some cases, the actualy point of contact may be different from the tip end. In other cases there are two contact points. (141)

existence of unreconstructable regions. It follows that an ideal AFM tip has an apex and sidewalls that are sharper and steeper, respectively, than those of the sample surface.(141)

#### 3.4.3.3 Image Artifacts

Another limiting factor in AFM imaging accuracy that is applicable to this work is the presence of artifacts within the images. Image artifacts can come from a number of sources, image dilation as described above is one such source of image artifacts. A second source of artifacts is that fact that the AFM tip can pick up debris or be damaged in such a way that the single AFM probe contains several nanotips (as shown in Figure 3.19(b)), this causes single features on a sample surface to be imaged multiple times as shown in Figure 3.19(a).

It is important to note that the above factors affecting image quality are not an exhaustive list of all possible limiting factors the AFM imaging, merely a list of those factors deemed most important and of most relevance to the AFM imaging used in this work. Further understanding of AFM limitations can be found here (141).

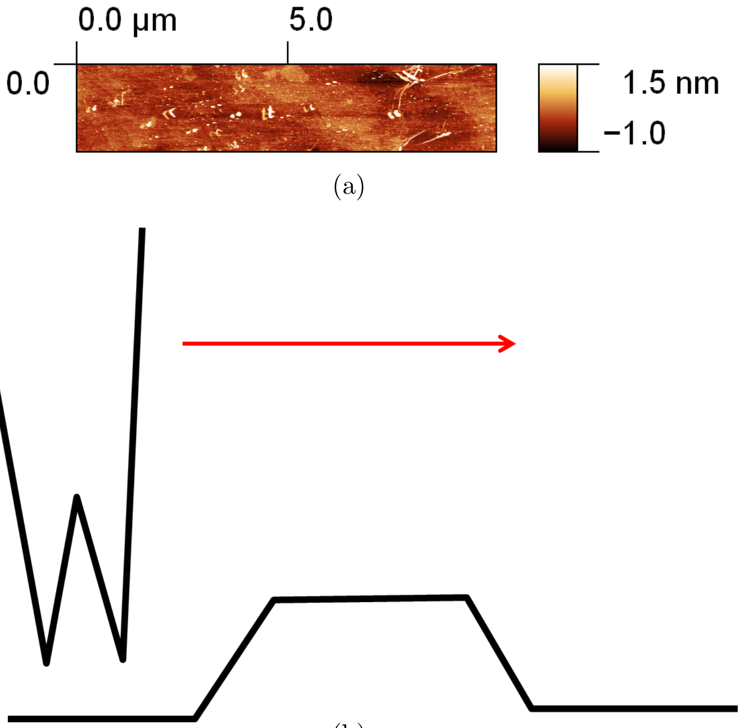

(a)

(b)

Figure 3.19: a) Phase image of an epitaxial graphene sample grown on SiC showing single features (grains) imaged multiple times b) A schematic of the type of tip distortion responsible for this image artifact. Adapted from (141).

### 3.4.4 AFM in Epitaxial Graphene

There are a number of key features in the production of epitaxial graphene on silicon carbide that can be imaged and understood via the use of AFM. One figure of merit for epitaxial graphene growth is the lateral grain size (134; 136; 145) of the graphene crystalline regions that form on the surface, AFM can be used to distinguish this grain size between samples grown under differing conditions. The nature of the substrate prior to graphene growth is very important to the growth process, AFM can be used to measure the topography of silicon carbide wafers before growth and at different points in the growth procedures to check for features such as polishing scratches, atomic steps in the silicon carbide, step bunching on silicon carbide substrates and defects in the silicon carbide such as screw dislocations which can all subsequently affect the quality of graphene produced.

As described above, absolute height measurements between graphene layers and the silicon carbide substrate in order to get a value of graphene thickness and overall graphene coverage on the substrate is difficult as the growth mechanism for epitaxial graphene complicates this measurement. However measurements such as root mean square (RMS) roughness of topographic AFM images can be used as a rough guide to see how uniform (smooth) a sample is and as described above, phase imaging can provide an indication of the sample composition.(73)

### 3.4.5 AFM Systems Used in This Work

Two different AFM systems have been used during this work. The first is a Veeco Multimode and the second a Veeco Nanoman system respectively. Both systems can be used to scan ranges up to a maximum scan size of around 100 $\mu$m × 100 $\mu$m. Typical scan parameters used were scan speeds of 1.5 Hz, free amplitude of 1.2 V and amplitude set points of 0.8 V although this could vary from sample to sample. In most situations, the cantilever is driven either at or close to the resonance frequency. Prior to imaging the samples, if deemed ‘dirty’, would be cleaned with acetone and isopropanol and dried using nitrogen gas.

## 3.5 Low Energy Electron Diffraction (LEED)

### 3.5.1 Basics of Low Energy Electron Diffraction (LEED)

The molecular beam epitaxy machine used for the ultra high vacuum growth of epitaxial graphene is equipped with a low energy electron diffraction (LEED) system. LEED as a technique has be shown to be very useful in the analysis of epitaxial graphene.(17; 18; 19; 21; 78; 146) A schematic layout of a typical LEED system is shown in Figure 3.20, an electron gun consisting of a tungsten-ruthenium filament and accelerating plates (see Figure 3.21) is used to produce an electron beam with energies typically ranging between 0-1 keV.(147) The electrons are produced by current heating a filament to high enough temperatures (typically $\sim$ 2500 K for tungsten filaments) so that electrons 'boil off' the wire via thermionic emission. The temperature at which this process occurs varies depending on the material used for the filament, and this temperature gives an overall energy resolution for the system as no energy filtering is applied to the emitted electrons. The emitted electrons will have a thermal spread of the order of $\frac{3}{2}$kT so if the boil off process occurs at 1000 K the overall energy resolution will be 0.1 eV and 0.3 eV if the process occurs at 3000 K.

The filament is all part of a cathode system. The current leaving the cathode can be controlled by a grid, this grid can be negatively biased by up to 30 volts. After the grid, there are three anodes. At higher beam energies, the anodes a1 and a3 (see Figure 3.21) are biased to the final energy of the electron beam whilst a2 takes a value somewhere between that of a1 and the cathode, but is adjustable, such that to allow the electrons coming out of the gun to be focused. At low beam energies a2 and a3 are connected together, a1 being used as the focusing grid this time. Using this type of configuration, the electron gun can be made to deliver more current. With this setup, the beams produced are parallel to better than 1°. Typically the electron gun will have dimensions of the order of 10 cms in length and a diameter of 2 cm. For this type of gun, a typical beam diameter is $\sim$0.1 cm and carries a current of the order 1 $\mu$A, however both these values can vary with respect to the chosen beam energy.

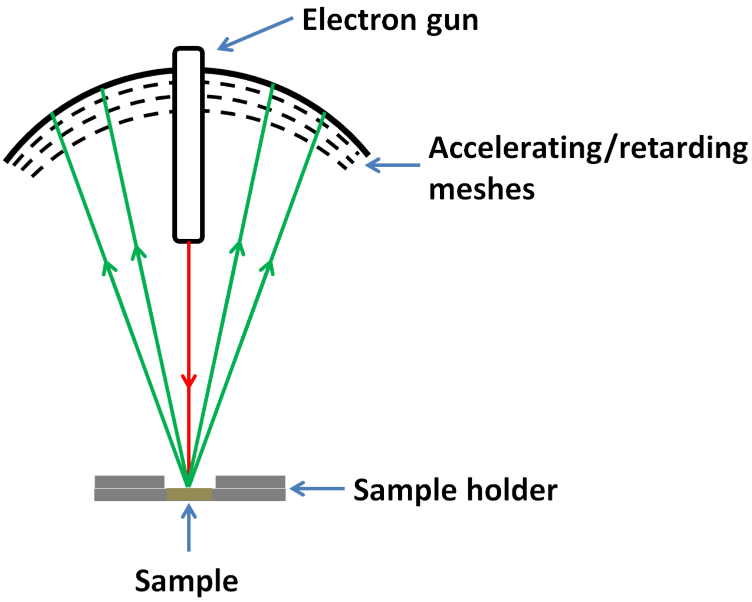

Figure 3.20: Schematic diagram of a low energy electron diffraction (LEED) system showing the positions of the electron gun.

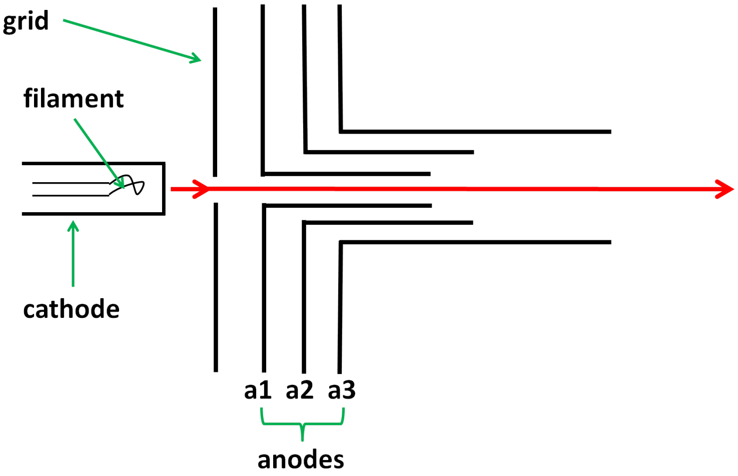

Figure 3.21: Schematic diagram of an electron gun, as used in a LEED system.

The sample is typically mounted at the centre of a system of hemispherical grids (accelerating/retarding meshes as shown in Figure 3.9), there are a number of different grid arrangements that can be used. The simplest of these involves two grids. The first of these (G1) is connected to the final anode (a3), and to the crystal so that once electrons are inside the region enclosed by G1 they are in a field free region. Electrons are diffracted from the sample (crystal) surface and then speed towards the grids. The second grid (G2) is usually biased relative to G1 so that only electrons that have lost less than 1-2 eV of their original energy can get through to the far side of G2. All electrons not fitting this criterion are then turned back and collected by G1. The final part of this system, the phosphor screen, is biased with a large accelerating potential, typically of the order 2 keV, this gives the electrons enough energy to excite the phosphor efficiently.

The LEED process must be carried out in ultra high vacuum, requiring pressures of the order of $10^{-9}$ to $10^{-10}$ Torr. These pressures are required to keep the sample surface sufficiently clean of contamination from residual gases and to prevent scattering events between the incident and diffracted electrons with the residual gases. In a vacuum of this quality, a sample obtains a monolayer of absorbed gases in around a day. There are processes for cleaning samples to the required level for LEED in-situ. These include flash heating to a temperature just below the melting point or surface reconstructions. Also bombardment techniques such as argon ion bombardment can be used to clean the surfaces. Alternatively surface adsorbates can be added to the surface to test for their effects on the diffraction patterns.

Varying the temperature of the sample during the diffraction process can also be desirable to test and observe how that affects the diffraction pattern. It is also useful to be able to move the sample in x-y motion to probe different area of the sample, and also to have at least one axis of rotation, so that different incident beam angles can be observed.

### 3.5.2 Interpretation of LEED Patterns

In most samples studied by LEED there is two-dimensional symmetry parallel to the surface. In many substances the symmetry present at the surface is given by the symmetry present in the bulk crystal in a plane parallel to surface considered. In other samples, surface reconstructions and rearrangements take place place, this forms a surface structure with less symmetry than expected if the surface were formed by truncation of a perfect bulk crystal at a plane.

The surfaces are conventionally named after the planes of the bulk crystal that they run parallel too, for example (001) and (010) etc. The two-dimensional structure within the surface plane can be described in terms of a unit cell. This unit cell can be repeated to form the whole surface. The two sides of the unit cell will be designated by vectors **a** and **b** which lie in the plane of the surface.

This allows the origin of any unit cell to be written as,

$$l\mathbf{a} + m\mathbf{b}, \tag{3.9}$$

Relative to the origin of a reference unit cell, where $l$ and $m$ are integers. Any lattice of points, for which the positions of all the points are given by the formula given in Equation 3.9, and contains points for all values of $l$ and $m$ is called a Bravais lattice. In two dimensions there are four possible Bravais lattices, or a fifth if the centered rectangular lattice is included, this is sometimes useful in describing a hexagonal lattice in rectangular coordinates. The unit cells of these five lattices are shown in Figure 3.22.

In the rest of this description of the LEED process, the symbols $x$,$y$,$z$ will always refer to a set of orthogonal right-handed axes. $x$ and $y$ will lie in the plane of the surface, whilst $z$ will be an axis pointing inward, normal to the surface (see Figure 3.23). Away from the surface, the bulk crystal will have symmetry in the $z$ direction, for the purposes of LEED analysis, the system can be simplified by allowing the bulk crystal structure to consist of identical layers of atoms, with the plane of each of these layers parallel to the surface. Each layer is displaced from the previous one by a vector $c$.

Layers near the surface can vary from those in the bulk crystal. This can involve a relaxation in the relative spacings within upper most surface layers in a crystal, and in some cases, complete rearrangement in the composition of atoms in the top plane is possible.

To describe the layers of the crystal, the following convention (taken from (147)) will be used. The planes of atoms in each layer will have their positions,

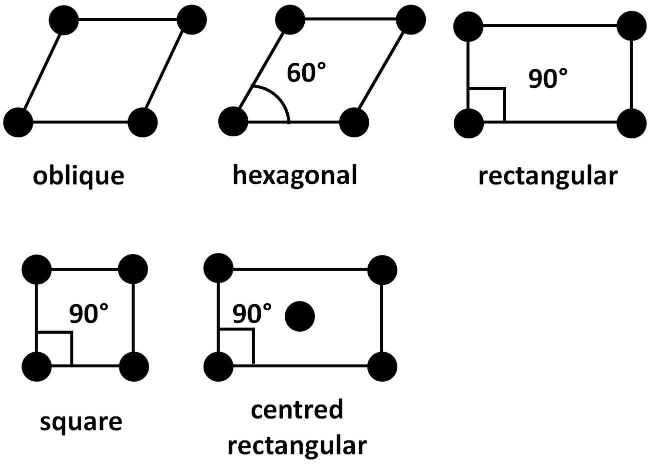

Figure 3.22: Five two-dimensional Bravais lattices. Adapted from (147).

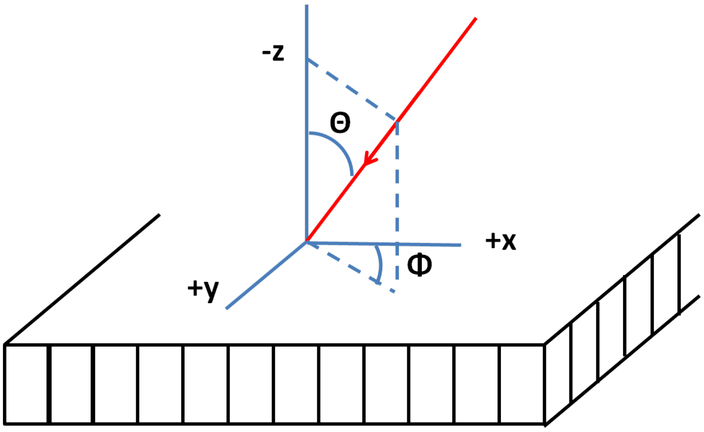

Figure 3.23: Conventions concerning the incidence of an electron beam on a surface. Adapted from (147).

taken relative to some origin in the layer, denoted by $\mathbf{d_p}$. Each plane can be decomposed into unit cells, with the displacement of each unit cell with respect to the origin of the plane, denoted by $\mathbf{R_j}$. The coordinates of atoms within each unit cell are denoted by the vector $\mathbf{r_k}$ with respect to the origin of the unit cell. This allows the position of the $k$th atom of the $j$th unit cell in the $p$th plane of a layer is given by

$$\mathbf{r_{(k)} + R_j + d_p}, \tag{3.10}$$

The detailed analysis of the electron diffraction within the crystal can be found in (147). For the purposes of understanding the diffraction patterns within this work we can assume that the diffracted wavefield consists of a series of discrete beams, each with a different parallel component of momentum, $(\mathbf{k_{0\parallel}} + \mathbf{g})$. Where $\mathbf{g}$ are two-dimensional unit vectors having only $x$ and $y$ components such that,

$$\mathbf{g \cdot a = integer \times 2\pi}, \tag{3.11}$$

$$\mathbf{g \cdot b = integer \times 2\pi}, \tag{3.12}$$

this is shown in Figure 3.25(a). The directions of the beams are determined by $\mathbf{K_g^-}$,

$$\mathbf{K_g^-} = [\mathbf{k_{0x} + g_x, k_{0y}, g_y}, -(\mathbf{2E} - |\mathbf{k_{0\parallel} + g}|^{\mathbf{2}})^{\frac{1}{2}}], \tag{3.13}$$

and therefore by $\mathbf{k_{0\parallel}}$, $\mathbf{g}$ and $E$, as shown in Figure 3.26.

There are only a finite number of beams that emerge from the crystal at finite incident energy. As $(\mathbf{k_{0\parallel}} + \mathbf{g})$ becomes larger, this means that the z component of momentum diminishes until beams for a certain value of $(\mathbf{k_{0\parallel}} + \mathbf{g})$ such that

$$|\mathbf{k_{0\parallel} + g}| \simeq \mathbf{2E}, \tag{3.14}$$

are traveling almost parallel to the surface. If values of $(\mathbf{k_{0\parallel}} + \mathbf{g})$ larger than this critical value are chosen the nature of the beam changes. The $z$-exponent becomes complex, implying that the beam becomes evanescent, thus dying away exponentially in amplitude away from the crystal surface. The beam therefore dies out within a couple of atomic units and as such, these beams are never observed on the screen. Equation 3.14 shows us that, as the beam energy is

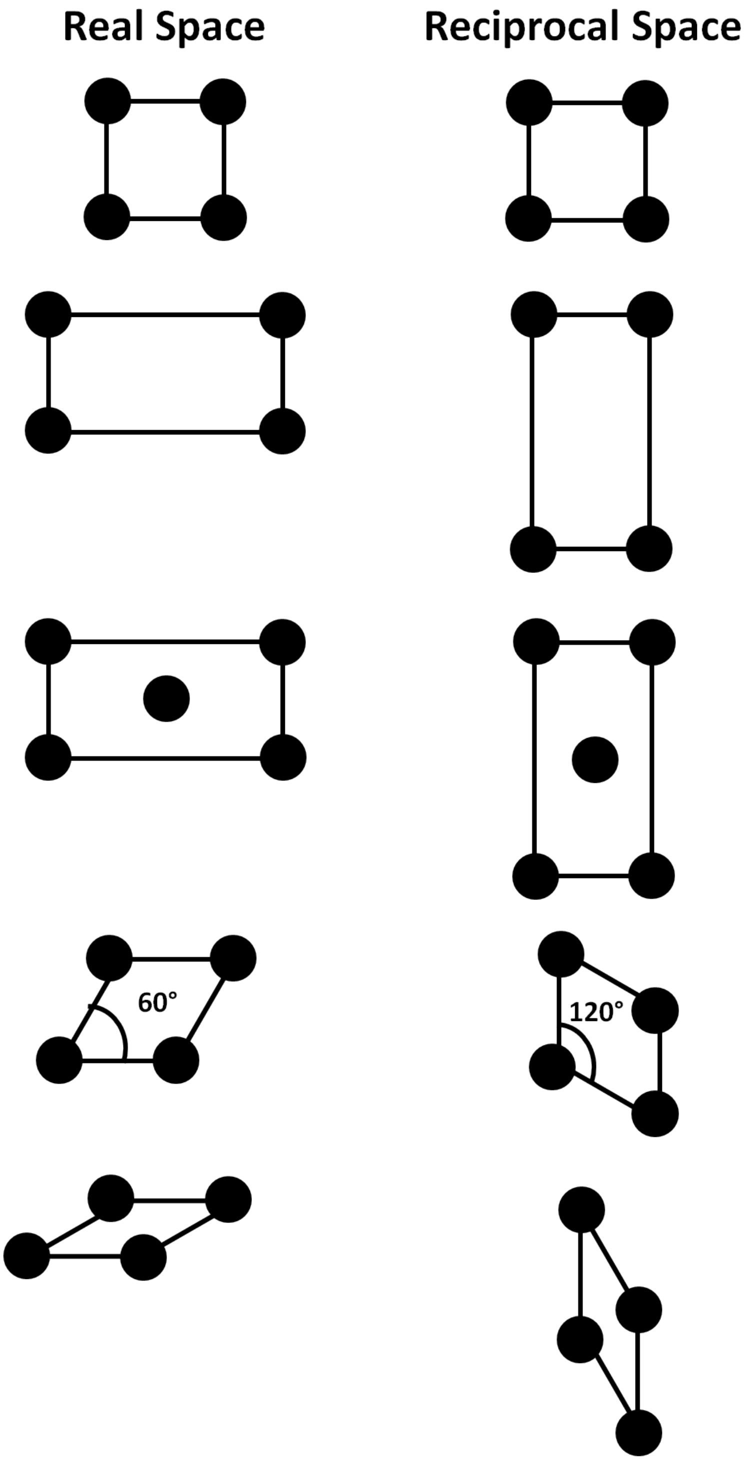

Figure 3.24: Unit cells of corresponding real and reciprocal two-dimensional lattices. Adapted from (147).

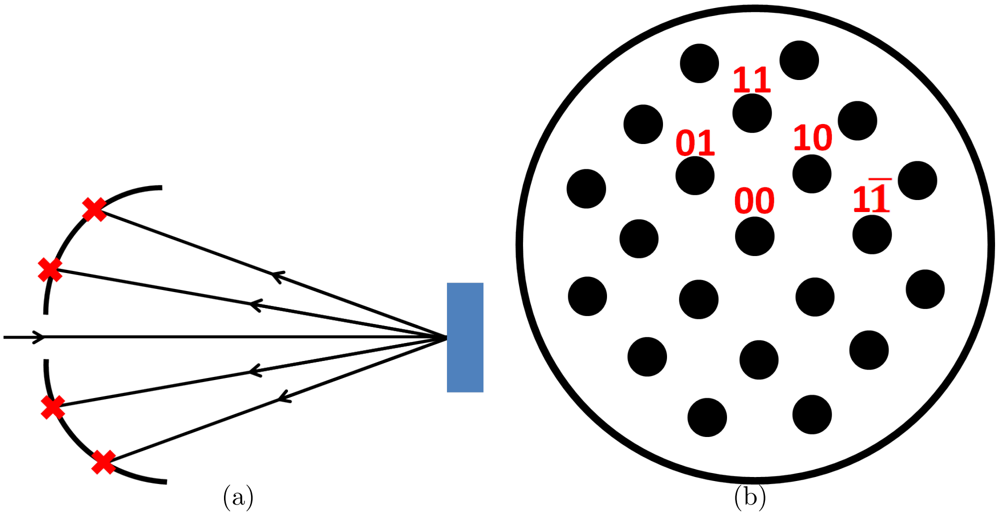

(a) (b)

Figure 3.25: a) Schematic showing the diffraction of an incident electron beam into a series of discrete beams, b) a plan view of a typical pattern made on the fluorescent screen by these beams. Adapted from (147).

increased, more and more Fourier components produce beams that can reach the screen. Figure 3.26 shows that the spot pattern produced, contracts to allow room for the larger number of spots.

For a given $\mathbf{k_0}$ and E, $\mathbf{g}$ controls the diffraction pattern. There is one spot on the screen for every value of $\mathbf{g}$. By making the screen spherical, and placing the crystal surface at the center of this sphere, the spot pattern obtained is a direct picture of the reciprocal lattice, or at least the part of the reciprocal lattice that produces beams that emerge from the crystal. Figure 3.25(b) shows the labelling convention for a diffraction pattern. Each spot is given the label $(hk)$ where the $h$ and $k$ values correspond to the $\mathbf{g}$ value as in equation 3.13 for each beam with parallel component of momentum $(\mathbf{k_{0\|}} + \mathbf{g})$.

As mentioned earlier, the diffraction pattern gives the reciprocal lattice of the surface, and hence the sides of the unit cell of that lattice, $\mathbf{A}$ and $\mathbf{B}$. Now, the unit cell of the real lattice can be found:

$$\mathbf{a} = (\mathbf{a_x}, \mathbf{a_y}) = \frac{\mathbf{2\pi}}{\mathbf{A_xB_y} - \mathbf{B_xA_y}}(\mathbf{B_y}, -\mathbf{B_x}), \tag{3.15a}$$

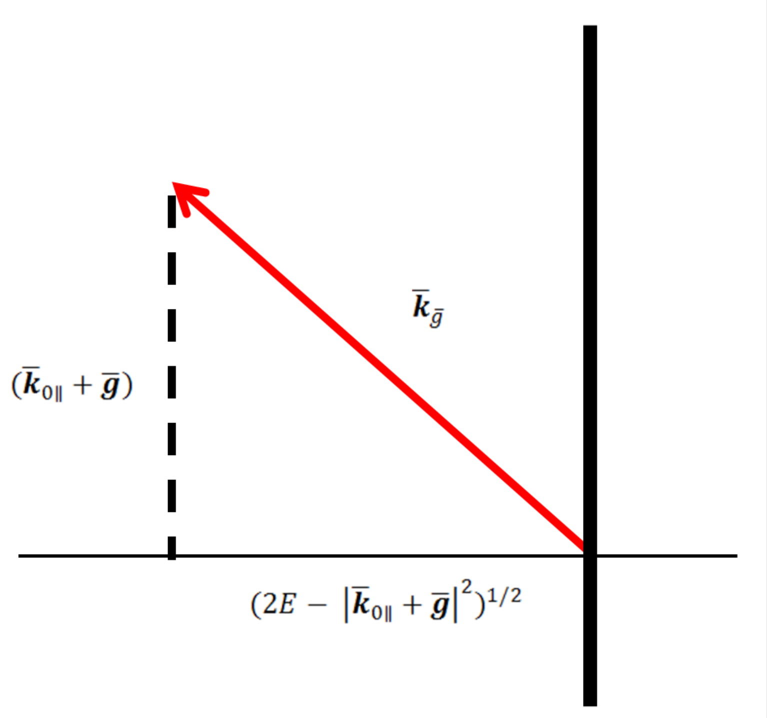

Figure 3.26: $(\mathbf{k}_{\mathbf{0}\|} + \mathbf{g})$ and $E$ determine the direction of a beam.(147)

$$\mathbf{b} = (\mathbf{b_x}, \mathbf{b_y}) = \frac{\mathbf{2\pi}}{\mathbf{A_x B_y} - \mathbf{B_x A_y}}(-\mathbf{A_y}, \mathbf{A_x}), \tag{3.15b}$$

So this covers the basics of interpreting surface structural using a LEED pattern. Now more specifics on using this technique on epitaxial graphene samples will be explored.

### 3.5.3 LEED of Epitaxial Graphene Samples

LEED has long been used to study the surface reconstructions of silicon carbide crystals with varying annealing temperature.(18) So as the field of epitaxial graphene research began to grow, LEED provided a tried and trusted technique for analyzing the surfaces of the produced epitaxial graphene and understanding the precursor surface reconstructions to this growth.(17; 18; 19; 21; 78; 146) One major use of LEED when analyzing epitaxial graphene structures is the stark difference in the diffraction patterns obtained for epitaxial graphene grown on the silicon-terminated and carbon-terminate faces of silicon carbide, SiC(0001) and SiC($000\bar{1}$) respectively. Figures 3.27(a) and 3.27(b) show examples of LEED patterns taken from each of these faces.

Figure 3.27(a) shows epitaxial graphene grown on the SiC(0001) face, the LEED pattern is well ordered and a $(6\sqrt{3} \times 6\sqrt{3})$R30 pattern is obtained with the graphene spots overlayed. This LEED pattern indicates that the graphene layer grows at a 30° angle to the silicon carbide substrate. The pre-cursor $(6\sqrt{3} \times 6\sqrt{3})$R30 reconstruction that the graphene grows on top of is regularly named as a 'buffer layer'.(17; 21; 146) It consists of almost enough carbon atoms to form a full graphene monolayer but is bonded to the underlying silicon carbide layer via its $\pi$-electrons and therefore does not behave like a graphene layer. Subsequent growth on SiC(0001) is well ordered due to this buffer layer and multilayer graphene systems are AB (Bernal) stacked. The sharp, well defined diffraction spots within the LEED patterns are indicative of this high level of order.(17; 21; 146)

Figure 3.27(b) shows epitaxial graphene grown on the SiC($000\bar{1}$) face, it is immediately obvious that this surface structure is much different to that seen on the SiC(0001) face. Again the main graphene diffraction spots are rotated by

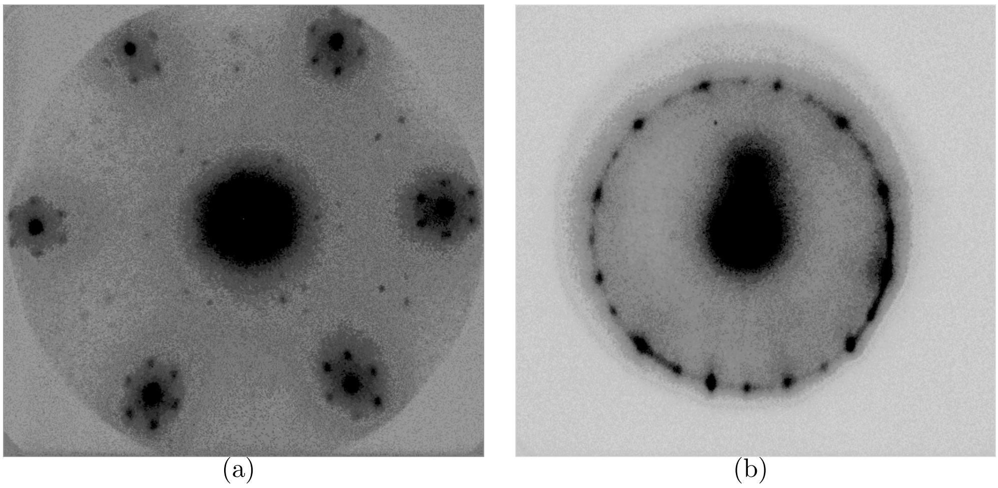
(a) (b)

Figure 3.27: a) LEED data taken from epitaxial graphene grown on silicon carbide (0001). b) LEED data taken from epitaxial graphene grown on silicon carbide ($000\bar{1}$). LEED data taken at Brookhaven National Lab in collaboration with Jurek Sadowski. Negative contrast used to try and make the images clearer for print. Rings observed in b) indicate the rotational disorder present between the graphene films and silicon carbide ($000\bar{1}$) substrate.

30° in relation to the silicon carbide spots. There is no buffer layer between the silicon carbide substrate and the first graphene layer, the graphene is therefore less coupled to the sample surface. Dashed ring structures are also visible in the LEED pattern, an indication that the layer on layer graphene growth on this surface does not stack in an AB fashion.(21) Instead there is preferential rotational disorder between each of the graphene layers. This leads to the decoupling of graphene layers and effects the properties of the graphene grown on this face, including its electrical properties (31; 34; 50) and structural properties.(23; 24; 33)

LEED has also been used to estimate the thickness of graphene layers in epitaxial graphene samples. If the intensity of the graphene diffraction spots are tracked with respect to the electron beam energy (148) peaks and dips appear to create a spectrum as shown in Figure 3.28. As the electron beam energy is increased, the penetration depth of the electrons increases.(147) The fingerprint regions described by Riedl et al (148) and shown in Figure 3.28 occur due to complex scattering processes that occur as the penetration depth increases and more graphene layers and SiC substrate layers are probed.(148)

Another method for estimating layer thicknesses in epitaxial graphene (149) has been to measure the ratio in intensity of the diffraction spots produced by the graphene and silicon carbide at a fixed energy (100 eV). A model then links the graphene:silicon carbide ratio to the graphene layer thickness via increased attenuation of the silicon carbide diffraction spots with the increase in graphene thickness.(149) The number of graphene layers are calibrated against experimental data from low energy electron microscopy measurements and fit well to the model mentioned above.

### 3.5.4 The LEED System Used Here

The LEED system used in this work is very similar in layout to the schematic diagram shown in Figure 3.20. The system is located in the preparation of an molecular beam epitaxy machine. The base pressure in this chamber is typically $10^{-9}$ mTorr, well within acceptable limits for LEED measurements. The sample holder allows for movement in the $x$ and $y$ direction in the sample surface plane and the sample can be rotated fully through the angle $\theta$ and partially through $\phi$ as shown in Figure 3.23. The diffraction pattern is captured by a phosphor screen, this is then imaged with the use of a clamped digital camera. During the process of this project, the LEED system has been upgraded to allow pre-programmed energy sweeps to be carried out and imaged simultaneously.

Typical electron beam energies used are between 50-250 eV. The lower bound on this value can depend on the uniformity of the graphene growth, for ‘incomplete’ graphene films, a charging effect is observed and low beam energy (50-100 eV) diffraction patterns are unobtainable.

In an ideal growth run, the sample will be heated to the required temperature and time and moved through to the LEED system for analysis as soon as it reaches ∼100°C during its cool down. If this is not possible and the sample is thought to have been left too long and has become contaminated, a ‘flash’ anneal can be performed at a temperature typically ∼200°C below the growth

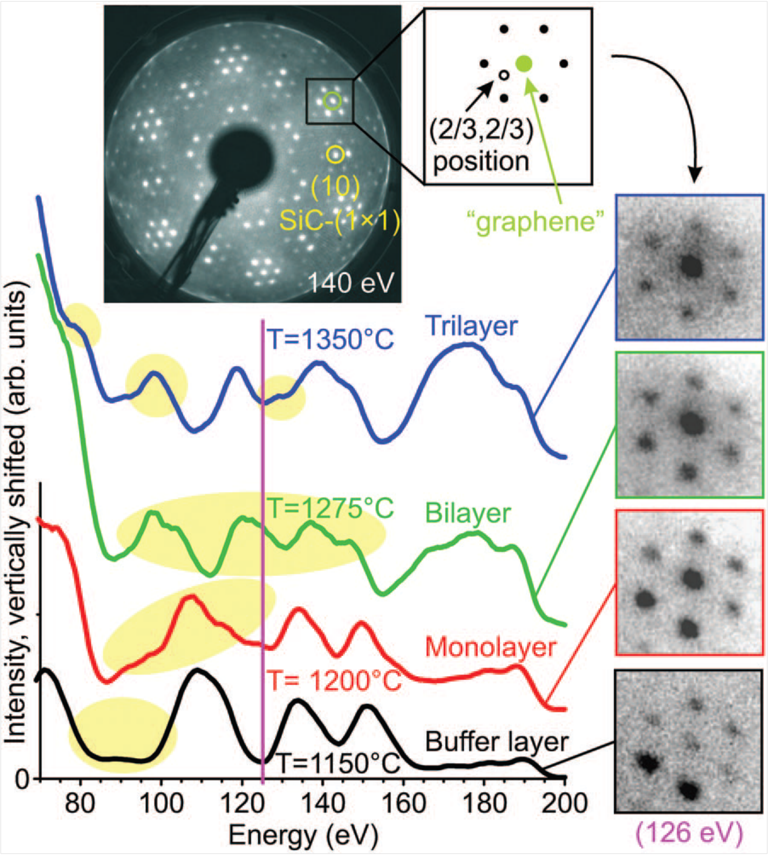

Figure 3.28: LEED spot intensity spectra for different numbers of epitaxial graphene layers grown (at the indicated temperatures) on 4$H$-SiC(0001). As indicated in the inset, the spectra were obtained for the green marked spot of the $(6\sqrt{3} \times 6\sqrt{3})$R30° reconstruction, which corresponds to the unit cell of graphene. The first order diffraction spot for the SiC substrate is indicated in the LEED pattern in yellow, the position of the (2/3, 2/3) spot of the $(6\sqrt{3} \times 6\sqrt{3})$ in the inset. The yellow patches indicate fingerprintlike features in the spectra that allow the unambiguous determination of the number of graphene layers. LEED patterns at 126 eV are shown on the right, also allowing for a discrimination.(148)

temperature, in order to outgas the sample and remove contaminants before obtaining a diffraction pattern.

As mentioned earlier, the typical sample size used is 5 mm ×10 mm, the electron beam spot in this LEED system is fairly large ∼1 mm, so when analyzing the diffraction patterns it must be very much as an average across the sample surface. However, LEED patterns obtained with this system have been shown to vary within a single sample and show areas covered by graphene and areas that are not.(33)

## 3.6 Low Energy Electron Microscopy (LEEM)

Low energy electron microscopy (LEEM) is a surface analysis technique, which, like low energy electron diffraction (LEED), makes use of the wave nature of electrons to analyze the sample surfaces. Much like other electron microscopy techniques, the instrumentation used in LEED utilizes electron lenses to focus the electrons on the surface, however the low energy electrons (1-100 eV) used in LEEM means that it is very surface sensitive. As with LEED, varying the energy of the incident electrons used in LEEM will result in varying the penetration depth of these electrons with the surface. This again results in depth profiling being possible with LEEM and monitoring changes in reflectivity with varying beam energy has proven to be a very useful technique in determining graphene layer thickness in epitaxial graphene samples.(24; 28; 150)

A benefit of LEEM as a technique is the ability to combine it with other techniques such as photoemission electron microscopy (PEEM) and angle-resolved photoemission electron spectroscopy (ARPES). The samples are very accessible in LEEM systems, allowing various in-situ studies to be carried out whilst LEEM analysis is being performed, this can include annealing and surface deposition.

### 3.6.1 Basics of LEEM

To understand the LEEM process as with LEED, we must look at the scattering effects that occur between the incident electrons and the sample surface. As the energy of electrons is decreased, the dominance of forward elastic events is lessened and inelastic scattering events and elastic backscattering events become more important. At very low energies (below 20 eV), reflectivity coefficients between 0.1-0.5 can be obtained.(151)

A LEEM image is produced by the use of the LEED pattern of the surface. Bright-field LEEM imaging involves the use to the specular (0,0) LEED spot, which is isolated via the use of an aperture. For dark-field imaging the aperture is used to remove a selected LEED spot from the pattern. To obtain the LEEM image, the sample area under investigation is illuminated and the diffracted beam enters an objective lens. This lens produces two images, the first is produced in its back-focal plane where all rays entering the lens parallel to each other are focused in one point, thus producing the diffraction pattern in this plane. The second image is produced in the imaging plane, where all rays resulting from a point in the sample are recombined.(151; 152; 153)

### 3.6.2 LEEM Instrumentation and Limitations

The typical layout of a LEEM system is shown in Figure 3.29 all of which sits in an ultra high vacuum chamber (series of chambers). As described in the LEED section of this report, an electron gun is used to create an electron beam. This electron beam is then focused and manipulated onto the sample via a series of quadrapole electron lenses. The illumination beam aperture allows a control on the area of the sample to be illuminated, thus allowing micro-diffraction to be carried out. An electrostatic immersion objective lens places the sample in a strong electrostatic field, up to 10 kV/mm for optimum resolution. The electrons travel through the focusing field of the objective lens (magnetic or electrostatic) at a relatively large beam energy (10-20 keV).(153)

The electrons are then decelerated between the objective lens and the sample, to a final energy in the range 0-100 eV. During this first pass through the objective lens, the objective lens acts as a final condenser lens, controlling the final path (angle) and focus of the electrons on the sample. Once the electrons have interacted with the sample, they are re-accelerated back to the electron gun energy on the return to the objective lens. This involves maintaining the sample at a potential close to that of the electron emitter in the gun, whilst grounding

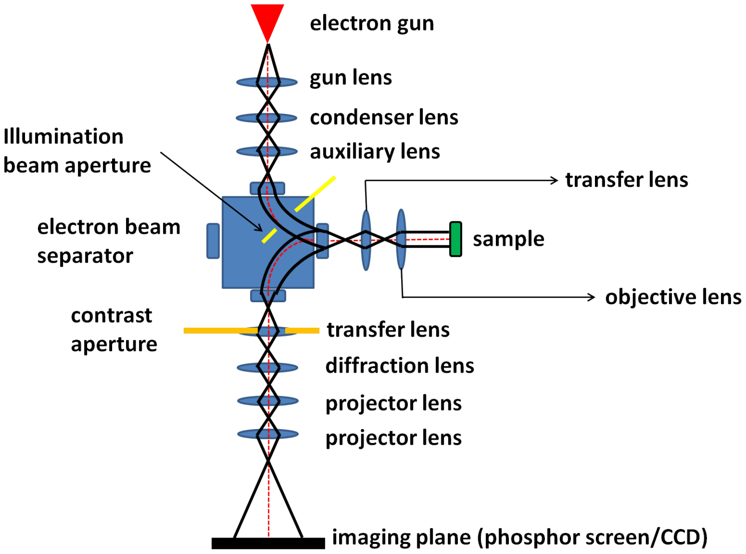

Figure 3.29: Schematic diagram showing the main components of a typical LEEM system. Adapted from (153).

the objective lens (or grounding the sample and maintaining everything else at high voltage). Now the electrons pass through the objective lens focusing field for a second time, this forms a real image of the sample.(151; 152; 153)

The electron beam separator, consisting of a magnetic beam splitter is used to spatially separate the illuminating electron beam optics and the imaging projector optics. Although this sounds straightforward, it is in fact a complicated process, details of which can be found in the following references (151; 152; 153). Once through the beam separator, the image beam passes through more lenses. A contrast aperture is placed in the center of the transfer lens in this section, this is the position at which the beam separator re-focuses the LEED pattern, this is where the selection of bright and dark-field can be made. The final image is then displaced on a phosphor screen and recorded with the use of a CCD camera.

There are a number of factors which affect the overall resolution limits and performance of a LEEM system. As the sample draws on the use of the wave nature of electrons, and surface features that are the same size region as the electron wavelength will cause diffuse scattering and limit contrast resolution. Spherical and chromatic aberrations as well as aperture aberrations will also contribute to the overall resolution to the overall resolution limit of the LEEM system.(152) A general formula for the resolution of an electron microscope is

$$d = \frac{V}{E}, \tag{3.16}$$

where e$V$ is the average electron energy and $E$ is the electric field in front of the specimen. Using general numbers found in LEEM systems leads to a resolution ($d$) in the range 10-100 nm. Which is important to note as the lateral grain size of graphene grown under certain conditions within this work is of the order of this experimental limit.

### 3.6.3 LEEM in Epitaxial Graphene

The surface senistivity of LEEM makes it a very good technique for studying epitaxial graphene systems. There are sharp contrasts in reflectivity between graphene layers of different thicknesses and between graphene and the silicon carbide substrate. This allows LEEM to image graphene domain structures (grains) and provide maps of graphene coverage on surfaces.(24; 28; 150) Tracking reflectivity with electron beam energy gives the thickness values of graphene present on the surface. As the beam energy is increased, the penetration depth into the sample surface increases, quantum interference effects between graphene layers leads to a series of peaks and dips in the profile as the beam energy is increased. The number of graphene layers can then be shown to be equal to the number of dips within this reflectivity versus electron beam energy profile.(24; 28; 150)

### 3.6.4 LEEM Systems Used in This Work

Two LEEM systems have been used in this work, the first, an Elmitec LEEM V system is located at the Centre for Functional Nanomaterials (CFN), at Brookhaven National Laboratory (BNL) in the USA. The second, also at BNL, is located in the National Synchrotron Light Source (NSLS) and is an Elmitec LEEM III system.

## 3.7 Nanoprobe

### 3.7.1 Basic Layout and Operation of the Nanoprobe

Experiments were carried out to locate graphene islands as produced during argon annealing of silicon carbide, and take local electrical measurements on these islands. To carry out these experiments, an Omicron nanoprobe was used. The Omicron nanoprobe consists of a Zeiss Gemini high resolution scanning electron microscope (SEM) and four independent Omicron scanning tunnelling microscopes (STMs), all of this is contained within an ultra high vacuum (UHV) system. The analysis chamber, as shown in Figure 3.30(a) contains a sample stage which fits a standard Omicron sample plate. Stepper motors allow this sample stage to be moved in the $x$ and $y$ directions. The SEM column is positioned directly above this stage. Four STM scanners are positioned around this sample stage, as shown in Figure 3.30(a).

A tip holder (Figure 3.30(b)) can be placed on each of these scanners and are secured in position by a small magnet. The tip holder has a long arm, on the end of which, a tip can be secured in place by a small screw, the tip is secured at an angle of 45° to the vertical. The analysis chamber is pumped by an ion pump and a titanium sublimation pump. This allows pressures of $\sim 10^{-11}$ mbar to be reached.

A carousel (Figure 3.30(a)) allows tips and samples to be stored in the analysis chamber prior to use. These samples and tips are then mounted to the sample stage or scanners respectively via the use of two wobble sticks. This carousel can house up to ten samples and tips in total. Samples are loaded in and unloaded out of the system via a load chamber, this load chamber can be isolated from the analysis chamber via a gate valve. Once isolated, this load chamber can be vented and opened. The load chamber has a second carousel, identical to that in the analysis chamber. Samples are loaded into this carousel and the load chamber is then closed. A turbo pump is then used to pump down the still isolated load chamber. After a few hours of pumping, the pressure in the load chamber can reach $\sim 10^{-10}$ mbar. At this pressure, the gate valve between the analysis chamber and the load chamber can be opened and samples and tips can

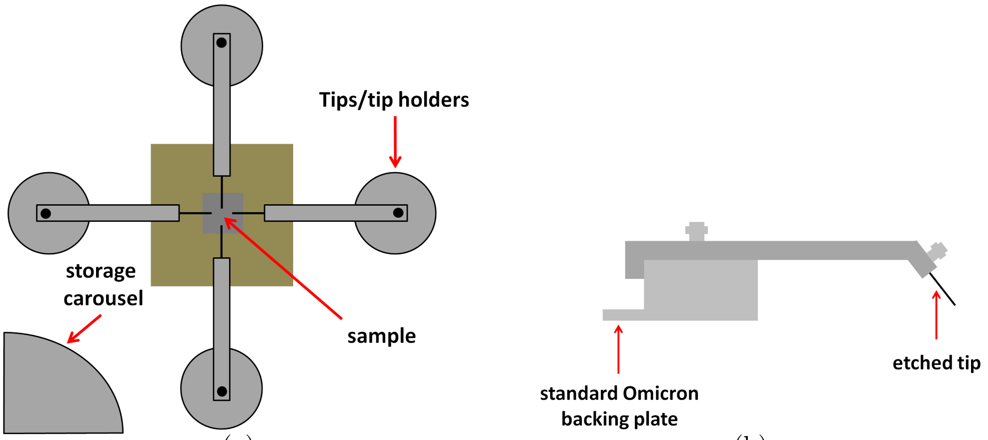

(a) (b)

Figure 3.30: a) Schematic diagram of the inside of the Nanoprobe analysis chamber, b) Schematic diagram of a Nanoprobe tip holder.

then be transferred between carousels via the use of a third wobble stick. The turbo pump can then be isolated via a second gate valve, to reduce vibrations, the turbo pump is switched off during measurements.

The graphene 'islands' were visible under the SEM, promising regions were then selected and approached with the STM tips. The SEM has an inlens detector, this gives a top-down view of the four STM tips relative to the sample. This means that the only indication of the tips position in the $z$ direction is the relative focus between the tips and sample (i.e if the sample is in focus, whilst the tip is not, the tip must be above the sample).

### 3.7.2 Nanoprobe Measurement Instrumentation

For taking localised electrical measurements, the four STM tips in the Nanoprobe were connected to four BNC outputs, measurement instruments and voltage sources can then be connected to these cables. The instruments used were a Keithley 2400 series sourcemeter and two Keithley 6514 series electrometers. The sourcemeter is used to source voltages down to a precision of $\pm 1$ $\mu$V. The sourcemeter was connected in series with one of the two electrometers, this was set to measure current and was capable of a measurement precision of $< 1$fA . However, noise introduced by the BNC cables and the wiring within the Nanoprobe increased the noise floor to ~1 pA.

For two-probe measurements, the sourcemeter and one electrometer were connected in series to two of the STM tips. To take four-probe measurements, the second electrometer was set to measure a voltage and was connected directly to the other two STM tips, thus forming the probe circuit. This electrometer also has a precision of ± 1 $\mu$V, and an extremely high input resistance (>200 T$\Omega$), thus allowing very resistive samples to be measured accurately.

## 3.7.3 Measurement Geometry

### 3.7.3.1 Four-Probe Square Measurements

The instrument setup required for taking four-probe square measurements is shown in Figure 3.31. As indicated in these diagrams, the silicon carbide substrate below the graphene islands is terraced in a set direction. These terraces are visible in the SEM image, this allows the probes to be aligned to these terraces. Four-probe measurements can then be made by sourcing a voltage parallel to these terraces and sensing a voltage perpendicular to this current (Figure 3.31) or at any chosen angle to these terraces such as 90° to allow measurements in the parallel direction to be carried out. This allows a difference between the resistance values obtained in the different setups to be found.

### 3.7.3.2 Four-Probe Collinear Measurements

Four-probe collinear measurements can also be made. The instrument setup for this measurement is shown in Figure 3.32, here only the measurement parallel to the substrate terrace steps is shown. To measure at different angles to the terraces, the whole circuit is simple rotated through the required angle.

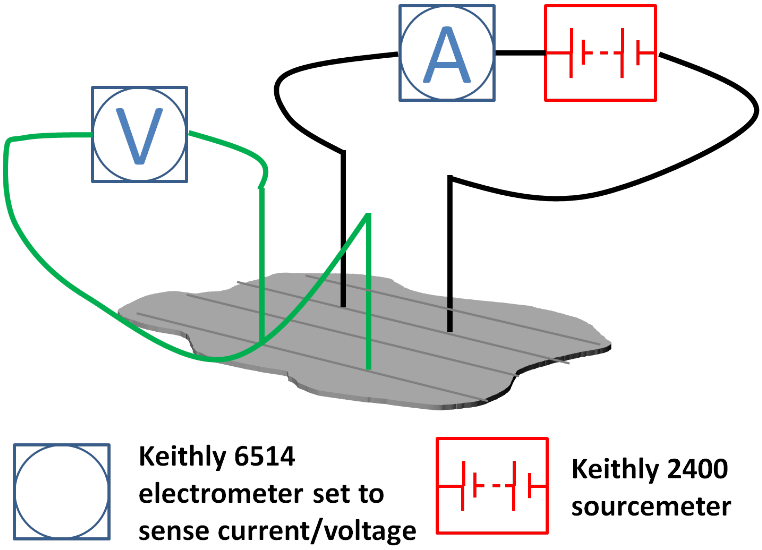

Figure 3.31: Schematic diagram showing the measurement setup for taking 4 probe square measurements perpendicular to SiC terraces. The terrace direction is indicated by the dark gray lines on the lighter gray graphene islands. To take measurements parallel to the terraces the setup is rotated through 90°.

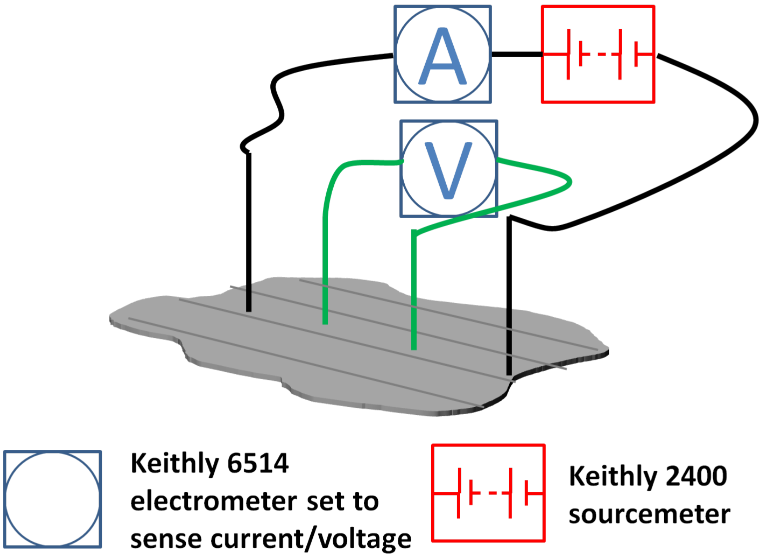

Figure 3.32: Schematic diagrams showing the measurement setup for taking 4 probe collinear measurements parallel to SiC terraces. The terrace direction is indicated by the dark gray lines on the lighter gray graphene islands. To take perpendicular measurements, the whole circuit is simply rotated through 90°.

# Chapter 4

# Epitaxial Graphene Growth in Ultra High Vacuum

## 4.1 Overview: Aims and Objectives

As described in section 1.1.1 the aim for this project was to produce large scale, good quality graphene films, with a view to these films being used towards the production of electronic devices. One key parameter for judging the quality of epitaxial graphene films is the lateral grain size present within the films, section 4.3 will describe how this grain size was increased from 10s nm at the start of this project, to 100s nm by the finish. Also key in growing epitaxial graphene is ensuring there is a complete graphene coverage on the surface such that standard top-down lithography processing techniques can be used to pattern electronic devices anywhere within a sample and yield similar device properties, this improvement in graphene coverage is discussed in section 4.2. The thickness of the graphene films (number of layers) can also play a part in controlling the properties, the understanding and measurements of this are shown in section 4.4.

Initially work concentrated on growth on the silicon carbide (0001) surface and finding the onset of graphene growth, this onset of graphene growth was observed via the use of low energy electron diffraction and the observation of the typical graphene $(6\sqrt{3} \times 6\sqrt{3})$R30 reconstruction after the appearance of other reconstructions at differing annealing conditions. This is shown in Figure 4.1 where surface reconstructions are shown for 15 minute annealing processes at a

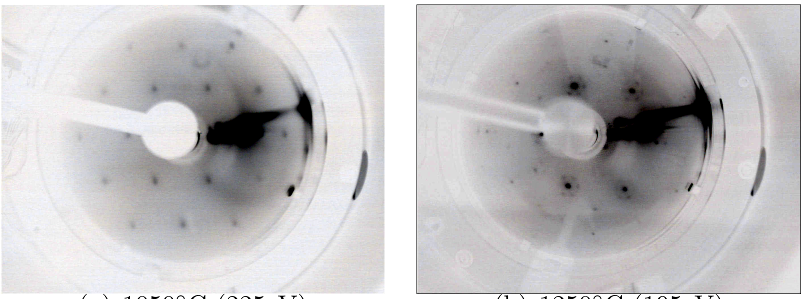

(a) 1050°C (225eV) (b) 1250°C (195eV)

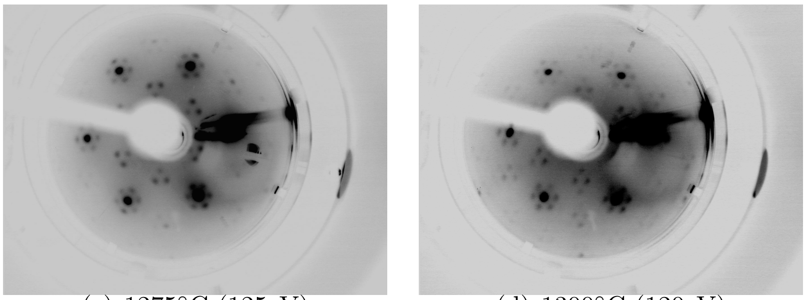

(c) 1275°C (125eV) (d) 1300°C (120eV)

Figure 4.1: LEED patterns taken at different beam energies for a series of samples annealed SiC (0001) up at differing annealing temperatures for an annealing time of 15 minutes. The evolution from a silicon carbide $(1 \times 1)$ reconstruction at a temperature of 1050°C to a graphene-like $(6\sqrt{3} \times 6\sqrt{3})$R30 reconstruction at 1300°C is shown. Negative contrast used for clarity.

number of different temperatures, the sample annealed at 1300°C is seen to show the typical epitaxial graphene-like $(6\sqrt{3} \times 6\sqrt{3})$R30 reconstruction. This result is comparable to results seen in the literature.(17; 18; 19; 21; 78; 146) Techniques such as Raman microscopy were used to show that the samples were indeed carbon-rich, though as shown in Figure 4.2 the signals in the expected graphene band regions are very weak, this can be attributed in part to a weak laser (with ∼100 counts per second on a silicon calibration sample compared to ∼10000 counts per second with the new laser) used in these early measurements. Atomic force microscopy showed the films had grain-like structures of 10s nm and the sheet resistance values (results taken by Graham Creeth) of these samples were very high.

Literature showed that the conductivity in epitaxial graphene grown on silicon

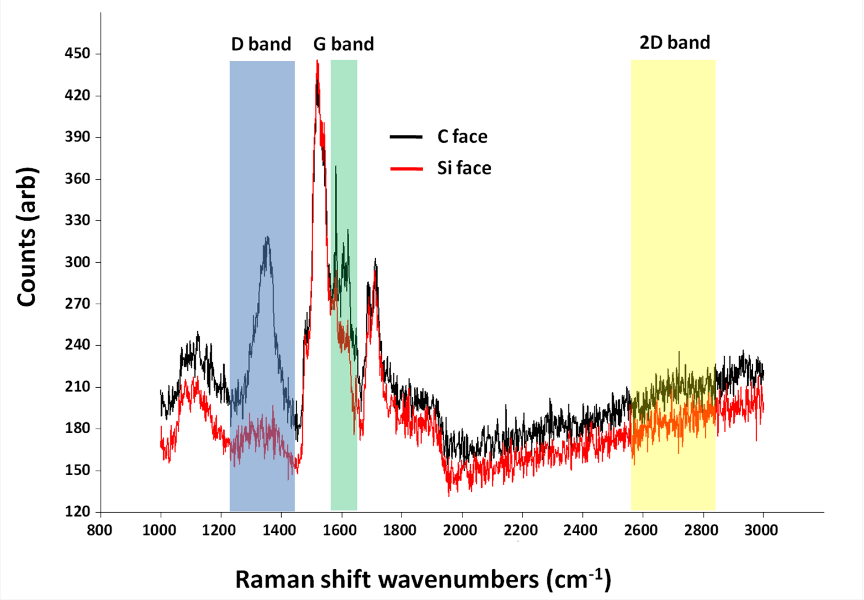

Figure 4.2: Raman spectra (no silicon carbide subtraction) for both C face (black) and Si face (red) growth from a sample annealed at 1300°C for 20 minutes. Shaded regions indicate the main graphene band regions D band (blue), G band (green) and 2D band (yellow). The small intensity and broadness of the 2D peak along with the large observed D bands (notably on C face) indicate that the graphene film is disordered.

carbide $(000\bar{1})$ was increased compared to the (0001) face due to the decoupling between graphene layer(s) and the substrate,(50) for this purpose, future work on ultra high vacuum growth concentrated on graphene production on this face. Again the onset of graphitisation was sought via the monitoring of the LEED patterns and the appearance of the typical ring pattern expected for graphene growth on silicon carbide $(000\bar{1})$ (21) as shown in Figure 4.3 where a set of LEED patterns taken on samples annealed at 1300°C for differing annealing times.

On this face, the graphene-like ring pattern occurred at around 1300°C after 30 minute anneals. The increase in time before the observation in a graphene-like LEED reconstruction when compared to growth on silicon carbide (0001) is surprising as growth on this face is observed to have a lower activation energy elsewhere.(31; 34) Also observed in this work is a graphene precursor recon-

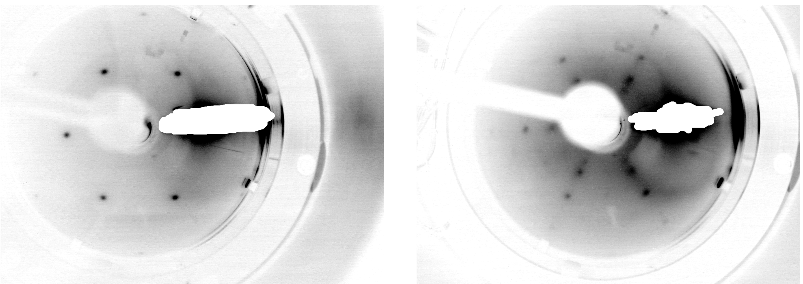

(a) 20 mins at 1300°C (120eV) (b) 20 mins at 1300°C (120eV)

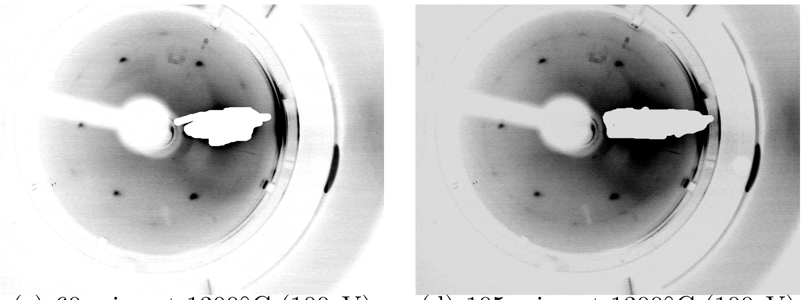

(c) 60 mins at 1300°C (100eV) (d) 105 mins at 1300°C (100eV)

Figure 4.3: LEED patterns taken at different beam energies for a series of samples annealed SiC $(000\bar{1})$ up at differing annealing times for an annealing temperature of 1300°C. a) and b) are taken for the same annealing time of 20 minutes from different samples showing the presence of a 'buffer-layer' in b). For longer annealing times in c) and d) the presence of a graphene ring pattern can be seen. Negative contrast used for clarity. The phosphor LEED screen was somewhat damaged, an attempt has been made to mask this.

struction (Figure 4.3(b)) similar to those found on silicon carbide (0001) during graphitisation and as recently observed on published work on the $(000\bar{1})$ face when grown in a Si-rich environment.(154)

Again Raman spectra (Figure 4.2) showed the samples to be carbon-rich, with stronger graphene bands observed on this face, although the D band region is large, indicating the presence of disorder (see section 3.3.3). This disorder is evident in atomic force microscopy images which once again showed grain-like structures with lateral grain size 10s nm. But once more, the sheet resistance of these samples was very high (Figure 4.5), especially at low temperatures (electrical measurements and analysis carried out by Graham Creeth) suggesting that the films were in fact incomplete. This led to longer anneals being carried out and a noticeable improvement in conductivity. Once complete conducting films were formed, the electronic properties suggested that an increase in lateral grain size was required, this led to increasing the annealing temperature and as such a set of iterating processes that led to an increase in lateral domain size and graphene uniformity.

In section 2.2.3 it was discussed that confining the space above the silicon carbide wafers during the annealing process can lead to improved graphene growth. An attempt was made to do this with a sapphire cap placed above the samples, the natural confinement introduced by the position of the heating element appears to be enough to have an effect, this can be seen in Figure 4.4 where atomic force microscopy from samples undergoing the same annealing times at 1400°C are given, one annealed with the $(000\bar{1})$ face towards under a sapphire cap (Figure 4.4(a)) and one with the $(000\bar{1})$ face away from the heater (Figure 4.4(b)).

The sample annealed towards the heater shows much larger lateral grain sizes compared to the sample annealed away from the heater. Also a sample annealed with no cap but with the $(000\bar{1})$ face towards the heater is shown in Figure 4.4(c) and shows similar lateral grain size to the sample annealed for the same conditions under an alumina cap indicating the presence of confinement with the positioning of the heating element in our annealing set-up.

Section 2.2.2 discussed how the quality of silicon carbide substrate plays a key role in the quality of graphene films, with surface defects such as mechanical polishing scratches providing nucleation points for graphene growth which can lead to uneven film coverage. In an attempt to improve the graphene growth in UHV the silicon carbide wafers were sent away to Novasic, a company which specialises in wafering and wafer polishing(30), for an extra polishing stage and to improve the surface uniformity on the silicon carbide substrate. The AFM micrographs shown in Figures 4.4(a) and 4.4(c) show graphene growth on an unpolished and polished silicon carbide wafer respectively with substrate scratches visible in the unpolished wafer and not in the polished wafer.

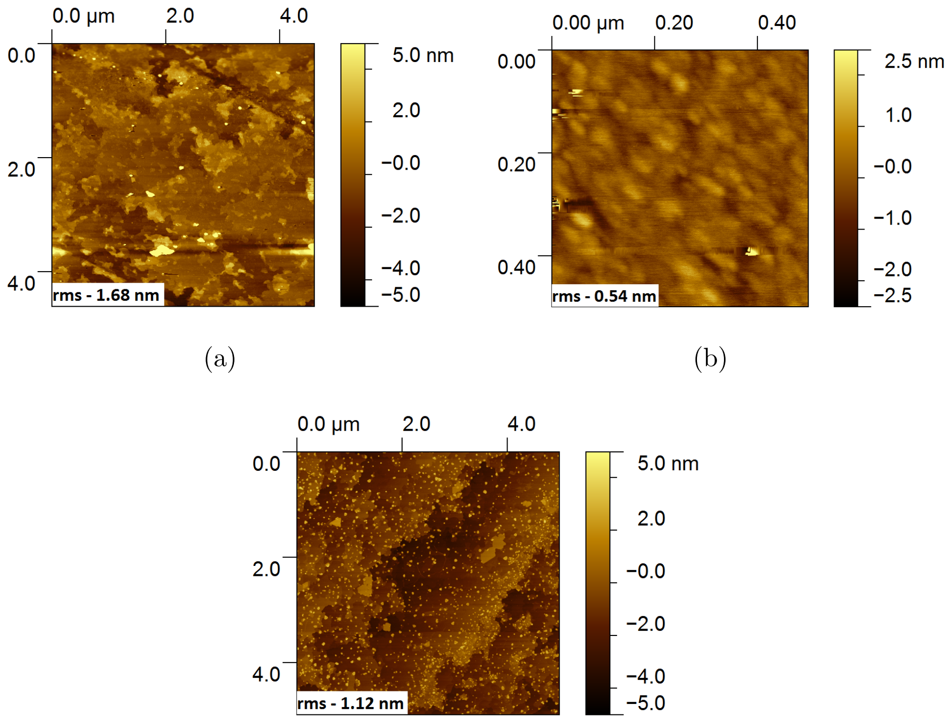

(a)

(b)

(c)

Figure 4.4: AFM micrographs of graphene films grown on silicon cabide $(000\bar{1})$ after a 30 minute anneal at 1400°C under differing levels of confinement. a) $(000\bar{1})$ face towards heater under alumina cap. b) $(000\bar{1})$ face away from heater towards UHV. c) $(000\bar{1})$ towards heater with no alumina cap. Larger grains are observed in images a) and c) when there is confinement above the target substrate.

## 4.2 Increasing the Coverage of Graphene

When discussing the coverage of graphene growth in our epitaxial graphene films it is important to distinguish between coverage on the mm scale (sample scale) and the $\mu$m scale (device scale). The graphene coverage on the sample scale has been tracked using techniques such as LEED and Raman spectroscopy that are somewhat surface averaging due to the scale of the area of sample probed by each technique in a single measurement. LEEM (taken at Brookhaven national laboratory with Jurek Sadowski) and electronic transport (taken by Graham Creeth) measurements are more applicable to measuring the coverage of graphene growth at the device scale. However, it seems that coverage on both scales can be improved by increasing the length of annealing time at a given sample temperature.

### 4.2.1 Coverage on the Sample (mm) Scale

As discussed later in increased detail in Chapter 5, due to the nature of our sample mounting during UHV annealing processes a thermal gradient forms across the silicon carbide chips during an annealing run. This leads to the edges of the chip becoming relatively hotter than the central regions. This results in increased graphene growth at the edges of the sample compared to the central regions. Section 5.4 shows how this can be observed as an increase in strains within graphene films at these edge regions and also how variations in surface reconstructions can be seen in LEED showing areas in central regions where the graphene film is yet to form and instead a buffer-layer like region exists. The exact magnitude of this temperature gradient had not been measured.

LEED data can also show the presence of an incomplete layer of graphene as at low accelerating voltages a ‘charging’ effect can be observed if the sample is in fact incomplete. This occurs for energies ∼100 eV or below as the sample becomes negatively charged due to excess electrons, at these lower beam energies the incident electrons are repelled from the surface and no scattering takes place.

Increasing the annealing time leads to increased sample uniformity with less variations in the amount of strain measured across samples with longer annealing times. Increasing annealing time also stops the observation of buffer-like LEED patterns with all patterns showing carbon-rich ring patterns on the silicon carbide $(000\bar{1})$ indicating the presence of a complete graphene film.

### 4.2.2 Coverage on the Device ($\mu$m) Scale

Earlier it was described how the original process for graphene growth in UHV focused on the onset of graphene growth as identified by the presence of a graphene-like reconstruction shown by LEED. The typical annealing process required to observe this reconstruction was 15 minutes at 1300°C and these samples appeared graphene-like under a number of surface science techniques such as LEED, Raman spectroscopy and AFM. However when the samples were prepared for low-temperature electrical transport measurements (28) the nature of the graphene films at the device-scale were observed.

During the production of these samples they where passed on to Graham Creeth within the condensed matter research group at Leeds for low-temperature electrical transport measurements to be carried out. The electrical transport measurements taken by Graham where dc measurements of sheet material carried out in a constant-flow cryostat with a four-probe geometry. The voltage-probe separation was 5 $\mu$m and the electrodes were patterned using standard optical lithography techniques and made from Ti/Au.

Measurements of the sheet resistance with varying temperature, $R_s(T)$, of samples annealed at 1300°C or below for varying anneal times are shown in Figure 4.5. All samples show a monotonic increase in resistance as they are cooled from room temperature. For all samples annealed at 1300°C, the behavior of $R_s(T)$ above ~5 K is well described by variable range hopping (VRH),

$$R_s(T) = R_0 \exp\left(\frac{T_0}{T}\right)^{\frac{1}{n+1}}, \tag{4.1}$$

where $n$ is the system dimensionality. The data shown in Figure 4.5 can be described by a $R_s(T) \sim T^{-1/3}$ , corresponding to a two-dimensional system. This behavior is not unexpected, observations such as the presence of substrate spots in LEED patterns indicates that the system present corresponds to a few layers of conducting material on an insulating substrate, therefore should behave in a two-dimensional fashion. Also observations from AFM taken on these samples

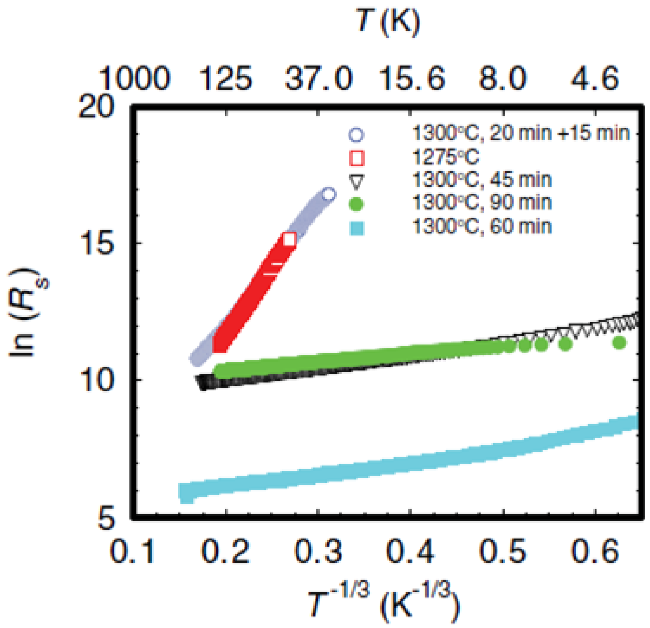

Figure 4.5: Resistance change with temperature for samples annealed for a variety of different temperatures and times. Samples are annealed at 1300°C and below. The axes are chosen to be appropriate for 2D variable range hopping type behavior. The most resistive samples become so poorly conducting at low temperature that they are unmeasurable. Taken from (28). Measurements and analysis carried out by Graham Creeth.

(see section 4.3) show that the samples exhibit a high level of disorder, this leads to variable range hopping.

Samples annealed for short times are effectively insulating at temperatures below ∼30 K, whereas longer annealing times lead to samples being conductive down to the lowest temperatures obtainable by the cryostat (∼1.3 K). This change in resistance (orders of magnitude) whilst cooling to liquid helium temperatures is indicative of a strongly nonmetallic regime.

Activation energies for samples annealed for shorter times are ∼7-10 eV whereas samples annealed for longer times have activation energies in the range ∼2-8 meV. The energy for the shorter annealing times is so large that it points to the conduction taking place via tunneling between grains that are not in electronic contact with each other. The lower energy scale observed for longer annealing times suggests now that the conduction is propagating through clustered granular material. Below 5 K the data does not fit to equation 4.1 and instead show a fairly linear relationship when plotted as ln $R_s(T)$ vs T. This is because at these low temperatures the temperature independent elastic scattering effects from point defects begin to dominate as the temperature dependent inelastic scattering events are 'frozen out'. This switch from variable range hopping to weak-localisation at low temperatures has been observed elsewhere for disordered carbon films grown via plasma deposition.(155)

This type of annealing time dependent behavior is not unexpected, from earlier sections with have dealt with the growth mechanisms involved in epitaxial graphene propagation, in most detail in section 2.2, it has been discussed that the graphene formation expands from areas of nucleation on the substrate surface. So areas of graphene can form that are isolated from each other till the annealing time is sufficient enough for the nucleated regions to have expanded to form a complete graphene film.

This expansion of graphene coverage on the surface is also observable in LEEM data with samples annealed at 1300°C for differing annealing times of 20 minutes (Figure 4.6(a)) and 60 minutes (Figure 4.6(b)). The increase in graphene coverage with clustering of smaller domains to form more complete films as expected from the electrical transport measurements is observed.

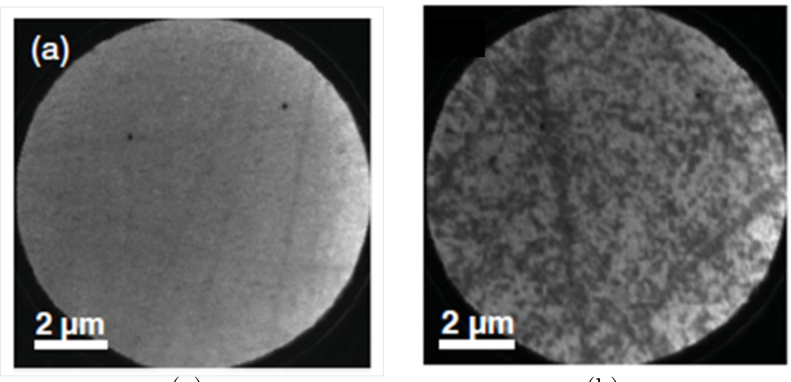

(a) (b)

Figure 4.6: LEEM data taken at an incident energy of 4.5 eV for silicon carbide $(000\bar{1})$ having undergone annealing in UHV for a) 20 minutes at 1300°C and b) 60 minutes at 1300°C. The longer annealing time of 60 minutes (image b) leads to the clustering of small graphene films (dark contrast) which leads to increased conductivity (decreased sheet resistance). The presence of substrate scratches can also be seen in both images. Adapted from (28). Data taken in collaboration with Jurek Sadowski at Brokhaven National Laboratory.

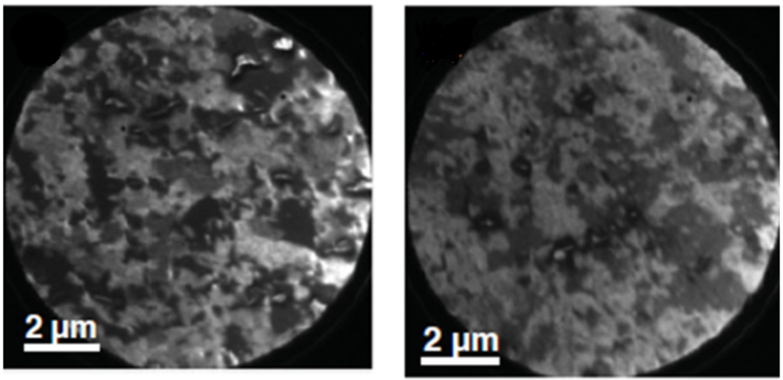

(a) (b)

Figure 4.7: LEEM data taken at an incident energy of 4.5 eV for silicon carbide $(000\bar{1})$ having undergone annealing in UHV for a) 30 minutes at 1400°C and b) 55 minutes at 1400°C. There is less contrast variation in image b) suggesting that the longer annealing time leads to more uniform layer thicknesses. Adapted from (28). Data taken in collaboration with Jurek Sadowski at Brokhaven National Laboratory.

The section following this describes how the lateral grain size appears to increase with annealing time. LEEM data shown in Figure 4.7 shows that increasing the annealing time still leads to an increase in sample uniformity with a sample annealed for 55 minutes at 1400°C (Figure 4.7(b)) showing less contrast than a sample annealed at 1400°C for 30 minutes (Figure 4.7(a)). Different contrast levels in the LEEM images correspond to different graphene thicknesses therefore indicating that the sample with longer annealing time has more uniformity. As will be discussed later, the typical thickness of samples in this annealing range is between 2-4 monolayers

AFM provides information at the sub-device scales and can be used to complement the LEEM and electrical transport measurements. The grain-like structure associated with graphene growth at 1300°C can be seen if Figure 4.8. Although there is no clear evidence of the $\mu$m scale clustering observed in LEEM images for samples annealed for longer annealing times, there is a general decrease in the rms roughness (numbers in Figure 4.8) as the annealing time is increased to 60 minutes backing up earlier suggestions that the graphene film is becoming more

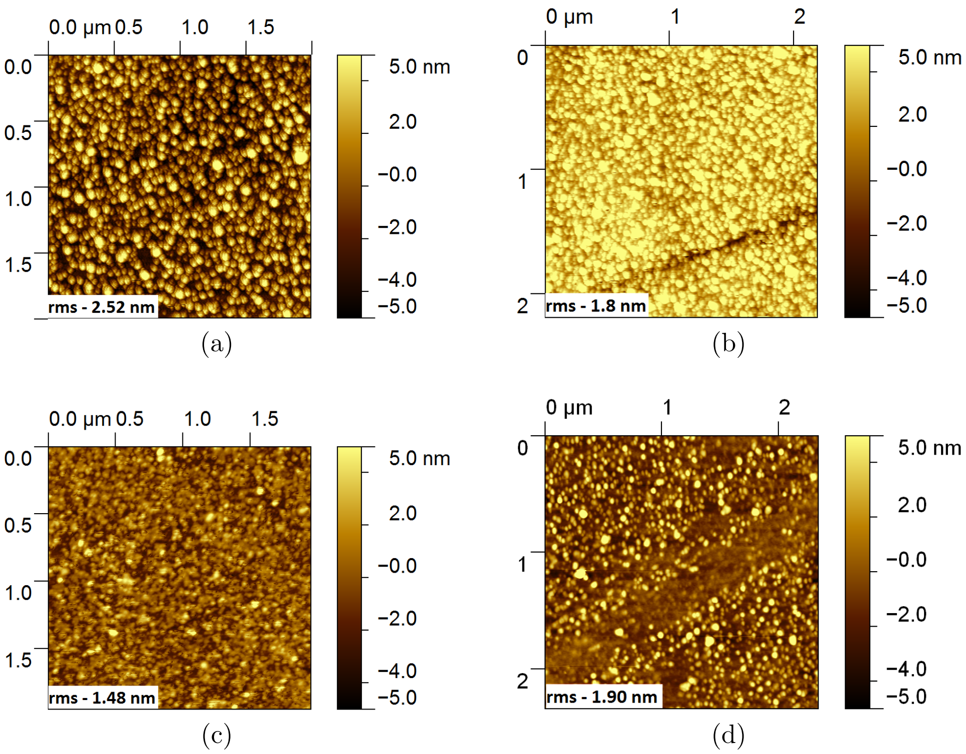

(a) (b) (c) (d)

Figure 4.8: AFM micrographs for silicon carbide ($000\bar{1}$) samples annealed at 1300°C for annealing times of a) 30 minutes. b) 45 minutes. c) 60 minutes. d) 105 minutes. Lateral and height scales of each image are given along with the rms roughness of each scan. Each image highlights the granular nature (10s nm grains) of the film growth at this annealing temperature.

complete. Also shown is a sample annealed for 105 minutes (Figure 4.8(d)) shows an increase in rms roughness, suggesting that this is the partial growth of (an) extra graphene layer(s).

AFM of samples annealed at 1400°C for differing annealing times are shown in Figure 4.9. Again there is a general decrease in rms roughness as the annealing time is increased. However, further analysis on a sample annealed for 50 minutes showed the presence of rips in the graphene film, which lead to an increase in the rms roughness. Unlike samples annealed at 1300°C the AFM reveals a faceted surface, exhibiting some of the features observed in LEEM data (Figure 4.7), the

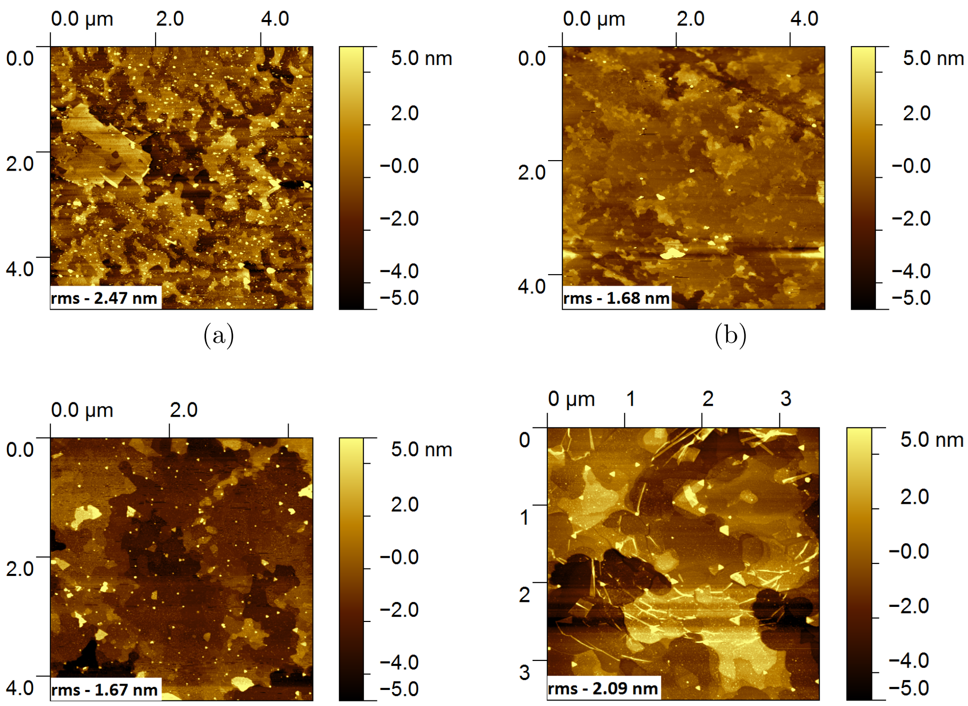

(a) (b)

(c) (d)

Figure 4.9: AFM micrographs for silicon carbide (000$\bar{1}$) samples annealed at 1400°C for annealing times of a) 15 minutes. b) 30 minutes. c) 50 minutes. d) is a micrograph taken on a different area of the same sample shown in c) indicating the presence of rips/wrinkles in the film. Lateral and height scales of each image are given along with the rms roughness of each scan. Larger grains are now observable (100s nm) when compared to samples annealed at 1300°C (Figure 4.8.

details of this difference between the grain-like 1300°C growth and the facet-like 1400°C growth will be discussed further in a later section.

Samples annealed at 1400°C appear to consist of a full graphene film at anneal times of ∼20 minutes. This has been seen via the absence of charging at low accelerating energies during the taking of LEED data and also via collaborative work with the University of York through STM measurements. A representative number of pre-prepared samples annealed at differing times and temperatures conditions were approached with an STM tip, those samples that had previously shown charging effects in LEED due to being annealed at too low a temperature

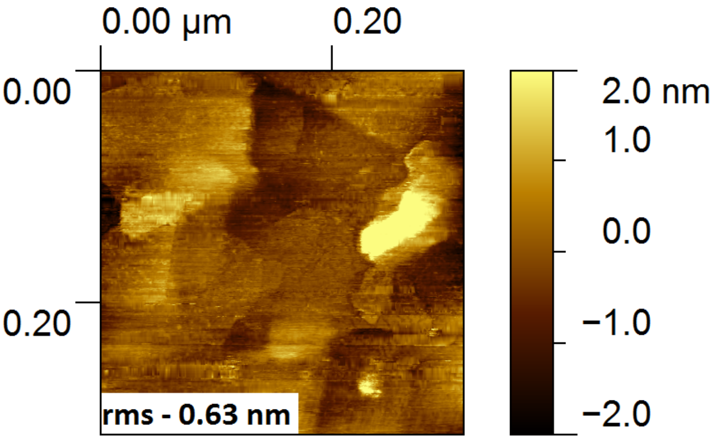

Figure 4.10: STM scan of a sample annealed at 1400°C for 20 minutes. Grain sizes are comparable to AFM measurements of samples annealed at this temperature (Figure 4.9). The successful approach of the STM tip and image acquisition shows that there is a complete conducting layer(s) of graphene present on the surface.

for too short an anneal time were difficult to approach with an STM tip, owing to the lack of surface conduction.

However a sample annealed for 20 minutes at 1400°C that showed no LEED charging effects, was also easy to approach via STM suggesting the presence of a conducting layer along the top surface (metal contacts along the sides of the chip were used to compensate for the insulating silicon carbide substrate). The STM image shown in Figure 4.10 is taken from this sample, the quality of tip limits the resolution of the image, here the tip used was incapable of atomic resolution. On the length scale obtainable similar faceted features can be observed to those obtained via LEEM and AFM imaging (Figure 4.7 and 4.9 respectively). Although atomic resolution was not obtainable, this matching of features and the added information afforded by STM about the conductivity of samples is very useful and complements other data well as it once more demonstrates the onset of a complete, conducting graphene film on the sample surface.

## 4.3 Increasing the Lateral Grain Size of Within the Graphene Films

Once complete graphene films were obtained on the device scale. It became apparent that the small grain sizes still present as imaged by AFM (Figure 4.8) and LEEM (Figure 4.6) were limiting the long range electronic order within the films and leading to the the non graphene-like transport behavior, with the transport data fitting to two-dimensional variable range hopping (as shown in Figure 4.5). To progress to more graphene-like electronic transport behavior an increase in the lateral grain size was required. Increasing the annealing time had lead to an increase in the graphene coverage on the sample surface, it was thought that the grain size could be increased by increasing the annealing temperature of the process. This section will track the process of increasing annealing temperature and its affects on the lateral grain size present within graphene films. Comparisons will be made with work carried out elsewhere which shows that increasing the annealing temperature leads to a coarsening of smaller graphene grains into larger ones with the increased mobility of the free carbon atoms on the surface.(24)

Section 3.3.3 discusses how Raman spectroscopy can be used to estimate the grain sizes present within a graphene film. The procedure utilizes the increase in D peak intensity as the number of defects present within a film increases.(134; 136) For grain size measurements, the grain boundaries act as defects, therefore the smaller the grains, the more edges are present and as such the D peak will become more intense. This relationship known as the Tuinstra-Koenig (TK) relation has been used to measure grain sizes in a number of different graphitic systems (134) including epitaxial graphene. (138; 139) Figure 4.11 shows the evolution of the grain size ($L_\alpha$) with increasing annealing time at an annealing temperature of 1400°C. There is a general trend in the observed grain size with increasing annealing time. As discussed below, this method of measuring $L_\alpha$ with Raman spectroscopy has limitations in measuring the true grain size value when multiple grains of different sizes are present, it is this reason that likely leads to the large scatter of data points in Figure 4.11. From microscopy techniques such as AFM and LEEM it has been shown that increasing the temperature is the dominant mechanism behind increasing the grain size due to increasing the mobility of the

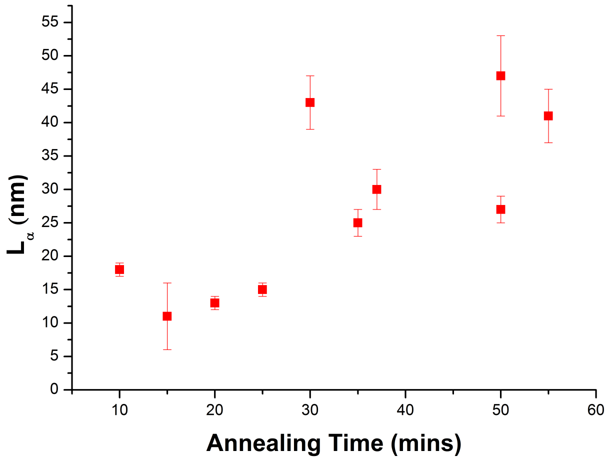

Figure 4.11: Plot of grain size ($L_\alpha$) with increasing annealing time for a set of samples annealed at 1400°C. The error bars are given from the statistical averaging of spectral data from a single sample. The calculation of $L_\alpha$ is described in section 3.3.3.

free carbon atoms on the surface during graphene formation and that increasing annealing time increases graphene coverage rather than grain size.

The actual value of $L_\alpha$ observed in Figure 4.11 is much less than the grain sizes observed in AFM and LEEM measurements for samples annealed under these conditions. This is true also from the samples annealed at 1450°C where the $L_\alpha$ values shown in Table 4.2 though higher than those observed for 1400°C anneals are still well below those observed via other techniques such as AFM and LEEM. However for the samples annealed at 1300°C there is a good agreement between the $L_\alpha$ values observed through AFM and those measured with with Raman spectroscopy.

A possible reason for this discrepancy is suggested by Ferrari et al (156) where the assumption made by Tuinstra and Koenig (134) that the graphite becomes uniformly nanocrystalline which is not the case here as we have a mix of domain sizes. This assumption leads to the small domains dominating the $L_\alpha$ values obtained via the T-K relation when the domain sizes are mixed as the overall

Table 4.1: Grain size measurements for samples annealed at 1300°C using Raman spectroscopy. Errors quoted are statistical averages of spectral data from each sample. The number of scans used for this averaging is given.

| Annealing Time | Grain Size (nm) | No of Scans |
|---|---|---|
| 30 minutes | $67 \pm 4$ | 30 Scans |
| 60 minutes | $51 \pm 4$ | 30 scans |

Table 4.2: Grain size measurements for samples annealed at 1450°C using Raman spectroscopy. Errors quoted are statistical averages of spectral data from each sample. The number of scans used for this averaging is given.

| Annealing Time | Grain Size (nm) | No of Scans |
|---|---|---|
| 10 minutes | $40 \pm 2$ | 40 Scans |
| 15 minutes | $69 \pm 4$ | 20 Scans |
| 20 minutes | $64 \pm 3$ | 20 Scans |

$_\alpha$ is given as a weighted average of all the domains within the laser spot.(156) Another possible reason for the observed higher grain size in the samples annealed at 1300°C compared to samples annealed at 1400°C is the use of the integrated intensities of the peaks within the ration calculation. As discussed by Ferrari et al (156) the peaks become broader in disordered films and therefore the integrated intensity calculation can become distorted and higher grain values obtained than expected.

Though the Raman spectroscopy does not yield the expected grain size values for samples annealed at temperatures of 1400°C and above (Raman yields $\sim$ 50 nm when $\sim$ 100s nm observed in other measurement techniques), there is a general trend for the spectra to look more graphene-like in these samples. This is highlighted in Figure 4.12 which shows selected (so not completely representative of the full sample area as with data used for grain calculations above) graphene spectra with the silicon carbide background subtracted for samples annealed. The 2D peak is seen to become much more prominent for the sample annealed at 1450°C with the ratio of G to 2D peak looking indicative of a monolayer flake produced by exfoliation. The D to G ratio is also an indication of order and is smaller in the sample annealed at 1450°C when compared to the sample annealed at 1300°C, showing those samples to be more ordered (larger grain sizes). Though the D to G ratio is lower in the sample annealed at 1400°C compared to the sample annealed for 1300°C the narrower bands present yield a smaller grain size due to the use of integrated intensities of the 2 bands for the calculation.(138; 139) This is a question of convention with some work using the overall intensity ratio (156) whereas others use the ratios of the integrated intensities as we do here.(138; 139) The G to 2D ratio in both the samples annealed at 1400°C and 1300°C respectively are comparable to a bilayer flake produced by exfoliation.

A possible explanation for this observation would be that the samples annealed at 1450°C are likely to have a single graphene domain of around 2 $\mu$m within a single Raman laser spot surrounded by smaller domains. This would make the Raman spectrum obtained a mix of that expected for an isolated flake with the addition of defects from the edge regions associated with the surrounding smaller domains contributing to the D peak amplitude. Due to a change in analysis protocol the data shown for the sample annealed at 1300°C has been normalized to the silicon carbide background spectra.

AFM micrographs as shown in Figure 4.13 show how the lateral grain size increases as the annealing temperature increases. The annealing time does not remain constant in the images chosen for Figure 4.13 but reflect roughly the annealing times to form a complete graphene film at each temperature. Figures 4.8 and 4.9 from the previous section show how the lateral grain size remains somewhat constant for samples annealed at the same temperature (1300°C and 1400°C respectively) for varying annealing times. The lateral grain size can be seen to increase with sample annealing temperature from 10s nm at 1300°C to grain sizes of 100s nm for samples annealed at 1450°C.

As described in section 2.2 earlier in this thesis the parameters linked with the growth process in epitaxial graphene and the mechanisms of how each parameter affect the quality of the graphene growth can be somewhat ambiguous. For example here, there is an increase in lateral grain size observed by increasing the annealing temperature. There are two competing mechanisms that could

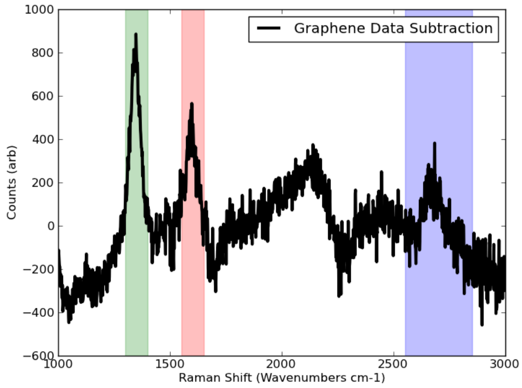

(a) 1300°C for 60 minutes. $L_\alpha$ = 60.04±0.02 nm

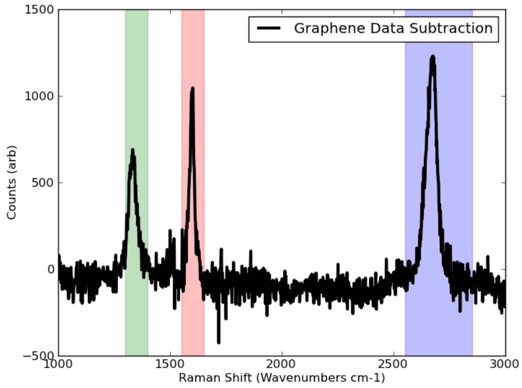

(b) 1400°C for 30 minutes. $L_\alpha$ = 28.93±0.02 nm

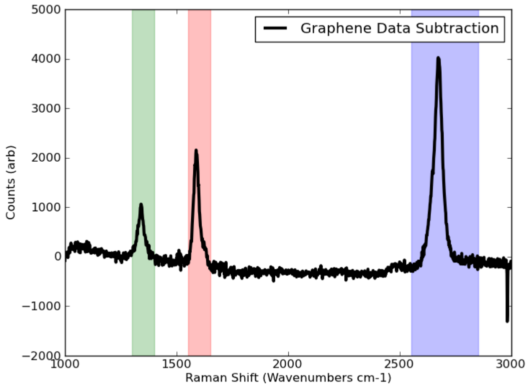

(c) 1450°C for 15 minutes. $L_\alpha$ = 91.58±0.03 nm

Figure 4.12: Raman spectra (silicon carbide spectra subtracted) for epitaxial graphene grown at differing annealing times and temperatures. $L_\alpha$ values for each graph are given as calculated from each spectra, error given by errors fitting the D and G bands. The shaded regions correspond to the key Raman bands in graphene D (green), G (red) and 2D (blue).

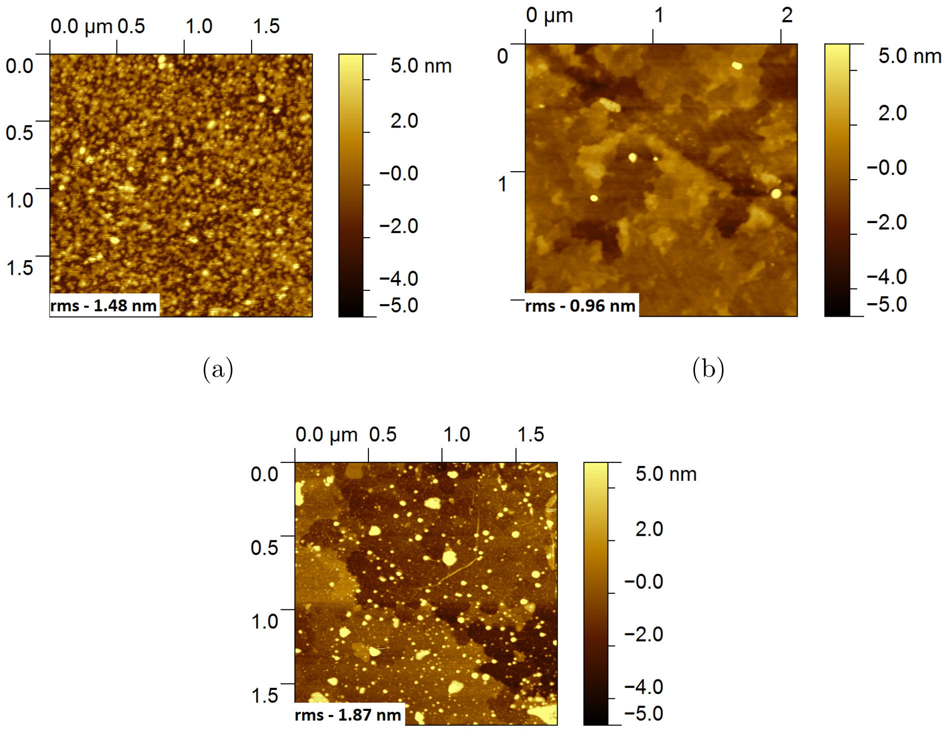

(a)

(b)

(c)

Figure 4.13: AFM micrographs for silicon carbide $(000\bar{1})$ samples annealed at varying annealing times and temperatures. a) 60 minutes at 1300°C. b) 30 minutes at 1400°C and c) 20 minutes at 1450°C. Lateral and height scales of each image are given along with the rms roughness of each scan. The scans show the general increase in lateral grain size as the annealing temperature is increased.

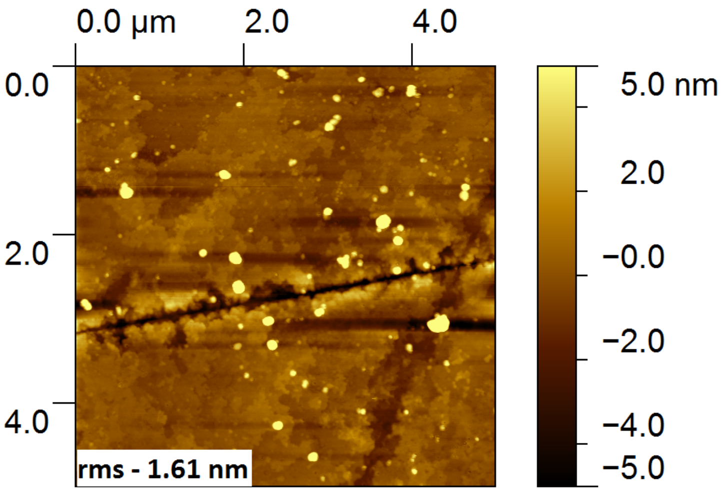

Figure 4.14: AFM micrograph of a sample that underwent a two-stage annealing process. Firstly annealed for 60 minutes at 1300°C then an extra anneal at 1400°C for 30 minutes, both carried out in-situ. Lateral and height scales of the image are given along with the rms roughness.

explain this kind of variation with increased temperature. The first is that the increase in temperature provides the free carbon atoms on the surface mobility affording faster propagation of individual grains from nucleating sites. The second mechanism suggests that the increasing temperature again increases the mobility of free carbon atoms on the surface, this time however, the increased mobility leads to the coarsening (24) or coalescence (28) of smaller grains to form the larger domains observed.

It is somewhat difficult to distinguish between these two mechanisms. One way is to carry out a two-stage annealing process as shown in Figure 4.14 AFM data from this sample shows that annealing at 1300°C for 60 minutes (as in Figures 4.8(c) and 4.13(a)) then further annealed for 30 minutes at 1400°C. The resulting surface corresponds to the faceted type of structure obtained for samples annealed at higher temperatures rather than the clusters of small grains observed at lower annealing temperatures. As the top graphene layer is the first to grow (157) this suggests that the growth mechanism responsible for the larger grain

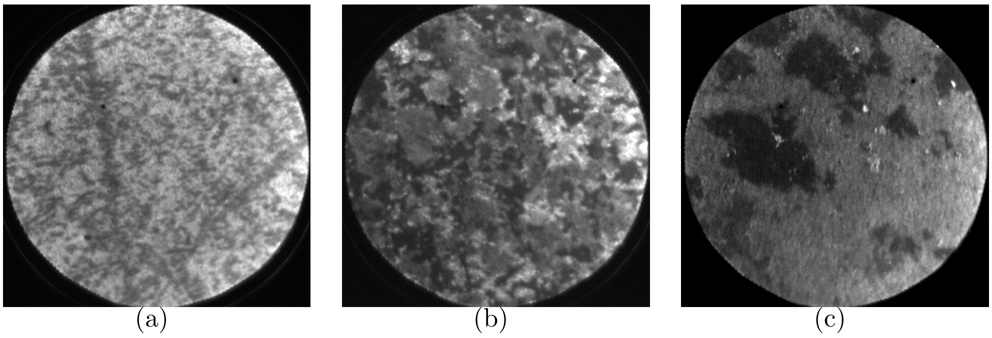
(a) (b) (c)

Figure 4.15: 10 $\mu$m field of view LEEM images taken for SiC(000$\bar{1}$) annealed for varying annealing times and temperatures. Differing incident energies were chosen to give the best contrast in each image. a) Sample annealed for 60 minutes at 1300°C imaged at 2.8 eV. b) Sample annealed at 1400°C for 30 minutes imaged at 3.9 eV. c) Sample annealed at 1450°C for 20 minutes imaged at 3.9 eV. The increase in domain size with increasing annealing temperature can be seen.

size observed is that of the coalescence of smaller domains into larger ones.

This increase in lateral grain size has also been observed in LEEM data. Figure 4.15 shows LEEM images from a set of samples annealed at various temperatures, the annealing times used again corresponds to roughly the time required to form a complete film at those temperatures. In agreement with AFM data, the lateral grain size shows an increase as the annealing temperature is increased. The sample annealed for 20 minutes at 1450°C (Figure 4.15(c)) shows very large grain sizes (∼4 $\mu$m), much larger than the features observed in AFM (Figure 4.13(c)). The contrast in these images is due to different thicknesses of graphene films, it is therefore likely that the smaller features observed in AFM are grains of the same thickness that are rotationally disordered with respect to each other.

The increase in grain size with annealing temperature is also apparent in electronic transport measurements. Figure 4.16 shows sheet resistance measurements at varying temperature R$_s$($T$) for samples annealed at 1400°C and above. As with the transport data shown in Figure 4.5 these are dc measurements taken with a four-probe geometry with voltage probe spacings of 5 $\mu$m. The electrodes are once more made of Ti/Au and are patterned using standard optical lithography techniques. Again these electrical transport measurements were carried out by Graham Creeth.

If inelastic scattering at grain boundaries was leading to the localisation nature of the electron transport and the variable range hopping behavior as observed in Figure 4.5 for samples annealed at 1300°C, then with the increase in lateral grain size as observed in AFM and LEEM presented in this section should lead to less inelastic scattering. As the inelastic scattering events are decreased it would be expected that elastic scattering events will dominate. In two-dimensional systems as elastic scattering events dominate, electrons moving in time-reversed paths remain phase-coherent and can interfere with each other destructively. Thus leading to weak-localisation behavior.(158) This move to weak-localisation type behavior would be expected here and has been observed elsewhere in epitaxial graphene systems.(17)

The electronic transport data for samples annealed at 1400°C and above still become less conducting as they are cooled however the observed behavior as expected, can no longer be fitted to the same variable range hopping functional form (equation 4.1). The increase in sample uniformity as discussed above leads to an increase in the electronic mean free path $l$, with the product of this mean free path and the Fermi wavevector $k_F$ is now greater than 1. As expected, the increase in uniformity (decrease in grain edges) leads to a decrease in the inelastic scattering events that occur and elastic scattering begins to dominate, this increases the possibility that electrons traveling in a closed path will remain phase-coherent, leading to weak localisation.(158; 159) In the weak localisation regimes, the correction to the conductance $G$ is given by

$$G = \left(\frac{ne^2\tau_0}{m}\right)\left(1 - \frac{1}{\pi k_F l}\ln\left(\frac{\tau_i}{\tau_0}\right)\right). \tag{4.2}$$

The elastic scattering time, $\tau_0$, is not temperature dependent. The temperature dependence is given by the inelastic scattering time, $\tau_i$. This leads to the change in resistance being proportional to ln$T$ (158; 159) as seen in Figure 4.16 and observed previously in epitaxial graphene samples.(17)

The data also shows that samples annealed at 1450°C are roughly two orders of magnitude more conducting than the samples annealed at 1400°C. Also shown

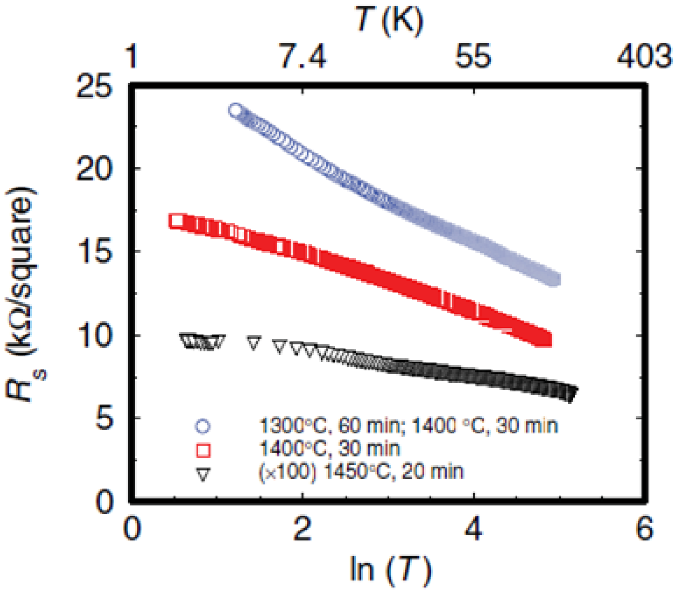

Figure 4.16: Resistance change with temperature for samples annealed for varying annealing times and temperatures. Here samples annealed at 1400°C and above, plotted on appropriate axes for a weak localisation-type behavior. It is important to note that data for the sample annealed at 1450°C has been scaled up by a factor of 100 in sheet resistance for visibility, due to the comparatively very high conductivity of this sample. Adapted from (28). Measurements carried out by Graham Creeth.

is that the sample where coalescence of grains was observed in AFM (Figure 4.14) via a two-stage annealing process also results in an increase in inelastic scattering time. This switch from variable range hopping behavior to more graphene-like weak localization with increasing annealing temperature is a key result in showing the improvement in graphene film quality obtained during this project.

## 4.4 Thicknesses of Graphene Films Grown in Ultra High Vacuum

When producing epitaxial graphene films it is important to know the number of graphene layers present within the films (the film thickness). In the following section a number of different procedures for measuring thicknesses will be presented and the results from these procedures discussed. The properties of graphene films vary with the number of graphene layers, for example the band structure of bilayer graphene is different to that of monolayer graphene and the charge carriers have an effective mass. Although multi-layer graphene grown on silicon carbide $(000\bar{1})$ has been shown to have decoupling between the graphene layers allowing multi-layer films to maintain the properties of monolayer graphene sheets,(50) the quantum hall effect was not observed in this material until good control of the film thickness was managed.(47) Thus having a good understanding of the film thickness is important when developing growth procedures for graphene films.

Elsewhere the growth of graphene on silicon carbide $(000\bar{1})$ is observed to produce very thick (10+ layers) graphene films for samples annealed in UHV at similar times and temperatures to the ones used in this work.(23) A very crude thickness estimate can be obtained from the simple fact that we can observe silicon carbide substrate spots in LEED patterns. This immediately puts a limit on the thickness of our graphene films at below $\sim$5 layers or less as typically the electron penetration depth at an energy of 100 eV is in the order of a few nanometers.(147) This suggests that the specific equipment and procedures used in this work helps to slow the rate of silicon evaporation from the surface and slow the rate of graphene production. The presence of a graphene precursor buffer layer reconstruction as shown in Figure 4.3(a) backs up this point as it compares well to work carried out elsewhere on graphene growth on silicon carbide $(000\bar{1})$ in silicon rich environments which resulted in the formation of a similar buffer layer reconstruction being observed.(154)

As shown in section 3.6.3 LEEM data can be used to obtain a thickness measurement for graphene films. Electron interference between layers leads to minima in the LEEM intensity vs excitation energy data. The number of minima observed then corresponds to the number of layers. Figure 4.17 shows LEEM IV data taken in a number of positions on a sample annealed at 1450°C for 20 minutes. The data shows that this sample consists of 2 (Figure 4.17(d)), 3 (Figure 4.17(c)) and 4 (Figure 4.17(b)) layer regions. This result is consistent with the crude thickness limit obtained from the observation of silicon carbide substrate spots in LEED data.

The larger grain sizes make taking IV data easier on samples annealed at 1450°C compared to lower temperatures. Fluctuations and positional drifts in the LEEM images can lead to blurring out of the minima in samples that have grain sizes that are comparable to the size of these fluctuations. LEEM IV data taken for samples annealed at 1400°C for 30 minutes and 55 minutes are shown in Figures 4.18 and 4.19 respectively. Both show evidence of oscillations though the 30 minute sample (Figure 4.18) is very washed-out. In the 55 minute annealed sample areas of 2 and 3 layers of graphene are observed. The increased uniformity in this sample allows clearer IV data to be obtained though the spectra still appear to consist of features from both 2 and 3 layer graphene due to drift in the images from one energy to the next.

A more direct measurement of graphene thickness has been made using cross sectional TEM images taken as part of a collaboration with the University of York. These high resolution TEM images effectively allow the number of graphene layers formed to be counted. As can be seen in Figure 4.20 a sample annealed at 1400°C for 20 minutes appears to consist of regions with 2 and 3 layers of graphene. This result is consistent with those obtained via LEEM and again shows that under these annealing conditions the graphene films produced here consist of few graphene layers. If regular access to this kind of TEM measurement was possible then the imaging of a wide range of epitaxial graphene films produced

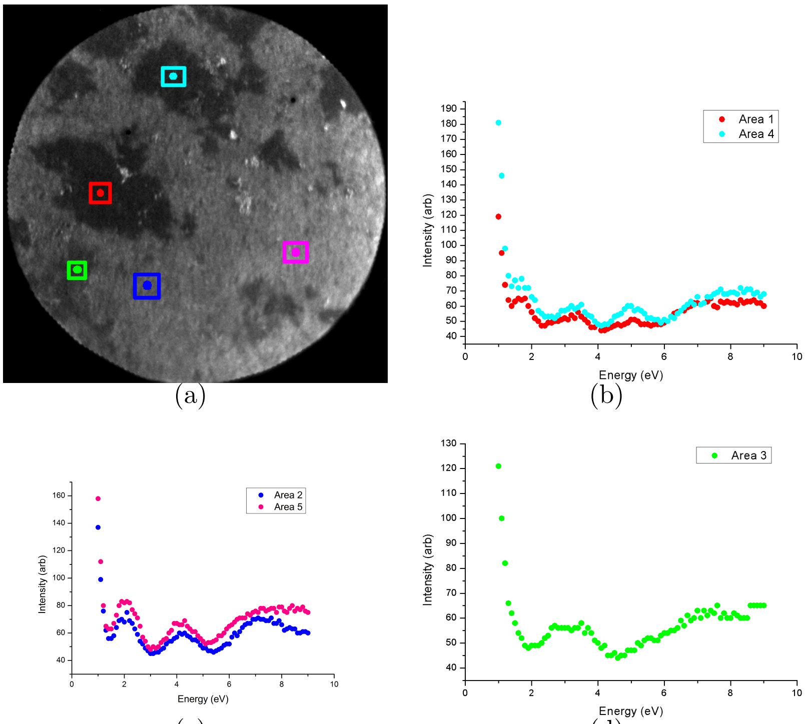

(a) (b)

(c) (d)

Figure 4.17: a) 10 $\mu$m field of view LEEM image taken at 3.9 eV for SiC(000$\bar{1}$) annealed at 1450°C for 20 minutes. Coloured regions (boxed for clarity) correspond to areas used to take IV data shown in b), c) and d). The number of minima in the LEEM I-V graphs indicate the number of graphene layers present in those areas.

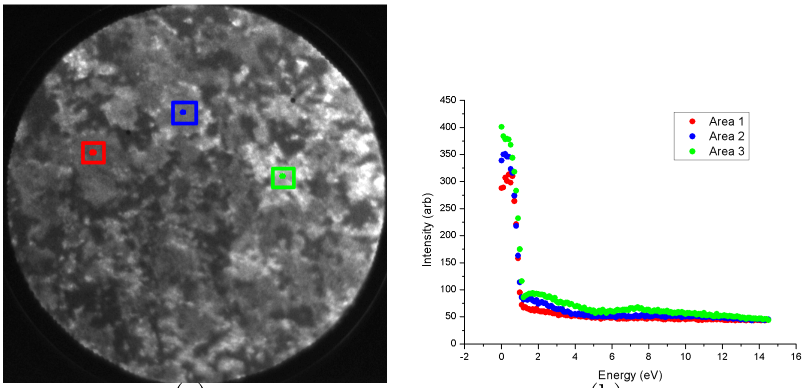

(a) (b)

Figure 4.18: a) 10 $\mu$m field of view LEEM image taken at 3.9 eV for SiC(000$\bar{1}$) annealed at 1400°C for 30 minutes. Coloured regions (boxed for clarity) correspond to areas used to take IV data shown in b). The number of minima in the LEEM I-V graphs indicate the number of graphene layers present in those areas.

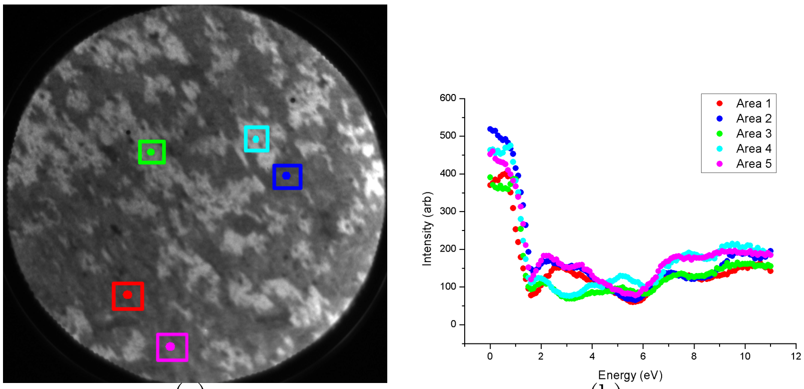

(a) (b)

Figure 4.19: a) 10 $\mu$m field of view LEEM image taken at 3.9 eV for SiC(000$\bar{1}$) annealed at 1400°C for 55 minutes. Coloured regions (boxed for clarity) correspond to areas used to take IV data shown in b). The number of minima in the LEEM I-V graphs indicate the number of graphene layers present in those areas.

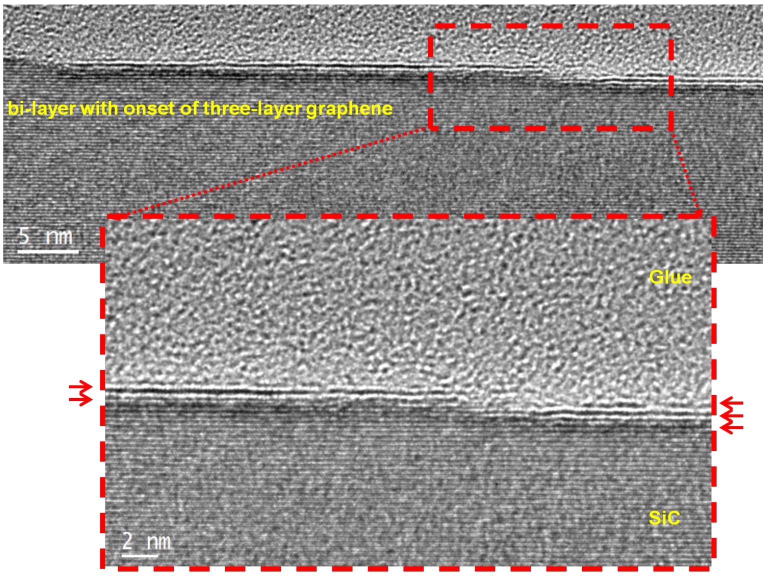

Figure 4.20: Cross sectional TEM image of a sample annealed at 1400°C showing the presence of 2 and 3 layers of graphene. Data taken by Vlado Lazarov at the University of York. Red arrows in the zoom in image highlight the presence of 2 and 3 graphene layers.

with different annealing times and temperatures would provide a fuller picture of the evolution of graphene thickness.

Another method that has been used elsewhere to estimate the thickness of epitaxial graphene films has been the use of Raman spectroscopy to track the attenuation of the underlying silicon carbide spectra due to the presence of graphene overlayers as outlined in section 3.3.6. Table 4.4 gives the results of Raman attenuation measurements carried out on samples where the thickness has been measured through either TEM or LEEM work (Table 4.3). The calculations are performed using three different values for the adsorption coefficient $\alpha$. An original version (later corrected) of a paper by Shrivraman et al (140) found an $\alpha$ value to be 0.03 per monolayer of graphene, this was later corrected to 0.02 per monolayer.(140) Measurements carried out on exfoliated graphene flakes in this group (160) suggested that an alpha value of 0.015 per monolayer.

For the samples annealed at 1400°C the Raman attenuation data appears to underestimate the thickness when compared to the other techniques with the

Table 4.3: Thickness measurements from other techniques.

| Annealing Conditions | LEEM result | TEM result |
|---|---|---|
| 20mins@1400°C | N/A | 2 and 3 layers |
| 30mins@1400°C | 2 and 3 layers | N/A |
| 55mins@1400°C | 3 and 2 layers | N/A |
| 20mins@1450°C | 4 and 3 layers | N/A |

Table 4.4: Thickness measurements (number of layers) from Raman attenuation data for different values of the absorption coefficient ($\alpha$)

| Annealing Conditions | $\alpha = 0.03$ | $\alpha = 0.02$ | $\alpha = 0.015$ |
|---|---|---|---|
| 20mins@1400°C | 0.67±0.08 | 1.0±0.1 | 1.3±0.1 |
| 30mins@1400°C | 1.00±0.06 | 1.51±0.09 | 2.0±0.1 |
| 55mins@1400°C | 0.63±0.07 | 0.94±0.09 | 1.2±0.1 |
| 20mins@1450°C | 2.5±0.2 | 3.8±0.3 | 5.1±0.4 |

$\alpha$ correction to 0.015 per monolayer not correcting for this discrepancy. For the sample annealed at 1450°C the Raman attenuation data when using an absorption coefficient of 0.02 per monolayer agrees well with the thicknesses observed via LEEM for this sample. It has been shown (140) that this method of measuring (estimating) graphene thickness improves in accuracy for thicker graphene films (∼5 layers and above) which is suggested by these results. For other thickness measurements an $\alpha$ value of 0.02 per monolayer will be used.

Figure 4.21 shows the evolution of the number of graphene layers with increasing annealing time for an annealing temperature of 1400°C. In agreement with previous techniques (LEEM and TEM) all the graphene films appear to be under 5 layers in thickness. There is a general increase in thickness with annealing time, though the previously mentioned discrepancies that arise when using this technique for measuring the thickness of graphene films under 5 layers mean that caution must be used when making such statements.

Tables 4.5 and 4.6 give a summary of layer thicknesses measured within sam-

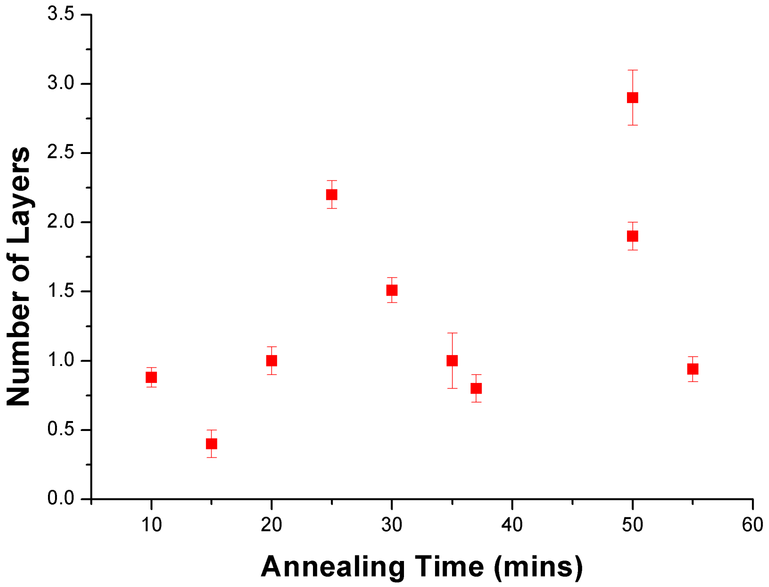

Figure 4.21: Plot of layer thickness with increasing annealing time for a set of samples annealed at 1400°C. The error bars are given from the statistical averaging of spectral data from a single sample. The large deviation of layer thickness values obtained from samples undergoing similar annealing conditions could be due to the issues with measuring layer thicknesses under 5 layers with this technique.(140)

Table 4.5: Thickness measurements (number of layers) using Raman spectroscopy for samples annealed at 1300°C. Calculated values used a value of 0.02 for the absorption coefficient ($\alpha$).

| Annealing Time | Raman Layer Thickness ($\alpha = 0.02$) |
|---|---|
| 60 mins | 3.1±0.4 |
| 30 mins | 1.00±0.06 |

Table 4.6: Thickness measurements (number of layers) using Raman spectroscopy for samples annealed at 1450°C. Calculated values used a value of 0.02 for the absorption coefficient ($\alpha$).

| Annealing Time | Raman Layer Thickness ($\alpha = 0.02$) |
|---|---|
| 20 mins | 3.8±0.3 |
| 15 mins | 3.8±0.3 |
| 10 mins | 2.0±0.2 |

ples annealed at 1300°C and 1450°C respectively. The samples annealed at 1300°C have higher thickness values and surprisingly the sample annealed for 30 minutes appears thicker than that annealed for 60 minutes. One explanation for this could be that as the annealing time is increased, the average surface roughness of samples annealed at 1300°C decreases. The rougher graphene overlayers seen at shorter annealing times could then possibly cause more more attenuation than smoother yet potentially thicker graphene overlayers for longer anneal times. For the samples annealed at 1450°C there is consistency in the thickness measurements and again there is a general trend for the thickness to increase with annealing time.

Also used as a thickness measurement in graphitic systems is the fitting of the graphene 2D peak to multiple Lorentzian peaks. (107; 135; 161) This technique is somewhat limited to monitoring film thickness in epitaxial graphene grown on the carbon terminated face of silicon carbide as the decoupling between graphene layers allows 2D band spectra from multi-layered films to still be fit with single

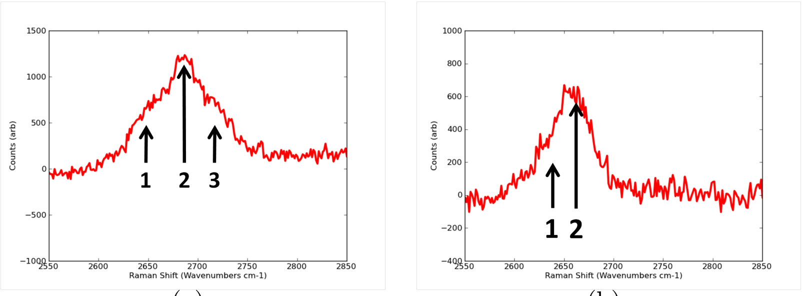

(a) (b)

Figure 4.22: Raman spectra taken from a sample annealed at 1400°C for 50 minutes showing peaks with a) 3 distinct components. b) 2 distinct components. Arrows and labels indicate the possible shoulder features.

Lorentzian fits.(162)

This is consistent with the results observed within this work and the notable shoulders observed in the fitting of the 2D peak in systems such as HOPG and multi-layered exfoliated graphene flakes not observed.(135) Here single Lorentzian fits to the 2D peak seem to be acceptable for all samples except some of the 1400°C anneals for longer annealing times (∼45 minutes plus). In these samples the 2D peaks can consist of two or three distinct components as shown in Figure 4.22. Detailed fitting of these components has not yet been carried out though early attempts suggest that the components arise from areas of differing graphene thickness within the size of the Raman laser spot.

In this section techniques used for measuring the thickness of graphene have been discussed and the results from the differing techniques compared and contrasted. During the course of this project an upgrade to the LEED system used has been completed. It is now possible to take LEED intensity vs energy data. This opens up the possibility to measure graphene film thicknesses via the technique mentioned in section 3.5.3, with this technique further enhanced by an extra upgrade due to equip the system with Auger spectroscopy capabilities. This would allow thickness measurements to be carried out in-situ on the UHV grown samples with both LEED IV data and Auger and to calibrate the two techniques as done elsewhere.(148)

## 4.5 Conclusions and Discussion

In this Chapter, improvements in the growth of epitaxial graphene films in ultra high vacuum conditions have been shown. These improvements have seen the films move from being incomplete in nature and with a lateral grain size in the order of 10s nm to being complete with grain sizes in the 100s nm range. These morphological advances in the graphene films as observed with techniques such as atomic force microscopy (AFM) and low energy electron microscopy (LEEM) resulted in the betterment of electronic transport measurements with a switch from variable range hopping type transport, indicative of disordered systems, to more graphene like weak-localisation behavior as the grain size increases. This grain size increase leads to elastic scattering events dominating over inelastic events and hence the switch in transport behavior. The linking of the electrical transport properties with the observations made from surface science techniques such as LEEM and AFM is the key result to report from this chapter and has lead to a publication.(28)

In general, the annealing time appears to control the graphene coverage on the surface with the films becoming more complete with prolonged annealing. Unlike work elsewhere (34) that sees rapid growth of multiple graphene layers (over 10) on the silicon carbide $(000\bar{1})$ face LEEM measurements show that for a range of annealing times the graphene thickness is still 4 layers or below. The reasoning behind this could be the observed existence of a buffer layer reconstruction in low energy electron diffraction (LEED) measurements that occurs as a precursor to the growth of graphene. A similar reconstruction has been observed for graphene growth under disilane environments due to the presence of excess silicon.(154) This reconstruction could make silicon desorption from the substrate surface less energetically favorable and therefore decrease the number of graphene layers that grow. In this work, the excess silicon is thought to be due to the natural confinement that exists between the carbon filament heater and the silicon carbide substrate or due to the presence of a sapphire cap 1 mm above the substrate during annealing. This confinement increases the partial pressure of silicon above the substrate and slows down the silicon evaporation rate as described elsewhere (34) and leads to improved graphene film morphologies as the graphene films grow with the underlying silicon carbide substrate in a more equilibrated state.

The progress achieved in increasing the grain size within the graphene films is linked to the increasing of annealing temperatures. A two-stage annealing process within which a sample was annealed at 1300°C for 60 minutes followed by 1400°C for 30 minutes in-situ showed the increased grain sizes of 100s nm in AFM and LEEM and weak-localisation electronic transport measurements as observed in single-stage annealing processes at 1400°C. This suggests that the grain size increase at higher annealing temperatures occurs as smaller grains coalesce (28) or coarsen (24) as the carbon atoms on the surface become more mobile.

With the current grain size of 100s nm (towards $\mu$m in 1450°C anneals) are comparable to those obtained elsewhere under similar annealing conditions.(24) It is within the specifications of high end electron beam lithography to be able to pattern devices within single grains or with few grain boundaries present. This could allow for the probing of quantum Hall effects within the grown films. The nature of the quantum Hall effect would confirm if the multi-layered graphene films grown here on the silicon carbide $(000\bar{1})$ are in fact electronically decoupled from those below and exhibit half-integer quantum Hall behavior expected for monolayer graphene or the standard quantum Hall effect observed for AB stacked graphene layers.

The nature of the grain boundaries are also relatively unknown within the samples grown here. Now the conditions are known for the regular production of continuous conducting graphene films, further STM measurements with improved tip quality would allow atomic scale imaging of these grain boundaries. The structure of the grain boundaries is important for the electronic transport of the graphene films. This is because different scattering processes occur dependent on whether the edge structure is zig-zag or armchair in nature.(163)

Once more it is important to note that some of the work presented during this chapter has been carried out as part of collaborations. The electrical transport measurements and results fitting were carried out by Graham Creeth at the University of Leeds, Graham also provided feedback and ideas towards the growth procedures. LEEM measurements were carried out by myself and Graham at BNL with the aid of Jurek Sadowski who operated the experimental apparatus with our input. TEM images shown were taken by Vlado Lazarov at the University of York as part of a collaboration. STM measurements were also carried out at the University of York by Steve Tear and Andrew Vick.

# Chapter 5

# Strain Measurements in Epitaxial Graphene Films Using Raman Microscopy

## 5.1 Overview

In section 2.4 it was discussed how straining graphene films can have a large effect on their properties, including the potential for introducing a band-gap into its electronic structure (96) and introducing pseudo-magnetic fields.(108; 109) It has been observed, initially in epitaxial graphene films grown on the silicon carbide (0001) face,(32) that a compressive strain builds up in the graphene films. This compressive strain is said to form due to the difference in thermal expansion coefficients between the graphene films and the underlying silicon carbide structure. (32)

As the graphene film is cooled down from the high synthesis temperature, it expands due to having a negative coefficient of thermal expansion.(103) Whilst the graphene film is expanding, the underlying silicon carbide substrate contracts, (104) thus causing a compressive strain to build up within the graphene films. The negative coefficient of thermal expansion in graphene is explained by the presence of the ZA bending mode phonon which is activated at the temperatures discussed here.(103) The frequency out-of-plane bending mode vibration mode increases as the in-plane lattice spacing increases. This is known as the 'membrane effect' and is comparable to the frequency of a vibration on a string increasing with increased tension within the string.(103)

Despite work being carried out on measuring the strains present within epitaxial graphene films on the silicon carbide (0001) face.(32) No such publications existed for the behavior of strains within epitaxial graphene films grown on the silicon carbide $(000\bar{1})$ face. As the bonding between the graphene and the silicon carbide substrate varies between the (0001) and $(000\bar{1})$ it was important to track the strain behavior of graphene films grown on this face.

Work here used Raman microscopy to track the build up of strains within these graphene films. The films were grown in ultra high vacuum with a sapphire cap 1 mm above the sample as shown in Figure 3.1(b). The build up of strains within the films was tracked as a function of annealing time leading to the first publication of strain values within films grown on the $(000\bar{1})$ face.(33) The aim was to observe whether the decoupling between the graphene films and the substrate that leads to higher electron mobilities leads to a relaxation in the strains that build up in graphene films grown on this face, this was seen to be the case with a maximum observed compressive strain of -0.5% being less than the -0.8% observed on the (0001) face with similar preparation conditions.(32)

## 5.2 Using the Graphene 2D Peak Position to Measure Strain Values

Raman microscopy has also been shown to be very useful in the measuring of strains within graphene films. (32; 33; 100; 101; 107; 161; 164) This can be done by measuring the shifts in position of the peaks, for instance in epitaxial graphene (33) the position of the 2D band can be used to track the amount of compressive strain present within the epitaxial graphene layers. A compressive strain builds up between the graphene and the silicon carbide substrate due to the difference in thermal expansion coefficients between the two materials.(32; 33; 161) As the epitaxial graphene is cooled from the high growth temperatures ($T_g \sim 1400°C$) the silicon carbide substrate contracts,(104) whilst the graphene expands.(103) The total strain ($\epsilon$) generated by this difference in thermal expansion coefficients

($\Delta\alpha$) as the epitaxial graphene is cooled from the growth temperature ($\mathrm{T}_g$) to room temperature (RT) is given by equation 5.1.

$$\frac{1}{1-\epsilon} = \exp\left(\int_{\mathrm{RT}}^{T_{\mathrm{g}}} \Delta\alpha(T')dT'\right), \tag{5.1}$$

This compressive strain will then affect the vibrational modes within the graphene film. For example, the 2D mode that can be visualized as a benzene ring breathing vibration will undergo phonon-hardening due to the presence of a compressive strain and the 2D peak position will shift to higher wavenumbers.(165) This shift in peak position ($\Delta\omega$) from a standard reference ($\omega$) taken for free-standing exfoliated graphene of 2642 $\mathrm{cm}^{-1}$ (135) can then be linked to the strain present within the graphene film via equation 5.2.

$$\frac{\Delta\omega}{\omega} = -\gamma_m \mathrm{Tr}(\epsilon_{ij}), \tag{5.2}$$

If the strain is assumed to be uniform (i.e when $\epsilon_{i\neq j} = 0$ in $\mathrm{Tr}(\epsilon_{ij})$) then the strain ($\epsilon$) is the trace of the tensor. (103; 161) $\gamma_m$ here is the Grüneisen parameter, where $m$ is the vibrational mode in question, in this case the 2D mode and $\gamma_{\mathrm{2D}}$ has a value of 2.7 (161). A typical Raman spectra taken during this work is shown in Figure 5.1, the silicon carbide substrate spectrum overlaps and somewhat dwarfs the graphene spectrum in the wavenumber range containing the graphene G and D bands, however the Raman 2D band in graphene is relatively unaffected by the silicon carbide substrate spectrum. For this reason, the position of the 2D band was used during this work.

The typical measurement process as described in (33) involved taking 4 measurements in each ‘rank’. A ‘rank’ is a region of the surface as shown in the inset of Figure 5.3, with 8 being measurements taken in the central region (‘rank 1’). As shown in Figure 3.7 (inset) a linear background was subtracted from the 2D peak region and the peak fitted with a single Lorentzian peak. This fit allows for the position of the peak to be determined to ±0.5 $\mathrm{cm}^{-1}$, an uncertainty that is better than that of the bare spectrometer (±6 $\mathrm{cm}^{-1}$). The peak position at each point was then compared to the value obtained for freestanding graphene of 2642 $\mathrm{cm}^{-1}$ (135), and a peak shift relative to this datum was calculated. The Raman shift $\Delta\omega/\omega$ that arises from a given strain tensor $\epsilon_{ij}$ is given by Equation 5.2.

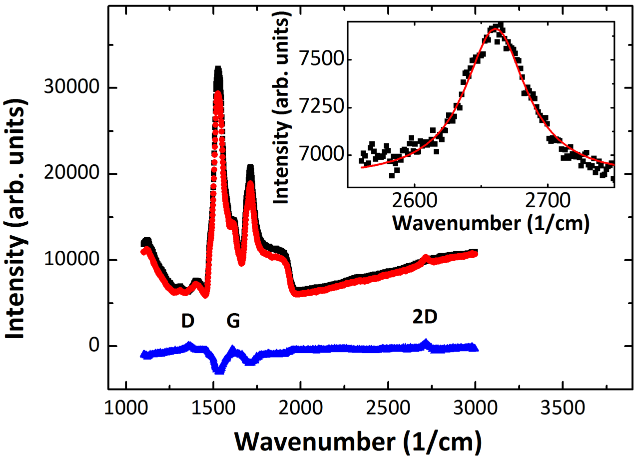

Figure 5.1: Examples of Raman spectra of epitaxial graphene on silicon carbide. Spectra are shown for the blank silicon carbide (black squares) and for epitaxial graphene after a 28 min anneal at 1400 °C (red circles). The results of subtracting the background are shown using the blue triangle data markers. The D, G, and 2D band peaks are marked. Only the latter is not obscured by features in the silicon carbide spectrum. Inset: example of a Lorentzian fit to determine the width and position of a 2D peak.(33)

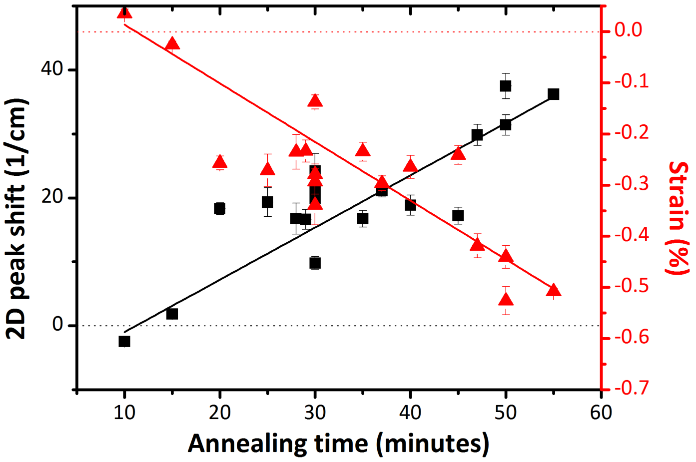

Figure 5.2: Variation of 2D peak position shift from that for freestanding exfoliated graphene of 2642 $cm^{-1}$ (squares) and calculated resulting strain values (triangles) as functions of UHV anneal time for an annealing temperature of 1400°C. The dotted lines are the zeros of the two ordinate axes. The straight lines are linear fits to the data and have a reduced $R^2$ value of 0.928. (33)

Thus allowing strain values at each point to be found. On certain samples not all Raman scans taken showed the features of a carbon-rich surface (no visible 2D peak) owing to the films being incomplete at lower annealing times as discussed in more detail in section 5.4.

## 5.3 Strain Dependence on Annealing Time

To compare with previous work carried out on measuring strains in epitaxial graphene films grown on silicon carbide (0001) the Raman 2D peak shift and the inferred strain were tracked with sample anneal time, as displayed in Figure 5.2 (Negative strains are compressive).

Each of the data points in Figure 5.2 corresponds to a full set of 32 scans as described in section 5.2, with the error bars corresponding to the standard deviation of all scans taken on each sample. Incomplete films that show no carbon signal (2D peak) in certain areas therefore have a larger statistical error associated with their data.

It is important to compare the results obtained here with previous work on epitaxial graphene grown on silicon carbide (0001) for similar annealing times at a growth temperature of 1300 °C. In that work, (32) it was found that the results could be fitted very well by a model, as described by equation 5.1.(32) In that work, the largest strain was obtained for the longest anneal times (60 minutes).

The model used to describe this relationship between the difference in thermal expansion coefficient and the strains is given by Equation 5.1, where the difference in thermal expansion coefficients ($\Delta\alpha$) between the silicon carbide ($\alpha_{\mathrm{SiC}}$) (see (104) for measurement value) and graphene ($\alpha_{\mathrm{g}}$) (see (103) for calculated value) and is approximately constant within the range of temperatures covered here from room temperature (RT) up to the growth temperature ($\mathrm{T_g} = 1400°\mathrm{C}$) with a value of $\Delta\alpha = -6.5 \times 10^{-6}\ \mathrm{K}^{-1}$. If we apply Equation 5.1 to the results obtained here for epitaxial graphene grown on silicon carbide ($000\bar{1}$), then a maximum strain value of $-0.9\%$ is obtained, which is larger than the maximum $-0.5\%$ observed in Figure 5.2. This is a key result and highlights differences between epitaxial graphene grown on the polar faces of silicon carbide (0001) and ($000\bar{1}$) with these results published (33) filling a gap in the literature that existed at that time.

There are a number of possible reasons for these observed differences and these must be addressed. Firstly, work elsewhere has shown the formation of pleats within graphene layers on both silicon carbide (0001) (106) and silicon carbide ($000\bar{1}$) (166) as part of a strain relief mechanism, which would limit the maximum strain achievable. Atomic force micrographs on samples grown under these conditions (as discussed in chapter 4) show no real evidence of such structures within films produced for this work (they are observed in samples annealed in UHV at 1450°C and samples annealed under argon atmosphere and as found after further analysis, intermittently on one sample annealed at 1400°C for 50 minutes as shown in Figure 4.9(d)) thus ruling out this possibility as an explanation for the discrepancy observed here. There is also no evidence in these micrographs for the presence of nanocrystalline graphite regions, which can also give rise to Raman shifts.(23)

On the other hand, this discrepancy could arise if an hour-long anneal does not lead to a strain-free mechanical equilibrium state at the growth temperature, which is the reason given for the maximum observed strain observed on the (0001) face.(32) This possibility cannot be ruled out as the silicon carbide wafer used during these measurements was used up before annealing runs with longer annealing times could be carried out, with future wafers purchased having undergone an extra polishing step, carried out by Novasic,(30) therefore would not be representative.

It is also known that epitaxial graphene films grown on the silicon carbide $(000\bar{1})$ face are not as strongly bound to the substrate,(50) when compared to those grown on the (0001) face, this could allow for some strain relaxation as the system contracts during cooling from the growth temperature and seems to provide the best explanation for the observations made.

## 5.4 Strain Uniformity Across Samples

Along with the variation in 2D peak position observed between samples with differing annealing times, we have also observed variations in peak position within single 5 mm × 10 mm samples. Figure 5.3 shows how there can be large variations in 2D peak position within single samples with differing anneal times at the 1400°C growth temperature used here, with the 2D Raman peak positions plotted for each 'rank'.

As described in earlier in section 3.1 there is a temperature gradient present across the 5 mm × 10 mm chips owing to the fact that the edges are in contact with a molybdenum sample holder plate, thus cannot radiate heat away as effectively as the center of the samples that are open to the ultra high vacuum, thus effectively making the edges hotter than the center.

This is illustrated in Figure 5.3, samples with shorter anneal times are very uniform, with small Raman shifts, indicating that little graphitisation has occurred at this point. These samples also show a graphene-growth precursor in the low energy electron diffraction (LEED) patterns (Figure 5.4b), indicating the presence of a far from complete graphene film. A similar precursor reconstruction

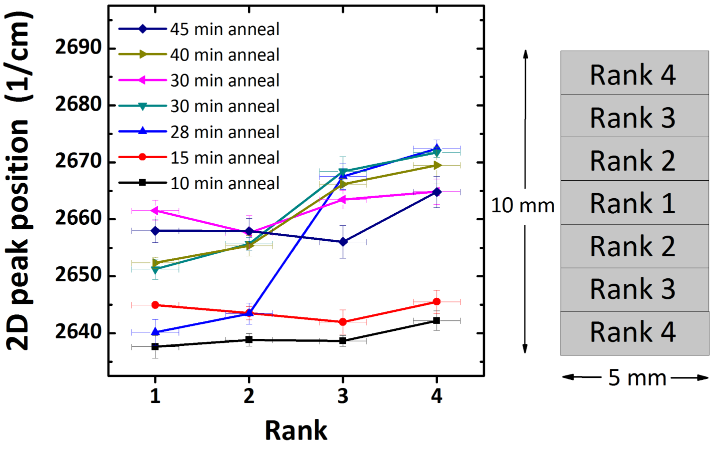

Figure 5.3: Variations in 2D peak position observed within each epitaxial graphene sample with varying anneal times. Inset: schematic showing the different sample areas (termed ranks) where data were taken on a 5 mm × 10 mm silicon carbide chip, with scans taken at random positions within each ~1 mm wide rank. (33)

has recently been reported for epitaxial graphene growth grown with the presence of disilane gas which leads to a silicon rich environment.(154) Here the silicon rich atmosphere is expected due to the presence of the sapphire cap leading to confinement above the silicon carbide substrate during the annealing processes.

The positive (tensile) strains observed in Figure 5.2 at these low annealing times could be connected to this reconstruction. Samples annealed for around 30 minutes show the most variation in 2D peak position across the chip, with large Raman shifts at the edges (higher numbered ranks) indicative of the thermal gradient across the samples.

The hotter edge regions lead to increased graphene growth and thus less 'room' for strain relaxation to occur. Samples annealed for longer times show relatively uniform and large Raman shifts across the samples, this indicates that the graphene material now covers the whole silicon carbide $(000\bar{1})$ surface. A typical LEED pattern for this kind of sample is shown in Figure 5.4 and shows the expected broken ring structure of misaligned graphene layers superimposed on the substrate spots, indicating the presence of rotational disorder and concomitant weak interlayer bonding.

This increase in sample uniformity with increased anneal time has also been observed via the use of other techniques including atomic force microscopy, low energy electron microscopy and electronic transport measurements as discussed in section 4.2.

## 5.5 Conclusions and Discussions

In conclusion, it has been shown that increasing the anneal time in ultra high vacuum for graphene growth on silicon carbide $(000\bar{1})$ at a growth temperature of 1400°C increases the compressive strain present within the graphene layer(s) to a maximum value of $-0.5\%$ for a 55 minute anneal. This apparent gradual increase in strain observed when spatially averaging all the data, is actually shown to result from thermal gradients present our chip surfaces, with a fairly abrupt increase from very low strains to $\epsilon \approx -0.5\%$ once a region has become graphitised. The graphitisation process starts at the edges of the chip and progresses inwards towards the center, taking 40-45 minutes for a complete graphene film to cover

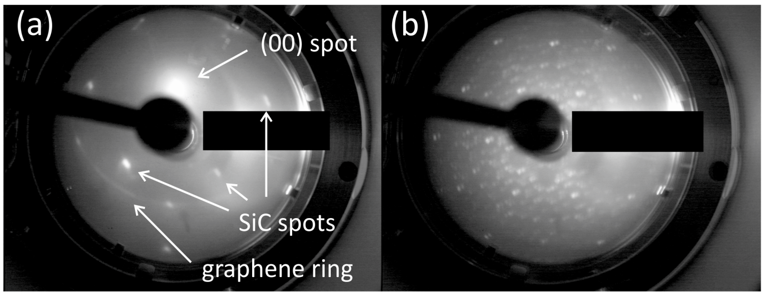

Figure 5.4: LEED images taken at different points from a sample annealed at 1400 C for 28 min. (a) Image taken at 78 eV showing the typical graphene rings and SiC substrate spots, taken in the rank 1 or 2 region; (b) image taken at 183 eV showing a pre-graphene reconstruction, taken in the rank 3 or 4 region. The LEED spot size is ∼ 1 mm and so often crosses rank boundaries. (33)

the surface under the conditions used here. The increase in strain with increased annealing time (therefore graphitisation) is thought to arise due to there being less room for the graphitised regions to strain relax at their edges as the films become more complete.(33)

There is a discrepancy in the maximum strain value observed here when compared to that observed in previous work on graphene grown on silicon carbide (0001) where a maximum compressive strain of -0.8% was observed under similar preparation conditions.(32) The lower strain value obtained has been attributed to the graphene layer decoupling from the substrate that occurs when grown on silicon carbide ($000\bar{1}$).(50) Rotational mis-stacking of epitaxial graphene layers on silicon carbide ($000\bar{1}$) leads to weak bonding and partial strain relief within the graphene films. This result had previously not been published despite the recognition of the importance of strain effects within graphene films, it is this finding that is most important from this work.(33)

Understanding the the mechanisms that cause strain within graphene films is paramount. Strains have been shown to control electronic properties within graphene films. This includes the potential opening of band gaps within graphene based devices via the application of a uniaxial strain to the graphene films.(96; 167) The uniaxial strain leads to the breaking of lattice symmetries present, thus allowing the opening of an energy band gap. This band gap is tunable with respect to the size of the applied strain.(96; 167)

The presence of non-uniform strains within graphene films grown via chemical vapour deposition has been shown to produce pseudo-magnetic fields. These fields occur as the hopping potential is altered within the strained film, thus causing the presence of a gauge potential.(108; 109) The strains responsible for these fields develop in a similar way to those found in epitaxial graphene films as they are caused by differential thermal expansion between the graphene and the metal substrates as they are cooled from the growth temperatures. Though the effect is exaggerated due to the trigonal directionality of the strain produced when Pt(111) substrates are used (108) leading to pseudo-magnetic fields with an effective magnitude of 100s Tesla being produced.

Non-uniform strains have been shown to affect the carrier mobilities within devices produced on epitaxial graphene films.(107) The non-uniformity of strains is seen to cause scattering potentials which lower the mobility. Devices which have a continuous strain across their length, even if this strain is relatively high show higher carrier mobilities than those with varying strains.(107) Future work here could see similar Raman mapping measurements of devices to be used for electrical transport carried out. However equipment in Leeds allows for the use of a micro cryostat within the Horiba Raman system. This would allow in-situ Raman mapping and electron transport characterization to be carried out at both low temperatures and higher temperatures.

# Chapter 6

# Preparation of Atomically Terraced Silicon Carbide via Annealing in Argon Atmosphere

## 6.1 Overview: Aims and Objectives

As discussed earlier in section 2.2.4, graphene growth in inert gas atmospheres has been shown to result in graphene films of superior quality in terms of lateral grain size and electronic properties to those produced in UHV.(25; 26; 27) In this section results are presented for annealing procedures carried out in argon gas atmospheres. The experimental setup of the tube furnace system used for these procedures is given in section 3.2, it is important to note that the majority of samples in this section (unless otherwise stated) were grown with the silicon carbide (0001) face touching the bottom of the graphite sample holder shown in Figures 3.3(a) and 3.3(b).

The aims of the argon gas annealing processes were to firstly produce better quality silicon carbide wafers for subsequent graphene growth. This relates to the removal of polishing scratches and the formation of an atomically stepped surface, as elsewhere produced via hydrogen etching.(29) The second aim was to produce continuous graphene films with larger lateral grain sizes than obtained via UHV growth (greater than 100s nm) on top of these improved silicon carbide substrates, the growth of these graphene films will be discussed later in Chapter 7.

The silicon carbide wafers used during this work were semi-insulating 4H silicon carbide wafers purchased from Cree (71) with a miscut angle from the (0001) plane of ±0.25°.

## 6.2 Low Temperature Anneals: Precursors to Graphene Growth

The annealing of silicon carbide wafers in argon gas atmospheres slows down the rate of silicon evaporation from the surface compared to annealing in ultra high vacuum, thus leading to an increase in the graphitisation onset temperature.(25; 26; 27) It follows that when beginning work on annealing silicon carbide wafers in argon atmospheres that the first temperature to attempt an annealing run should be higher than the common graphitisation observed in previous work carried out in UHV as discussed in Chapter 4. This lead to annealing the wafers at a temperature of 1500°C under a 1.5 slm flow of argon gas at atmospheric pressure.

The results of this annealing process were somewhat surprising. As shown in Figures 6.1, 6.2 and 6.3 the previously scratched silicon carbide wafer (Figure 6.3 inset) is smoothed out into a stepped (terraced) surface. This type of surface is similar to that observed elsewhere for silicon carbide wafers after hydrogen etching treatment.(29) The hydrogen etching process requires the annealing of silicon carbide wafers at high temperatures (∼1400°C) in the presence of a hydrogen-rich gas atmosphere. Due to the extremely flammable nature of hydrogen gas, this process has safety concerns, therefore the observation of atomically terraced silicon carbide substrates from just annealing in inert argon gas atmospheres is beneficial in potentially removing this hazardous substrate preparation step from growth procedures.

Once these atomically stepped terraces were observed, experiments to try and understand the nature of this terrace formation were required. As always with annealing processes, the key parameters to vary are the annealing time and

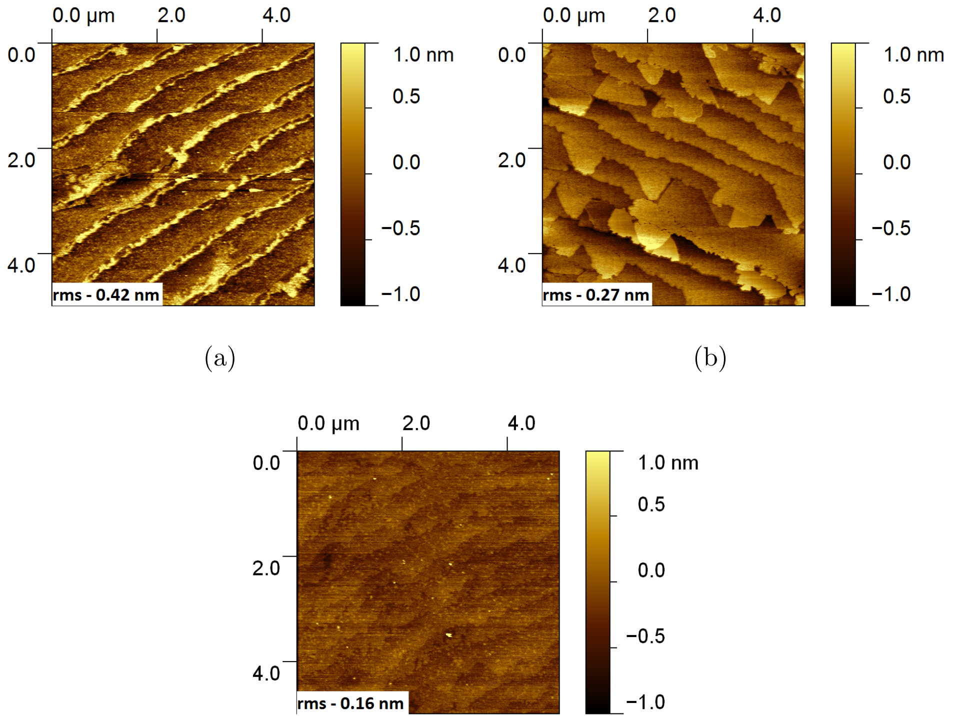

(a)

(b)

(c)

Figure 6.1: 5 $\mu$m × 5 $\mu$m AFM scans taken for a sample annealed at 1500°C for a) 15 minutes b) 30 minutes and c) 60 minutes. The samples all exhibited atomic terraces, the sample imaged in b) shows evidence for the movement/expansion of terrace steps.

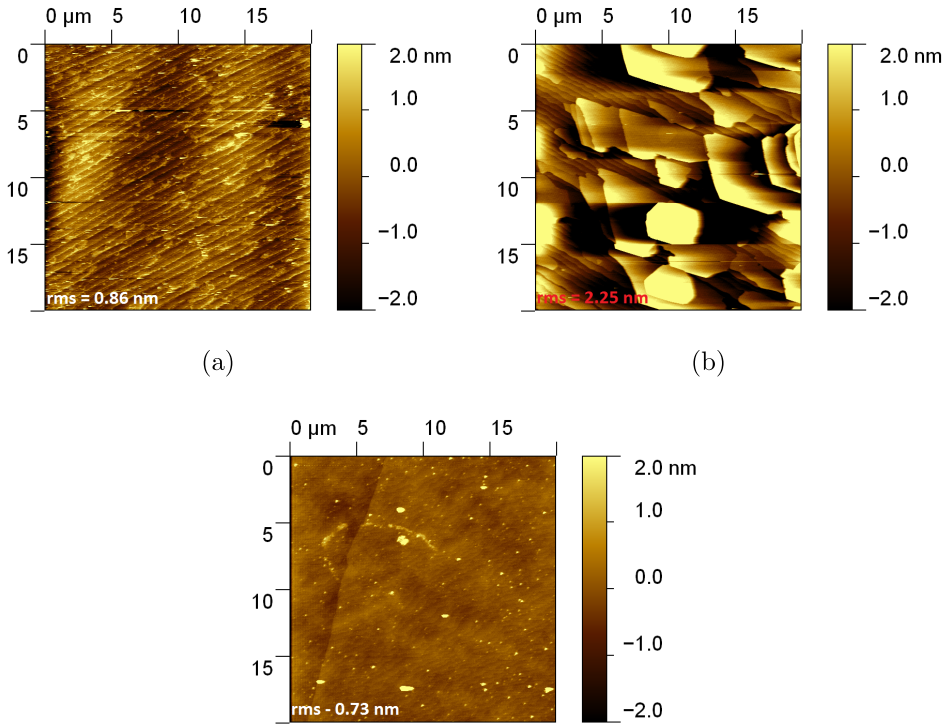

(a)

(b)

(c)

Figure 6.2: 20 $\mu$m × 20 $\mu$m AFM scans taken for a sample annealed at 1500°C for a) 15 minutes b) 30 minutes and c) 60 minutes. The samples all exhibited atomic terraces, the sample imaged in b) shows evidence for the movement/expansion of terrace steps, there are also some large debris features present at this scale on this sample.

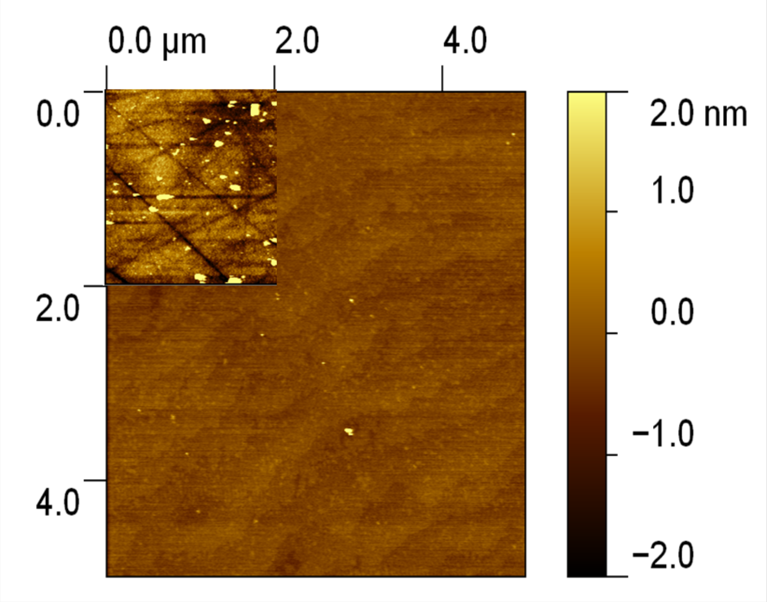

Figure 6.3: AFM micrographs of a sample annealed at 1500°C for 60 minutes and inset: AFM of an un-annealed silicon carbide (0001) surface. Both micrographs are set to the same lateral and height scales. A vast difference can be seen between the two images owing to the smoothing out of polishing scratches and the formation of atomic terraces post-argon annealing.

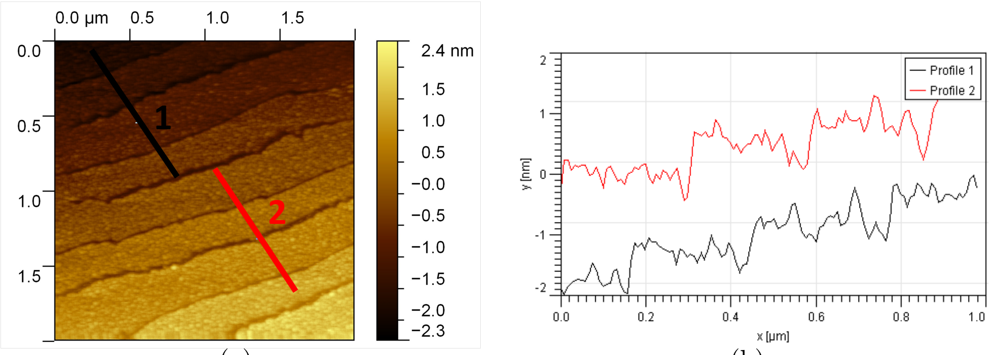

(a) (b)

Figure 6.4: a) AFM micrograph from a sample annealed for 15 minutes at 1500°C, . b) 2 line profiles taken from the micrograph in a).

temperature. Figures 6.1 and 6.2 shows the evolution of the sample surfaces with increased annealing time for an annealing temperature of 1500°C.

Terraces, with step heights ∼0.3 nm and widths ∼1 $\mu$m, are formed after a 15 minute anneal (Figures 6.1(a), 6.2(a) and 6.4). These terraces appear to expand and flatten out further with increased time (to 60 minutes) with the sample annealed for 30 minutes (Figures 6.1(b) and 6.2(b)) showing an intermediate state with terrace expansion consisting of regions with ∼0.3 nm stepped terraces and regions of wider (∼2 $\mu$m) terraces with step heights ∼1-2 nm.

Figure 6.5 shows a sample annealed at 1400°C for 60 minutes. This sample shows areas that have begun to terrace interspersed with areas that have not, this again suggests a thermally driven model for the terrace formation as suggested elsewhere.(29; 82) A sample annealed for 60 minutes at 1500°C returns to having ∼1 $\mu$m wide terraces with step heights ∼0.3 nm though the terraces themselves are flatter with a decrease in RMS roughness observed when compared to the sample annealed for 15 minutes. This again is in agreement with work carried out elsewhere (73) where the change in silicon to carbon atom ratios at the sample surface. This change in ratio drives reconstructions to occur, it is therefore possible that the ‘sweep’ in terraces across the sample is related to a change in silicon to carbon ratio at the sample surface, this will be discussed again later when analysing LEED data.

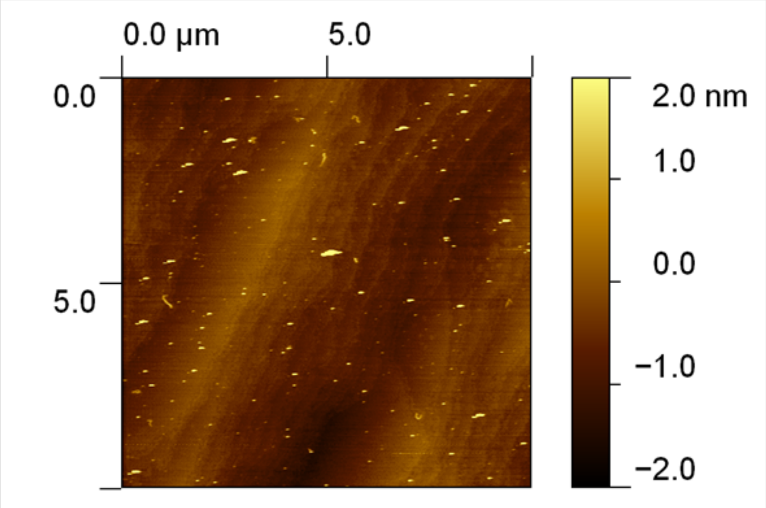

Figure 6.5: AFM micrograph of a sample annealed for 60 minutes at 1400°C. The sample shows atomically terraced regions interspersed by wide, non-terraced regions.

Raman spectroscopy was also used to probe these samples in an attempt to identify the materials present on the sample surfaces. Figure 6.6 shows Raman data taken from three different regions on the same sample annealed for 15 minutes at 1500°C. The majority of Raman spectra taken after annealing at this temperature show the features of a silicon carbide spectrum only. However, as shown in Figure 6.6, there are regions that show carbon-rich Raman data, with evidence of weak and broad peaks in positions associated with the graphene (carbon) D and G bands at $\sim$1400 cm$^{-1}$ and $\sim$1550 cm$^{-1}$ respectively however there is no evidence of the 2D band expected at $\sim$2600 cm$^{-1}$ suggesting that the carbon present is non-graphene like.

However the presence of bands in the G and D band regions fit with the model that there is an increase in carbon atoms at the surface (loss of silicon atoms) driving the reconstructions. The measuring of carbon-rich signals in Raman is somewhat sporadic, on the sample shown in Figure 6.6 annealed for 15 minutes at 1500°C only 3 out of 9 Raman spectra taken at representative areas on the sample (spread out evenly over the sample area) are carbon-rich.

Another sample (not shown) with the same annealing conditions showed 0 out of 9 carbon-rich scans, a sample annealed for 30 minutes at 1500°C (not shown) showed 2 out of 9 carbon-rich scans and a sample annealed for 60 minutes at 1500°C showed no evidence of carbon-rich signals. This could be a case of just missing areas that are carbon-rich in certain samples. As AFM micrographs show terrace structures extending continuously over ~20 $\mu$m it would suggest that the carbon-rich signals do not correspond to the material present that is intrinsic to these reconstructions but merely due to ‘pockets’ of free-carbon that form, this could be due to increased levels of silicon evaporation in those areas, or possibly due to the presence of extrinsic carbon from contamination.

To observe the surface reconstructions that had taken place, the original sample annealed for 15 minutes at 1500°C was mounted into the MBE system and examined via LEED. The sample was initially annealed for one hour at 1000°C to remove surface contaminents to ensure a clean LEED pattern. 1000°C was been observed to be well below the graphitisation temperature in this system as discussed during chapter 4.1, it was therefore surprising that evidence of a graphene film was shown in the LEED data (Figure 6.7(a)).

Raman microscopy taken after this UHV anneal (Figure 6.8(a)) shows an increased carbon-rich signal than observed in Figure 6.6 and evidence of the 2D peak is seen. This suggests that there is free carbon present at the surface post argon annealing at these temperatures, and that the subsequent UHV anneal allowed this free carbon to become mobile and form graphene-regions. Further annealing in UHV at 1450°C leads to a much more prominent graphene signal in both the LEED data (Figure 6.7(b)) and Raman spectra (Figure 6.8(b)). The surface morphology of the sample after this final anneal in UHV is shown in Figure 6.9 where the terraced silicon carbide structure now has pitted regions (~3 nm deep) a growth mechanism that has been observed elsewhere. In that work, the formation of epitaxial graphene was carried out at varying argon gas pressures and under vacuum ($/sim10^{-5}$ mbar) on the (000$\bar{1}$) face after the silicon carbide has been made atomically terraced via hydrogen etching.(168) Except for the presence of these pits, there is no real noticeable changes in surface morphology observed. As mentioned in earlier section 3.4.4 it can be hard to distinguish between graphene layers and areas of bare substrate and even in phase imaging there is no noticeable variations.

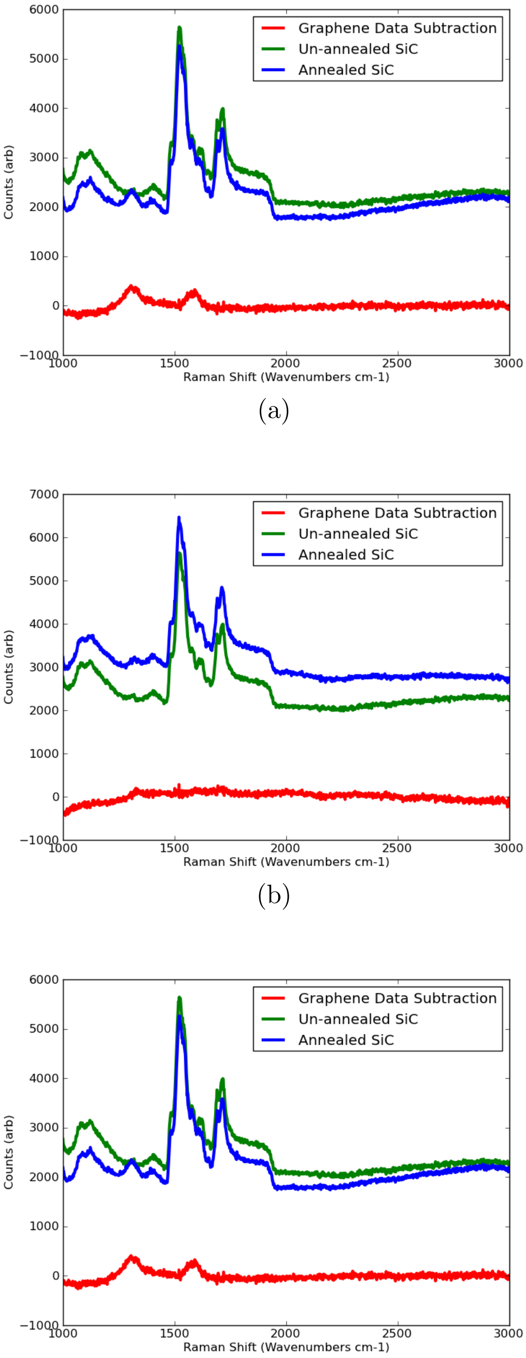

(a)

(b)

(c)

Figure 6.6: Raman spectra taken at different points on a silicon carbide wafer after annealing for 15 minutes at 1500°C. Red graphene data show the existence of weak and broad D($\sim$1300 cm$^{-1}$) and G($\sim$1300 cm$^{-1}$) Raman bands indicative of the presence of disordered carbon on the sample surfaces.

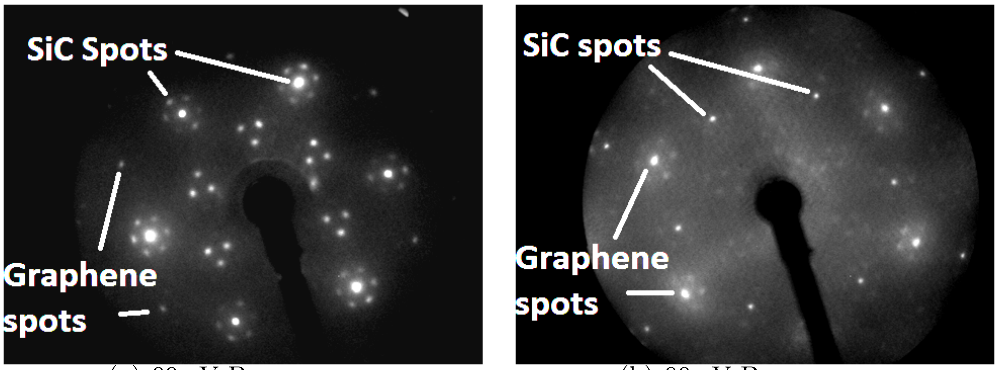

(a) 99 eV Beam energy (b) 99 eV Beam energy

Figure 6.7: LEED data taken on a sample annealed in the furnace system for 15 minutes at 1500°C in the furnace system after further annealing at a) 1000°C and b) 1450 °C in UHV. The main spots associated with silicon carbide and graphene are labeled.

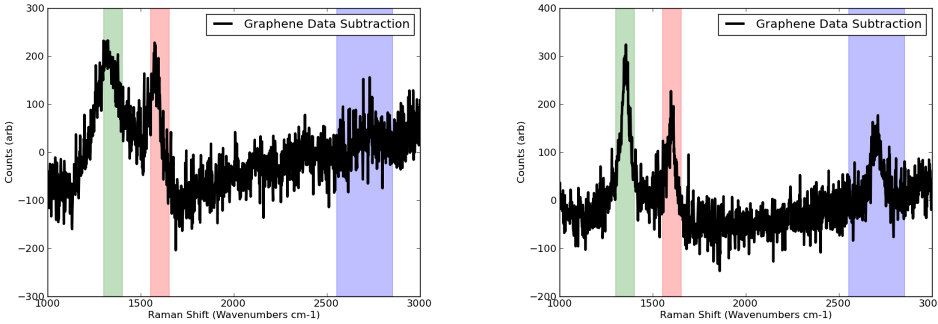

(a) (b)

Figure 6.8: Raman data taken on a sample annealed in the furnace system for 15 minutes at 1500°C in the furnace system after further annealing at a) 1000°C and b) 1450 °C in UHV. The main Raman band regions are highlighted D band (green), G band (red) and 2D band (blue). The sample annealed at shows narrower and more prominent bands, indicating a more ordered graphene-like spectra.

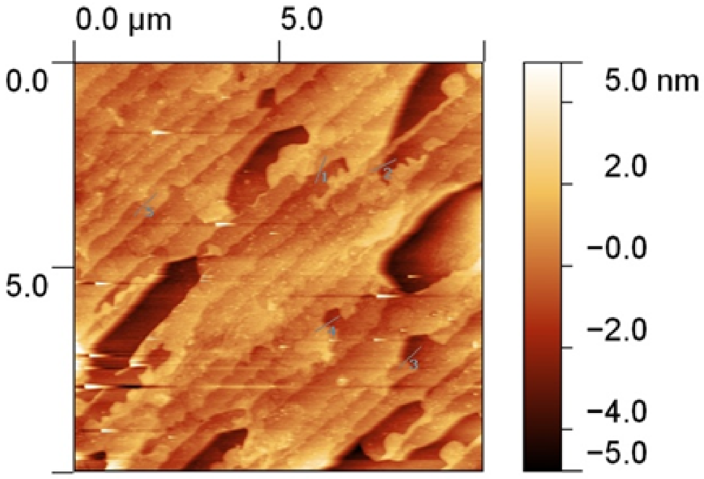

Figure 6.9: 10 $\mu$m × 10 $\mu$m AFM micrograph of a sample annealed for 15 minutes at 1500°C after subsequent anneals at 1000°C and 1450°C anneals in UHV. Atomic terraces within the silicon carbide wafer can still be seen as can the presence of ∼3 nm deep pitted regions.

The inconsistent nature of the carbon-rich Raman spectra observed and its essential absence in subsequent samples with annealing times of 15 minutes and above at this temperature suggested that the carbon source responsible for this LEED reconstruction could well be extrinsic. Unfortunately the second sample annealed for 15 minutes was destroyed, however samples annealed for 30 minutes and 60 minutes were annealed to 900°C in UHV to remove surface contaminants and then underwent LEED examination. Diffraction patterns from these samples can be seen in Figure 6.10.

The sample annealed for 30 minutes (Figure 6.10(a)) showed a $(1 \times 1)$ reconstruction and exhibit LEED charging effects for beam energies up to ∼160 eV suggesting the presence of a highly insulating surface. The sample annealed for 60 minutes (Figure 6.10(b))exhibits a ‘buffer-like’ reconstruction. It is not the classic $(\sqrt{3} \times \sqrt{3})$R30 or $(6\sqrt{3} \times 6\sqrt{3})$R30 reconstructions observed elsewhere for silicon carbide (0001) prior to graphitisation.(17; 18; 19; 21; 78; 146) The pattern does show 6-fold symmetry and exhibits charging effects up to ∼100 eV suggesting that the surface is more conductive than the sample annealed for 30

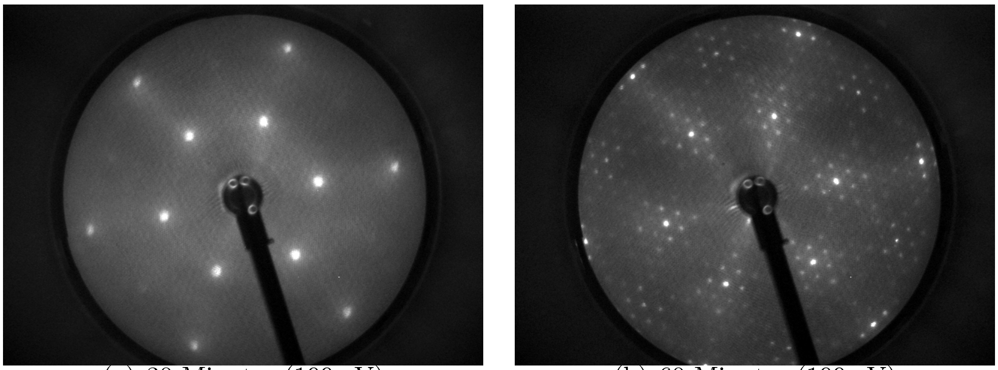
(a) 30 Minutes (199 eV) (b) 60 Minutes (199 eV)

Figure 6.10: LEED data taken for samples annealed under inert argon gas atmosphere at 1500°C for varying times after being cleaned with a 900°C anneal in UHV. The sample in b) exhibits a buffer-layer-like reconstruction with six-fold symmetry.

minutes.

This would infer that the sample annealed for 60 minutes is C-rich (it could just be 'cleaner') despite the lack of a carbon signal in Raman spectroscopy. These LEED patterns lend support to the model that the reconstructions observed via LEED and the terrace formation observed in AFM are driven via a change in silicon to carbon atom ratio at the sample surface as the silicon evaporation increases with both annealing time and temperature. This is consistent with work elsewhere on the propagation of surface reconstructions seen elsewhere with the change in silicon to carbon atom ratio at the sample surface.(73) The formation of terraces at high temperatures is also consistent with a minimization of the surface free energy as observed for the hydrogen etching process commonly used to prepare defect free silicon carbide substrates.(29) The sample annealed at 15 minutes that exhibited areas with carbon-rich Raman spectra and a $(6\sqrt{3} \times 6\sqrt{3})$R30 LEED pattern (Figure 6.7(a)) that also contained a weak spot pattern at the correct lattice spacing to correspond to a graphene overlayer (see labels in Figure 6.7(a)). The carbon responsible for this pattern could well be due to an extrinsic source (potentially from the graphite sample holder) present during the annealing process.

It has been observed that for annealing of silicon carbide $(000\bar{1})$ surfaces under silicon-rich disilane environments can result in the formation of a buffer layer that does not have the regularly observed $(6\sqrt{3} \times 6\sqrt{3})$R30 pattern.(154) The introduction of a silicon-rich environment above the silicon carbide (0001) surface during these annealing processes could account for the observation of the none $(6\sqrt{3} \times 6\sqrt{3})$R30 'buffer-like' region as observed in Figure 6.10(b) for a sample annealed at 1500°C for 60 minutes.

## 6.3 Conclusions and Discussion

In conclusion, it has been observed that annealing silicon carbide wafers at temperatures of 1500°C results in the formation of terraces, with step heights ~0.3 nm (third of a 4H-silicon carbide unit cell) and widths of ~1 $\mu$m. These wafers show a Raman signal indicative of bare silicon carbide for the majority of scans. However carbon-rich Raman spectra were observed, mainly on a sample annealed for 15 minutes at 1500°C. LEED analysis of this sample showed the presence of a silicon carbide 'buffer-layer' $(6\sqrt{R30} \times 6\sqrt{R30})$ reconstruction with the evidence of a weak graphene signal, possibly due to free-carbon on the surface forming sp$^2$ carbon during the 1000°C pre-LEED anneal. Further annealing in UHV at a higher temperature of 1450°C increased the graphene signal in both the LEED pattern and the Raman spectra, thus suggesting graphene had been successfully grown. AFM micrographs after the second UHV annealing stage show evidence of pitting of the terraced surface but no distinguishable regions of graphene growth.

LEED analysis of samples annealed for 30 minutes and 60 minutes at 1500°C showed the evolution of reconstructions from a $1 \times 1$ reconstruction obtained for the 30 minute anneal to a more complex buffer-like reconstruction observed for the 60 minute anneal. This evolution, along with decreased charging effects within the sample annealed for 60 minutes suggested a carbon-rich layer to be responsible for the buffer-like reconstruction. This suggests a mechanism based on the changing silicon to carbon ratios at the sample surface being responsible for the reconstructions taking place at the sample surface and causing the terracing effects observed with AFM imaging.

The details of this mechanism behind the terrace formation are not yet known. A simplistic view would be that during the long annealing processes carried out, there is a large time window in which the silicon carbide surface is mobile. This allows the surface to 'flow' to a certain extent and 'fill in' defects present on the surface such as polishing scratches. Once the temperature at which silicon begins to evaporate is reached, the change in silicon to carbon atom ratio at the sample surface drives surface reconstructions, as observed elsewhere.(73) This potentially explains the expansion of terraces as reconstructions 'sweep across' the surface with the evolving silicon to carbon ratio at the surface.

Work elsewhere, on the hydrogen etching process of silicon carbide wafers has shown that terraces form in particular directions in order to minimise the total surface free energy.(73) This is consistent with the proposed model here, whereby it could become energetically preferential for terraces to form on the silicon carbide substrates at these elevated temperatures, especially after the onset of silicon evaporation. It would also suggest that the silicon evaporation would be occurring in preferred directions from the silicon carbide lattice. From the 'inverse step flow' mechanism proposed by (29) the preferential etching directions lead to the faceted substrate, so it follows that for faceted surfaces to be observed here, there must by an element of directional preference.

A key reason behind the development of furnace annealing capabilities in this work was to provide an increase in backscattering probability for silicon atoms evaporating away from the silicon carbide substrate. Work elsewhere (82), has observed atomic terracing of silicon carbide terraces via the annealing of silicon carbide in UHV with the presence of an external silicon source. In that work, the external silicon flux replenishes the outgoing silicon atoms and prevents the silicon carbide substrate graphitising at temperatures greater than the observed onset. This allows higher temperatures to be reached pre-graphitisation, with this increase in temperature leading to the induction of surface reorganization and the formation of atomic terraces.(82)

Here the backscattering of silicon atoms back to the substrate due to the presence or argon gas and the graphite sample holder leads to an increase in the graphitisation onset temperature. In a similar mechanism to (82) this increase in temperature could be sufficient enough to induce surface reconstructions and as mentioned earlier the requirement to minimise the surface free energy (29) lead to the formation of terraces.

The full details of the mechanism are not yet known. To help further investigate and understand the mechanism responsible for these observations there are a number of key experiments we could carry out. The first would be accurate measurements of the amount of material lost throughout the annealing process (if any). This would help to distinguish between silicon loss (change in silicon to carbon atom ratio) and temperature driven surface free energy minimisation mechanisms for surface reconstruction.

Also a full investigation with different silicon carbide wafers could be useful to see how dopant levels, polytype and perhaps more importantly miscut angle affects the formation of atomic terraces under argon annealing. It has been shown (34; 169) that the miscut angle of the silicon carbide wafer controls the width of the atomic terraces produced by chemical processing (169) and hydrogen etching.(29; 34)

Another measurement that would help further understand the processes occurring would be to carry out LEED measurements from a wider range of samples prepared at different annealing times and temperatures. This would allow more information to be acquired as to how the surface reconstructions evolve under these varying annealing conditions. Also important would be the measurement of LEED over a number of samples annealed under the same conditions to check the consistency of the reconstructions taking place to show the repeatability and consistency of the results from these annealing processes.

After the observation of these atomically terraced silicon carbide substrates, it was decided that higher temperature anneals in argon atmosphere should be carried out in an attempt to graphitise the samples under atmospheric pressure, with a view to creating large single domain graphene sheets as described elsewhere.(26; 27) As shown, attempts to graphitise these atomically stepped silicon carbide substrates in UHV conditions have been shown to give less than favourable results. Though LEED patterns showed a typical reconstruction for epitaxial graphene growth on silicon carbide (0001), the surface appeared pitted and grainy surfaces were observed via AFM imaging.

If successful this would allow substrate preparation and graphene growth to be carried out in a single process without the need for potentially dangerous hydrogen etching procedures. To obtain this surface graphitisation, annealing processes conducted at higher temperatures were proposed. The results of these higher temperatures are to be discussed in the following Chapter 7.

After the completion of this work it became apparent that similar results had been observed elsewhere (170) for the annealing of silicon carbide wafers below the graphitisation temperatures in a graphite enclosure to induce a confined geometry. The external pressures within this work where $10^{-4}$-$10^{-5}$ Torr with the steps seen to form at a temperature of 1200°C as the native silicon oxide is removed from the sample surface and step flow can occur.(170)

The observation of this atomic terracing of the silicon carbide whilst annealing under atmospheric pressures of argon gas is original and allows a safer method for terrace production without the use of flammable hydrogen gas (29) and compliments work carried out elsewhere were other processes outside the use of argon gas have been used to slow the silicon evaporation rate to obtain similar results. These include the use of an external silicon flux in UHV(82) and the use of a confined geometry in a moderate vacuum.(170)

# Chapter 7

# Graphitisation of Atomically Terraced Silicon Carbide via Higher Temperature Annealing in Argon Atmosphere

## 7.1 Overview: Aims and Objectives

After observing the formation of atomically terraced silicon carbide substrates as described in Chapter 6, work was carried out to attempt to graphitise these terraced silicon carbide substrates under an argon gas atmosphere. This involved the increasing of the annealing temperature used from those used to produce the atomic terraces in Chapter 6. Carbon-rich Raman spectra were obtained for an annealing time of 15 minutes at 1600°C and AFM micrographs showed the presence of ripples and wrinkles under these annealing conditions. However the graphene sheet seemed far from uniform and complete, as indicated by the presence of a large Raman D peak and by the ripped nature of the graphene sheets imaged via AFM. In order to improve uniformity, a series of samples were produced at varying annealing times and temperatures and their properties measured. This chapter will discussed the findings of this work and the quality of graphene films produced.

Once more, during the higher temperature annealing processes, silicon carbide wafers used during this work were semi-insulating 4H silicon carbide wafers purchased from Cree (71) with a miscut angle from the (0001) plane of ±0.25°. Again the experimental setup of the tube furnace system used for these procedures is given in section 3.2, once more it is important to note that for the majority of samples in this section (unless otherwise stated) were grown with the silicon carbide (0001) face touching the bottom of the graphite sample holder shown in Figures 3.3(a) and 3.3(b).

Throughout this and the following chapter there will be a number of references to 'tube-like structures' these features should not be confused with carbon nanotubes. The structures correspond to thin (100s nm or less) with a height of a few nanometers that have been observed in AFM micrographs. The exact nature of these features is still unknown and are therefore described as 'tube-like'.

## 7.2 Sample Graphitisation

As described earlier in section 3.2, the ramping rates for both increasing and decreasing the temperature in this furnace system is limited by the need to protect the alumina tube from cracking. This leads to ramping rates of typically 5°C per minute and a typical annealing cycle is shown in Figure 7.1. These ramp rates are somewhat slower than used elsewhere (26) and could be the reason behind the observation of terraces when annealing under inert gas atmospheres and perhaps some of the properties of the graphene layers grown in this work which differ from those observed elsewhere such as the presence of larger Raman D band, indicative of the the presence of disorder withing graphene films.(134; 156)

The graphene films grown under inert gas atmospheres have been analyzed with a number of different techniques, these include AFM, LEEM, LEED, Raman microscopy and have been locally contacted via the use of a Nanoprobe for the purposes of taking electrical measurements (details of the Nanoprobe work to be discussed in chapter 8). The following sections will summarize the findings from these techniques and show the current level of graphene quality obtainable in our furnace systems and the future plans for increasing the quality of these films yet further.

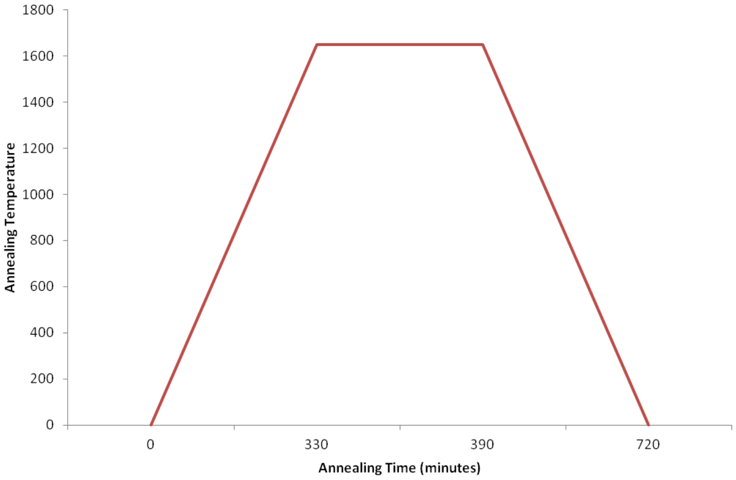

Figure 7.1: Typical programmed temperature vs time profile for an annealing run in the tube furnace system. Once over ∼100°C the programmed temperature and actual temperature are within ∼1°C of each other.

### 7.2.1 Raman Data

Raman spectra taken of epitaxial graphene films grown under argon atmosphere seem to vary from those found after UHV annealing. An example of a spectrum obtained from a sample annealed at 1650°C for 60 minutes is shown in Figure 7.2. In this spectrum there are some key features that differ from those observed in graphene samples grown under UHV conditions. The D band present is in many regions much more prominent than observed in in samples produced in UHV. The G band region is also different and shows evidence of splitting into two distinct components.

The spectrum shown in Figure 7.2 has been chosen to highlight these differences and is somewhat of an extreme case. The large D peak and the level of G band splitting is seen to vary with annealing conditions and even within single samples. These variations will be discussed in the sections to immediately follow. At this stage the differences highlighted prove useful as an early indicator to suggest that the mechanisms present during the graphene growth here under inert gas atmospheres are somewhat different to those observed during UHV growth.

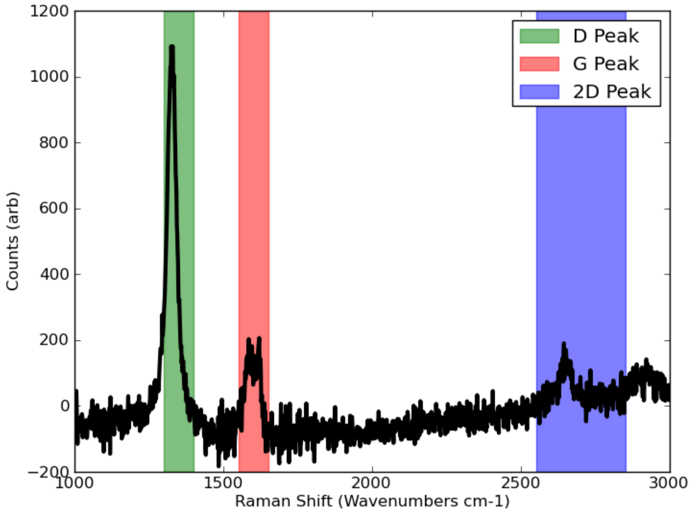

Figure 7.2: Typical Raman spectrum (silicon carbide background subtracted) for a sample annealed at 1650°C for 60 minutes at a wavelength of 633 nm. The shaded regions correspond to the main Raman bands associated with graphene D (green), G (red) and 2D (blue). The D band is seen to be large, indicative of disorder within the films. The G band is also seen to split, this is discussed in detail within the main text.

#### 7.2.1.1 Raman G:D Ratio - Grain Size Measurements

The ratio of the Raman G band to the D band is often used in graphene samples and carbon samples in general as a measure of the sample quality.(134; 135; 139; 145; 156) The reasoning behind this, as discussed in greater detail earlier in section 3.3.3. In summary, the method allows a grain size to be calculated for the graphene films via the use of the ratios of the G and D bands and the equation 3.1.(134) Earlier results were presented in section 4.3 for grain size calculations for graphene films grown in UHV and limitations pointed out for the actual final values of grain size obtained. There is a tendency for this technique to underestimate the absolute grain size present within the films, never the less it can be used as a general measure of graphene uniformity if not to gain the actual grain size value.(145; 156)

Figure 7.3 shows the evolution of the lateral grain size with annealing time for samples annealed at 1600°C and 1650°C. For samples annealed at 1600°C there is a general increase in grain size with increasing annealing time. For 15 minute anneals, AFM work (to be discussed in section 7.2.3) has shown the graphene growth to be very patchy and island-like with increasing annealing time this is seen to improve and the graphene coverage become more uniform which fits with the increase in grain size value. It is important to note here that the grain size values presented here are from 'successful' fits to the D and G peaks post silicon carbide subtractions. This somewhat skews the data to show the lower annealing times producing relatively more complete films than is actually true from other microscopy techniques. There is also a skew to measuring sample edge regions, which again appear to be more graphene-rich at these temperatures than central regions.

The actual grain size measured is much smaller than the island sizes observed in other microscopy techniques, where island sizes, when present are in the micron size range compared to the 10s nm grain size measured here. This again is typical of the sampling method used here. Essentially when the graphene growth consists of isolated island regions it is somewhat random whether the laser spot lies within an island and produces a relatively small D peak or mainly on the edge of an island(s) thus producing a large D peak. There appears to be sharp contrast

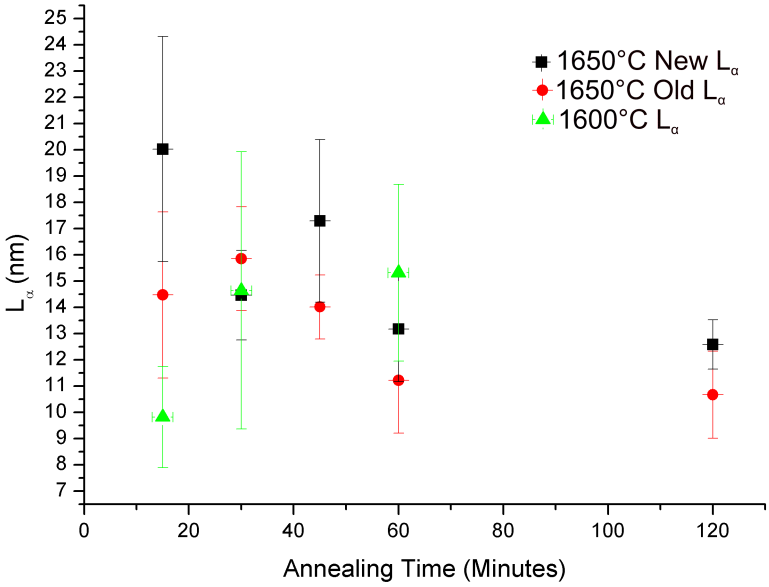

Figure 7.3: Evolution of the lateral grain size ($L_\alpha$) with increasing sample anneal time for annealing temperatures of 1600°C and 1650°C. Error bars shown as from statistical averages of grain sizes measured successfully within a sample. 2 values of grain size measured at 1650°C correspond to fitting a single Lorentzian to the G peak ('old') and a double Lorentzian ('new').

shown in AFM images between areas of graphene and silicon carbide, with well defined boundaries, this is a little different from what is observed in UHV grown samples. Also, there is much more evidence of rippling, folding and even ripping of the graphene films annealed at these temperatures (discussed in section 7.2.3). Again this can increase the amount of 'edge' within a Raman scan and folded regions themselves have been shown to produce increases in the Raman D bands .(98)

For samples annealed at 1650°C, the lateral grain size value is much less than the grain size observed via the use of other microscopy techniques. There is no apparent increase in grain size with increased annealing time here, there are also two values of grain size given per sample. One is for the area obtained when a single Lorentzian peak is used to fit the G peak and the other is for a double peak fit to account for G peaks splitting occurring at this temperature (Figure 7.3). Even with the use of a double fit, the grain size appears to vary little with annealing time. One possible reason for this is that at this temperature bilayer regions appear to form. These bilayer regions and many of the monolayer regions in between them are seen to be very disordered and contain many rips,ripples and folds. The presence of rips within a graphene film will increase the amount of edge region present and increase the intensity of the Raman D band(134; 156). Folds and ripples can also contribute to an increase in the Raman D band intensity due to the creation of long range changes in potentials that allows scattering events.(98) The formation of these features within the bilayer regions will be discussed in greater detail in section 7.2.3.

As the annealing time is increased, though the coverage of graphene maybe increasing, the levels of the disordered regions also increases thus the ratio of G to D bands remains roughly consistent. A single sample has been prepared with an annealing time of 60 minutes at a temperature of 1690°C. This sample has a lateral grain size of (12±2 nm) for a double Lorentzian fit and (16±3 nm) for a single fit. This is comparable with the grain sizes obtained from samples annealed at 1600°C, again this sample exhibits areas of folded bilayer regions and ripped monolayer regions that lead to an increase in D peak intensity and affect the overall grain size value.

#### 7.2.1.2 Splitting of the G band

The next major distinguishing feature of the Raman spectra obtained from samples grown in inert gas atmospheres in this work is the splitting of the Raman G band into two distinct regions. The reason for this observation is not fully understood, the following section will outline possible reasons for the observation and evidence for and against each of them. It is first important to remember that as discussed earlier in section 3.3.5 the $E_{2g}$ mode responsible responsible for the G band present in Raman spectra of graphene consists of two phonons, the transverse optical (TO) phonon and the longitudinal optical (LO) phonon. It is this reason that the G band can split, with each of the split peaks assigned to one or the other phonon present.

The first reason to be addressed for the possible causing of the G peak splitting is the presence of strain withing the graphene films. It has been shown (99; 100) that the action of a uniaxial strain on a graphene film can result in the splitting of the G band. Figure 7.4 shows the evolution of strains within our graphene films, measured using the change in position of the 2D band (as discussed in detail within chapter 5) with increasing annealing times for samples annealed at 1600°C and 1650°C (Figure 7.2.1.2) respectively.

The samples annealed at 1600°C show a switch from positive (tensile) strain to negative (compressive) strain with increasing annealing time. This behavior has been observed for graphene in UHV conditions but with the tensile strains being less extreme than observed here (see Figure 5.2). This suggests that the strains present are not from direct substrate interactions and are potentially from local folding and rippling within individual graphene islands. The strain values present here are large enough to cause a G band split if the strain present was uniaxial. (99; 100) When G band splitting occurs for samples annealed at this temperature (annealing time of 60 minutes) the separation between the split peaks is $(31.3 \pm 0.5)$ cm$^{-1}$. This separation is much larger than the 10 cm$^{-1}$ observed for similar strain values elsewhere.(99; 100) This limits the validity of strain as a cause for the splitting observed here.

For samples annealed at 1650°C the strain values are all compressive and appear to decrease with increasing annealing time. Again this is very different

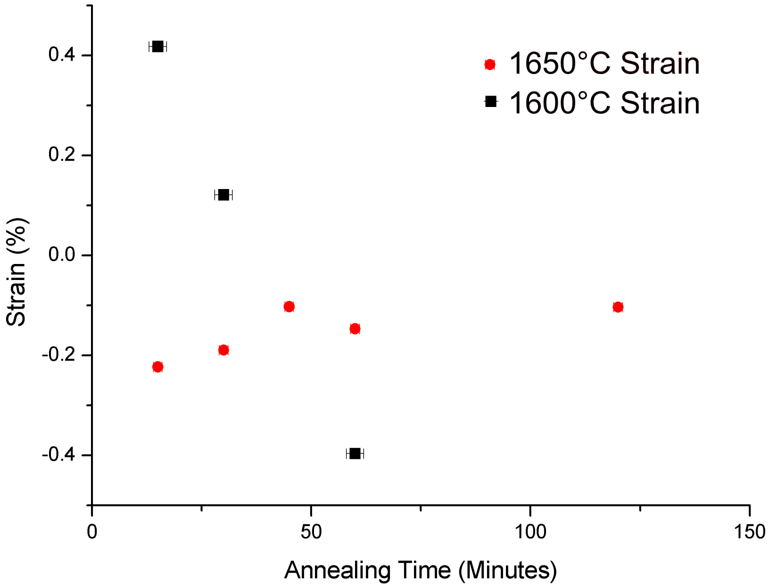

Figure 7.4: Evolution of the strain with increasing sample anneal time for annealing temperatures of 1600°C and 1650°C. Error bars shown as from statistical averages of grain sizes measured successfully within a sample. Positive strain values correspond to tensile strain, negative strain values correspond to compressive strain. The strains have been calculated from shifts in the 2D peak position as described in Chapter 5.

to behavior observed for samples grown in UHV (see Figure 5.2) and suggests a difference in the interactions present between the substrate and the graphene films in the samples annealed under inert gas atmospheres. The strain values present in these samples are lower than those observed to give notable G peak splitting elsewhere. (99; 100) To distinguish between the two components of the G peak when split, they have been labeled as G1 and G2 as shown in Figure 7.5(a). The evolution of the separation between the G1 and G2 components as a function of annealing time at 1650°C is shown in Figure 7.5. Again the ~30 cm$^{-1}$ separations observed are still large for those observed from the application of strains to graphene films, thus suggesting a different mechanism is behind the G band splitting.

If strain is eliminated as a possible cause for the observed splitting then other possible causes must be investigated. Such causes could include the introduction of confinement and curvature into the graphene films. (132) Figure 7.6(a) shows the evolution of the shifting observed in both the G1 and G2 bands away from a reference value of 1598 cm$^{-1}$ (a value determined via the average position of unsplit G peaks). The effects of confinement act only on the longitudinal Optical (LO) phonon due to the null electron phonon coupling in the transverse optical (TO) phonon. Figure 7.6(a) shows that both the G1 and G2 components are shifted with the G1 component moving to lower wavenumber values and the G2 component shifting to higher wavenumber values. This shifting of both the phonons suggests that confinement cannot be the mechanism responsible for the G peak split. If the reference point for the G peak position is moved to 1580 cm$^{-1}$ as observed in graphene flakes (136). As shown in Figure 7.6(b), now both the components are shifted to higher wavenumbers, the shift in the G1 peak is small. This could allow for the assumption that only one phonon is affected as expected for confinement.

Confinement effects in semi conducting nanotubes has been shown to produce this kind of shift with the LO phonon seen to shift to higher wavenumbers whilst the TO phonons remain unmoved as the tube diameter is decreased (132)(therefore increasing the amount of confinement). This causes a splitting of around 10 cm$^{-1}$ for confinement of 1.5 nm (about the size of the smallest features measured with AFM in this work). So the effects of confinement also seem to

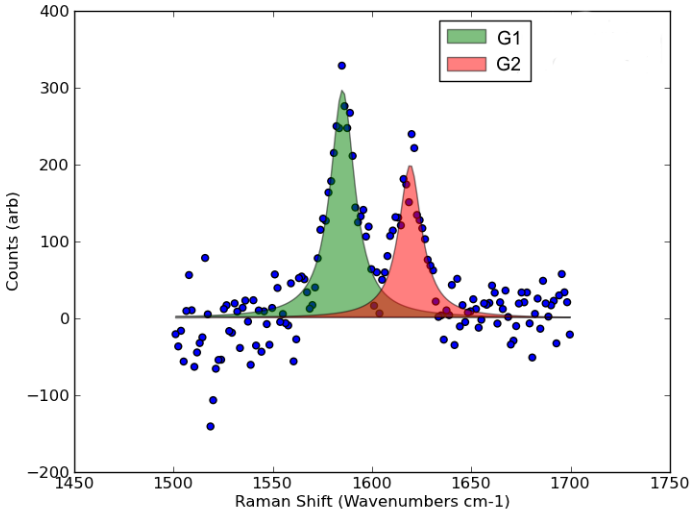

(a)

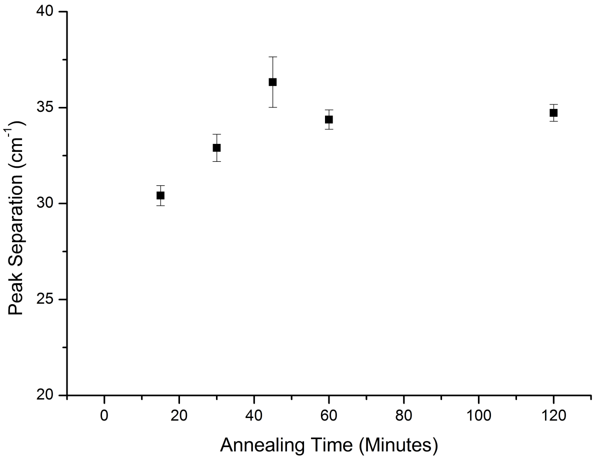

(b)

Figure 7.5: a) Example Raman spectra taken from a sample annealed for 60 minutes at 1650°C showing the G band splitting and the associated labeling of the G1 and G2 components. b) The evolution of the peak separation between the G1 and G2 components with increasing annealing time at an annealing temperature of 1650°C, the split separation appears constant with annealing time, error bars given by statistical averaging of all measurements within a sample.

fall short of explaining the situation here. Also the DOS in semi-conducting carbon nanotubes is different to graphene. Therefore for this to be a possibility the 'structures' seen in AFM (see section 7.2.3.3) would have to be semi-conducting carbon nanotubes.

If the 'structures' are confined graphene ribbons, then work carried out on the measurement of G band splitting in hydrogen-terminated graphene nanoribbons (171) shows the Raman G band splitting in such systems. Again though the observed splitting is only ∼few $\text{cm}^{-1}$s and the edge termination appears crucial in the observation of the G band splitting. So it seems somewhat unlikely that the simple assignment of the structures present in AFM images as graphene nanoribbons is enough to explain this G band splitting.

Curvature effects in carbon nanotubes have been shown to cause Raman G band splitting.(60; 132) Curvature acts to change the C-C bond lengths, the C-C bond planarity and causes $sp^2/sp^3$ bond hybridisation. The bond hybridisation causes phonon softening to occur. This can allow to peak splitting in the 30 $\text{cm}^{-1}$ range observed here but unfortunately the peak shifts in our samples exhibit phonon hardening and therefore the effects cannot be explained through confinement.

This leaves there to be no definitive answer at this stage as to the true cause of the G band splitting within these samples. All that can be done is to discuss what has been observed in other microscopy techniques along with the Raman measurements to piece together a set of conditions that must be met for whatever is causing this effect. Firstly the absence of the G band splitting in samples annealed at 1600°C is useful to note. This along with the the behavior of the G1 to G2 areas as shown in Figure 7.7 that suggests that for samples annealed for 30 minute and above there is an increase in the G2 area. This fits in with the AFM observation of more ribbon-like structures on the sample surfaces.

The G2 to G1 area ratio for a sample annealed at 1690°C for 60 minutes is ($0.54\pm0.07$) again consistent with the observation of bilayer regions and ribbon-like structures on the surface. There is evidence from AFM attempts to manipulate these structures (section 7.2.3.3) and Nanoprobe work (section 7.2.5.3) to cut through the structures that they actually exist below the graphene sheet and are fairly tightly bound to the surface.

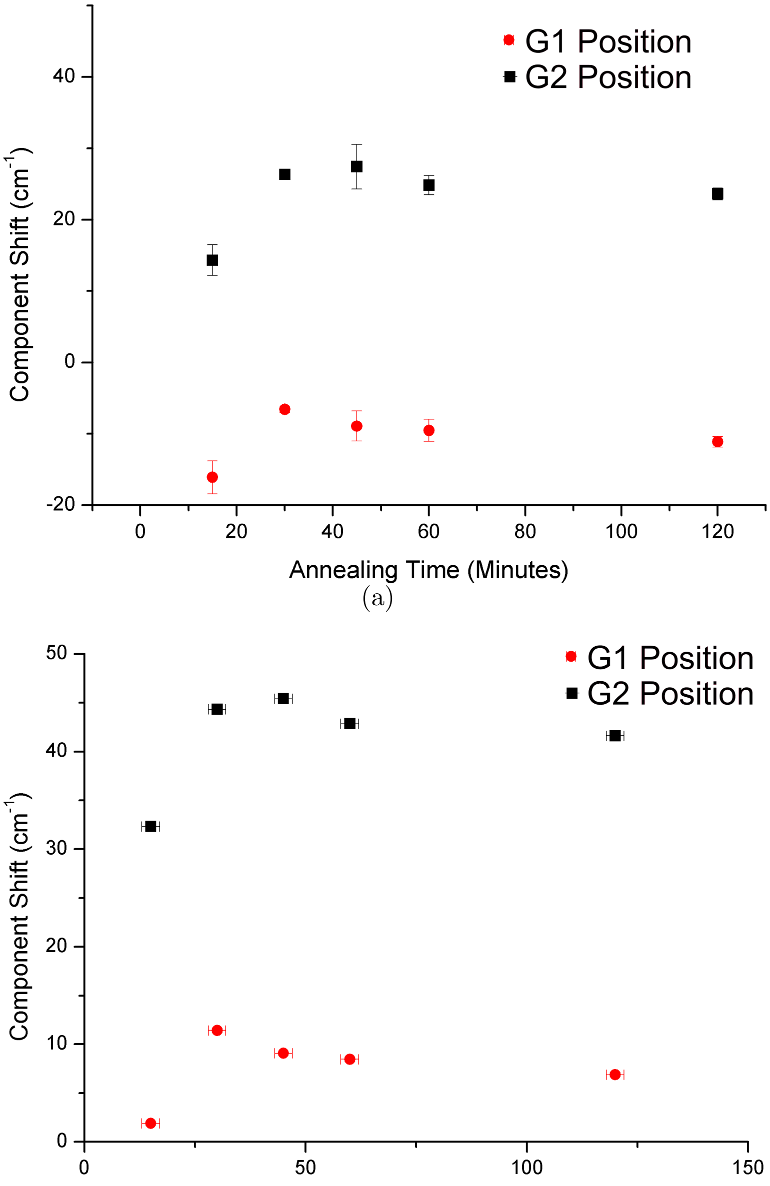

(a)

(b)

Figure 7.6: Shows the evolution of the shifts in position of both the G1 and G2 away from a reference peak of a) 1598 cm$^{-1}$ a value chosen from average G peak positions measured when no splitting is present. b) 1580 cm$^{-1}$ a measurement of the g peak position in exfoliated graphene (136).

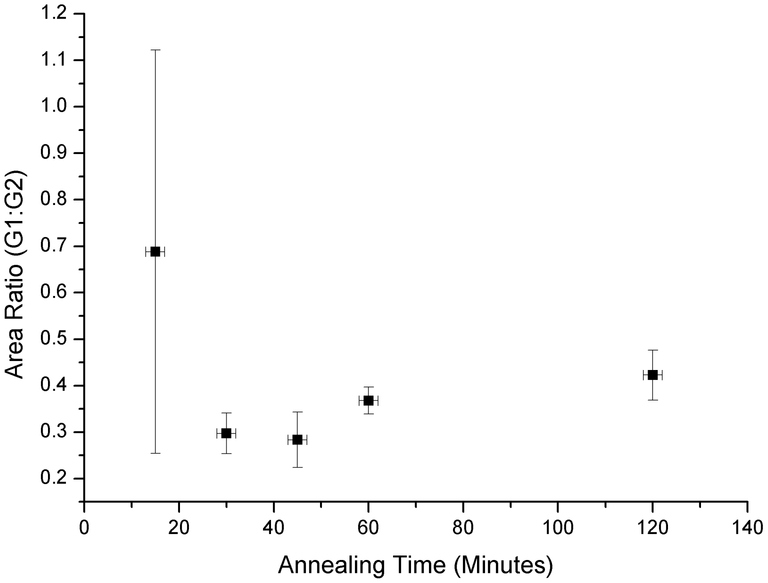

Figure 7.7: Shows the evolution of area of the G2 component divided by the area of the G1 component with varying annealing time for an annealing temperature of 1650°C. Away from the 15 minute point that has a large uncertainty, there is a general increase in ratio, this compares to an increase in tube-like structures and bilayer regions in AFM images.

For these structures to be responsible for the observed shifts their must be significant alteration of the graphene structure taking place between the substrate and the graphene-like material within the structures with significant hardening of either the LO or TO phonon taking place. This proposal is somewhat speculative and more measurements would be required to obtain a definitive answer for this observed splitting effect. The potential to use atomic scale scanning tunneling microscopy on these structures would be very useful to analyze the bonding present and try to link this with the observed G band splitting.

#### 7.2.1.3 Raman Uniformity and Raman Mapping

As described previously, the graphene growth observed in some of the samples annealed under an argon atmosphere is on occasion quite patchy and often leads to Raman spectra being non-carbon-rich when the laser spot lies within one of these bare substrate regions. To highlight this 3 Raman spectra were taken with a roughly 15 $\mu$m separation between each point in the central region of a sample annealed at 1600°C for 60 minutes. Figure 7.2.1.3 shows these spectra and how 2 of the 3 areas measured are carbon-rich whilst the other region shows no carbon signal at all.

This kind of measurement highlights the non-uniformity of some of the graphene films grown in this manner. Also highlighted is the ability of Raman microscopy to track these changes from carbon-rich regions to non-carbon-rich regions. This lead to the taking of Raman maps. This was possible after the purchase of a new Horiba Raman microscope towards the end of this project. This allows for Raman spectra to be taken whilst a mirror is used to move the laser light around on the sample in the $xy$ plane with a maximum scan size ~40×40 $\mu$m. The system also has a laser of wavelength 532nm (green) as well as a 633nm (red).

Figure 7.9 shows Raman map data obtained from fitting D peak parameters whilst varying the laser position on the sample. Island-like features are observed as with AFM. The D peak width fit (Figure 7.9(a)) suggests there are regions of multi layer graphene.(107; 161) The position variation (Figure 7.9(b)) is relatively small, hinting at low strains within this region. Due to the nature of how the laser is positioned during the mapping procedure, it has so far proved difficult

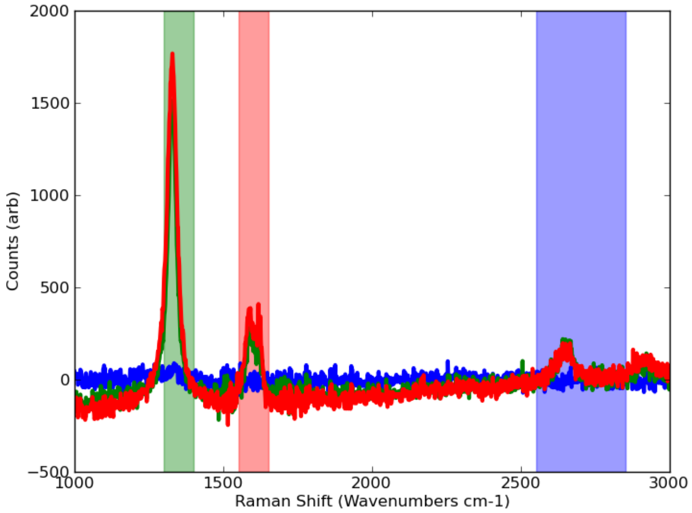

Figure 7.8: Raman spectra (silicon carbide background subtracted) taken at 3 points each separated by ∼20 $\mu$m. The sample had been annealed for 60 minutes at 1600 °C . The shaded regions correspond to the main Raman bands associated with graphene D (green), G (red) and 2D (blue). Incident laser wavelength of 633 nm. The blue spectrum shows no carbon signal at all thus highlighting the non-uniformity of the samples.

to obtain a reliable graphene spectrum with the silicon carbide subtracted. This means that the G band has not been able to be fitted. The 2D band, as expected provides complementary data to the D band.

Although Raman mapping alone showed evidence of the island-like growth due to the presence of areas with graphene-like spectra and areas with spectra associated with blank silicon carbide within a scanned region.. It was decided that complementary AFM and Raman mapping of the same regions would be required. Attempts to use optical lithography to pattern alignment marks on the sample proved unsuccessful. A crude method was developed for aligning the AFM and Raman map regions, this involved the use of distinguishing marks on the sample surface. These marks were a sequence of scratches made on the surface and areas of debris around these scratches.

Figures 7.10, 7.11 and 7.12 shows the intensity of the D bands and 2D bands mapped out across a sample annealed for 120 minutes at 1650°C at different points with the AFM image corresponding to each respective area given. There is correspondence between the AFM images and the Raman maps. For example in Figure 7.10 the thicker regions observed in AFM have increased Raman 2D and D band intensity. The D band intensity suggests the regions towards the center of the thicker area are quite disordered, suggesting that ripples and wrinkles could be responsible for increasing the D band intensity.

In Figure 7.11 the AFM image shows a rip in the graphene film that shows up in the Raman maps with an absence of the D and 2D bands. The graphene film here can be identified as being bilayer due to presence of thinner monolayer regions around the rip. Despite this there is not the strong D peak observed in Raman maps from the area shown in Figure 7.10. This would appear to be due to the bilayer film being much more complete in this region, the absence of tube - like structures from the AFM images would suggest that they are responsible for the D peak increase in Figure 7.10.

The data shown in Figure 7.12 act as a good indication of the increased graphene coverage obtained with increasing annealing time. The only large D peak is found in and around the defect used to align the Raman maps to the AFM image. Around this defect an unbroken film is observed in AFM and a defect free but carbon-rich Raman signal indicates that this film is graphene. SEM images

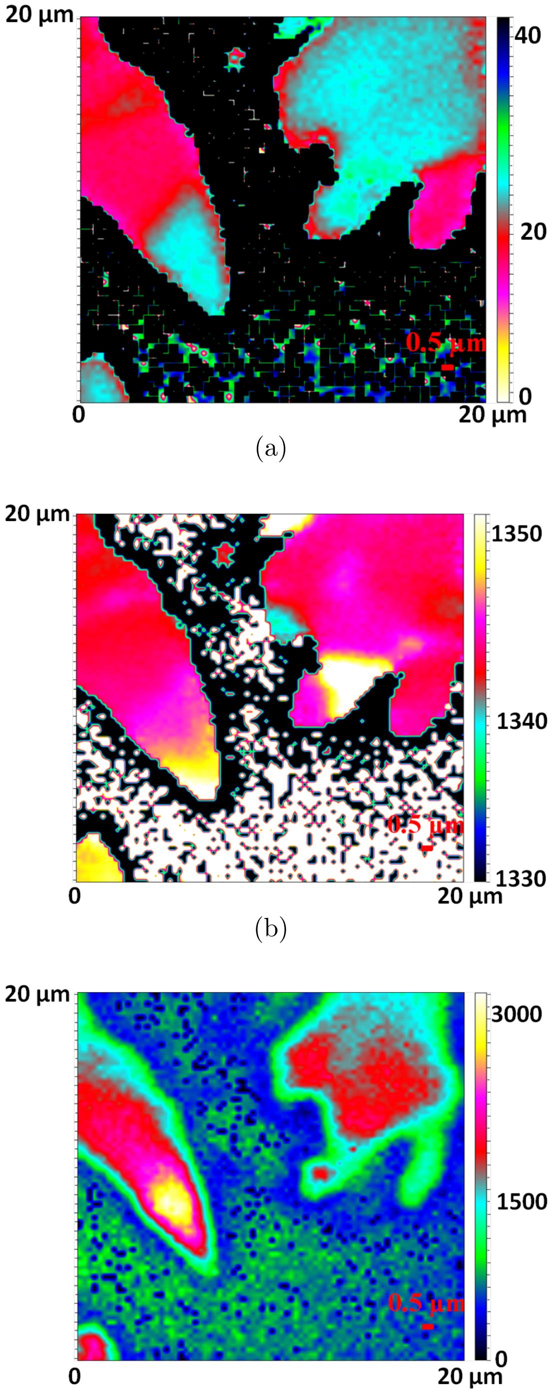

(a)

(b)

(c)

Figure 7.9: Raman map data for a sample annealed at 1650°C for 60 minutes. The maps shown have been acquired by fitting a) D band width (graphene coverage). b) D band position (strain) and c) D band area (graphene coverage) whilst varying laser position. Incident laser wavelength of 532 nm.

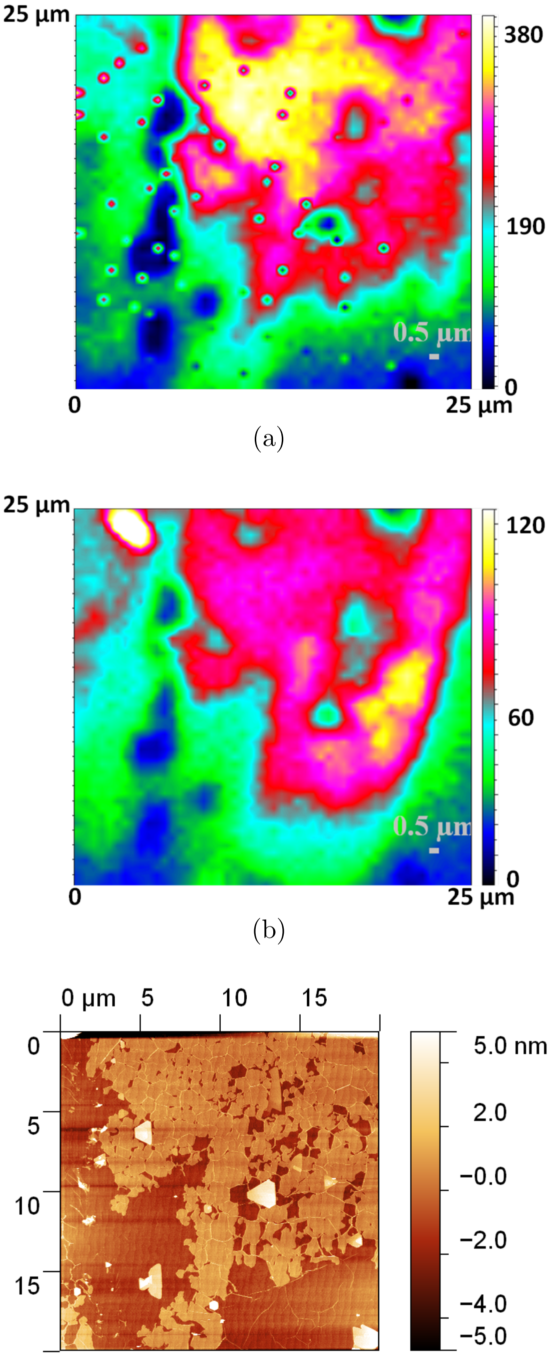

(a)

(b)

(c)

Figure 7.10: Raman map and AFM data for a sample annealed at 1650°C for 120 minutes. The Raman maps shown have been acquired by fitting a) D band intensity (disorder) and b) 2D band intensity (graphene coverage) respectively. c) The corresponding AFM image of the area Raman mapped. Incident laser wavelength of 532 nm used during the Raman mapping.

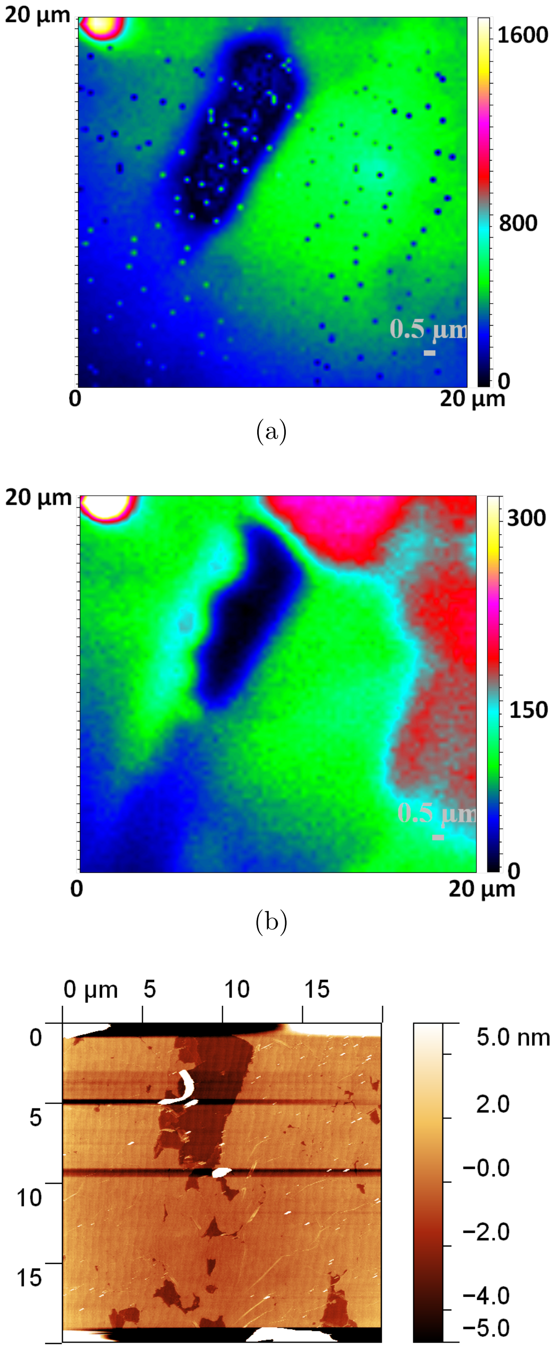

(a)

(b)

(c)

Figure 7.11: Raman map and AFM data for a sample annealed at 1650°C for 120 minutes. The Raman maps shown have been acquired by fitting a) D band intensity (disorder) and b) 2D band intensity (graphene coverage) respectively. c) The corresponding AFM image of the area Raman mapped. Incident laser wavelength of 532 nm used during the Raman mapping.

(Figure 7.37(a)) suggest that the films in this region are monolayer graphene and extend to even larger length scales (∼100 $\mu$m). Though the majority of this sample (away from the center) consists of mainly bilayer regions as shown in Figures 7.10(c) and 7.11(c).

The use of Raman mapping has been somewhat qualitative at this stage. Further improvements to subtraction procedures and the ability to extract the G peak data would greatly improve this. That would allow G:D ratios to be mapped along with quantities linked to the G splitting such as split separation (as in Figure 7.5) and peak component ratios (as in Figure 7.7).

#### 7.2.1.4 Thickness Estimations From Raman Attenuation Data

The process used for using the attenuation of laser light whilst taking Raman spectra to measure graphene film thickness has been described in section 3.3.6 and has been used to measure the thickness of graphene films grown in UHV during Chapter 4. The attenuation of the silicon carbide Raman spectrum due to the presence of graphene over layers can be used to estimate the thickness of graphene films. (140) After work on measuring the thicknesses of films in UHV, a value of 0.02 for the absorption coefficient, $\alpha$, is used and the values calculated for layer thicknesses of graphene films grown at different annealing times and temperatures are given in Table 7.1.

There is no overall clear variation within the values calculated for layer thickness with increasing annealing time or temperature. All values come out to be ∼2 layers or below which is expected from observations through other microscopy techniques. Once more it must be understood that these layer thickness measurements are an estimate, with the technique shown to have limitations in measuring thin graphene films.(140)

Extra limitations could arise from discrepancies between the transparency of the reference substrate which is a piece of as-purchased silicon carbide wafer and therefore still marred by substrate scratches. It has been shown that during the formation of atomic terraces on silicon carbide, this silicon carbide becomes more transparent (29) thus the silicon carbide underneath the graphene being measured will reflect the laser light differently to the reference wafer.

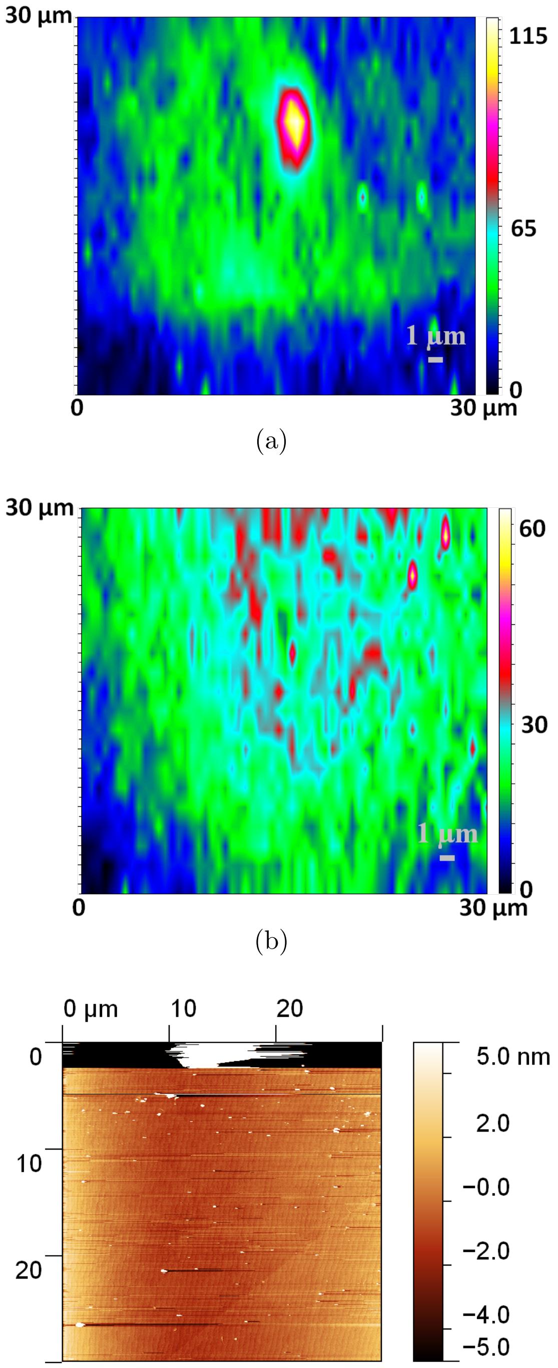

(a)

(b)

(c)

Figure 7.12: Raman map and AFM data for a sample annealed at 1650°C for 120 minutes. The Raman maps shown have been acquired by fitting a) D band intensity (disorder) and b) 2D band intensity (graphene coverage) respectively. c) The corresponding AFM image of the area Raman mapped. Incident laser wavelength of 532 nm used during the Raman mapping.

Table 7.1: Thickness measurements using Raman spectroscopy for samples annealed in inert argon gas

| Annealing Conditions | Raman Layer Thickness ($\alpha = 0.02$) |
|---|---|
| 1600°C for 15 mins | 1.2±0.2 |
| 1600°C for 30 mins | 0.57±0.09 |
| 1600°C for 60 mins | 0.5±0.1 |
| | |
| 1650°C for 15 mins | 0.9±0.2 |
| 1650°C for 30 mins | 0.34±0.07 |
| 1650°C for 45 mins | 2.3±0.2 |
| 1650°C for 60 mins | 2.1±0.2 |
| 1650 (c face down) °C for 60 mins | 2.0±0.2 |
| 1650 °C for 120 mins | 0.7±0.2 |
| | |
| 1690°C for 60 mins | 1.4±0.2 |

#### 7.2.1.5 C-Face Raman Spectroscopy Data

Work here has concentrated on the growth of graphene on the (0001) face of silicon carbide. This has been in part due to the absence of graphitisation of the c-terminated $(000\bar{1})$ face. This lack of graphitisation can be observed by the non-carbon-rich Raman spectra of samples annealed within the temperature ranges allowed by this furnace system. The absence of graphitisation on the $(000\bar{1})$ face is not unexpected for annealing processes carried out in inert gas atmospheres at these temperatures.(24; 35)

Figure 7.13 shows Raman spectra from a number of selective samples annealed under varying conditions. All show no evidence of Raman bands in the expected regions for graphene growth post the subtraction of the silicon carbide substrate spectrum. The spectrum shown in Figure 7.13(a) is taken from a sample annealed at 1650°C with the $(000\bar{1})$ face towards the graphite sample holder for protection. This sample has been shown to have structures on top of the silicon carbide substrate in AFM micrographs (Figure 7.30) yet the Raman spectra is still non-

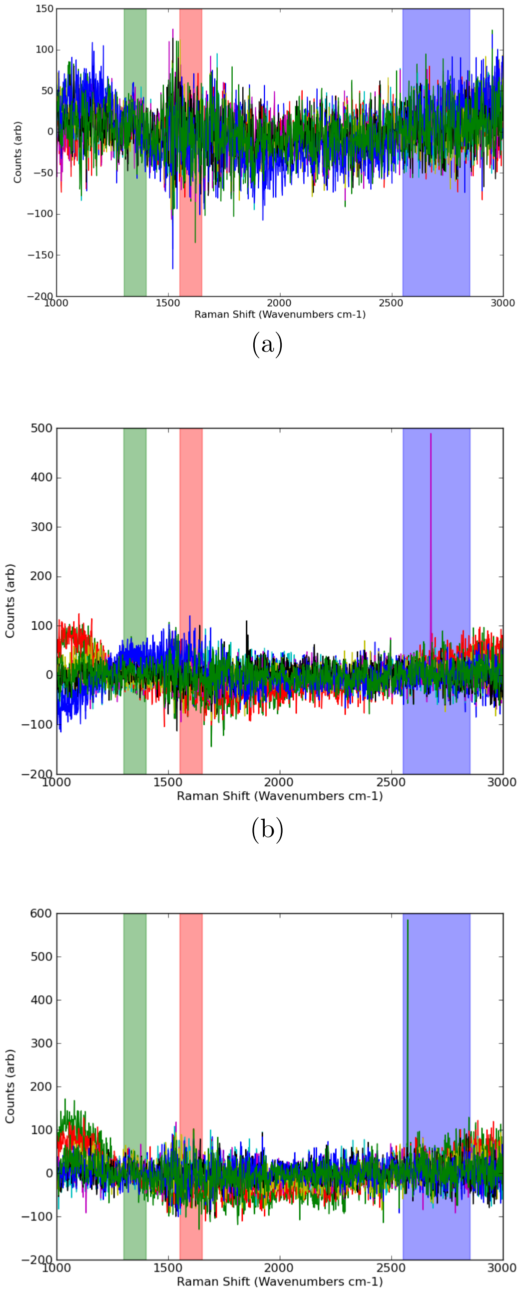

(a)

(b)

(c)

Figure 7.13: Raman spectra(silicon carbide background subtracted) taken from the $(000\bar{1})$ face for samples after varying annealing processes. a) 60 minute anneal at 1650°C $(000\bar{1})$ face down. b) 120 minute anneal at 1650°C (0001) face down. c) 60 minute anneal at 1690°C (0001) face down. The shaded regions correspond to the main Raman bands associated with graphene D (green), G (red) and 2D (blue). Incident laser wavelength of 633 nm. Absence of peaks shows samples are non-carbon-rich.

carbon rich. There is also no carbon signal observed in samples annealed (0001) face towards the graphite holder at 1650 °C for 120 minutes (Figure 7.13(b)) and at 1690°C for 60 minutes (Figure 7.13(c)). Again these results fit with observations made elsewhere (24; 35) on the suppression of graphene growth in inert gas atmospheres. To graphitise this face, higher temperatures or lower gas pressures would be required. The higher temperatures are not possible with this furnace system and lower pressures could lead to contamination issues such as oxidation of the silicon carbide substrates without modification to the system.

### 7.2.2 LEED Data

To understand the surface reconstructions taking place during the high temperature annealing processes, a select few samples were chosen to be analyzed in the LEED system. Time constraints on the use of the LEED system limited the number of samples that could be analyzed in this fashion, this means that the results obtained are a guide to the processes taking place rather than a full explanation.

Figure 7.14 shows a set of LEED data from a sample annealed in the furnace system for 15 minutes at 1600°C under a flow of argon gas. Figures 7.14(a) and 7.14(b) show LEED images taken at 99 eV and 199 eV respectively after a 600°C clean up anneal in UHV. The samples show a clear silicon carbide $1 \times 1$ reconstruction with a surrounding graphene spot pattern rotated at 30° from the silicon carbide reconstruction with the expected lattice ratio of $0.80 \pm 0.01$ for graphene compared to silicon carbide (measured in 99 eV image, Figure 7.14(a)). This pattern was also observed during LEEM measurements at Brookhaven National Lab (section 7.2.4) and appeared strange due to the absence of the buffer-layer expected between the graphene layer and silicon carbide substrate on the (0001) face.

A possible reason for this could be that argon gas during the growth process had got trapped under the graphene layer that was not successfully removed during the 600°C anneal in UHV. In a similar observation to those made with the intercalation of molecules such as hydrogen, (172; 173) germanium (174) and lithium (175) under epitaxial graphene sheets. To attempt to remove this gas and recover the expected $(6\sqrt{3} \times 6\sqrt{3})$R30 reconstruction a further anneal was

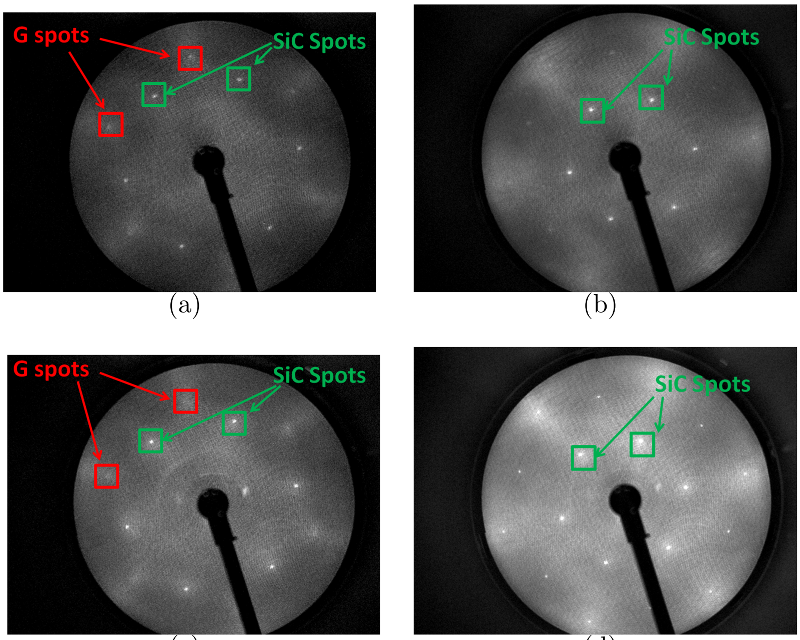

(a) (b) (c) (d)

Figure 7.14: LEED data taken on the (0001) face from a sample annealed in the furnace system for 15 minutes at 1600°C. a) Taken at 99 eV after a 600°C anneal in UHV. b) Taken at 199 eV after a 600°C anneal in UHV. c) Taken at 99 eV after a further 1100°C anneal in UHV. d) Taken at 199 eV after a further 1100°C anneal in UHV. The key diffraction spots associated with graphene and silicon carbide are labeled were appropriate. Diffuse nature of graphene spots in a) and c) shows film to be disordered.

carried out at 1100°C. The LEED patterns from this are shown in Figures 7.14(c) and 7.14(d). There is no switch to a $(6\sqrt{3} \times 6\sqrt{3})$R30 pattern, the only change is that the spots become clearer and the same reconstruction remains with graphene spots rotated at 30° to the silicon carbide substrate.

The absence of a buffer layer in graphene rich surfaces on silicon carbide (0001) has been observed for the oxidation of the buffer layer.(176) This could provide one possible explanation for the observations made on these surfaces, though more data would be required to analyze this fully.

However, these observations would suggest that there is some differing mechanism between the graphene layer and the silicon carbide substrate than commonly observed elsewhere. To probe this further, a sample annealed for 30 minutes at 1600°C was analysed with LEED. This sample had already been observed to be 'patchy' under AFM and Raman spectroscopy with islands of isolated graphene growth. This is somewhat surprising as the sample annealed for 15 minutes was seen to be slightly more uniform in graphene film growth. This perhaps suggests that 1600°C is somewhat of an onset temperature for graphene growth and that the difference between a 15 anneal minute and a 30 minute anneal is minimal. Given time, multiple runs at these annealing times and temperatures would show how consistent the graphene growth is between samples and how much this change in annealing time affects the growth procedure.

The LEED patterns obtained from the sample annealed for 30 minutes at 1600°C are shown in Figures 7.15(a) and 7.15(b), the samples underwent a clean up anneal at 1000°C in UHV prior to the LEED patterns being taken. The patterns observed show a buffer-like reconstruction, similar to that seen for samples annealed at 1500°C for 60 minutes (see Chapter 6) and is consistent with AFM images showing patchy islands on the surface and Raman which also indicates that the graphene growth is fairly inconsistent across this sample. Once more, the buffer-like reconstruction observed is not the expected $(6\sqrt{3} \times 6\sqrt{3})$R30 pattern but a different complex pattern that still maintains 6-fold symmetry. This could be explained by the silicon-rich environment introduced by the presence of the argon gas, which has been seen to produce similar reconstructions on the silicon carbide $(000\bar{1})$ surface.(154)

In conclusion, these LEED patterns show that the mechanism behind the graphene growth procedure present in this furnace system differs from those observed elsewhere. This can be ascertained from the absence of a buffer-layer signal from the graphene-rich sample and from the non $(6\sqrt{3} \times 6\sqrt{3})$R30 buffer layer pattern obtained from the patchy graphene sample. The patterns also show that when a graphene-rich LEED signal is obtained the ratio between the ratio in LEED spot separation between the silicon carbide spots and graphene spots is as expected and that the graphene film is rotated by 30° to the substrate. The blurred nature of the graphene spots obtained in Figures 7.14(a) and 7.14(b) are consistent with the disordered Raman signals obtained from these samples and also the rippled nature of the films observed under AFM.

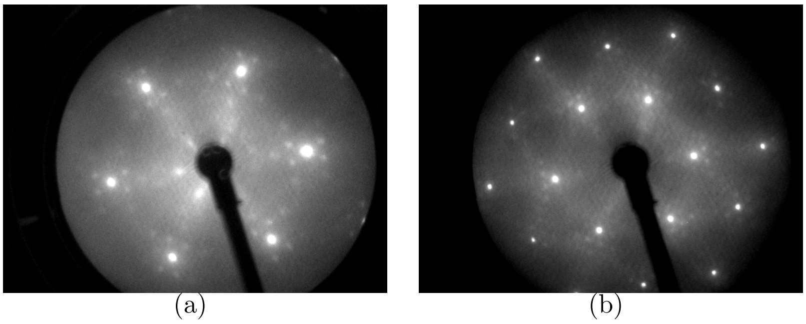
(a) (b)

Figure 7.15: LEED data taken on the (0001) face from a sample annealed in the furnace system for 30 minutes at 1600°C. a) Taken at 99 eV after a 1000°C anneal in UHV. b) Taken at 199 eV after a 1000°C anneal in UHV. Both show the presence of a reconstruction with six-fold symmetry.

To obtain a full picture of the processes taking place, LEED data from samples annealed at all temperatures and times would be required. This would allow the imaging of samples with thicker graphene regions to observe the multilayer structure and how that varies. Once more, the images shown here prove that a single annealing run under argon can be used to graphitise samples and that the mechanism behind this graphitisation varies somewhat compared to those obtained elsewhere.

### 7.2.3 AFM Data

#### 7.2.3.1 Graphene Growth on Atomically Stepped Terraces

Atomic force microscopy can be used to probe the structure of epitaxial graphene films as discussed in section 3.4.4 and shown previously in this work for graphene films grown in UHV in Chapter 4. As discussed earlier, the aim of annealing silicon carbide at higher temperatures in inert gas atmospheres was to graphitise the atomically stepped terraces formed during lower temperature. Evidence for this graphitisation has already been presented through Raman spectroscopy data. Figure 7.16 gives evidence that the graphene films formed during higher temperature anneals do indeed grow over the top of the atomically stepped substrate.

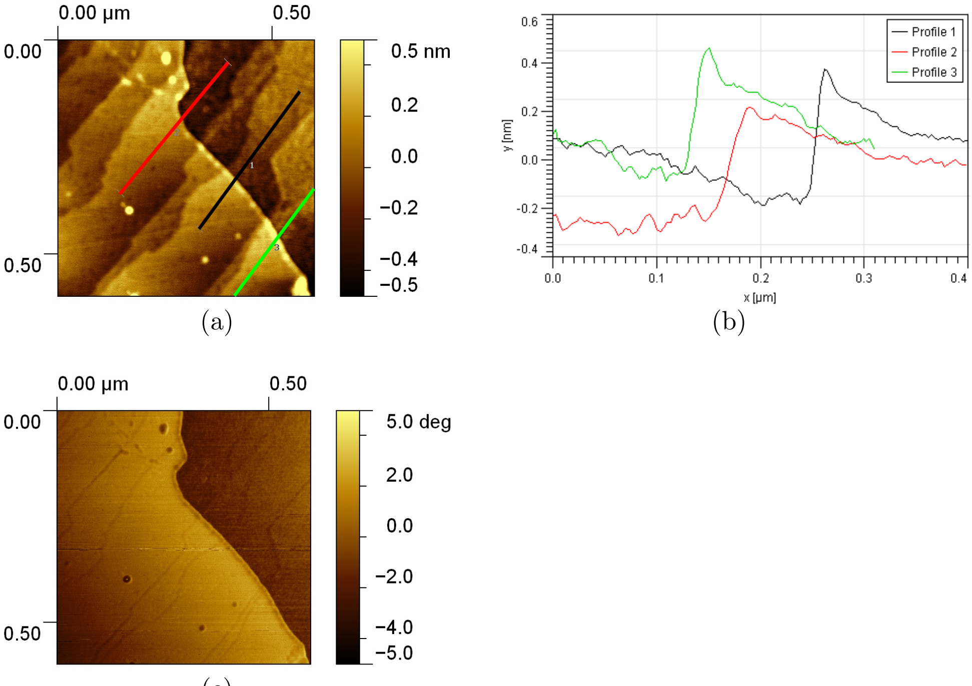

(a)

(b)

(c)

Figure 7.16: AFM data for a sample annealed $(000\bar{1})$ face down for 60 minutes at 1650°C. a) AFM height data. b) height profiles as colour coded in a). c) AFM phase data from the same image. The light region in the phase image is the graphene film, this is confirmed by the step height profiles which show the expected ~0.3 nm step for a monolayer graphene film.

Phase imaging (Figure 7.16(c)) compliments the height image (Figure 7.16(a)) well, highlighting the differences between the silicon carbide substrate and the graphene film. Height profiles (Figure 7.16(b)) taken from the height image indicate that this particular area of graphene is monolayer with a ∼0.3 nm step height observed between the film and the silicon carbide substrate, comparable to the expected interlayer spacing of a graphene sheet. It is important to note that the sample chosen in Figure 7.16 was annealed with the $(000\bar{1})$ face touching the carbon sample holder. This was purely due to the images from this sample looking clearer, a sample annealed under the same conditions (60 minutes at 1650°C) but with the (0001) face touching the carbon sample holder exhibited very similar film properties.

The graphene growth appears to follow after the formation of the atomically stepped silicon carbide substrate as the film is found to flow over the atomic terraces that form at the lower annealing temperature. Thus allowing substrate preparation and graphene growth to be carried out within a single annealing process under a flow of inert gas, without the need for the hydrogen etching step (29) or chemical etching step (27) used elsewhere. However as shown and discussed in the previous section the graphene films produced by this method are far from perfect and the following section will use atomic microscopy to probe some of these imperfections and show how varying the annealing conditions affect the graphene film appearance under AFM.

#### 7.2.3.2 Varying the Annealing Times and Temperatures

**7.2.3.2.1 Varying the Annealing Temperature** In Chapter 4 it was shown for graphene films grown in UHV that increasing the annealing temperature increased the lateral grain size present within the graphene films. In this short section AFM data will be used to discuss how increasing the annealing temperature affects the quality of the graphene films grown. Figure 7.17 shows examples of AFM height and phase images taken from samples annealed for 60 minutes at temperatures of 1600°C (Figures 7.17(a) and 7.17(b) ), 1650°C (Figures 7.17(c) and 7.17(d) ) and 1690°C (Figures 7.17(e) and 7.17(f)) respectively. For the sample annealed at 1600°C (Figures 7.17(a) and 7.17(b)) the area selected shows an isolated graphene region that appears to contain many ripple like structures, as will be shown later, this is more apparent for samples annealed at lower annealing times than 60 minutes at this temperature (see Figure 7.18)).

For the sample annealed at 1650°C (Figures 7.17(c) and 7.17(d)) there is some evidence of the joining of island like regions. The inter lying regions between islands seem to be fragmented and there is evidence of tube-like structures at the joining points between the island regions, this will be discussed in more detail later. There is also evidence of folding within the fragmented graphene films. The sample annealed at 1690°C (Figures 7.17(e) and 7.17(f)) the graphene regions appear to extend further in between the tube-like structures and there is evidence of a fold and rip in the graphene film.

So much like in UHV growth, there is evidence that increasing the annealing temperature can lead to larger graphene domains within films grown under argon atmosphere. However, this increase in temperature can be seen to increase the presence of ripples and fragmentation of the grown films.

**7.2.3.2.2 Varying the Annealing Time** In Chapter 4 it was shown that for graphene films grown in UHV increasing the annealing time led to an increase in the coverage of the graphene films on the surface. In this section, the evolution of the graphene film morphology with varying the annealing time will be discussed for the three main annealing temperatures used of 1600°C, 1650°C and 1690°C respectively.

The lowest annealing temperature that has been used to successfully graphitise the silicon carbide substrates is 1600°C. In general graphene films grown at this temperature appear to be more rippled than fragmented. A sample annealed for 15 minutes seems to consist of 2 distinct regions in the phase image (Figure 7.18(b)), this is consistent with the presence of just monolayer graphene and bare silicon carbide as suggested by LEED images from this sample (Figure 7.14). Also consistent with the LEED images is the presence of ripples and folds within the film, the effects of which can show up as blurring within the graphene diffraction spots.

A sample annealed at this temperature for 30 minutes showed a buffer-like LEED pattern (Figure 7.15), AFM of this sample shows up 3 distinct regions in

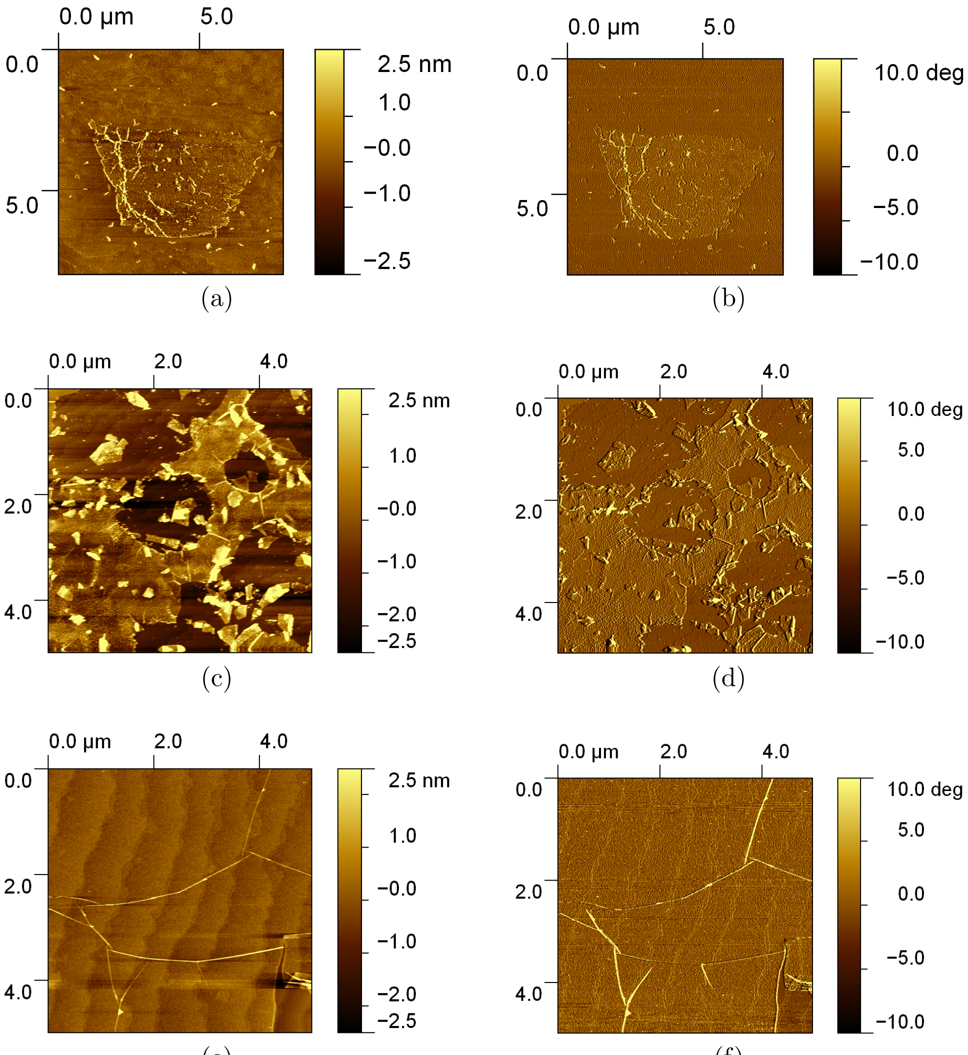

(a) (b)

(c) (d)

(e) (f)

Figure 7.17: a) & b) Height & Phase images from a sample annealed at 1600°C for 60 minutes. c) & d) Height & Phase images from a sample annealed at 1650°C for 60 minutes. e) & f) Height & Phase images from a sample annealed at 1690°C for 60 minutes. The change from isolated island-like growth to larger complete graphene regions is shown with increased annealing temperature. This trend is typical with increasing temperature though AFM images can vary between different imaged regions on a single sample (due to incomplete growth).

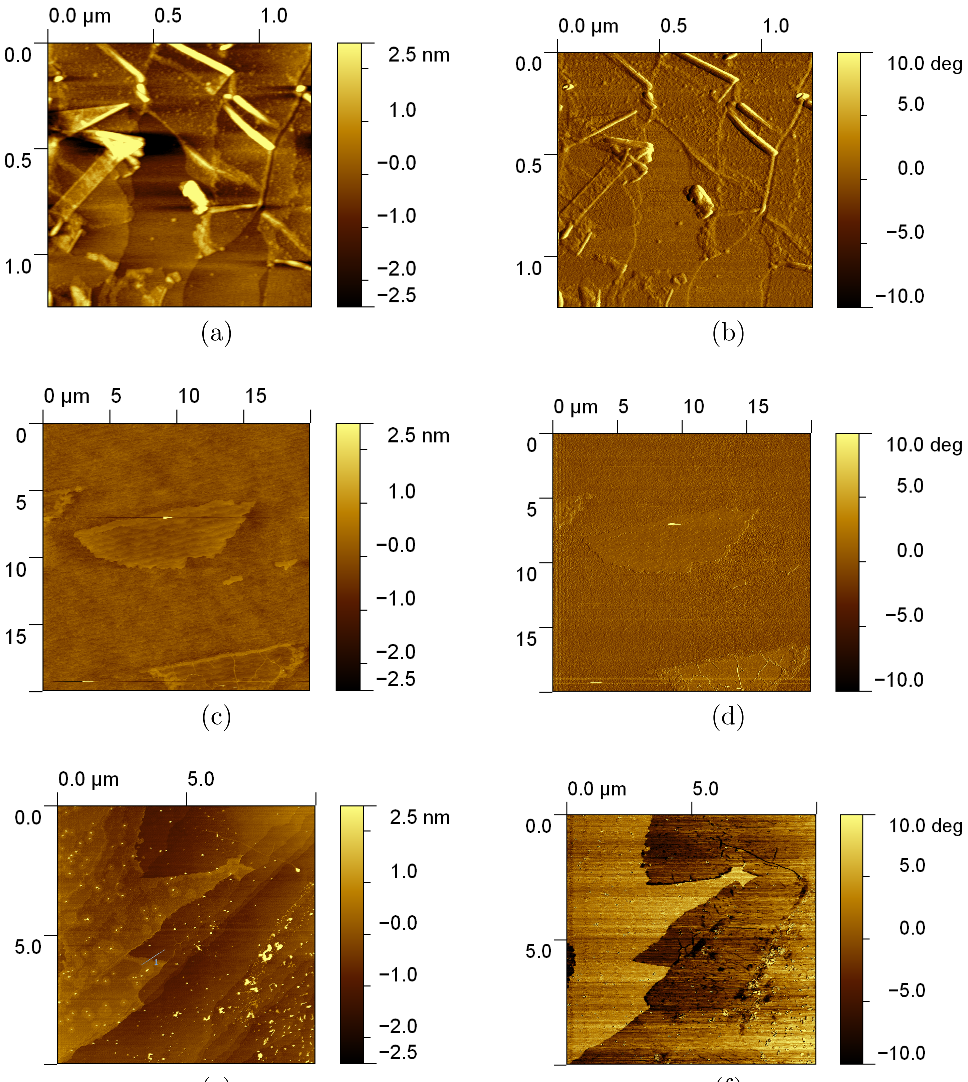

(a) (b)

(c) (d)

(e) (f)

Figure 7.18: a) & b) Height & Phase images from a sample annealed at 1600°C for 15 minutes. c) & d) Height & Phase images from a sample annealed at 1600°C for 30 minutes. e) & f) Height & Phase images from a sample annealed at 1600°C for 60 minutes. In general a change from fragmented graphene regions to more complete graphene islands is observed with increasing anneal time.

the phase image (Figure 7.18(d)). There are 3 large island regions, the central one having a different phase contrast to the one located towards the bottom of the image and the one located to the left of the image, both of these islands are similar in appearance. The height image (Figure 7.18(c)) shows that the large area which covers the majority of the image is of a similar structure to that observed for a sample annealed at 1500°C for 60 minutes (Figure 6.1(c)) which is consistent with LEED images from both samples.

The central island region is raised and appears uniform across its entirety, this could perhaps suggest it is a graphitic island, the step heights onto this island from the buffer layer are between ~0.5 nm to 1 nm, a little high for a single step onto a graphene sheet which is ~0.3 nm. As mentioned earlier the growth mechanisms present in epitaxial graphene growth mean that this does not rule out the island being graphitic as the surrounding silicon carbide could be silicon deficient pre-graphitisation and therefore relatively lower, also if the interface bonding between the graphitic layer and the silicon carbide is weaker due to a different interface structure then the spacing between the two layers could be higher. The other two islands present are far from uniform and contain some very interesting structures.

Figure 7.19 shows the height and phase images from one of these islands. Tube-like structures appear to run from the edges of the buffer layer across the island region. Tube-like structures also seem to spring out from step edges. From these tube like structures, there appears to be 'construction' taking place within the island. Little patches within the island appear similar to the surrounding buffer-layer region, suggesting that the progress of the buffer-layer is mediated by these tube-like filaments 'carrying' material across the sample. The emergence of the reconstructions from step edges has been observed elsewhere (73; 80) though its mediation via tube-like structures has not been.

Samples annealed for 60 minutes at 1600°C continue to show island-like regions as shown in Figures 7.17(a),7.18(e),7.17(b) and 7.18(f). These islands seem to vary in lateral size and the height images again suggest a step height between between ~0.5 nm to 1 nm. Many of the islands observed are wrinkled as the island in Figure 7.17(a) shows. Some islands such as shown in Figure 7.18(e)

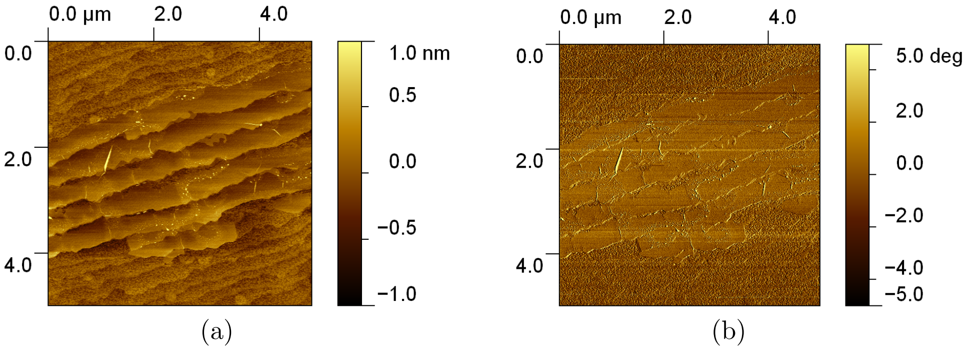

(a) (b)

Figure 7.19: a) & b) Height & Phase images from a sample annealed at 1600°C for 30 minutes. This figure highlights the presence of tube-like structures within this sample.

appear less wrinkled and observations of tube-like structures springing off these islands to perhaps facilitate extra growth can be seen.

Attempts were made to improve graphene film morphology by carrying out the graphitisation process at higher temperatures as well as at different annealing times. The variation in the graphene film morphology produced for varying annealing times at these higher temperatures will now be discussed. The first increase in annealing temperatures saw growth processes carried out at 1650°C. At this temperature, the graphene growth still appears to be island-like as shown in Figure 7.17(c) with the islands that do exist looking more fragmented. As expected, there is a general increase in graphene coverage as the annealing times are increased. SEM imaging of a sample annealed for 30 minutes (Figure 7.36) at this temperature also backs up AFM observations of graphene islands that are wrinkled, with bilayer regions that are very disordered. A sample annealed at this temperature for 120 minutes exhibiting very large regions of monolayer graphene coverage as observed in Raman mapping (Figure 7.12) and full coverage of monolayer and bilayer graphene as observed through SEM (Figure 7.37) thus highlighting the improvement in graphene coverage.

Figures 7.20 and 7.21 show a set of AFM micrographs taken for samples annealed at 1650°C at varying annealing times. The sample annealed for 15 minutes (Figure 7.20(a)) shows island-like graphene growth with the islands appearing

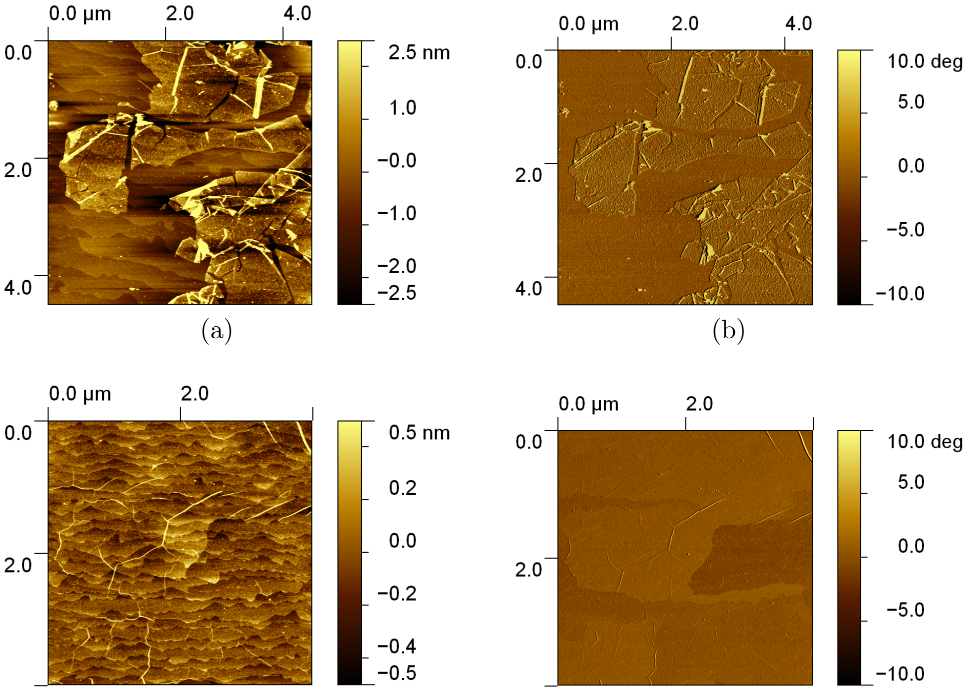

(a) (b)

(c) (d)

Figure 7.20: a) & b) Height & Phase images from a sample annealed at 1650°C for 15 minutes. c) & d) Height & Phase images from a sample annealed at 1650°C for 30 minutes. The graphene regions become more complete with increasing annealing time though ripple and fold structures can be observed. Light contrast in phase images correspond to the graphene film.

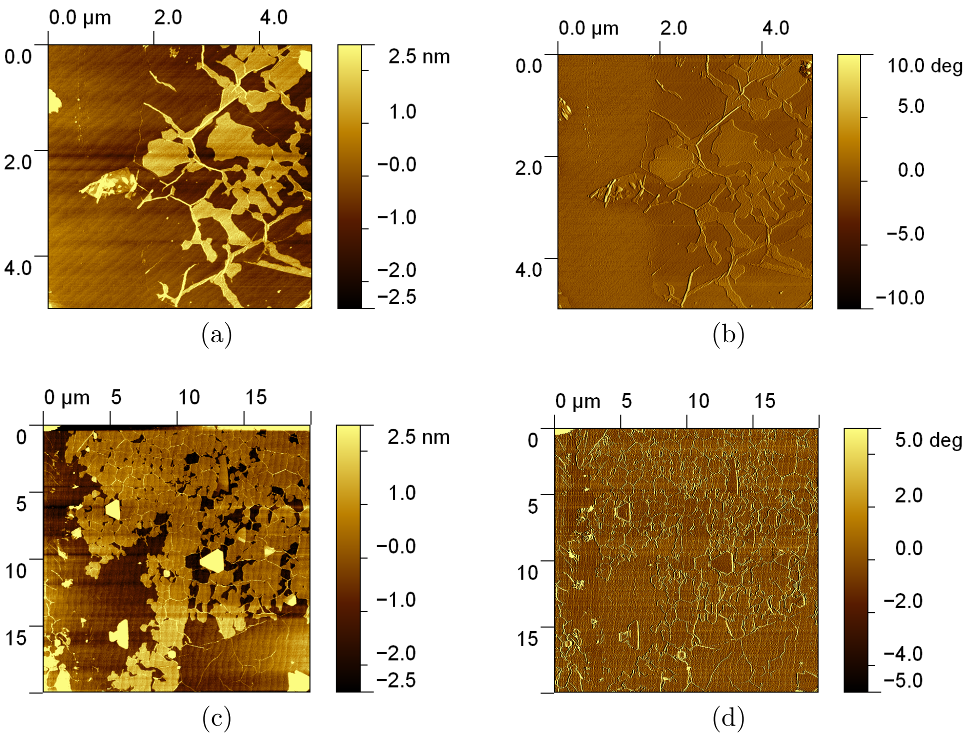

Figure 7.21: a) & b) Height & Phase images from a sample annealed at 1650°C for 60 minutes, this sample had (0001) face away from graphite holder. c) & d) Height & Phase images from a sample annealed at 1650°C for 120 minutes. The observation of bilayer regions (brightest contrast in height images) becomes more notable with increased annealing time. These bilayer regions appear incomplete and contain rips and folds.

fragmented and folds and ripples present within the films. There is also some evidence of tube-like structures within those graphene films. The step heights from the apparent silicon carbide substrate to the graphene layer is ∼1 nm, perhaps an indicator of decoupling between substrate and the film. The sample annealed for 30 minutes (Figure 7.20(c)) shows 3 areas with differing color contrasts in the phase image (Figure 7.20(d)) this is consistent with the presence of monolayer graphene, bilayer graphene and bare silicon carbide wafer as observed in SEM imaging. Again the graphene films look disordered with evidence of ripples and folds within the films. The thicker films films appear to have step heights consistent with bilayer regions, also the appear more disordered than the monolayer films, again consistent with SEM imaging (section 7.2.5). Once more there is evidence of tube-like structures within the graphene, there is evidence in SEM images taken on this sample for these structures to be tightly bound to the surface and unbreakable by nanoprobe STM tips (section 7.2.5.3).

For the sample annealed for 60 minutes (Figures 7.17(c) and 7.21(a)) the phase images (Fig 7.17(d) and 7.21(b)) again appear to show the presence of 3 different contrasts. The height image (Figure 7.21(a)) shows that the thicker regions exhibit step heights between 1-2 nm above the surrounding layers, suggesting the films are thicker than bilayer graphene, or perhaps that there is some decoupling between the graphene layers present. There is again evidence that the growth of the thicker layers is mediated via tube-like filaments that spread out with the growth occurring of these filaments.

The sample annealed for 120 minutes has been shown already to exhibit large areas of uniform graphene growth from Raman maps and corresponding AFM images in Figures 7.10, 7.11 and 7.12. Figure 7.21(d) is the phase image data for the AFM height measurements shown in Figures 7.21(c) and 7.12(c). Again there is evidence of 3 different contrasts in the phase images, this is consistent with the Raman map (Figure 7.12). Again the thicker layers have step heights of 1-2nm and appear to grow out from tube-like filaments that spread over the sample surface.

A single sample was grown at an annealing temperature of 1690°C AFM micrographs of both phase and height for this 60 minute anneal are shown in Figures 7.17(e), 7.17(f) and 7.22. In general there are only 2 different contrast

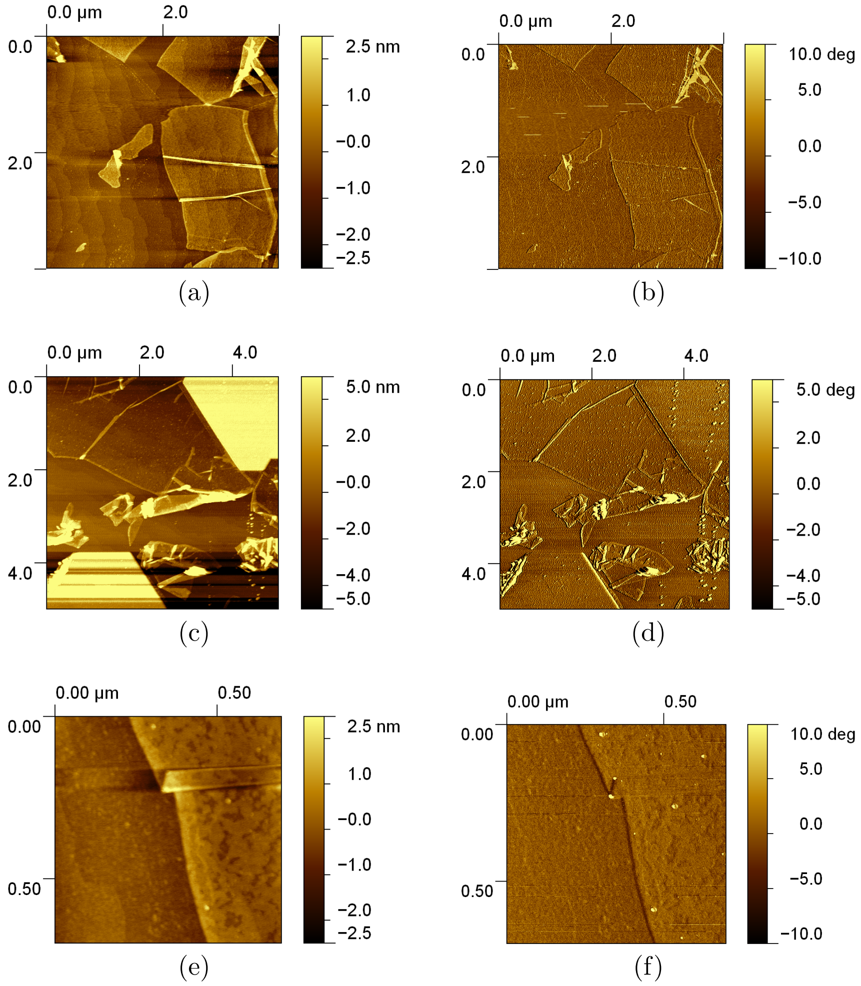

Figure 7.22: a), c) and e) Height images taken from different areas of a sample annealed at 1690°C for 60 minutes and b), d) and f) the corresponding phase data. Graphene sheets still appear fragmented under these growth conditions and still exhibit folds and ripples. c) shows very bright features these are thought to be plateaus in the underlying silicon carbide substrate due to the lack of phase contrast change within this region in d).

levels observed within the phase images showing that the samples seem to mainly consist of single layer graphene regions. The AFM height images also back this up with step heights comparable to a single graphene sheet observed. The graphene films still appear to be disordered and contain ripples, folds and rips. A close up of a graphene fold can be seen in Figures 7.22(e) and 7.22(f).

There is an interesting feature in the height image shown in Figure 7.22(c) where there is are a couple of 10 nm sized features in the image (very bright regions), however the corresponding phase image (Figure 7.22(d)) appears to show that the graphene growth is continuous over this structure, indicating that the structure is within the silicon carbide substrate. There is less evidence of tube-like structures within these samples, with only Figure 7.17(e) showing their presence, and even here it is debatable whether they are just ripples within a graphene film.

#### 7.2.3.3 Evidence of Tube-Like Structures

Throughout the sections on AFM and Raman microscopy of graphitised samples from the furnace system there have been referrals to tube-like structures. This section will concentrate on the observation of these structures and some suggestions made for their origin made from these observations. Firstly it must be said that within graphene films it is somewhat difficult to distinguish between the presence of tube-like structures and the natural ripples (97) that occur within graphene films. However there has been clear observation of these structures outside of graphene films, which means they cannot be ripples.

Evidence of the structures springing out from areas of bare silicon carbide are shown in Figure 7.23 which shows an AFM height micrograph. The tube-like structures are shown emerging from holes in bare silicon carbide regions of a sample annealed at 1600°C for 30 minutes. Figure 7.23(b) shows the presence of excess material around these defects, and shows the defect and subsequent ‘tube’ growth occurring at a step edge on the atomically stepped silicon carbide substrate. This shows that the tube-structures are separated from the graphene films and shows them in isolation to distinguish them from graphene film ripples and folds.

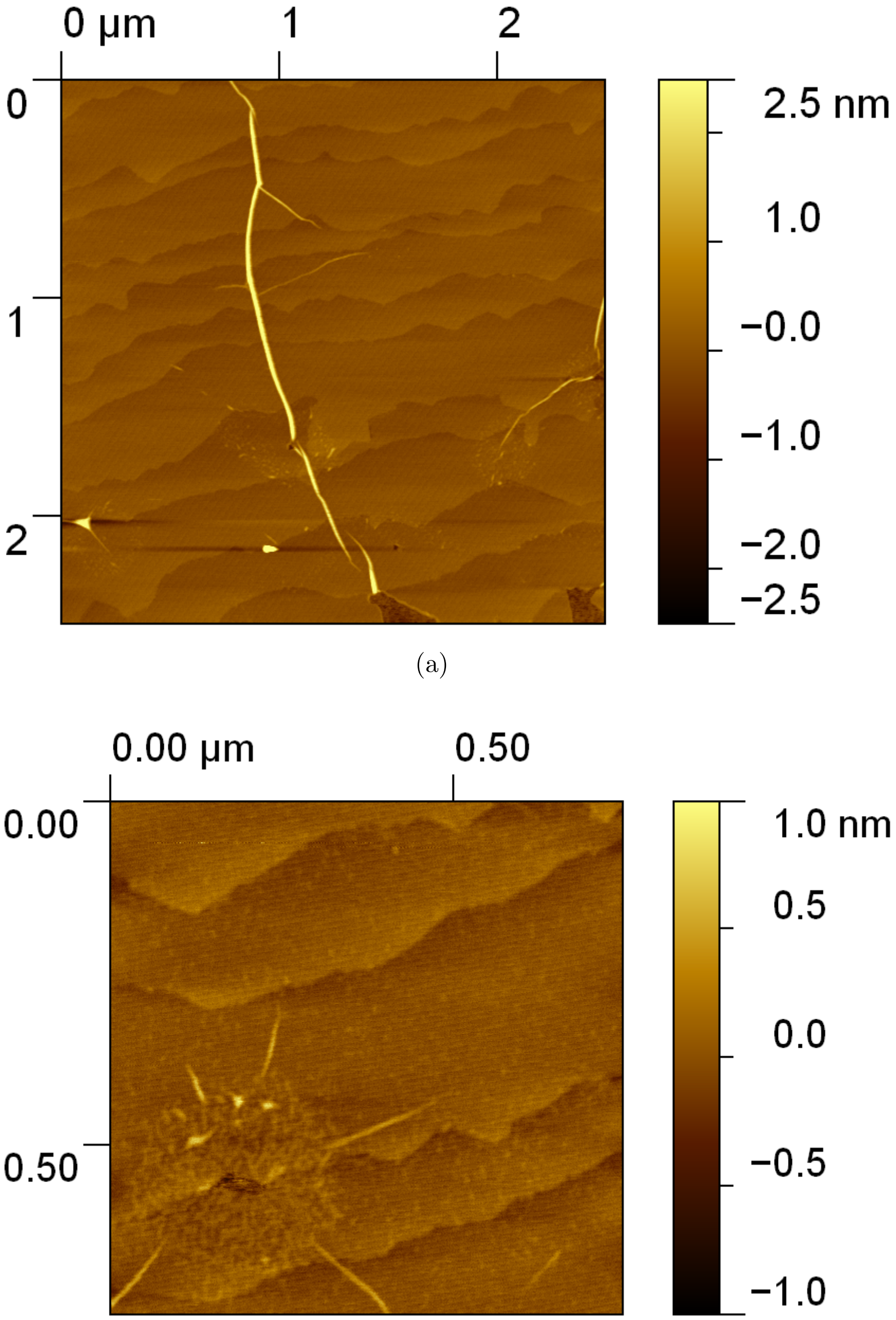

(a)

(b)

Figure 7.23: a) and b) Height images from a sample annealed at 1600°C for 30 minutes taken at different lateral scales on the same sample region. b) concentrates on highlighting the emergence of a tube-like structure from an apparent hole in the silicon carbide wafer.

Figure 7.24 again shows AFM micrographs of height and phase from the same sample annealed for 30 minutes at 1600°C. Here the images highlight tube structures apparently mediating the progress of a buffer-layer region across a bare silicon carbide island. Figure 7.24(b) concentrates on the boundary between the expanding buffer layer region and the silicon carbide wafer. The 'decoration' with material of the following step in the bare silicon carbide region can be seen and the start of formation of the buffer-layer. This complements the model for step formation mentioned in Chapter 6 which describes the mechanism driving surface reconstructions as the change in silicon to carbon atom ratio at the sample surface.

Figure 7.25 shows AFM micrographs of height and phase for a sample annealed at 1600°C for 60 minutes. Here there is evidence of the tube-like structures spreading out from the edge of a graphene layer region. This suggests that the growth of graphene layers is also mediated by these structures and them 'carrying' that material across the sample surface.

The suggestion that thicker areas of graphene growth also being mediated by these structures is shown in Figure 7.26 where the thicker regions appear to grow in between the tube like structures. As the thicker layers are on top of single layer graphene it is harder to distinguish the tube-like structures from ripples and folds within the graphene layers.

An attempt to move these tube like structures and manipulate them as done with ripples elsewhere with STM (177) was attempted for structures observed in a sample annealed for 45 minutes at 1650°C. These structures were observed within a graphene film, if they were ripples then this procedure would be expected to move when imaged (100 nm scan on the structure) with a free amplitude ($A_0$) of 5.25 V and and amplitude setpoint ($A_{sp}$) of 0.1 V. The fact that they do not move suggests that these tube-like structures are tightly bound to the underlying silicon carbide substrate. This is an observation that agrees with SEM images taken after cutting of graphene films within Nanoprober work that show these structures still present when the films have been cut (see section 7.2.5.3).

Here evidence has been given for the presence of tube like structures within furnace grown samples and images suggesting that these structures facilitate the mediation of surface reconstructions and graphene growth on the surface have

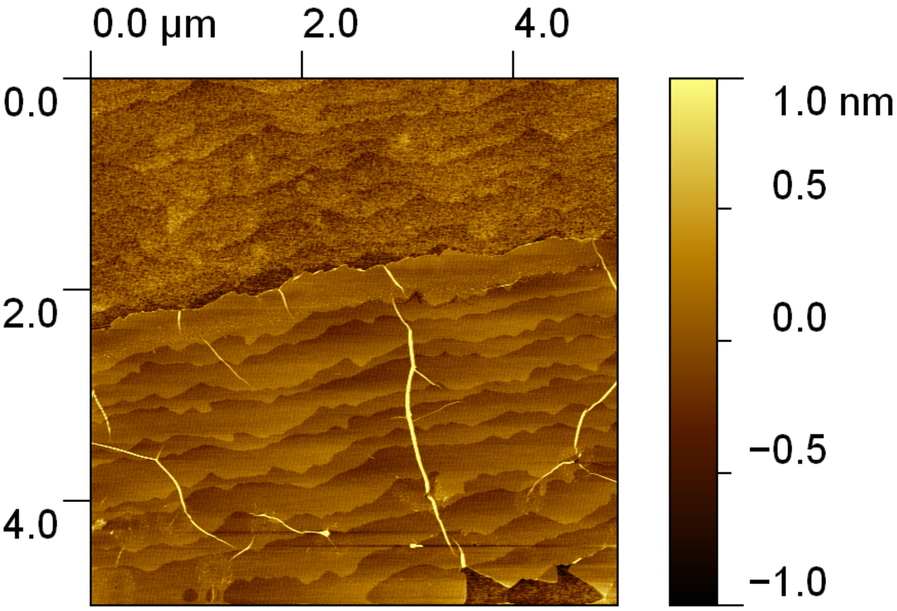

(a)

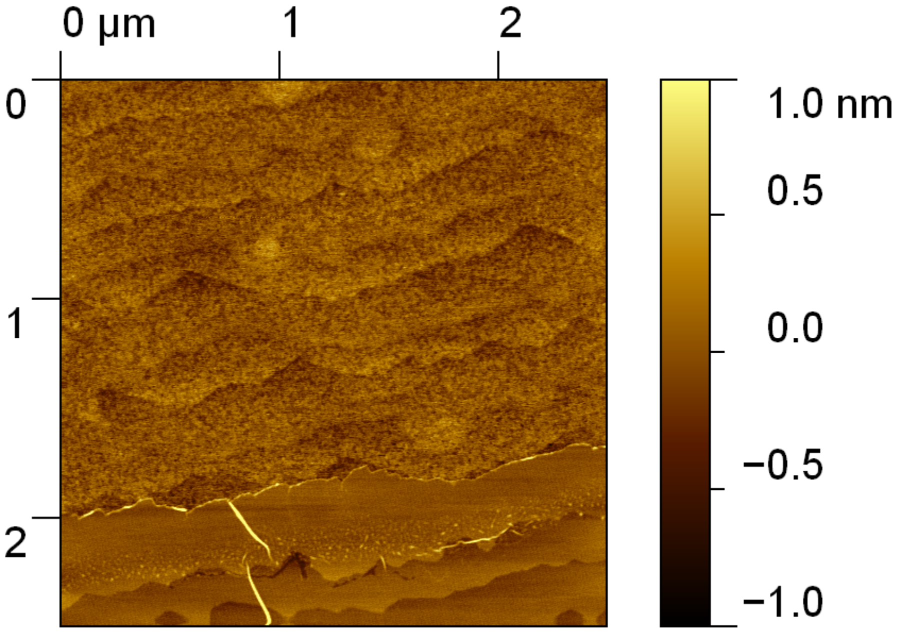

(b)

Figure 7.24: a) and b) Height images from a sample annealed at 1600°C for 30 minutes taken at different lateral scales on the same sample region. b) concentrates on highlighting the emergence of tube-like structures from the edge of a domain change and the 'decoration' of material around step edges.

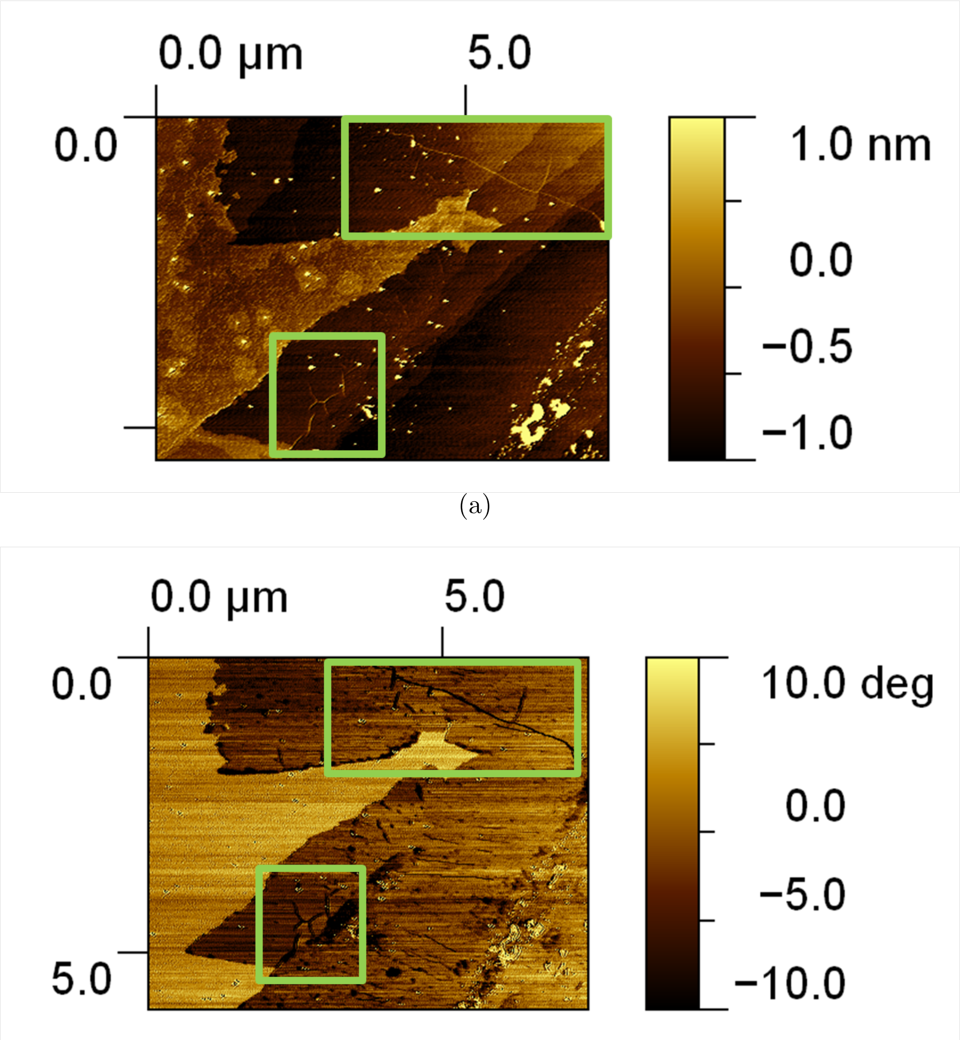

(a)

(b)

Figure 7.25: a) & b) Height & Phase images from a sample annealed at 1600°C for 60 minutes. Tube-like structures are boxed for clarity. The tube-like structures appear to mediate outwards from the graphene film region.

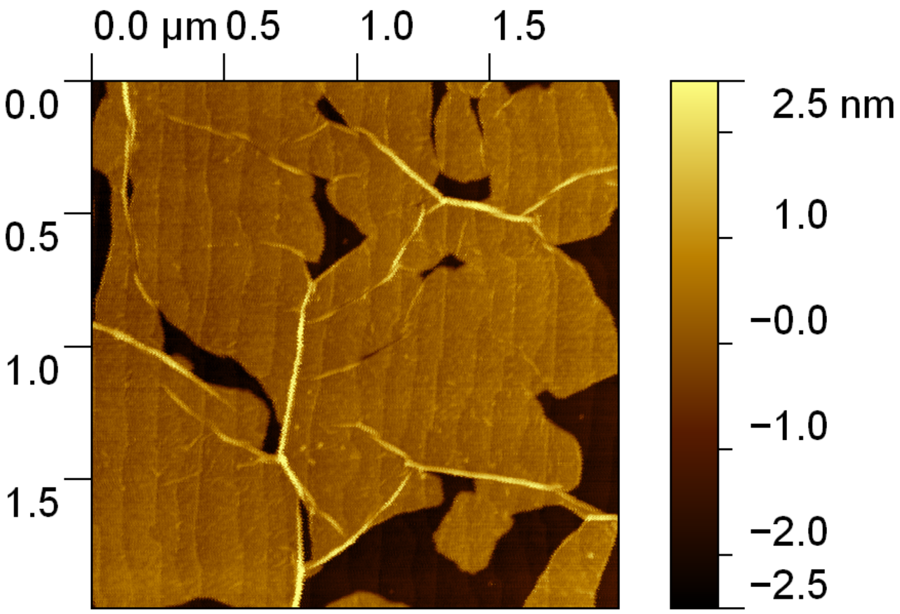

(a)

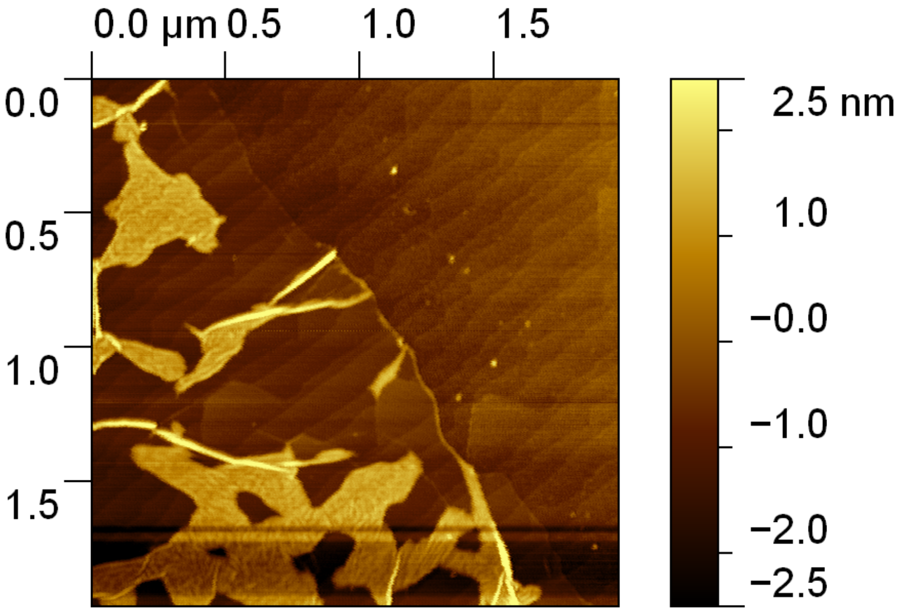

(b)

Figure 7.26: a) and b) Height images from a sample annealed at 1650°C for 60 minutes at differing positions on the sample. Both images used to show the presence of tube-like structures around areas of thicker graphene growth.

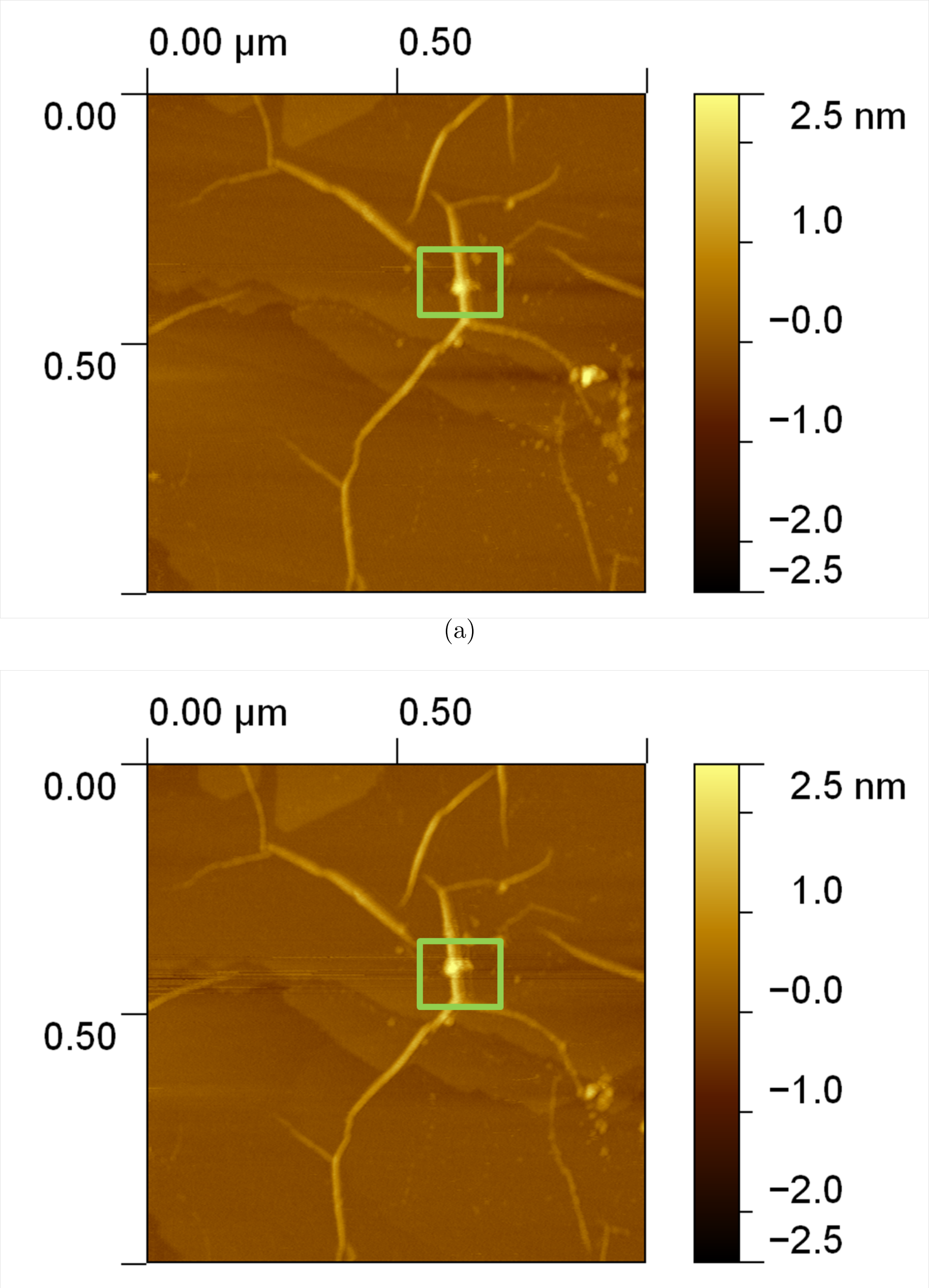

(a)

(b)

Figure 7.27: a) Height image from a sample annealed at 1650°C for 45 minutes before attempting to move boxed feature. b) Height image from a sample annealed at 1650°C for 45 minutes after attempting to move boxed feature. The tube-structure was approached and scanned in tapping mode with a free amplitude of 5.258 V at a setpoint of 0.1 V (very hard tapping) and still could not be moved as observed when re-imaged under standard conditions in b).

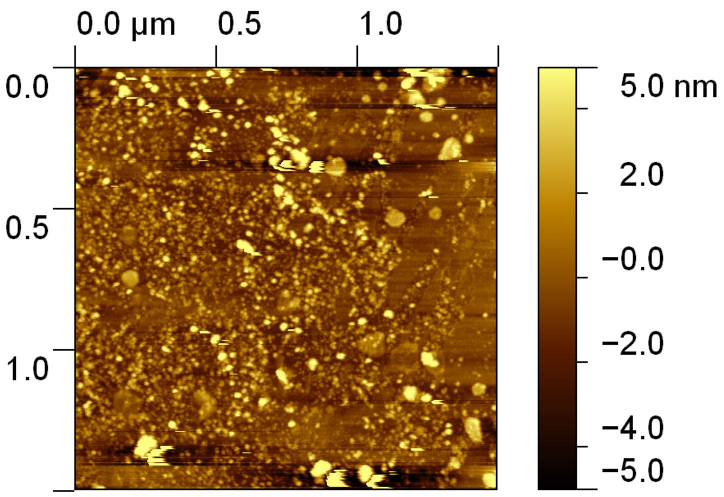

Figure 7.28: AFM height micrograph from a sample annealed at 1650°C for 15 minutes. The presence of debris on the sample surface dominates the micrograph.

been presented. Further evidence to prove this mechanism for graphene growth is required but it does provide an explanation as to why the reconstructions observed in LEED data from these samples appear different those those observed elsewhere for epitaxial graphene on silicon carbide (0001). Atomic resolution STM to show the structure present within the tube-like structures would provide an insight into exactly what these structures are made out of.

#### 7.2.3.4 C-face AFM Imaging

In section 7.2.1.5 Raman microscopy has shown that the carbon face of the samples annealed in the furnace system does not appear to be carbon-rich. This is not unexpected and has been observed elsewhere in the temperature ranges used here that carbon face graphene growth is suppressed at atmospheric pressures. (24; 35) As described earlier, the majority of these samples are grown with the silicon carbide (0001) face flat on the carbon sample holder to provide extra protection to the sample surface.

This leaves the silicon carbide $(000\bar{1})$ face more exposed to contamination, this has been observed in AFM with many samples proving very difficult to AFM.

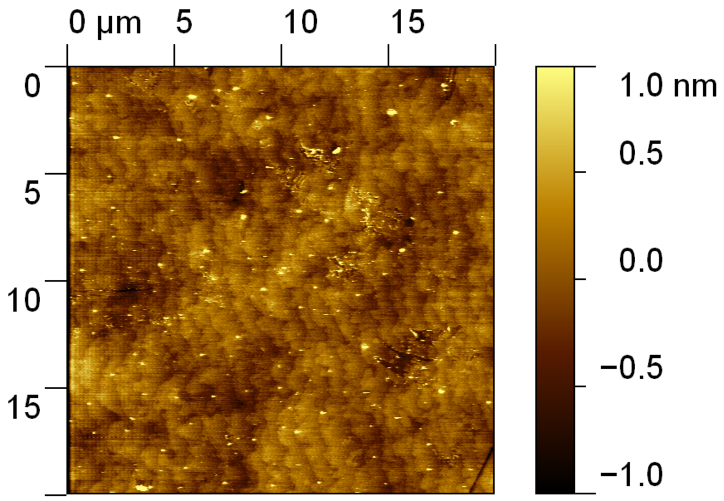

Figure 7.29: AFM height micrograph from a sample annealed at 1600°C for 60 minutes. The presence of atomic terraces on the substrate surface can be seen.

This is surprising as a control sample grown with the (0001) face exposed for 60 minutes at 1650°C showed clear AFM as shown in Figures 7.16, 7.21(a), 7.26(a) and 7.26(b). Figure 7.28 highlights this contamination for samples annealed at a temperature of 1650°C for an annealing time of 15 minutes with the micrograph dominated by the presence of 'debris' on the sample.

Figure 7.29 show a micrograph for a sample annealed at 1600°C for 60 minutes. The sample can be seen to be atomically terraced with these terraces extending over a large area. The terrace widths and step heights are comparable to those observed on the (0001) face as expected due to these properties being intrinsic of the wafer used.(169) Debris is still seen on the sample and it cannot be ruled out that this comes from the wafer itself and worsens with increasing sample temperature to cause the issues observed in Figure 7.28.

To observe the behavior of the $(000\bar{1})$ at 1650°C a run was carried out at this temperature for 60 minutes with the $(000\bar{1})$ touching the graphite sample holder for protection. This experiment was also carried out to try and observed the ribbon-like graphene growth observed elsewhere (86) with the use of a graphite cap touching the $(000\bar{1})$ face during the annealing process. AFM micrographs

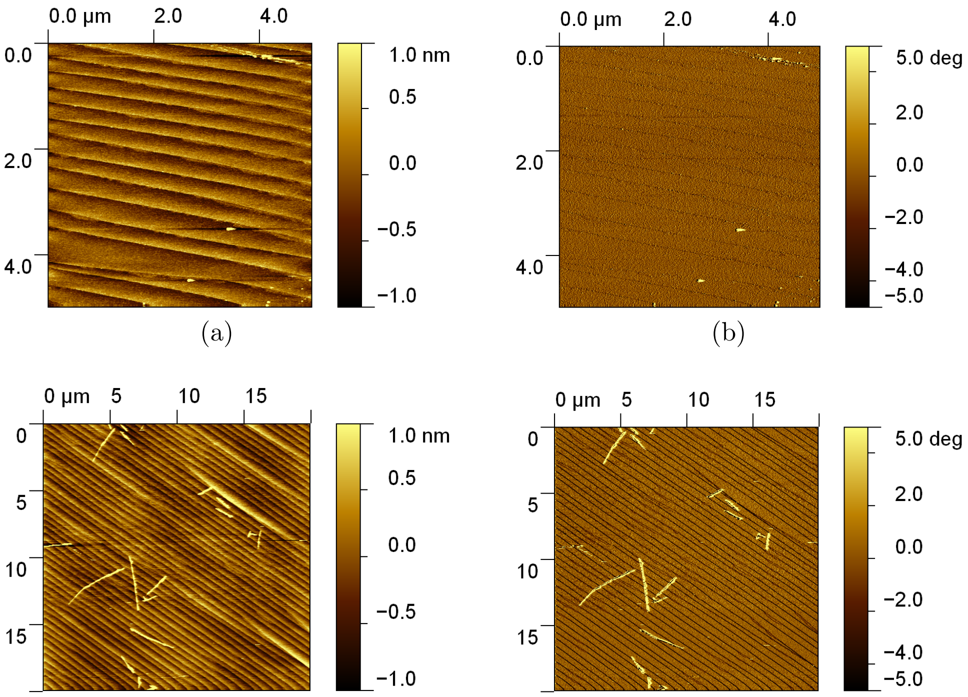

(a) (b) (c) (d)

Figure 7.30: a) and c) AFM height micrographs from a sample annealed at 1650°C for 60 minutes with the $(000\bar{1})$ face towards the graphite sample holder. b) and d) Corresponding AFM phase micrographs from the same scans. Atomic terraces and the presence of tube-like structures can be seen.

obtained from the $(000\bar{1})$ of this run can be observed in Figure 7.30. Raman spectra taken from the $(000\bar{1})$ face of this sample show it to not be carbon-rich as shown in section 7.2.1.5. Figures 7.30(a) and 7.30(b) confirm that this sample exhibits atomic terraces, again with terrace widths and heights consistent with those seen on the (0001) face.

Figures 7.30(c) and 7.30(d) show evidence of some step bunching and also begins to show tube-like structures on the surface. These structures do not appear to be similar to the nano-ribbons seen grow in work elsewhere.(86) They appear to be similar to the tube-like structures observed on the (0001) face. These structures have a step height of ∼2 nm from the substrate surface.

The evidence of these structures suggest that the C-face could be about to undergo graphitisation. There has not been the same evidence observed of these structures branching out from step-edges and defects in the substrate as observed in the previous section for the (0001) face, suggesting that perhaps and extrinsic source of carbon is responsible. Again atomic resolution STM measurements to determine the exact nature of these structures would help indicate their origin.

In general the AFM images obtained from the $(000\bar{1})$ face post annealing at temperatures of 1600°C and above correlate with the Raman spectroscopy data showing that these samples are not carbon-rich. Atomic terraces can be seen in samples annealed at 1600°C and show the same structure as those obtained on the (0001) face. Tube-like structures have been observed to grow on an atomically terraced sample that was annealed at 1650°C for 60 minutes with the $(000\bar{1})$ towards the graphite holder. The difficulty in taking AFM data on the $(000\bar{1})$ face for samples annealed in the general way with the (0001) face towards the graphite holder at temperatures of 1650°C and above have been highlighted. Better cleaning techniques could perhaps improve this and allow for the tracking of the production of these tube-like structures, though Raman spectroscopy shows that actual graphene film growth has not been obtained.

Once more, these results are consistent with observations made elsewhere (24; 35) on the suppression of graphene growth in inert gas atmospheres. To graphitise this face, higher temperatures or lower gas pressures would be required. The higher temperatures are outside the highest possible working temperature with this furnace system and lower pressures could lead to contamination issues without modification to the system.

### 7.2.4 LEEM Data

Due to time restraints and equipment availability only a single sample from the high temperature furnace annealing process has been analyzed with LEEM. This work was carried out at Brookhaven National Laboratory (BNL) by Jurek Sadowski (BNL) and Graham Creeth (University of Leeds). This sample had been annealed at 1600°C for 15 minutes and has showed a carbon-rich Raman spectrum (Figure 7.31) and island-like AFM growth (Figures 7.18(a) and 7.18(b)). The sample also showed graphene diffraction spots in LEED as shown in Figure

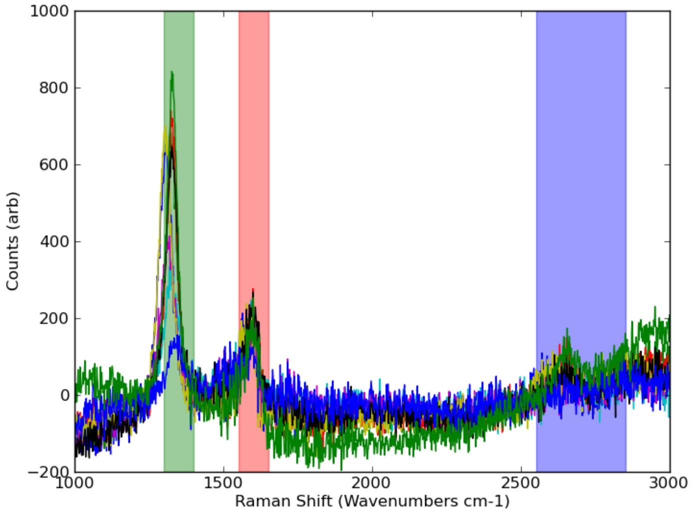

Figure 7.31: Raman spectroscopy (silicon carbide background subtracted) taken from the (0001) face for a sample annealed with (0001) towards graphite holder for 15 minutes at 1650°C. The shaded regions correspond to the main Raman bands associated with graphene D (green), G (red) and 2D (blue). Incident laser wavelength of 633nm. Spectra show the sample to be carbon-rich though the presence of a large D band and broadened G and 2D bands suggest the graphene film is disordered.

7.14 taken in Leeds and Figure 7.32 at Brookhaven during the taking of these LEEM measurements.

In total there where 3 LEEM I-V (Image contrast intensity (I) vs electron excitation voltage (V)) measurements made on this sample as shown in the Figures 7.33, 7.34 and 7.35. The first of these, Figures 7.33(a), 7.34(a) and 7.35(a) show a LEEM images obtained at an energy of 3.9 eV from different areas of this sample. In these images island-like regions, as observed in other microscopy techniques, can be seen. Also there appears to be very bright regions, these are likely to be the highly wrinkled and rippled regions.

LEEM I-V data is also shown for each of these sets of images, with the areas corresponding to the I-V data color coded. As described earlier in section 3.6.3 LEEM I-V data can be used to measure the thickness of graphene films

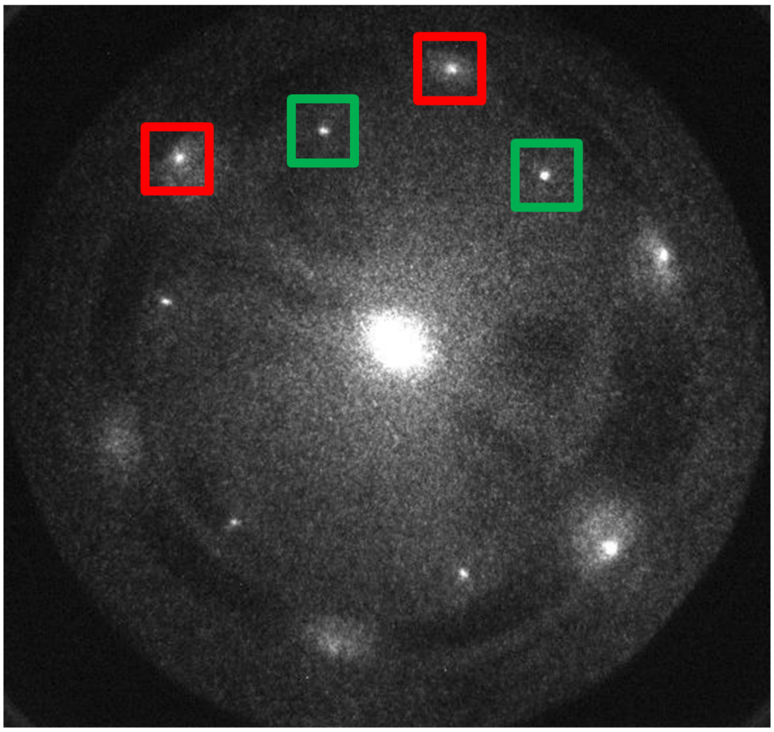

Figure 7.32: LEED diffraction pattern taken from a sample annealed for 15 minutes at 1600°C. Image taken at 31 eV. Green (red) boxes highlight a number of the diffraction spots associated with silicon carbide (graphene). Note the diffuse nature of the graphene spots, this is indicative of surface disorder.

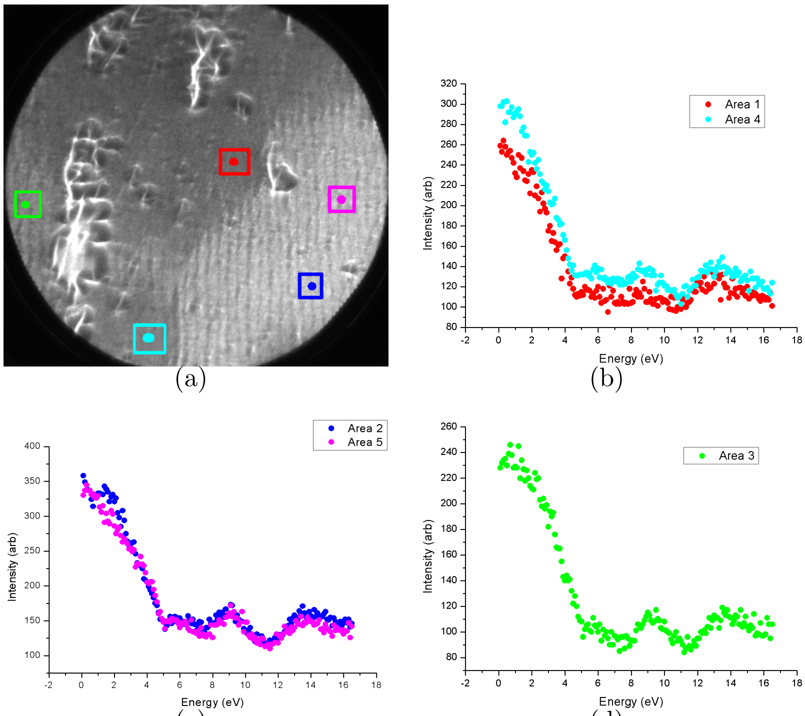

(a)
(b)
(c)
(d)

Figure 7.33: a) LEEM image taken at an energy of 3.9 eV. b),c) and d) Corresponding LEEM I-V data from the coloured regions indicated in a), graphs have been split to marry up areas that have similar I-V behavior. Regions also boxed for clarity in a). Number of minima in I-V data should yield the number of layers present, discrepancies from this will be discussed in the main text.

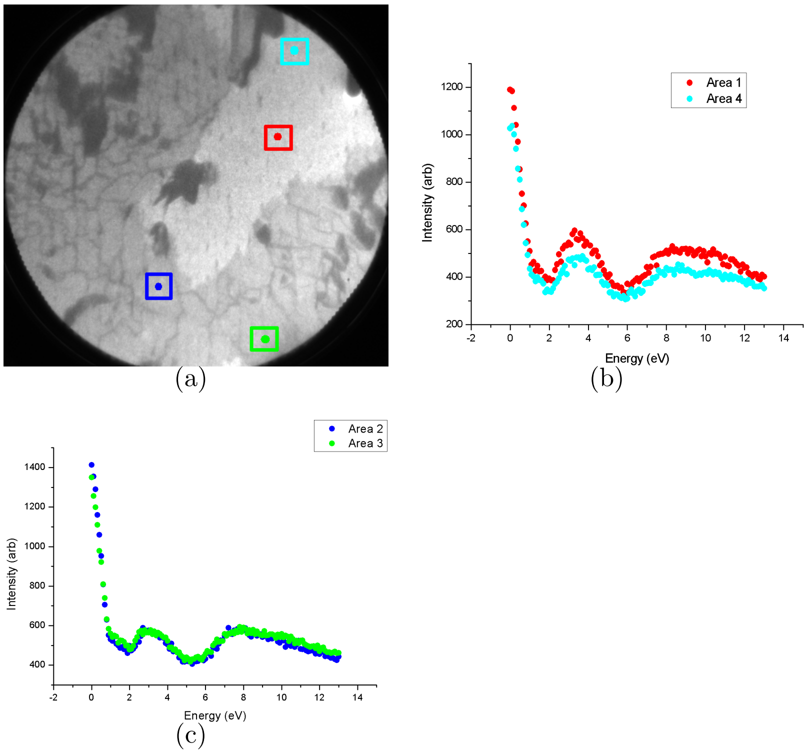

(a) (b) (c)

Figure 7.34: a) LEEM image taken at an energy of 3.9 eV. b) and c) Corresponding LEEM I-V data from the coloured regions indicated in a), graphs have been split to marry up areas that have similar I-V behavior. Regions also boxed for clarity in a). Number of minima in I-V data should yield the number of layers present, discrepancies from this will be discussed in the main text.

by monitoring the number of minima present in the I-V sweeps. This technique was used to measure film thicknesses in samples grown under UHV conditions as discussed in chapter 4 were the thickness measurements corresponded well to other thickness measurement techniques.

The IV data obtained here appears to be a little harder to understand. Seemingly independent of the sample area chosen to image (despite differences in contrast in the still images taken at 3.9 eV) the I-V sweeps obtained in Figures 7.33, 7.34 and 7.35 all appear to show 2 minima in the spectra. The only difference observed is that the spectrum shown in Figure 7.33 are somewhat blurred out till ∼5 eV potentially due to the bright regions caused be wrinkles in this region.

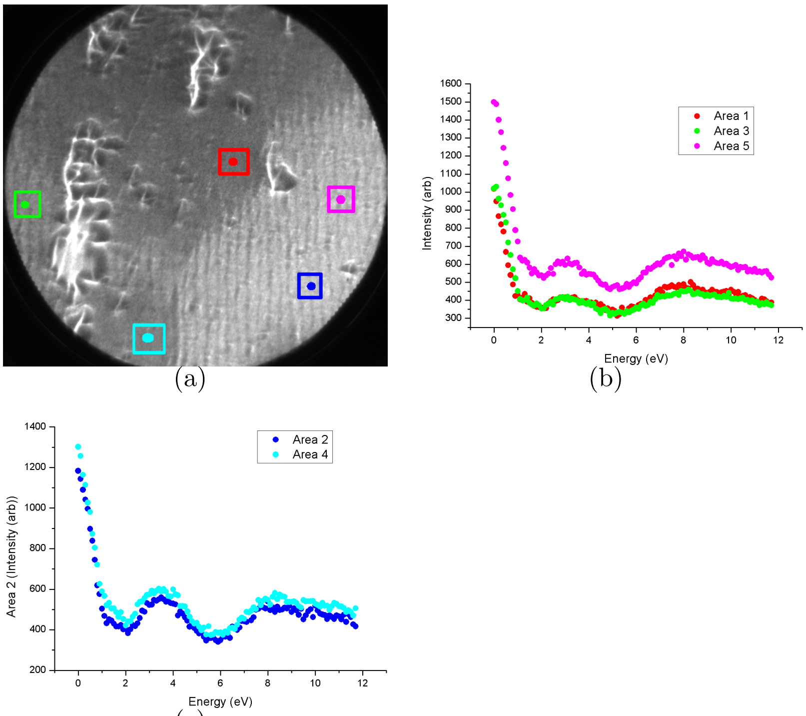

(a) (b)

(c)

Figure 7.35: a) LEEM image taken at an energy of 3.9 eV. b) and c) Corresponding LEEM I-V data from the coloured regions indicated in a), graphs have been split to marry up areas that have similar I-V behavior. Regions also boxed for clarity in a). Number of minima in I-V data should yield the number of layers present, discrepancies from this will be discussed in the main text.

Intercalation of hydrogen gas between the buffer layer and first graphene layer has also been shown to alter the LEEM I-V characteristics within epitaxial graphene films grown on the (0001) face.(173) The change in interface between the graphene layer and silicon carbide substrate alters the quantum interference of electrons between the layers causing a more complicated LEEM I-V behavior with the presence of extra minima present.(173) The intercalation of gas has been ruled out due to the consistent nature of the LEED patterns even when annealed to 1100°C in UHV (see Figure 7.14).

Similar differences in LEEM I-V measurements have been seen elsewhere within graphene films on the $(000\bar{1})$ face (24; 154) and explained by the oxidation of the silicon carbide substrate altering the I-V characteristics, a similar oxidation effect has also been observed on the (0001) face.(176) It is possible that some oxidation of the silicon carbide substrate has occurred during the argon annealing processes and could be causing these observed discrepancies. Again the LEED patterns shown in both Figures 7.14 and 7.32 show no evidence for the presence of an oxide interface between the graphene and silicon carbide substrates.

From the LEEM measurements carried out on this single sample it is hard to interpret the observed behavior and ascertain the reliability of these measurements. It is very unlikely that the whole sample is covered with bilayer graphene as suggested by the number of minima in the I-V spectra as this contradicts with the patchy nature of Raman spectra obtained on similar samples. A LEEM run on a number of samples annealed at different conditions would be required to get a full picture of the processes taking place. Once more, this does provide evidence that the graphene grown under inert argon gas in this way differs from that grown under UHV conditions.

### 7.2.5 Scanning Electron Microscopy (SEM)

Whilst carrying out local transport measurements with a Nanoprobe system (to be discussed in detail in Chapter 8) SEM images of two samples annealed under argon atmosphere were obtained. The two samples consisted of one sample annealed for 30 minutes and one annealed for 120 minutes at 1650°C. Though the main details of the Nanoprobe measurements are not discussed here, the use of the SEM images to highlight the increased uniformity of graphene films with increase annealing time is useful in this section. Island-like growth is observed in the sample annealed for 30 minute whereas the sample annealed for 120 minutes shows higher uniformity and more complete films. Also visible in SEM is the presence of the tube-like structures mentioned earlier and these will also be discussed within this section.

#### 7.2.5.1 SEM of Sample Annealed for 30 minutes at 1650°C

The 3 SEM images shown in Figure 7.36 give a good overview of the graphene film growth observed within this sample annealed for 30 minutes at 1650°C. Figure 7.36(a) is taken in the central region of this sample and highlights the island-like growth observed previously in AFM and suggested in the large D bands observed in Raman spectroscopy. Isolated regions (darker contrast) of graphene can be observed on the silicon carbide substrate with these films appearing folded and wrinkled at the edges.

Figures 7.36(b) and 7.36(c) are taken nearer the edge of the sample. Figure 7.36(b) shows 3 major contrast regions with the 4th very dark regions corresponding to dirt or debris on the sample. The other 3 contrasts suggest the presence of blank silicon carbide, monolayer graphene and bilayer graphene. This is again consistent with observations in AFM images.

This is also the case for the SEM image shown in Figure 7.36(c) again taken at the edge of the sample. In both Figures 7.36(b) and 7.36(c) the bilayer graphene regions at times appear very disordered and wrinkled with large rips present within them on occasions, this is consistent with the Raman spectroscopy observations of large D peaks within these samples.

The sparse nature of the graphene coverage in the central region (Figure 7.36(a)) could be due a decrease in silicon evaporation rate in the central region. The samples are grown with the target (0001) face lying flat on the graphite sample holder, therefore the escape of silicon atoms could occur preferentially at the edges thus causing more graphene growth at the edge regions (Figures 7.36(b) and 7.36(c)).

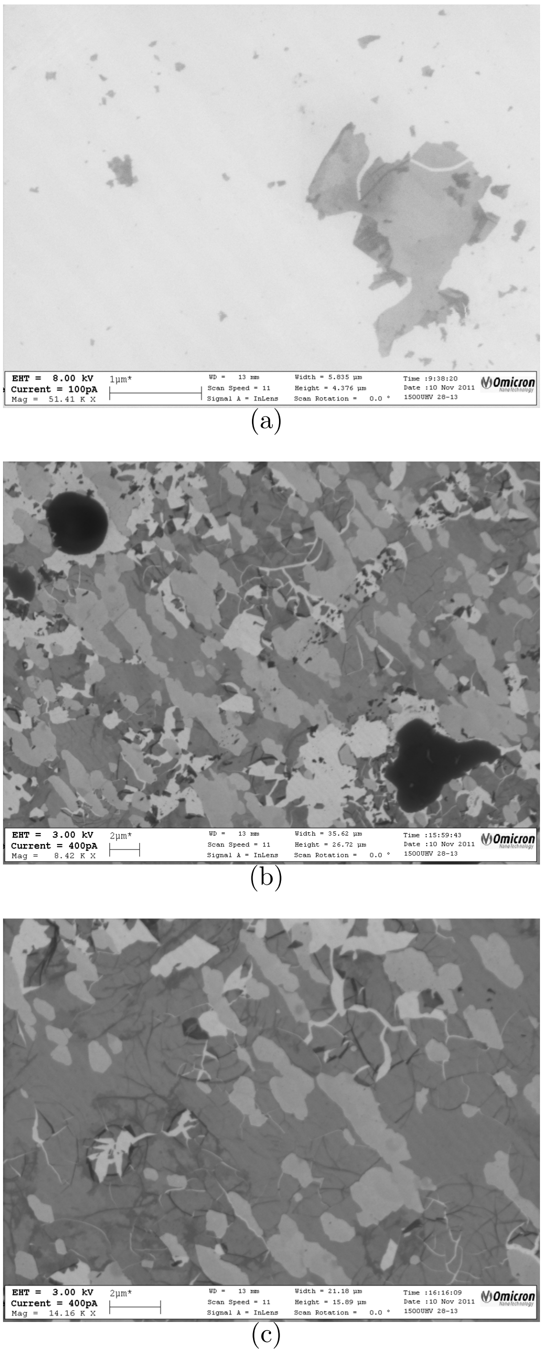

(a)

(b)

(c)

Figure 7.36: SEM images from differing regions of a sample annealed for 30 minutes at 1650°C. a) Image taken in a central region. b) and c) images taken towards the edge of the sample. Imaging conditions and scale bars shown in images. The 3 contrast regions correspond to bare silicon carbide (white), monolayer graphene (light gray) and bilayer graphene (dark gray) regions respectively. Black contrast comes from debris.

#### 7.2.5.2 SEM of Sample Annealed for 120 minutes at 1650°C

Once again the SEM images from this sample have been reduced to 3 images that give the best overview of the graphene growth on the sample surface. These images are given in Figure 7.37. The central region of the sample is shown in Figure 7.37(a), unlike the central region of the sample annealed for 30 minutes (Figure 7.36(a)) there is a good graphene coverage with the majority of the region consisting of monolayer graphene with small regions of bilayer (darker contrast) regions and small rips revealing silicon carbide (lighter contrast) regions. This is consistent with Raman maps and AFM data taken from this region as shown in Figure 7.12. There is also evidence of tube-like filaments (boxed in Figure 7.37(a)) mediating the growth of the thicker graphene regions as discussed previously (Figure 7.26).

SEM images from towards the edge of the sample are shown in Figures 7.37(b) and 7.37(c). The presence of bilayer regions is much more prominent consistent with the mechanism suggested earlier for the increased silicon evaporation rates at the sample edges. Unlike in the sample annealed for 30 minutes (Figures 7.36(b) and 7.36(c)) these bilayers appear much less disordered. The presence of rips and folds within the graphene films can still be observed, with the lighter silicon carbide substrate visible in regions where these rips and folds have occurred. The decrease in the appearance of rips and holes with the increased uniformity in both the bilayer and monolayer regions suggests that the films become resistive to the mechanism causing these defects as the film size increases. This could suggest that compressive strains building up as the films cool(32; 33) are causing the defects, with a strain acting on small islands and at grain boundaries between adjoining having a more noticeable effect than on a large graphene sheet.

#### 7.2.5.3 Evidence of Tube-Like Structures in SEM imaging

During the manipulation of graphene films with the STM tips in order to cut them to form the measurement geometries to be described in greater detail in the following chapter, it became apparent that tube-like filament structures could be observed similar to those previously observed in AFM imaging (see Figures 7.23 to 7.27). These structures are seen to regularly stay in position despite the

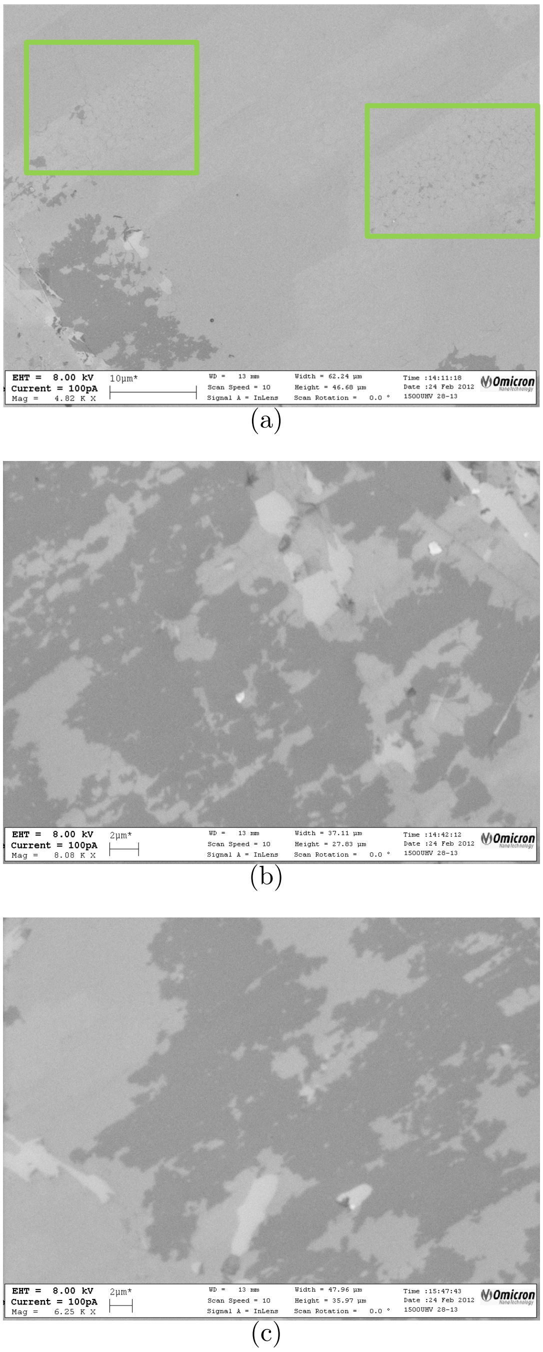

(a)

(b)

(c)

Figure 7.37: SEM images from differing regions of a sample annealed for 120 minutes at 1650°C. a) Image taken in a central region. Boxed regions highlight the presence of tube-like structures. b) and c) images taken towards the edge of the sample. Imaging conditions and scale bars shown in images.The 3 contrast regions correspond to bare silicon carbide (white), monolayer graphene (light gray) and bilayer graphene (dark gray) regions respectively. Black contrast comes from debris.

successful cutting of the surrounding graphene sheets as shown in the highlighted regions within Figure 7.38.

This lack of movement shows the structures to be separate from the graphene films and show them not to be wrinkles within the films. This rigidity and resistance to the cutting procedure corresponds well to the resistance of these structures to a manipulation procedure carried out during AFM imaging as shown in Figure 7.27. Again suggesting that the structures are well bound to the underlying substrate.

## 7.3 Conclusions and Discussions

Here work has been presented to shows the formation of atomically stepped silicon carbide substrates and their subsequent graphitisation within a single annealing process carried out under an inert argon gas atmosphere. The preparation of atomically stepped terraces via annealing under argon atmospheres provides a safer alternative to the regularly used high temperature hydrogen annealing processes.(29) The subsequent single-stage graphitisation of these atomically stepped substrates provides convenience over substrate preparation techniques such as chemical etching.(27)

The analysis of the surface reconstructions taking place after sample graphitisation via LEED data taken from a single sample which shows no evidence of the $(6\sqrt{3} \times 6\sqrt{3})$R30 buffer-layer expected for graphene grown on silicon carbide (0001).(17; 18; 19; 21; 78; 146) This suggests that graphene layer is decoupled from the underlying silicon carbide substrate. Blurred graphene spots in the LEED data are indicative of disorder present within the graphene film, this disorder has also been observed in other microscopy techniques. In order to gain better understanding of this silicon carbide/graphene interface we could carry out LEED measurements on a range of samples graphitised at differing annealing times and temperatures. This was not possible in this work due time restraints and equipment availability.

The observation of a large D band signal in Raman spectroscopy (when using a ~5 $\mu$m laser spot) is indicative to the presence of disorder within the graphene films. The D band is regularly associated with the presence of 'edge' regions

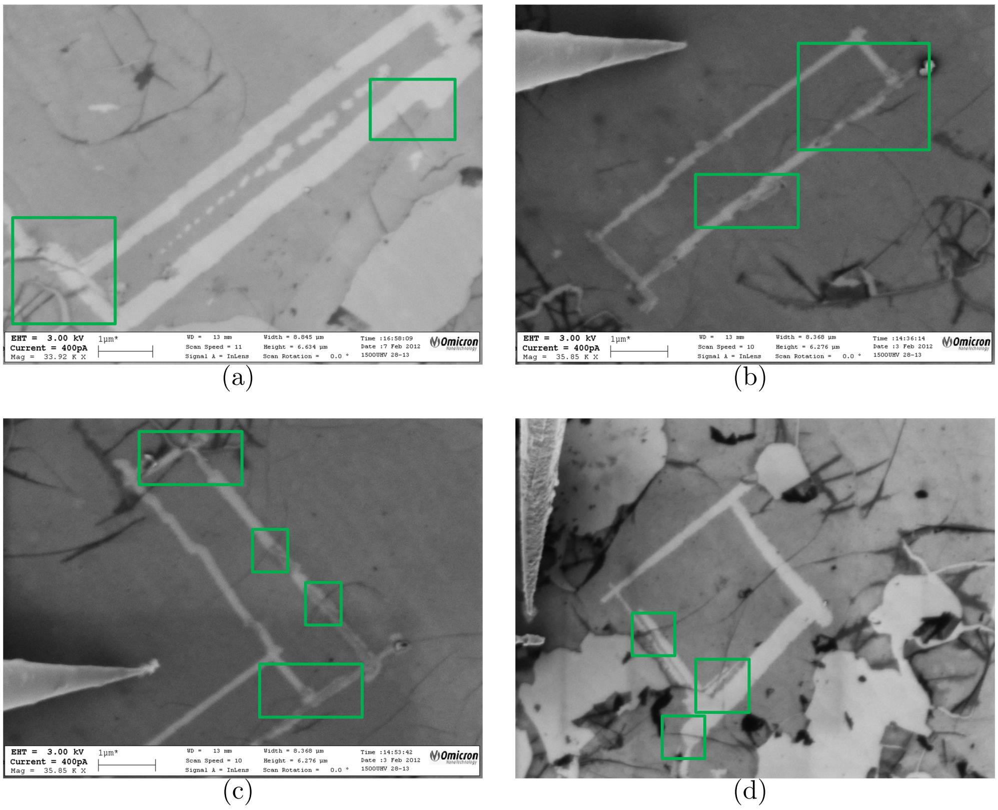

(a) (b) (c) (d)

Figure 7.38: a)- d) SEM images from differing regions of a sample annealed for 30 minutes at 1650°C where the STM tips have been used to cut the graphene films into ‘bar’ and ‘square’ structures. Boxed regions highlight areas where tube-like structures remain intact despite the cutting of the graphene films. The STM tips used to carry out the film cutting are still visible in images b), c) and d). Image a) was taken after nanoprobe electrical measurements were made and evidence of this can be seen with damage to the graphene film in the ‘bar’ region. Imaging conditions and scale bars shown in images.

within graphene films.(63; 134; 135; 139; 145; 156) Here that can correspond to either areas around rips within the graphene films or the edges of the graphene islands formed during this process. This island-like growth has been observed with AFM, LEEM and SEM imaging. Raman mapping (using ~1 $\mu$m spot size) within a complete graphene film free of defects (shown by AFM imaging) showed the D band to be of very low intensity in this area. Further Raman mapping with complementary AFM imaging would lead to further understanding of the cause of the large D band present when surface averaging Raman is taken.

AFM images of the graphene films suggest that an increase in annealing time leads to the graphene films becoming more complete. This is highlighted in samples annealed at 1650°C for 120 minutes which shows areas 10s $\mu$m across of unbroken graphene growth in AFM imaging (SEM suggests areas 100s $\mu$m across). Samples annealed at 1650°C do exhibit areas of thicker graphene growth which is not observed in samples annealed at 1600°C. For lower annealing times, these thicker graphene regions have been observed to be disordered and contain many rips, folds and wrinkles. Again as the annealing time is increased these thicker graphene regions increase in uniformity.

AFM images also showed the existence of tube-like structures within samples. Though the exact nature of these structures is unknown, there is evidence that these structures spring out from holes within the silicon carbide substrate and even mediate the growth of graphene layers and surface reconstructions within the samples. Attempts to manipulate these tube-like structures with AFM 'nano-ironing' were unsuccessful suggesting they are tightly bound to the silicon carbide substrate. SEM imaging has shown these structures to exist underneath graphene films and remain intact even when the over lying graphene film has been cut and destroyed using nanoprobe STM tips.

Splitting of the Raman G band has been observed, with the causes of this splitting somewhat unknown. The Raman shifts observed during the splitting suggests phonon hardening processes are causing the splitting which rules out curvature present within the graphene films being the cause of the splitting. Both confinement and strain can cause phonon hardening in graphitic films though the magnitude of the splitting observed here is larger than observed for those two processes. This observation has lead to the hypothesis that there could well be an interaction present between either the graphene film and the substrate or within the observed tube-like structures that cause this phonon-hardening process.

The splitting appears more frequent in the samples annealed at 1650°C and above. It is possible that the splitting is due the presence of tube-like structures (which occur with increased frequency under these annealing conditions) and the bonding between those structures and the substrate. Further measurements are required to probe this hypothesis further. One such experiment that we could carry out would be to attempt atomic resolution STM measurements on the tube-like structures. These measurements could be used to show the structure present and lattice spacings measured to show the presence of phonon hardening effects.

A further measurement we could carry out to further increase our understanding of the cause of the G band splitting requires improvements to the current Raman mapping experiments to allow for consistent subtraction of a silicon carbide background. If a consistent subtraction could be achieved then the properties of the split G band could be fitted within Raman maps and compared to AFM data from the same sample area to ascertain structural causes for the observed splitting. Also the variation of properties such as split peak separation and intensities within an area of sample can be observed to observe how consistent these values are and how they correspond to structural features of the sample.

There has been no evidence of graphene growth on the $(000\bar{1})$ face during these annealing procedures. This has been shown from the absence of a carbon-rich signal in Raman spectra taken on these surface. AFM micrographs show atomic terraces do form on this face and despite the presence of sparsely arranged tube-like structures on the surfaces, there is no evidence for the presence of graphene films. This result is not surprising and is in line with results observed elsewhere for the onset temperature of graphene growth on this face which is increased due to the formation of an oxide layer during the annealing process. (24; 35)

In conclusion, this chapter and chapter 6 have shown the successful production of atomically terraced silicon carbide substrates via the use of an argon annealing process. These atomically terraced substrates have been prepared and subsequently graphitised through a single-stage annealing process under argon gas, this is an original result.

Though initial growth procedures lead to the production of disordered island-like regions of graphene, improvements have lead to the production of more complete graphene films and the observation of large scale areas (100s $\mu$m via SEM imaging) of single graphene domains. This is comparable to work shown elsewhere for the production of graphene films post hydrogen etching under argon atmospheric growth (26) and for growth carried out within confined geometries post hydrogen etch treatment.(34) The domain sizes obtained via this annealing technique show a great improvement on the 100s nm obtained from annealing in UHV as described in Chapter 4 and show a move towards large scale single domain graphene production.

Though more understanding into the graphene formation mechanism and graphene-substrate interaction is required, this result of single-stage annealing to both prepare and graphitise substrates is promising for the integration of epitaxial graphene growth into industrial scale production.

# Chapter 8

# Nanoprobe: Local Transport Measurements on Argon Grown Epitaxial Graphene

Following the observation of the island-like graphene growth obtained via argon atmosphere annealing from techniques such as AFM and Raman mapping it was decided that an Omicron Nanoprobe should be used to locally approach and contact these islands for the purposes of taking transport measurements. This work has been carried out in collaboration with Alex Walton at the University of Leeds who has demonstrated the effectiveness of the Nanoprobe at taking these kinds of local transport measurements on small scale systems.(178) During the experiments, Alex operated the Nanoprobe system whilst guided by myself as to which sample regions to approach and contact, all data analysis was conducted by myself. As described earlier (section 3.7), the Nanoprobe consists of an SEM imaging system and 4 STM tips that can be individually manipulated. The SEM imaging capabilities of the system have been show earlier (section 7.2.5), once a suitable sample area for probing is identified, the STM tips can be moved into position. The sample can then be contacted by the 4 STM tips, allowing for 4-probe electrical transport measurements to be carried out.

As well as the ability to contact the graphene films, the STM tips and their maneuverability also allows us to manipulate the graphene films themselves. This allows the cutting of films into specific measurement geometries on the $\mu$m scale to aid the understanding and quantifiability of the electronic transport measurements made. The aim of the work with the Nanoprobe was to make measurements of the sheet resistances of the graphene-islands and to also see if anisotropies in resistance measured parallel and perpendicular to the atomic step edges present within the silicon carbide substrate could be observed. Work elsewhere suggests that there is an anisotropy present that exists at the step edges.(36; 37; 38)

There are a number of differing explanations for this anisotropy, Yakes et al suggest the anisotropy is due to the presence of silicon atoms at the step edge that leads to increased scatter events leading to a resistance contribution of 42 $\Omega$ per step.(37) Perhaps the most comprehensive model shows the anisotropy to be due to abrupt variations in doping levels that occur at step edges,(38) which was shown to fit well with experimental data.(36) This work leads to a resistance contribution of $\sim$15 $\Omega$ per 1 nm of step height.(38) Each model predicts an increase in scattering events at step edges. This results in the resistances measured when the current path flows over a large number of terraces (perpendicular direction) being greater than when the current path flows in a along the terraces (parallel direction).

The following section will discuss results obtained from the local contacting of graphene-islands from samples grown under argon atmosphere as discussed within chapter 7. The reasoning behind the specific measurement geometries used and the effects of these geometries on the transport measurements will be addressed along with any limitations within the techniques used. The measurement of anisotropies within the films, or absence of, will also be discussed along with future plans for extending this technique further in the measurement of graphene transport properties.

## 8.1 Local Transport Measurements: Preliminary Measurements

During the initial stages of taking measurements with the Nanoprobe system a region which appeared to be blank silicon carbide was approached and contacted in a square 4-probe geometry as described in section 3.7.3.1 and used

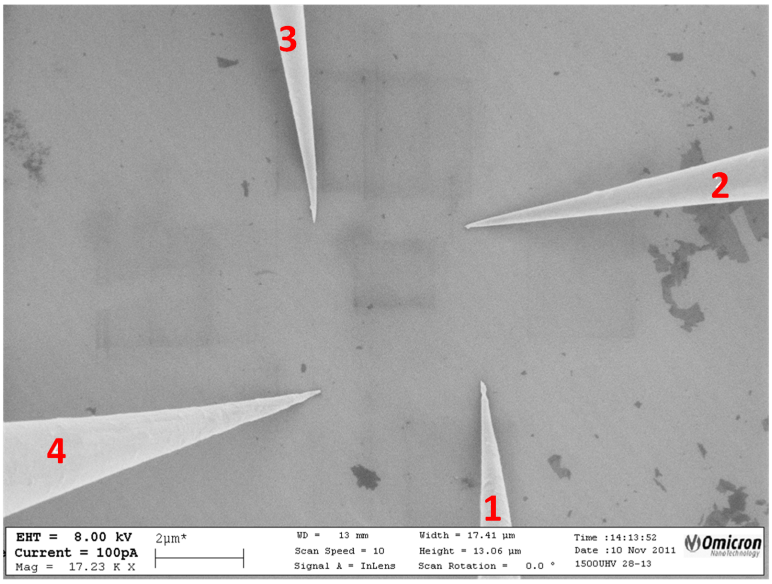

Figure 8.1: SEM image from the Nanoprobe system showing an area of blank silicon carbide contacted from the sample annealed for 30 minutes at 1650°C. The tip numbers are labeled.

elsewhere.(37; 179; 180) The contact geometry used is shown in Figure 8.1 with the current flowing through tips 1 and 2 and the voltage being sensed through tips 3 and 4, this gave extremely non-linear IV characteristics as shown in Figure 8.2(a). This data can be trimmed and a straight line fitted to obtain a resistance of 1.1±0.1 GΩ as shown in Figure 8.2(b) which is within the range of the resistances this system can measure accurately as the Keithley 6154 electrometer has femtoamp sensitivity.

This is a very high resistance value and shows the silicon carbide substrate to essentially be an insulator as expected from the specifications given by the manufacturer Cree that states the resistivity for this type of wafer to be ≥0.1 MΩ.cm. The measured 1.1±0.1 GΩ resistance above is difficult to convert into a resistivity as the exact current flow paths are unknown as is the thickness of the silicon carbide wafer that the current flows through. The important result is that the silicon carbide wafer is insulating in nature of the substrate.

During the preliminary measurements, a small graphene island was approached

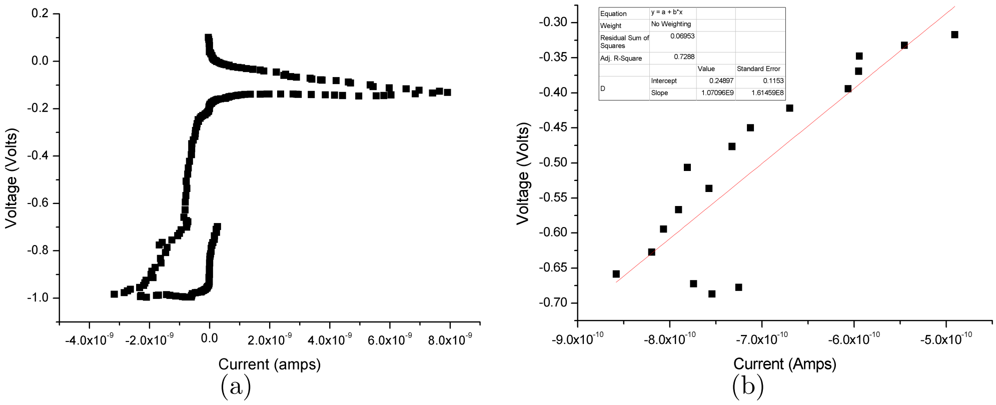

| | | | |
|---|---|---|---|
| Equation | y = a + b*x | | |
| Weight | No Weighting | | |
| Residual Sum of Squares | 0.06953 | | |
| Adj. R-Square | 0.7288 | | |
| | | Value | Standard Error |
| D | Intercept | 0.24897 | 0.1153 |
| | Slope | 1.07096E9 | 1.61459E8 |

(a) (b)

Figure 8.2: IV graphs taken from an area of blank silicon carbide contacted from the sample annealed for 30 minutes at 1650°C. a) Full IV trace showing non-linear behavior. b) Trimmed data from a) showing a linear region, a linear fit to this region leads to a resistance of 1.1±0.1 GΩ.

with a similar 4-probe measurement geometry used for the blank silicon carbide region as shown in Figure 8.3. This geometry is shown in Figure 8.3 with the 2 IV graphs shown in Figure 8.4 obtained by switching the current and voltage probes around the square as described in section 3.7.3.1 to the positions labeled in Figure 8.4.

The average resistance from the graphene island region was measured to be 17±2 kΩ, which is many orders of magnitude lower than the resistance of the underlying silicon carbide substrate, thus justifying the assumption that the current flows through the graphene sheet only. It is also important to note the difference in resistance values measured with switching the current and voltage probes through 90°. This suggests a possible anisotropy in resistance within the graphene films, a phenomenon that has been ascribed to the presence of underlying atomic steps in the silicon carbide wafer elsewhere. (36; 37; 38)

During these preliminary measurements there was no attempt made to align the contacts to the angle of the substrate steps and the measurement geometry used makes it somewhat difficult to obtain actual sheet resistance values. The rest of this chapter will concentrate on trying to probe this anisotropy with experiments designed to use the Nanoprobe to cut and manipulate the graphene films

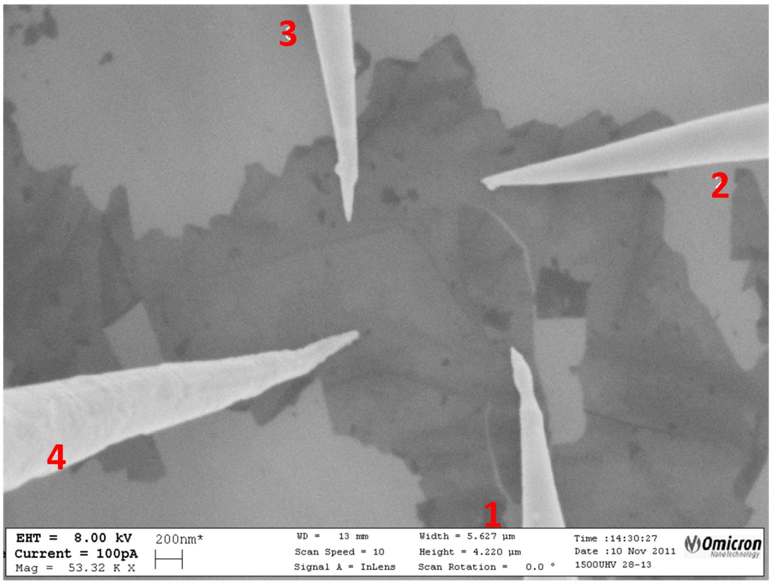

Figure 8.3: SEM image from the Nanoprobe system showing a graphene island contacted from the sample annealed for 30 minutes at 1650°C. The tip numbers are labeled.

in order to align simple geometric structures both parallel and perpendicular to these steps to reveal the nature of this anisotropy.

## 8.2 Local Transport Measurements: Investigation of Anisotropy Within Graphene Films

### 8.2.1 Measurement Geometry

The island-like growth of graphene observed within samples annealed under argon atmospheres in this work limits the measurement geometries that can be used when probing the graphene films. In work carried out elsewhere, probing techniques have been used to measure the electronic properties of large scale graphene films. (36; 37) The rotational four-probe measurement technique used by Yakes et al (37) was deemed unsuitable for measurements here. As placing the STM tips causes damage to the graphene film, with the small graphitic islands observed on

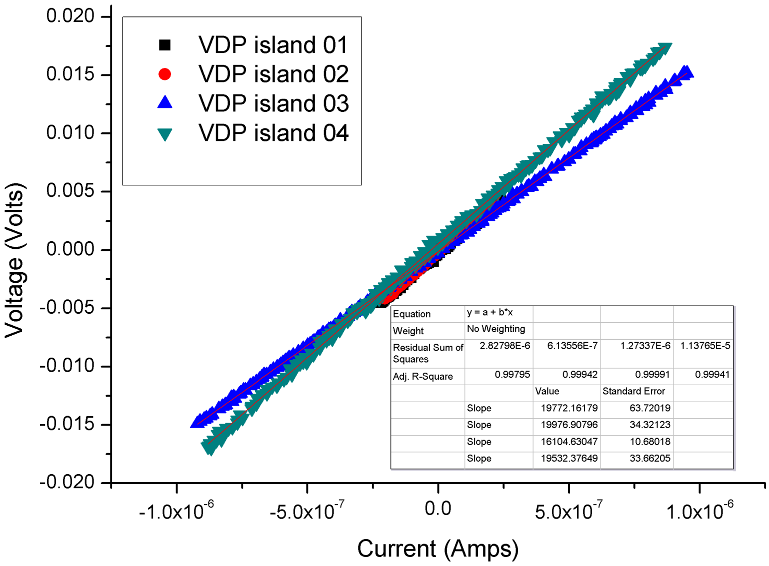

| | | | | |
|---|---|---|---|---|
| Equation | y = a + b*x | | | |
| Weight | No Weighting | | | |
| Residual Sum of Squares | 2.82798E-6 | 6.13556E-7 | 1.27337E-6 | 1.13765E-5 |
| Adj. R-Square | 0.99795 | 0.99942 | 0.99991 | 0.99941 |
| | | Value | Standard Error | |
| | Slope | 19772.16179 | 63.72019 | |
| | Slope | 19976.90796 | 34.32123 | |
| | Slope | 16104.63047 | 10.68018 | |
| | Slope | 19532.37649 | 33.66205 | |

Figure 8.4: IV graphs taken from a graphene island contacted from the sample annealed for 30 minutes at 1650°C. The IV curves shown are from varying the current and voltage directions around the square 4-probe geometry. The source and measuring tip configurations are labeled on the graphs. Linear fits to the data are shown and the gradients lead to an average resistance of 17±2 kΩ.

the sample annealed for 30 minutes, very few rotations could be performed before the graphene film was completely destroyed. The 3-probe measurement technique used by Ji et al (36) requires a high resolution imaging capability on the voltage probe and a large separation between the current probes. This resolution in the voltage probe separation is not possible in this system and once more island sizes limit the current probe separations that can be used.

To counteract the problems obtained from the irregular shaped island-like graphene film growth, one of the STM tips was used to define areas within the islands for measurements via a cutting technique. The structure deemed most appropriate for these measurements was that of a bar structure. Within the bar structure, if the current probes are sufficiently far apart and the bar is long and thin then the current path directions in the central bar region will be uniform and the measured voltage will not depend on where along the bars width it is measured. This kind of structure allows for a simple calculation of the sheet resistance to be made, as described later in this section.

The bars were cut in pairs with one running parallel to the substrate steps and the other running perpendicular. The typical width of a bar is $\sim$1 $\mu$m which is roughly equal to the width of the atomic steps observed for these samples via AFM as shown in sections 6.2 and 7.2.3. The bars are aligned to the substrate steps by taking a high contrast SEM image in which the substrate steps are visible. The steps are at a consistent angle across the wafer so once measured, the substrate step angle appears not to vary. The Nanoprobe measurements carried out were taken on two samples, each of these samples were mounted at differing angles into the Nanoprobe and therefore required two measurements of the terrace angle.

Figure 8.5 shows the terrace angles for both the samples annealed at 1650°C for 30 minutes (Figure 8.5(a)) and 120 minutes (Figure 8.5(b)). There is roughly a 90° difference in the terrace angle between the 2 samples, owing to the fact that the samples were mounted at differing angles. As mentioned earlier, once measured these angles can be used to align measurements to the terraces across the whole sample.

Once the alignment has been carried out, geometries for measurements can now be defined in the graphene films via the use of a cutting technique using one of the STM tips. Figure 8.6 shows a bar structure cut from a graphene film by

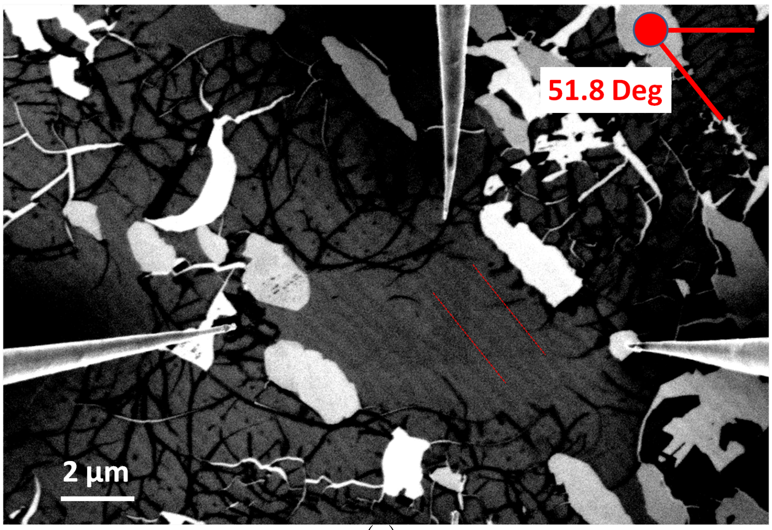

(a)

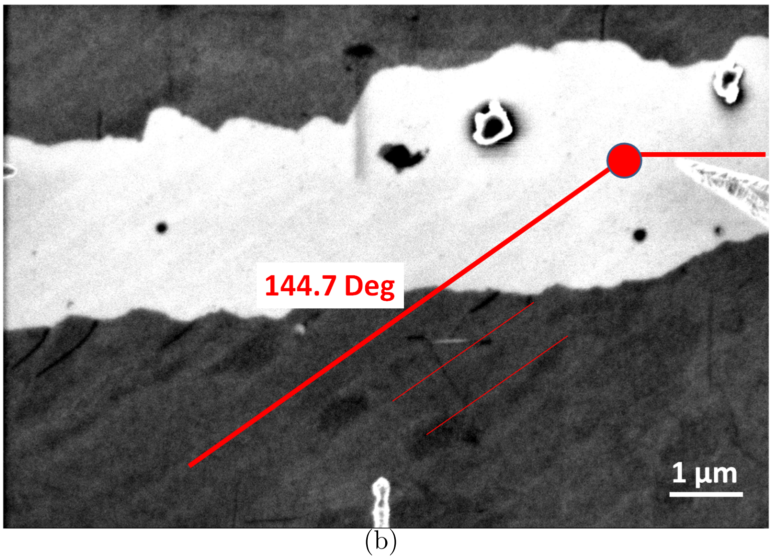

(b)

Figure 8.5: SEM images from the Nanoprobe system showing terrace angles. a) Sample annealed for 30 minutes at 1650°C. b) Sample annealed for 120 minutes at 1650°C. The contrast in each image has been varied to make the step edges clearer the light areas correspond to bare silicon carbide and the dark regions are graphene. Also visible in the images are STM tips. Thin red lines indicate terrace direction in a) are spaced 2 terraces apart, in b) are placed on adjacent terraces. Scale bars are indicated in each image.

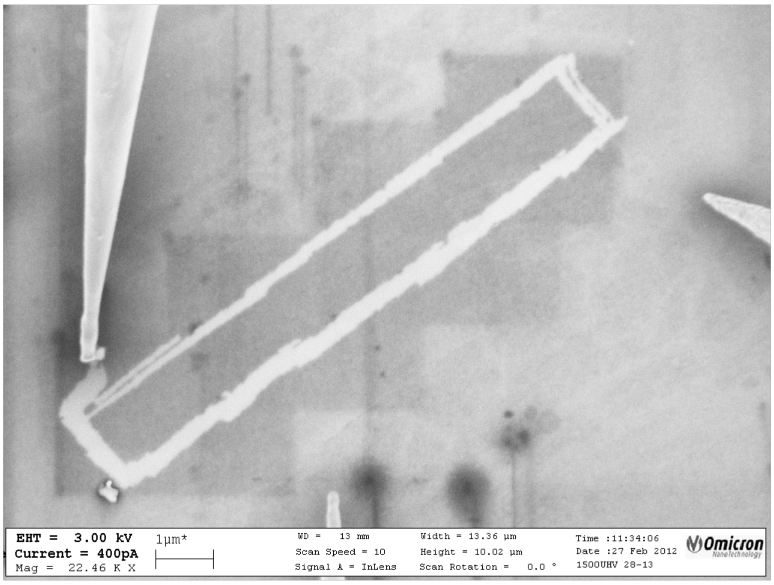

Figure 8.6: SEM image from the Nanoprobe system showing a cut bar from the sample annealed for 120 minutes at 1650°C. The STM tips are still visible in this image.

one of the STM tips. This bar is running parallel to the atomic terrace steps on the sample annealed for 120 minutes. Once cut, these bar patterns can then be contacted by the 4 STM tips and 4-probe electrical measurements carried out.

Schematic diagrams of the measurement setups used within these cut bar structures are given in Figure 8.7. In both of these schematics a current flows between the tips numbered 1 and 3 placed near the edge of the bar structure driven by a Keithley 2400 sourcemeter with this current measured by a Keithly 6514 electrometer in series and set to sense current. The voltage drop is measured across the tips numbered 2 and 4 using a Keithley 6514 electrometers set to sense voltage as discussed in greater detail in section 3.7.2. Within the bar structures the voltage probe separation ($L$) is varied. This was done in either one of two ways. The first is shown in Figure 8.7(a) whereby one of the voltage probe tips (here tip 4) remains stationary whilst the second voltage probe tip (here tip 2) is moved towards it. This was the final kind of measurement system used and was seen as beneficial to the method highlighted in Figure 8.7(b) where both the

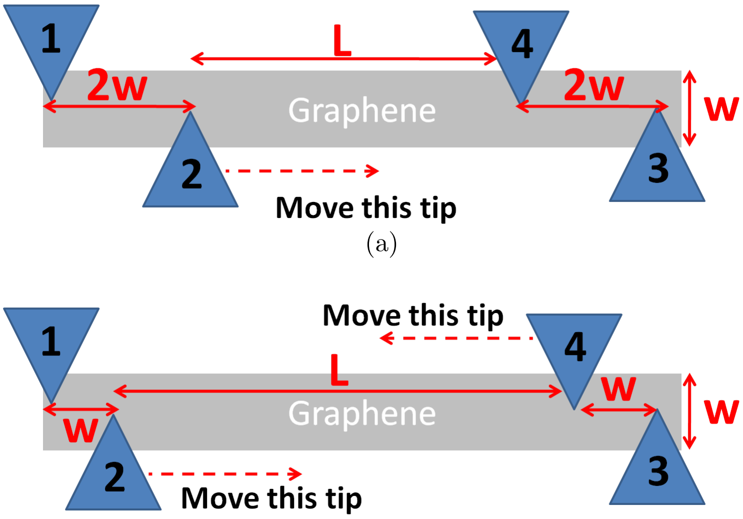

(a)

(b)

Figure 8.7: Schematic images of the Nanoprobe system showing measurement configurations. a) One voltage probed moved towards the other. b) Each voltage probe moved towards each other. Current flows between tips 1 and 3, the voltage drop is measured between probes 2 and 4.

voltage probe tips are moved towards each other to the central region.

The measurements taken with the measurement arrangement highlighted in Figure 8.7(a) also take greater care in ensuring that the first measurements take place with the distance between each of the voltage probes and its nearest current source (or drain) being at least twice the width ($W$) of the bar device, this is to try and ensure that the current paths are uniform in the measurements taken. This was not the case in earlier measurements taken with the arrangement shown in Figure 8.7(b) where this separation is only typically equal to the width of the bar.

A schematic of the lines of current flow within a bar structure is shown in Figure 8.8, ideally the voltage probes should always be placed in the 'linear' region, the size of this region will depend on the aspect ratio ($L/W$) of the bar structures. If the voltage probes are placed too close to the source/drain electrodes then the resistance value measured ($R$) cannot be simply converted to

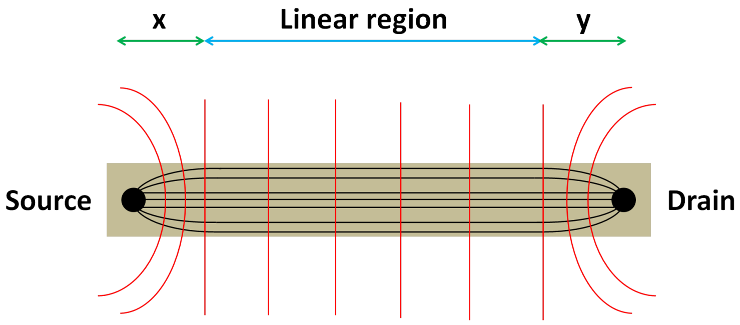

Figure 8.8: A schematic drawing to highlight the presence of a region within the bar structure where the lines of current flow (solid black) are uniform and parallel to the bar structure thus leading to uniform equipotential lines (solid red). This region is labeled as the 'linear' region with the separation of this region and the source electrode labeled x and the drain electrode y.

a sheet resistance ($R_s$) via,

$$R = R_s \frac{L}{W} \tag{8.1}$$

and attempts to plot $R$ against $L/W$ and extract a sheet resistance from a linear fit to this data will show points at high $L/W$ that deviate away from this straight line fit as the voltage probes are now positioned outside the 'linear region' and these points should be discounted.

The ability to cut and manipulate the graphene films with the STM tips has been shown to be beneficial in the ability to define specific measurement geometries within the graphene films. However potential issues arise from the damage caused upon lifting the STM tips after contacting the films to make transport measurements, this damage can be seen in the SEM images shown in Figures 8.9, 8.13(b) and 8.16 that have been taken after measurements have been carried out. All measurements are carried out with the voltage probe separation starting at high $L$ and being reduced, this could result in the ripped regions caused by taking measurements causing disruption to the current flow paths and distorting the observed values. The linear IV characteristics observed at all separations as shown in Figure 8.10 suggest that this is not the case, as does the linear variation of the measured resistance with increasing $L/W$ at lower voltage probe separations. The 'long and thin' nature of the measurement geometry and the 'linear region' it creates also counteracts the discrepancies that not having equally spaced measurement probes (181) would have on the sheet resistance measurements.

### 8.2.2 Bar Structures Measured Within a Sample Annealed for 120 Minutes at 1650°C

As described earlier, measurements of elctrical conduction anisotropies present within epitaxial graphene samples grown on atomically terraced silicon carbide wafers have been made, demonstrating that there is a scattering contribution at the step edges leading to increased resistance in currents passing perpendicular to the terrace direction compared to parallel.(36; 37) In an attempt to measure the same anisotropy in the graphene films grown here 4 probe measurements were carried out on isolated bar structures as shown in Figures 8.6 and 8.7 and discussed in the previous section.

The most comprehensive measurement of anisotropy was carried out on a double bar setup shown in Figure 8.9 cut from the sample annealed for 120 minutes. The measurement setup shown in Figure 8.7(a) was used to vary the position of one of the voltage probes and thus change the separation between the probes. The IV characteristics from one of the 4 bars for all the voltage probe separations measured is shown in Figure 8.10. As can be seen, all the IV graphs are linear and straight line fits to these results leads to a measured resistance value ($R$) being obtained for each probe separation. (same in other 3 bar structures, just not shown)

This measured resistance value ($R$) is linked to the actual sheet resistance ($R_\mathrm{s}$) via equation 8.1 where once more $L$ is the probe separation and $W$ is the average width of the bar structure being probed. It therefore follows that a plot of $L/W$ against $R$ will lead to a straight line graph which will have a gradient equal to the sheet resistance ($R_\mathrm{s}$). The measured resistance at each point is taken as the statistical average of the resistance values measured whilst forward biasing and reverse biasing with an error value extracted from the difference between the resistance measurements with reversed polarity.

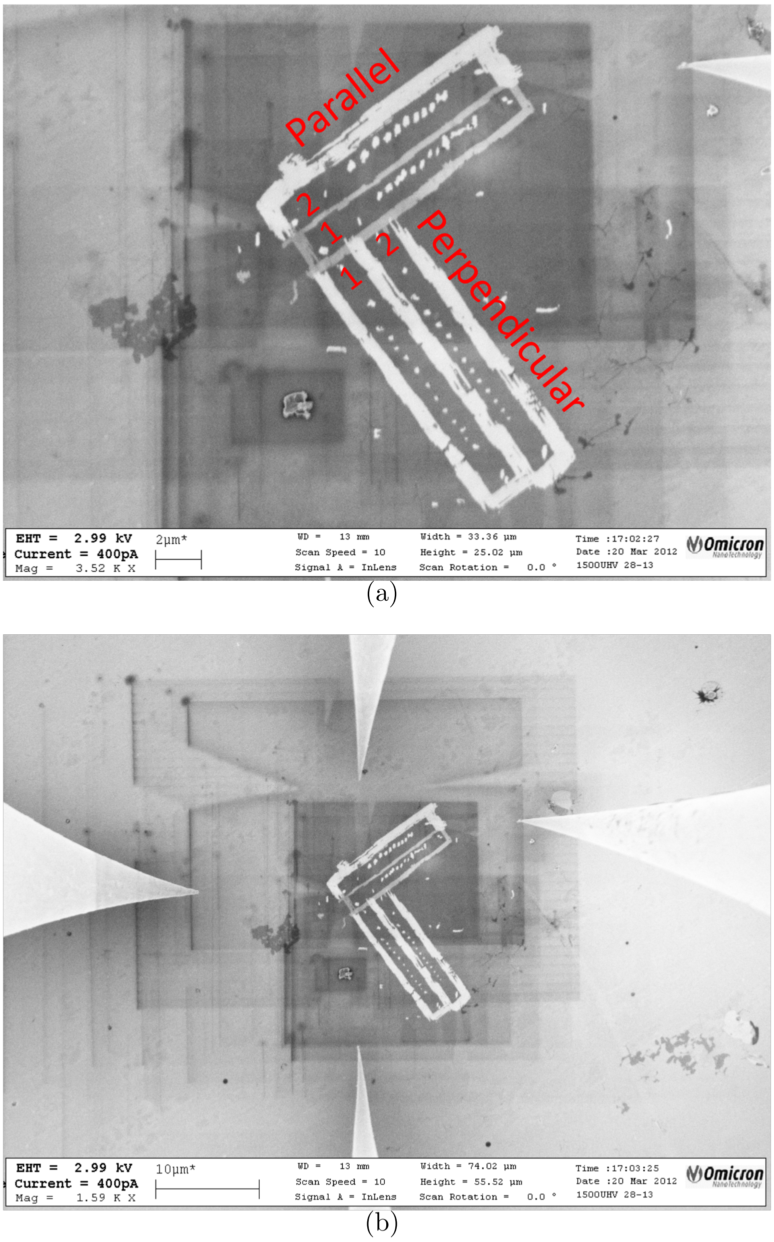

(a)

(b)

Figure 8.9: SEM images from the Nanoprobe system showing bar structures cut into a sample annealed at 1650°C for 120 minutes. a) Imaging defining the labeling of the parallel and perpendicular bars post electronic measurements. b) Taken at a lower magnification to show the uniformity of the graphene film surrounding the bar structure. Both are images taken post contacting for electrical measurements and the tip induced damage can be seen in all of the bar structures. The size of the tip damage spot is dependent on the exact nature of the tip as the measurement is taken and can vary across a set. 'Drawing' damage from the SEM imaging can also be seen as squares of dark contrast. Scale bars given in images.

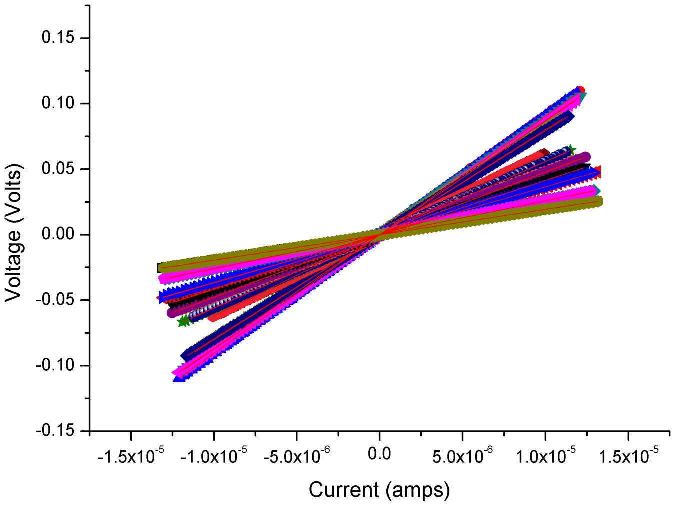

Figure 8.10: IV characteristics for the bar structure ‘parallel 1’ from a graphene film grown for 120 minutes at 1650°C in argon atmosphere. The IV graphs all follow linear fits indicating Ohmic behavior and good contact between the STM tips and the graphene film. Each individual graph is one of a pair (positive and negative bias) taken at different voltage probe separations. The higher resistances (steeper gradient) correspond to the higher separations.

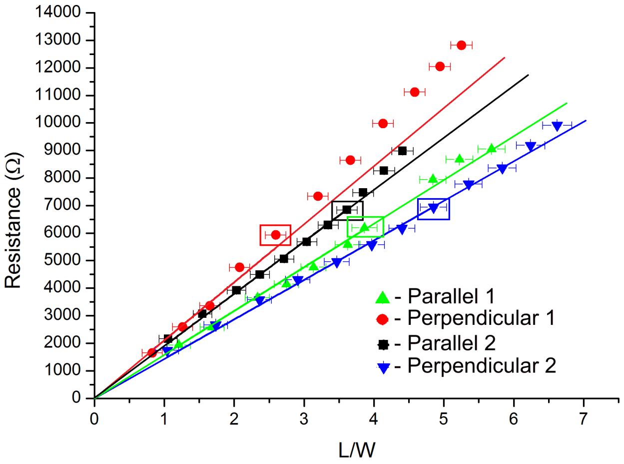

Figure 8.11: Measured resistance vs L/W for all bar structures measured from graphene films grown after a 120 minute at 1650°C in argon atmosphere, deviations from linear behavior can be seen at high L/W values. The linear fits are shown with solid lines. The last point used for the linear fits in each case is highlighted with a box. This point is chosen by eye to be the last point on the linear fit before a deviation occurs. Each of the linear fits has a fixed intercept at 0.

If there is anisotropy caused at the step edges then a notable contribution should be observed in the $R_s$ measurements with those measured parallel to the terraces being smaller than those measured perpendicular to the terraces. The results from this set of bars are shown in Figure 8.11, it can be seen that there is no obvious increase in sheet resistance in the bars cut perpendicular to the terraces and as shown in Table 8.1 the smallest sheet resistance measured was measured in the 'Perpendicular' 2 bar.

To attempt to clarify the absence of any anisotropy due to the presence of atomic steps, the sheet resistance at each point was calculated using Equation 8.1 by dividing the measured resistance ($R$) by ($L/W$) where $L$ is the probe separation and here, $W$ is the average width of the bar being measured. Figure 8.12 shows these values plotted with increasing voltage probe separation ($L$). It

Table 8.1: Sheet Resistance from Double Bar Measurements for Sample Annealed at 1650°C for 120 Minutes. Sheet resistance measured by Yakes et al(37) were ∼300 Ω.

| Bar | Sheet Resistance (Ω) |
|---|---|
| Parallel 1 | 1588±12 |
| Parallel 2 | 1898±12 |
| Perpendicular 1 | 2107±55 |
| Perpendicular 2 | 1433±18 |

would be expected that the sheet resistance measurements in the parallel direction would remain invariant with the increase in voltage probe separation with the sheet resistance measurements in the perpendicular direction showing a step-like response when an atomic terrace is crossed as seen elsewhere. (36) As previously mentioned the atomic terraces have been observed to be located every ∼1 $\mu$m on these samples.

Therefore on the length scales of voltage probe separations used in Figure 8.12 we would expect to see around 5 steps in sheet resistance values with increasing voltage probe separation in the perpendicular direction. Despite some evidence of steps in the bar labeled ‘perpendicular 1’, the periodicity of these steps is not as expected for the terraces observed in these samples. Also the complete lack of a stepped like increase in sheet resistance in the bar labeled ‘perpendicular 2’ suggests that there is no anisotropy present (due to the underlying stepped substrate surface) within this graphene film.

### 8.2.3 Bar Structures Measured Within a Sample Annealed for 30 Minutes at 1650°C

Bar measurements were also carried out on the sample annealed for 30 minutes at 1650°C. These consisted of 2 sets of parallel and perpendicular bars cut from separate areas of graphene growth. These bars are shown in Figure 8.13. As can be seen in the SEM images, the graphene films formed under these annealing conditions is somewhat more disordered than those formed when annealing for

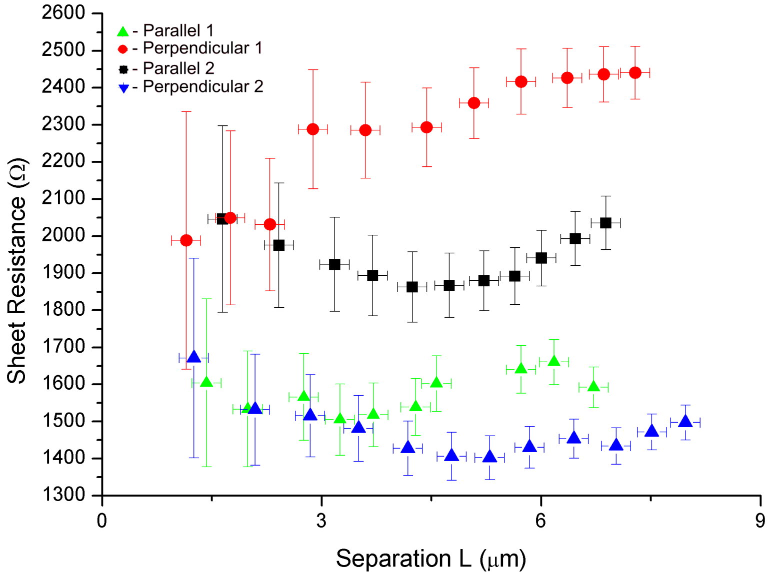

Figure 8.12: Sheet Resistance measured with varying voltage probe separation ($L$) for 4 different bar structures cut from the same area of graphene from a sample annealed for 120 minutes at 1650°C. A step-like response in resistance values is expected in the perpendicular direction as atomic terraces are crossed with increasing $L$.

120 minutes. Ripples and folds can be seen as well as the presence of the tube-like structures as discussed in greater detail during Chapter 7. These tube-like structures are observed to run through (most probably underneath) each of these patterned bars.

Once more the 4-probe IV characteristics (not shown) appear linear at each position within all the bars measured. Again each measured resistance is taken is the statistical average of both forward biasing and reverse biasing the current flow direction with the error in resistance measured extracted from the difference in resistance values measured with reverse polarity.

When measuring these bar structures the method shown in Figure 8.7(b) was used to vary the voltage probe separation. Again anisotropies were investigated via the measurement and comparison of the sheet resistance values obtained from the parallel and perpendicular bars. These results are shown in Figure 8.14 and summarized in Table 8.2. In both sets of bars the sheet resistance measured in the perpendicular direction are lower than those in the parallel direction, again suggesting that there is no anisotropy due to the atomic terraces. The sheet resistances measured in the first set of bars (labeled parallel 1 and perpendicular 1) is much higher than those measured in both the parallel and perpendicular direction in the second set of bars (labeled parallel 2 and perpendicular 2). The sheet resistance values measured in the second set of bars are comparable to those measured within the sample annealed for 120 minutes (Table 8.1). This would suggest that the region of film measured within the first set of bars is more disordered than the other films measured.

Table 8.2: Sheet Resistance from Bar Measurements for Sample Annealed at 1650°C for 30 minutes. Sheet resistance measured by Yakes et al(37) were ∼300 Ω.

| Bar | Sheet Resistance (Ω) |
|---|---|
| Parallel 1 | 5795±65 |
| Parallel 2 | 1823±36 |
| Perpendicular 1 | 2869±23 |
| Perpendicular 2 | 1410±43 |

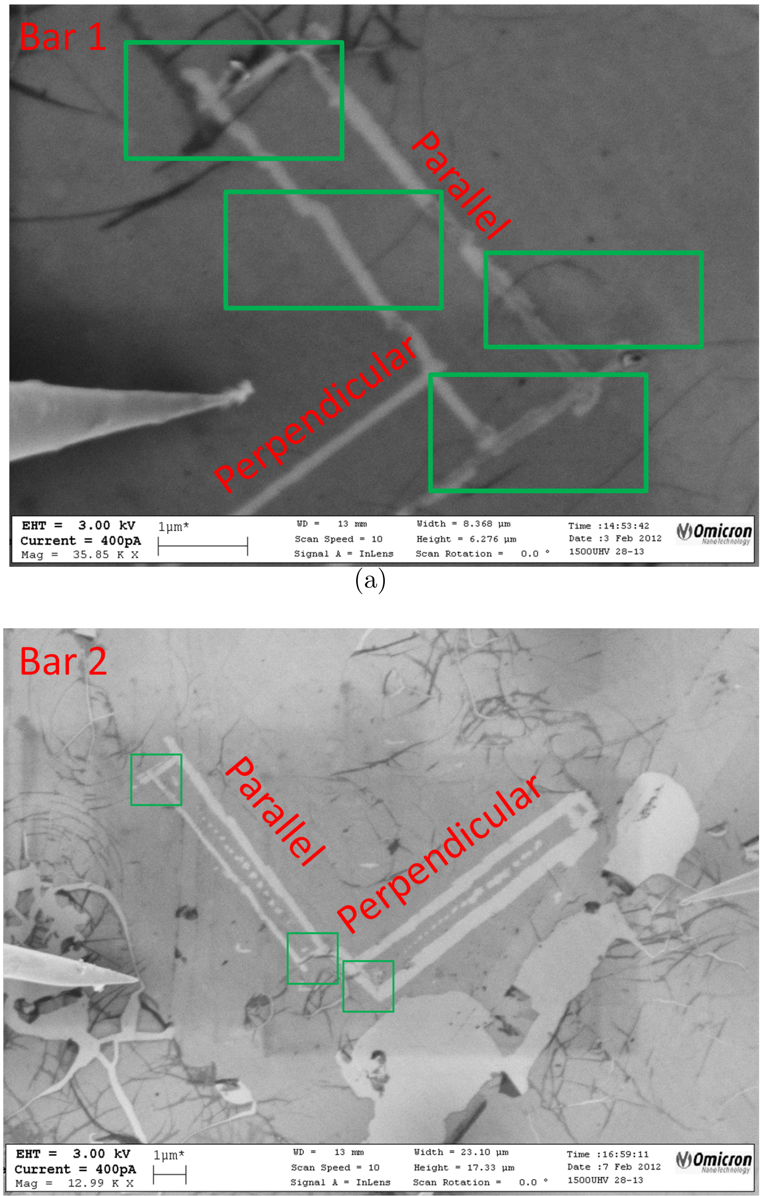

(a)

(b)

Figure 8.13: SEM images from the Nanoprobe system showing bar structures cut into a sample annealed at 1650°C for 30 minutes. a) Set of bars 1. b) Set of bars 2. Scale bars given in images. Green boxes used to highlight the presence of tube-like structures in the region of the bars.

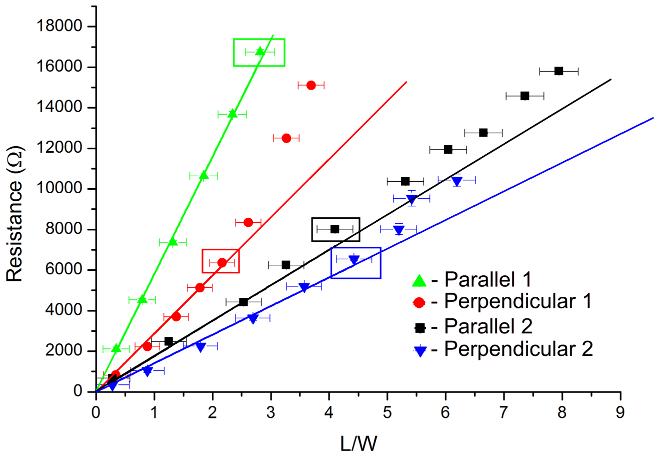

Figure 8.14: Measured resistance vs L/W for all bar structures measured from graphene films grown after a 30 minute at 1650°C in argon atmosphere, deviations from linear behavior can be seen at high L/W values. The linear fits are shown with solid lines. The last point used for the linear fits in each case is highlighted with a box. This point is chosen by eye to be the last point on the linear fit before a deviation occurs. Each of the linear fits has a fixed intercept at 0.

There are a number of possible causes of this disorder and the observed larger sheet resistance measurements in the first set of bars. The effects of tip-induced damage can be ruled out as a possible cause for the large difference as each of the sets of bars exhibit a linear relationship of $R_s$ and $L/W$ as shown in Figure 8.14 at low separations $L$ where you would expect the tip induced damage to have the most effect. The island region used for the first set of bars is smaller and in general shows more wrinkle/tube structures per unit length than the larger area used for the second set of bars. This can be seen in Figure 8.13 where there are 4 wrinkle/tube regions identified within one bar structure in the first set of bars ( Figure 8.13(a)) compared to 3 across the whole of the much larger bar structures in the second set of bars ( Figure 8.13(b)). It is this general disorder within the graphene films that is likely to cause this large variation in sheet resistance values.

Again to try and identify the presence or absence of anisotropy due to the presence of substrate steps, the sheet resistance at each point was tracked with increasing voltage probe separation (L). Figure 8.15 shows these results, from the first set of bars (shown in Figure 8.15(a)). For the voltage separations used in these measurements and with a terrace width of ∼1 $\mu$m we would expect to see 3 distinct steps within the sheet resistance values with increasing voltage probe separations in the perpendicular direction.

The sheet resistance in the parallel direction does appear to remain invariant with increasing voltage probe separation as expected. In the perpendicular direction there is a general increase in the sheet resistance as the voltage probe separation increases, though this behavior is not step-like for increasing $L$ values between 0.5 $\mu$m and 2.5 $\mu$m where at least 2 clear steps would be expected. There is a step observed between 2.5 $\mu$m and 3.0 $\mu$m though, it must also be noted that this increase could be linked to the non linearity in the measured resistance measured with increasing $L/W$ for this bar past $L/W$ values of 2.0 (as shown in Figure 8.14) rather than the presence of anisotropy due to substrate steps.

Figure 8.15(b) show the results from the second set of bars cut on this sample. Here there is no notable increase in the sheet resistance values in the perpendicular direction with increasing voltage probe separation (L). Surprisingly there is a slight increase in sheet resistance observed in the parallel direction, suggesting

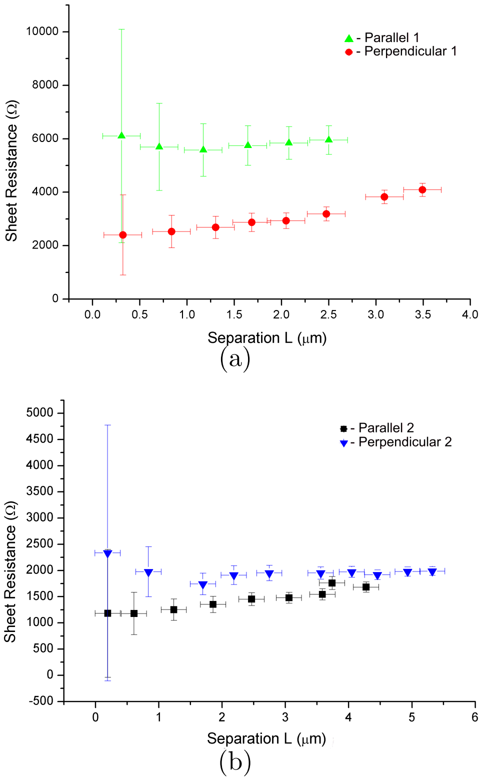

(a)

(b)

Figure 8.15: Sheet resistance measurements with varying voltage probe separations (L) for bar structures cut into graphene films grown after a 30 minute anneal at 1650°C. a) Results from first set of bars. b) Results from second set of bars. A step-like response in resistance values is expected in the perpendicular direction as atomic terraces are crossed with increasing $L$.

that there is anisotropy present within the film material itself and limits the suggestion that the increase observed in the perpendicular direction for the first bar (Figure 8.15(a)) is due to presence of substrate steps.

### 8.2.4 Cross Structure Measured Within a Sample Annealed for 30 Minutes at 1650°C

As well as bar structures cut separately being used to measure anisotropies, a cross structure was also used within films grown for 30 minutes at 1650°C. Figure 8.16(a) shows the cut cross structure prior to the measurement of resistance values, Figure 8.16(b) shows the structure after the resistance measurements have been taken. Again in this series of measurements the voltage probe separation was varied using the technique shown in Figure 8.7(b) with both voltage probes moving towards the central region.

Again the IV characteristics at each point were linear (not shown) with the measured resistance again taken as the statistical average of the resistance values measured with both forward and reverse biased currents with the error value extracted from the difference in these resistance measurements. As shown in Figure 8.16(b) the central region of the cross was left unprobed, meaning that the cross structure can be roughly treated as 2 separate bar structures thus allowing the sheet resistance values to be calculated in the same way as previously carried out for bar structures.

Once more there is no clear difference in the sheet resistance measured between the parallel and perpendicular orientations as shown in Figure 8.17 and summarized in Table 8.3. The resistance in the parallel direction is lower than that in the perpendicular direction as would be expected if the substrate steps were causing anisotropy. However, this difference is small (74 Ω) and is comparable to the size of the error present from the straight line fits to obtain the sheet resistance in the parallel direction (50 Ω) so attributing it to the presence of substrate steps is difficult.

Again to try and clarify the results in the cross structure the sheet resistance at each point is calculated and plotted with varying voltage probe separation (L). Figure 8.18 shows this data which again suggests that there is no substrate step

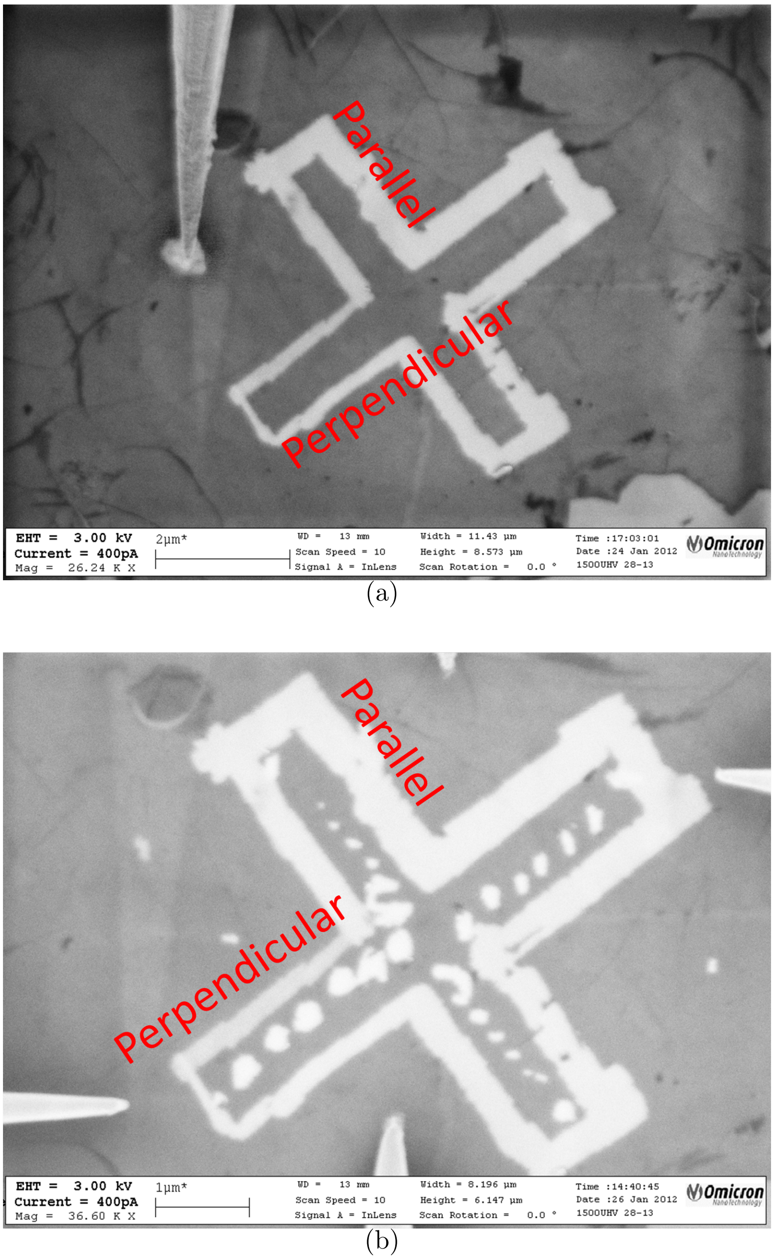

(a)

(b)

Figure 8.16: SEM images from the Nanoprobe system showing the cross structure cut into a sample annealed at 1650°C for 30 minutes. a) Cross structure pre resistance measurements. b) Cross structure after resistance measurements. (scale bars in images).

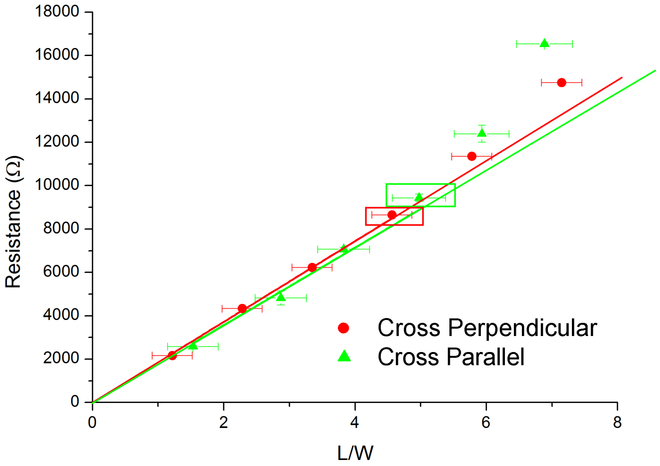

Figure 8.17: Measured resistance vs L/W for the cross structure structure from graphene films grown after a 30 minute at 1650°C in argon atmosphere, deviations from linear behavior can be seen at high L/W values. The linear fits are shown with solid lines. The last point used for the linear fits in each case is highlighted with a box. This point is chosen by eye to be the last point on the linear fit before a deviation occurs. Each of the linear fits has a fixed intercept at 0.

Table 8.3: Sheet Resistance from Cross Measurements for Sample Annealed at 1650°C for 30 minutes. Sheet resistance measured by Yakes et al(37) were ~300 Ω.

| Bar | Sheet Resistance (Ω) |
|---|---|
| Parallel | 1787±50 |
| Perpendicular | 1861±3 |

induced anisotropy within these graphene films. Unexpectedly sheet resistance in the parallel direction show some dependence on the voltage probe separation whereas the sheet resistance measurements in the perpendicular direction remain fairly constant. This again suggests that inconsistencies within the films themselves and perhaps quality of contacts (despite the linear IVs) could be causing the variations rather than the presence of any substrate step induced anisotropies.

The measurements carried out on the bar structures cut from the samples annealed for 120 minutes and 30 minutes at 1650°C, and from the cross structure cut from the sample annealed for 30 minutes suggests that there is no substrate step induced anisotropy within these graphene films unlike observations made elsewhere. (36; 37) The absence of an anisotropy is beneficial for the integration of epitaxial graphene into industrial production methods.

## 8.3 Conclusions and Discussions

In this chapter it has been shown that the Nanoprobe system provides a very useful technique to locally probe the properties of epitaxial graphene films on silicon carbide substrates. This is especially true for the case when the graphene film is very non-uniform and graphene islands exist on the surface making standard optical lithography and electron beam lithography processes difficult for electrically contacting the films. Once contacted 4-probe electronic transport measurements can be made, this is possible due to the silicon carbide substrate being insulating, ensuring that all the current flows through the graphene films.

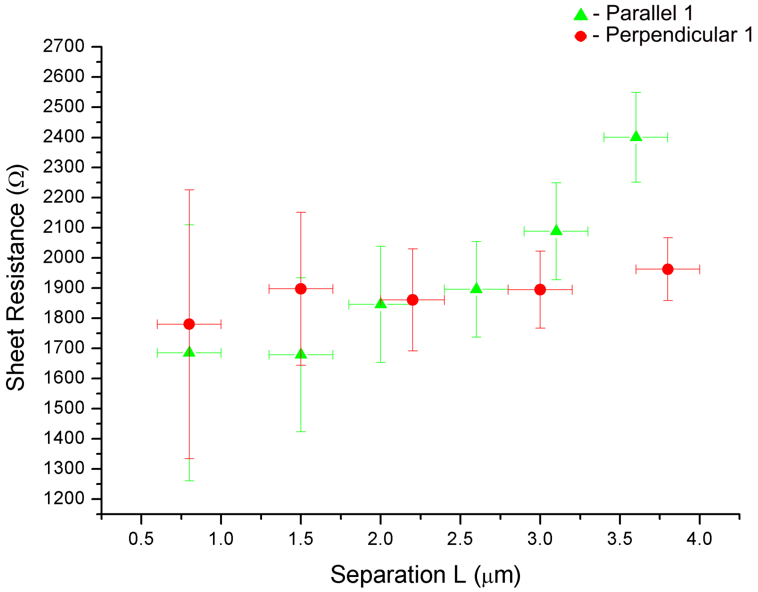

Figure 8.18: Sheet Resistance measured with varying voltage probe separation (L) for the cross structure cut from an area of graphene from a sample annealed for 30 minutes at 1650°C. A step-like response in resistance values is expected in the perpendicular direction as atomic terraces are crossed with increasing $L$.

It is also possible to use the Nanoprobe STM tips to cut the graphene films into well defined measurement geometries and align these geometries to the presence of atomic terraces within the silicon carbide terraces. This allowed for attempts to be made to measure anisotropies in resistance within the graphene films running parallel and perpendicular to be investigated. Work elsewhere (36; 37; 38) has shown that there is a resistance cost associated with passing current within graphene films over these substrate steps, making the resistance perpendicular to the steps greater than in the parallel direction. There was no such dependence observed within the films probed in this work.

The exact reasoning for this lack of anisotropy is not known, though there are a number of reasons why this result could occur. Firstly the sheet resistances measured in these graphene films is ∼2 kΩ which is higher than those observed elsewhere when measuring substrate induced anisotropies i.e in work by Yakes et al where the sheet resistance values were ∼300 Ω. This increased sheet resistance could perhaps be due to the disordered nature of the graphene films as mentioned in discussed in greater detail in Chapter 7 and here could lead to the 'blurring out' of the substrate step anisotropy. The presence of wrinkles in the graphene film due to local strains will lead to changes to the lattice spacings within the graphene film, non uniform strains have been shown to decrease the mobility of graphene films (increase resistance) by a factor of 10.(107) An experiment we could carry out to investigate this is to pattern an array of bar structures (via optical lithography and focused ion beam etching) into a region of complete graphene growth and measure the sheet resistances of these bars before carrying out Raman mapping of the same device to check the strain uniformity. This array of bar structures would also allow the consistency of the sheet resistance within a film to be measured.

Though the damage to the graphene films caused by the STM tips during the electrical measurements are thought not to contribute to this increase in sheet resistance due to the linear behavior of the measured resistance with varying the voltage probe separation, the patterning of contact pads along the side of the previously mentioned bar arrays would help to remove this damage within the bar structures altogether.

Also important to note is that experimental work carried out by Ji et al (36) and theoretical calculations carried out by Low et al (38) suggest that graphene films flowing over substrate steps of ~0.3 nm (as measured in these samples via AFM) will have a step contribution of ~5 Ω per step which is much lower than the 42 Ω per step measured in the work by Yakes et al (37) on stepped bunched substrates. This would require the resistance measurements to to be sensitive to a 5 Ω change in a ~2 kΩ sheet resistance. For the sheet resistance with varying probe separation measurements as shown in Figures 8.12, 8.15 and 8.18 the error bars given are much bigger than the 5 Ω required.

To improve upon this, better control on the tip positioning is required. In the current setup, when the widths of the tips are taken into account there is a ± ~0.2 $\mu$m error in the positioning of the tips which leads to large areas in the calculated sheet resistance values. This improved resolution could also aid the observation of step-like changes in sheet resistance with varying voltage probe separation. Multiple IV sweeps at each separation to lower the uncertainty associated with the measured resistance values could also help improve the resolution of the experiments and maybe help to show up any small anisotropy caused by the substrate steps.

The well defined measurement geometries defined by the cutting of these bar and cross structures negate the need for complex corrections to the resistance values measured to obtained sheet resistance values for varying probe separations as described by Wells et al (181) for 4 probe measurements in more open geometries. Deviations from non-linear behavior of measured resistance values with increasing L/W can be attributed to the current paths being non-uniform at those positions and those points are therefore discounted when fitting straight lines to obtain sheet resistance values. One more limiting factor in these results is the width of the cut bars and crosses. The ~1 $\mu$m widths mean that even in the parallel directions, there is the possibility to be at least 1 substrate step edge present as the terrace width is also observed to be ~1 $\mu$m from AFM, ideally the parallel bars would be cut within a single terrace. If there is a terrace within a parallel bar structure then the current paths will be distorted due to the presence of this step, this would lead to an increase in the sheet resistance.

The process of cutting the bar structures leads to uneven edges with $\sim 100$ nm variations in width across the bar. This could lead to the variations in sheet resistances measured (discounting the large difference measured in the first set of bars on the sample annealed for 30 minutes) within this work. A modification to the process again would see the use of focused ion beam etching to obtain even edges and remove this possible cause of variation from the experiment. Removing this variation is important for identification of the presence or absence of anisotropy as it will increase the resolution of the experimental procedure.

In conclusion, work carried out in this chapter to identify the presence of a conduction anisotropy withing the graphene films grown on a terraced substrate has yielded no strong proof for its existence. This absence of anisotropy has been identified to be due to a combination of the high sheet resistances measured within these films compared to in other work (37) and the smaller atomic steps in the substrate observed here leading to a smaller resistance cost associated with passing currents through the graphene film perpendicular to these steps.(38) This lack of anisotropy would have benefits for electrical devices patterned within the graphene films where anisotropies in resistance and therefore conductivity could lead to poor device quality. Though the observed larger sheet resistances still suggests that the quality of graphene films produced still needs improving and is far from optimized.

Improvements to the experimental technique to try and investigate the presence of anisotropy due to the substrate steps has already been suggested. Further work to probe the conductivity behavior in regions were bilayer and monolayer regions overlap could be useful to further understand the growth mechanisms present within these samples. These should now be possible with the increased uniformity observed in bilayer regions within the sample annealed for 120 minutes at 1650°C and could be compared with work carried out elsewhere (36) to understand the coupling between thicker graphene films grown via this technique.

# Chapter 9

# Conclusions and Outlook

## 9.1 Conclusions

The key aims of this project were to understand and improve the growth of epitaxial graphene on silicon carbide, with a view to providing a consistent method for producing high quality, large scale graphene films that can be integrated into electronic devices within the group here in Leeds. This has been achieved, with a number of key results showing improvements to graphene film growth in ultra high vacuum and in the development of an argon annealing process whereby atomically terraced silicon carbide substrates can be produced and graphitised within a single stage process.

The key improvements to the graphene films grown in ultra high vacuum have been an increase in graphene coverage on the substrate surfaces to ensure the presence of a complete graphene films and the increase in the lateral grain sizes of graphene domains within these films from 10s nm to 100s nm. These improvements in film quality lead to improvements in the electronic properties measured within these films (measurements taken by Graham Creeth) with a move away from inelastic scattering dominated variable range hopping behavior to more graphene-like weak localisation behavior as the lateral grain sizes increase and elastic scattering processes dominate. (28)

The improvements in graphene coverage and lateral grain size were gained by varying the times and temperatures used within the final annealing step for growth. In a simplistic view the growth time was observed to control the completeness of the graphene films whilst the growth temperature controlled the mobility of the carbon atoms on the substrate surface and therefore the lateral grain size. A picture of how varying these two parameters affects the quality of the graphene films as built up with the use of surface science techniques such as low energy electron diffraction, atomic force microscopy, low energy electron microscopy and Raman spectroscopy.

Raman spectroscopy was also used to track the development of strains within the graphene films grown in ultra high vacuum over a range of different annealing times at an annealing temperature of 1400°C via the tracking of the 2D band position. This work (33) showed that compressive strains build up between the graphene films and the silicon carbide substrates due to their differing thermal expansion coefficients.(32) The strain values are seen to increase with increasing annealing time owing to the increased graphene coverage allowing for less strain relaxation to take place. The maximum strain value obtained during this work (33) of 0.5% for graphene grown on the silicon carbide ($000\bar{1}$) is less than the 0.9% obtained for growth on the (0001) face carried out elsewhere with similar annealing conditions.(32) This suggests decoupling of the graphene layers from the substrate allows for strain relaxation with this decoupling also observed elsewhere.(50) Variations in strain values and graphene coverage across single samples suggests the presence of a thermal gradient during the annealing process.

Alongside work carried out on improving the growth procedure for graphene films in ultra high vacuum, a procedure for annealing silicon carbide wafers under an inert argon gas atmosphere was also developed. Work elsewhere published during this project(26; 27) demonstrated improved graphene film growth under these conditions owing to the slowing down of the net silicon evaporation rate due to the backscatter of evaporating silicon atoms due to the presence of the inert gas.(26; 27)

Initial annealing runs, carried out at 1500°C lead to surprising results with the silicon carbide (0001) substrate that was previously marred by mechanical polishing scratches now exhibiting atomic terraces, a result regularly observed via the use of a potentially dangerous hydrogen etching technique elsewhere.(29) Increasing the annealing temperature to ∼1600°C led to the graphitisation of these atomically stepped terraces with the graphene films observed to grow 'carpet-like' over the underlying substrate. This single step procedure for both preparing the silicon carbide substrates and subsequently graphitising these substrates has potential benefits for the integration of epitaxial graphene into industrial processes as does the removal of the potentially hazardous hydrogen etching step.

However surface science techniques such as atomic force microscopy, scanning electron microscopy and Raman spectroscopy showed these films to be less than perfect. The observation of island-like graphene growth via atomic force microscopy and scanning electron microscopy with rips and folds observed within these islands tied in well with the Raman spectroscopy measurements which showed the presence of a large defect induced (134; 135; 145; 156) D band. Improvements to the growth procedures saw the final sample grown during this project (annealed for 120 minutes at a temperature of 1650°C) exhibit large areas ∼100s $\mu$m of single domain graphene growth (seen in SEM imaging) thus demonstrating the potential for this growth procedure, though further optimization and understanding of the growth mechanism is still required.

A Nanoprobe system has been used to locally probe the graphene 'islands' grown under inert argon gas and carry out 4-probe electrical measurements. The STM tips have also been used to manipulate the graphene films and carry out cutting procedures to define measurement geometries within the films. This had allowed sheet resistance values to be calculated for these films which have been shown to be comparable to those measured elsewhere though are larger by a factor of 4, again suggesting that the graphene growth procedure needs improvement. The measurement geometries have also been cut into the film to allow bar structures that run both parallel and perpendicular to be probed with a view to measuring anisotropies in resistance caused by the presence of the underlying atomic terraces within the silicon carbide substrate as observed elsewhere.(36; 37) These anisotropies have not been observed with this being attributed to the smaller step heights present within the atomic terraces (∼0.3 nm) formed during this work which has been predicted to produce a small resistance cost when a current flows in a graphene film over these terrace steps.(38) The absence of anisotropy is again beneficial for future integration of epitaxial graphene into nanoelectronic applications.

### 9.1.1 Outlook

The single step argon annealing process to both prepare atomically terrace silicon carbide substrates and graphitise these substrates as shown promise in the production of large scale epitaxial graphene films. This procedure is also the main area in this work for where there is scope for both improvement of the graphene film quality and for further understanding of the processes that are taking place. Some of the potential improvements to the experiment would require alterations and modifications to the existing equipment as well as just extra time to prepare more samples and carry out more in-depth characterisation of these samples.

The first system modification that would prove useful would be the purchase of a new furnace system that allow both higher temperatures to be reached as well as allowing increased ramp rates to these temperatures. Due the formation of an oxide layer on the sample surface the graphitisation of the carbon terminated face occurs at higher temperatures when compared to the silicon terminated face under argon annealing.(35) Higher temperatures (to ∼1800°C) would allow for the graphitisation of the carbon terminated face (35) to be achieved under argon atmospheres and for the growth of graphene on this surface under these conditions to be studied. The increase in ramp rates would allow the investigation of how the terrace formation varies with the temperature ramp rates used. If the terraces can be formed under argon gas atmospheres during rapid (or at least quicker) annealing processes then this would again lead to benefits for the yield of graphene attainable via this growth technique.

The ability to vary the pressure during the annealing processes would also allow further optimization of the growth parameters and could allow for the graphitisation of the carbon terminated face within the temperature ranges attainable by the current furnace system.(35) The current process which involves the flowing of argon gas at atmospheric pressures through the tube furnace during the annealing runs has been carried out through necessity to limit contamination (mainly oxidation) of the silicon carbide wafers. An improved pumping system, including the introduction of a turbo pump and better couplings to the tube would allow for a cleaner environment to be achieved during the flush and pump stage due to the better vacuum achieved. This improved vacuum and cleaner system could negate the need to constantly flow gas through the tube to keep it clean and allow for pressure variations during annealing processes.

In-depth characterization on the argon annealed samples such as carrying out low energy electron diffraction measurements on a range of samples annealed for differing times and temperatures would allow for a more complete picture of the surface reconstructions that take place on the silicon carbide substrate during the formation of terraces then the subsequent graphitisation. The characterization of the tube-like structures is also important. Atomic resolution scanning tunneling microscopy to try and observe if they consist of an ordered structure could help with this. Energy-dispersive x-ray spectroscopy could be used to try and identify the chemical make-up of the structures, knowing whether the 'tubes' are carbon-rich or silicon-rich could help explain the observation of graphene films and surface reconstructions being mediated by these structures. Cross-sectional transition electron microscopy could also prove useful in analyzing these structures as well as probing the interface structure between the graphene films and underlying silicon carbide substrate.

After the local probing of the electrical transport properties of the argon grown graphene films. Progress would be to see these graphene films integrated into the low temperature electronic transport and magnetotransport measurements carried out within the group here in Leeds. This would see electronic devices patterned via the use of either optical or electron beam lithography to potentially allow the probing of effects such as Shubnikov-de Hass oscillations and the weak localisation within these films and to compare these results to those obtained for graphene films grown in ultra high vacuum in Leeds and to literature results obtained on argon annealed samples elsewhere.

# References

[1] K. S. Novoselov, A. K. Geim, S. V. Morozov, D. Jiang, Y. Zhang, S. V. Dubonos, I. V. Grigorieva, and A. A. Firsov. Electric field effect in atomically thin carbon films. *Science*, 306(5696):666–669, 2004. 1, 5, 21

[2] Andreas Barth and Werner Marx. Graphene - a rising star in view of scientometrics. *arxiv*, 0808.3320, 2008. 1, 5

[3] Changgu Lee, Xiaoding Wei, Jeffrey W Kysar, and James Hone. Measurement of the elastic properties and intrinsic strength of monolayer graphene. *Science*, 321(5887):385–388, 2008. 1, 6

[4] K. S. Novoselov, Z. Jiang, Y. Zhang, S. V. Morozov, H. L. Stormer, U. Zeitler, J. C. Maan, G. S. Boebinger, P. Kim, and A. K. Geim. Room-Temperature quantum Hall effect in graphene. *Science*, page 1137201, 2007. 1, 7, 10, 21

[5] K.I. Bolotin, K.J. Sikes, Z. Jiang, M. Klima, G. Fudenberg, J. Hone, P. Kim, and H.L. Stormer. Ultrahigh electron mobility in suspended graphene. *Solid State Communications*, 146(910):351–355, 2008. 1, 6

[6] S. Das Sarma, Shaffique Adam, E. H. Hwang, and Enrico Rossi. Electronic transport in two-dimensional graphene. *Reviews of Modern Physics*, 83(2):407, 2011. 1, 7, 8, 33

[7] A. H. Castro Neto, F. Guinea, N. M. R. Peres, K. S. Novoselov, and A. K. Geim. The electronic properties of graphene. *Reviews of Modern Physics*, 81(1):109–162, 2009. 1, 6, 7, 8, 9, 33

[8] E.W. Hill, A.K. Geim, K. Novoselov, F. Schedin, and P. Blake. Graphene spin valve devices. *Magnetics, IEEE Transactions on*, 42(10):2694 –2696, oct 2006. 1, 5

[9] Frank Schwierz. Graphene transistors. *Nat Nano*, 5(7):487–496, 2010. 1, 5, 10, 26, 30, 31

[10] Sukang Bae, Hyeongkeun Kim, Youngbin Lee, Xiangfan Xu, Jae-Sung Park, Yi Zheng, Jayakumar Balakrishnan, Tian Lei, Hye Ri Kim, Young Il Song, Young-Jin Kim, Kwang S. Kim, Barbaros Özyilmaz, Jong-Hyun Ahn, Byung Hee Hong, and Sumio Iijima. Roll-to-roll production of 30-inch graphene films for transparent electrodes. *Nature Nanotechnology*, 5:574–578, 2010. 1, 2, 5, 22, 23, 31, 33

[11] Yu-Ming Lin, Alberto Valdes-Garcia, Shu-Jen Han, Damon B. Farmer, Inanc Meric, Yanning Sun, Yanqing Wu, Christos Dimitrakopoulos, Alfred Grill, Phaedon Avouris, and Keith A. Jenkins. Wafer-Scale graphene integrated circuit. *Science*, 332(6035):1294 –1297, 2011. 1, 31

[12] Xuesong Li, Yanwu Zhu, Weiwei Cai, Mark Borysiak, Boyang Han, David Chen, Richard D. Piner, Luigi Colombo, and Rodney S. Ruoff. Transfer of Large-Area graphene films for High-Performance transparent conductive electrodes. *Nano Lett.*, 9(12):4359–4363, 2009. 1

[13] Keun Soo Kim, Yue Zhao, Houk Jang, Sang Yoon Lee, Jong Min Kim, Kwang S. Kim, Jong-Hyun Ahn, Philip Kim, Jae-Young Choi, and Byung Hee Hong. Large-scale pattern growth of graphene films for stretchable transparent electrodes. *Nature*, 457(7230):706–710, 2009. 1, 22

[14] Roie Yerushalmi, Zachery A. Jacobson, Johnny C. Ho, Zhiyong Fan, and Ali Javey. Large scale, highly ordered assembly of nanowire parallel arrays by differential roll printing. *Applied Physics Letters*, 91(20):203104–3, 2007. 2

[15] Se Hyun Ahn and L. Jay Guo. High-Speed Roll-to-Roll nanoimprint lithography on flexible plastic substrates. *Advanced Materials*, 20(11):2044–2049, 2008. 2

[16] Alfonso Reina, Hyungbin Son, Liying Jiao, Ben Fan, Mildred S. Dresselhaus, ZhongFan Liu, and Jing Kong. Transferring and identification of single- and Few-Layer graphene on arbitrary substrates. *The Journal of Physical Chemistry C*, 112(46):17741–17744, 2008. 2, 22

[17] Claire Berger, Zhimin Song, Tianbo Li, Xuebin Li, Asmerom Y. Ogbazghi, Rui Feng, Zhenting Dai, Alexei N. Marchenkov, Edward H. Conrad, Phillip N. First, and Walt A. de Heer. Ultrathin epitaxial graphite: 2D electron gas properties and a route toward graphene-based nanoelectronics. *The Journal of Physical Chemistry B*, 108(52):19912–19916, 2004. 2, 9, 12, 13, 14, 65, 74, 88, 110, 145, 211

[18] A.J. Van Bommel, J.E. Crombeen, and A. Van Tooren. LEED and auger electron observations of the SiC(0001) surface. *Surface Science*, 48(2):463–472, 1975. 2, 3, 13, 39, 65, 74, 88, 145, 211

[19] I. Forbeaux, J. -M. Themlin, and J. -M. Debever. High-temperature graphitization of the 6H-SiC face. *Surface Science*, 442(1):9–18, 1999. 2, 3, 13, 14, 15, 65, 74, 88, 145, 211

[20] Taisuke Ohta, Aaron Bostwick, Thomas Seyller, Karsten Horn, and Eli Rotenberg. Controlling the electronic structure of bilayer graphene. *Science*, 313(5789):951–954, 2006. 2, 30

[21] Th. Seyller, A. Bostwick, K. V. Emtsev, K. Horn, L. Ley, J. L. McChesney, T. Ohta, J. D. Riley, E. Rotenberg, and F. Speck. Epitaxial graphene: a new material. *physica status solidi (b)*, 245(7):1436–1446, 2008. 2, 3, 13, 14, 15, 65, 74, 75, 88, 89, 145, 211

[22] Luxmi, Shu Nie, P.J. Fisher, R.M. Feenstra, Gong Gu, and Yugang Sun. Temperature dependence of epitaxial graphene formation on SiC(0001). *Journal of Electronic Materials*, 38(6):718–724, 2008. 2

[23] Luxmi, P. J Fisher, N. Srivastava, R. M Feenstra, Yugang Sun, J. Kedzierski, P. Healey, and Gong Gu. Morphology of graphene on SiC(000-1) surfaces. *Applied Physics Letters*, 95:073101, 2009. 2, 14, 75, 112, 129

[24] Luxmi, N. Srivastava, Guowei He, R. M. Feenstra, and P. J. Fisher. Comparison of graphene formation on c-face and si-face SiC 0001 surfaces. *Physical Review B*, 82(23):235406, 2010. 2, 3, 14, 15, 16, 17, 75, 78, 81, 102, 108, 122, 173, 175, 197, 200, 206, 214

[25] Luxmi, N. Srivastava, R. M. Feenstra, and P. J. Fisher. Formation of epitaxial graphene on SiC(0001) using vacuum or argon environments. *Journal of Vacuum Science & Technology B: Microelectronics and Nanometer Structures*, 28(4):C5C1, 2010. 2, 3, 17, 35, 39, 135, 136

[26] Konstantin V. Emtsev, Aaron Bostwick, Karsten Horn, Johannes Jobst, Gary L. Kellogg, Lothar Ley, Jessica L. McChesney, Taisuke Ohta, Sergey A. Reshanov, Jonas Rohrl, Eli Rotenberg, Andreas K. Schmid, Daniel Waldmann, Heiko B. Weber, and Thomas Seyller. Towards wafer-size graphene layers by atmospheric pressure graphitization of silicon carbide. *Nat Mater*, 8:203–207, 2009. 2, 3, 4, 14, 17, 35, 37, 39, 135, 136, 149, 152, 215, 247

[27] C. Virojanadara, M. Syvajarvi, R. Yakimova, L. I. Johansson, A. A. Zakharov, and T. Balasubramanian. Homogeneous large-area graphene layer growth on 6H-SiC(0001). *Physical Review B (Condensed Matter and Materials Physics)*, 78(24):245403–6, 2008. 2, 3, 13, 17, 35, 39, 135, 136, 149, 180, 211, 247

[28] G. L. Creeth, A. J. Strudwick, J. T. Sadowski, and C. H. Marrows. Surface morphology and transport studies of epitaxial graphene on SiC(000-1). *Physical Review B*, 83(19):195440, 2011. 2, 16, 35, 78, 81, 94, 95, 97, 98, 108, 111, 121, 122, 246

[29] V. Ramachandran, M. F. Brady, A. R. Smith, R. M. Feenstra, and D. W. Greve. Preparation of atomically flat surfaces on silicon carbide using hydrogen etching. *J. Electron. Mater.*, 27(4):308–312, 1998. 2, 4, 13, 14, 35, 135, 136, 140, 146, 148, 149, 150, 171, 180, 211, 248

[30] Novasic. Savoie Technolac - Arche Bat.4, Allee du Lac d'Aiguebelette, BP 267, 73375 Le Bourget du Lac Cedex, France. 2, 13, 14, 91, 130

[31] Walt A de Heer, Claire Berger, Xiaosong Wu, Mike Sprinkle, Yike Hu, Ming Ruan, Joseph A Stroscio, Phillip N First, Robert Haddon, Benjamin Piot, Clément Faugeras, Marek Potemski, and Jeong-Sun Moon. Epitaxial graphene electronic structure and transport. *Journal of Physics D: Applied Physics*, 43(37):374007, 2010. 3, 7, 8, 9, 75, 89

[32] Nicola Ferralis, Roya Maboudian, and Carlo Carraro. Evidence of structural strain in epitaxial graphene layers on 6H-SiC(0001). *Physical Review Letters*, 101(15):156801–4, 2008. 3, 25, 124, 125, 129, 130, 133, 209, 247

[33] A. J. Strudwick, G. L. Creeth, N. A. B. Johansson, and C. H. Marrows. Probing residual strain in epitaxial graphene layers on 4H-SiC(000-1) with raman spectroscopy. *Applied Physics Letters*, 98(5):051910, 2011. 3, 25, 35, 75, 78, 125, 126, 127, 128, 129, 131, 133, 209, 247

[34] Walt. A de Heer, Claire Berger, Ming Ruan, Mike Sprinkle, Xuebin Li, Yike Hu, Baiqian Zhang, John Hankinson, and Edward H Conrad. Large area and structured epitaxial graphene produced by confinement controlled sublimation of silicon carbide. *Proceedings of the National Academy of Sciences*, 108(41):16900 –16905, 2011. 3, 14, 15, 16, 35, 38, 75, 89, 121, 149, 215

[35] J. L. Tedesco, G. G. Jernigan, J. C. Culbertson, J. K. Hite, Y. Yang, K. M. Daniels, R. L. Myers-Ward, C. R. Eddy, J. A. Robinson, K. A. Trumbull, M. T. Wetherington, P. M. Campbell, and D. K. Gaskill. Morphology characterization of argon-mediated epitaxial graphene on c-face SiC. *Applied Physics Letters*, 96(22):222103, 2010. 4, 14, 17, 173, 175, 197, 200, 214, 249

[36] Shuai-Hua Ji, J. B. Hannon, R. M. Tromp, V. Perebeinos, J. Tersoff, and F. M. Ross. Atomic-scale transport in epitaxial graphene. *Nature Materials*, 11(2):114–119, 2011. 4, 217, 219, 220, 222, 227, 231, 241, 243, 244, 245, 248

[37] Michael K. Yakes, Daniel Gunlycke, Joseph L. Tedesco, Paul M. Campbell, Rachael L. Myers-Ward, Charles R. Eddy, D. Kurt Gaskill, Paul E. Sheehan, and Arnaldo R. Laracuente. Conductance anisotropy in epitaxial graphene sheets generated by substrate interactions. *Nano Lett.*,

10(5):1559–1562, 2010. 4, 217, 218, 219, 220, 227, 231, 233, 241, 243, 244, 245, 248

[38] T. Low, V. Perebeinos, J. Tersoff, and Ph. Avouris. Deformation and scattering in graphene over substrate steps. *Physical Review Letters*, 108(9):096601, 2012. 4, 217, 219, 243, 244, 245, 248

[39] P. R. Wallace. The band theory of graphite. *Physical Review*, 71(9):622, 1947. 5, 6, 7

[40] F. Schedin, A. K. Geim, S. V. Morozov, E. W. Hill, P. Blake, M. I. Katsnelson, and K. S. Novoselov. Detection of individual gas molecules adsorbed on graphene. *Nature Materials*, 6(9):652–655, 2007. 5

[41] S.D. Bader and S.S.P. Parkin. Spintronics. *Annual Review of Condensed Matter Physics*, 1(1):71–88, 2010. 6

[42] F. Bonaccorso, Z. Sun, T. Hasan, and A. C. Ferrari. Graphene photonics and optoelectronics. *Nat Photon*, 4(9):611–622, 2010. 6, 31, 32, 33

[43] Charles Kittel. *Introduction to Solid State Physics*. John Wiley & Sons, 8th edition, international edition edition, 2004. 7, 8, 9

[44] Tsuneya Ando, Takeshi Nakanishi, and Riichiro Saito. Berry's phase and absence of back scattering in carbon nanotubes. *Journal of the Physical Society of Japan*, 67:2857–2862, 1998. 7

[45] T. Shen, J. J. Gu, M. Xu, Y. Q. Wu, M. L. Bolen, M. A. Capano, L. W. Engel, and P. D. Ye. Observation of quantum-Hall effect in gated epitaxial graphene grown on SiC (0001). *Applied Physics Letters*, 95(17):172105–3, 2009. 7

[46] Csaba Toke, Paul E. Lammert, Vincent H. Crespi, and Jainendra K. Jain. Fractional quantum Hall effect in graphene. *Physical Review B (Condensed Matter and Materials Physics)*, 74(23):235417–5, 2006. 7

[47] Xiaosong Wu, Yike Hu, Ming Ruan, Nerasoa K Madiomanana, John Hankinson, Mike Sprinkle, Claire Berger, and Walt A. de Heer. Half integer quantum Hall effect in high mobility single layer epitaxial graphene. *Applied Physics Letters*, 95(22):223108, 2009. 7, 10, 16, 18, 112

[48] Y. Zhang, Z. Jiang, J. P. Small, M. S. Purewal, Y.-W. Tan, M. Fazlollahi, J. D. Chudow, J. A. Jaszczak, H. L. Stormer, and P. Kim. Landau-Level splitting in graphene in high magnetic fields. *Physical Review Letters*, 96(13):136806–4, 2006. 7

[49] Yisong Zheng and Tsuneya Ando. Hall conductivity of a two-dimensional graphite system. *Physical Review B*, 65(24):245420, 2002. 7

[50] J. Hass, F. Varchon, J. E. Millan-Otoya, M. Sprinkle, N. Sharma, W. A. de Heer, C. Berger, P. N. First, L. Magaud, and E. H. Conrad. Why multilayer graphene on 4H-SiC(000-1) behaves like a single sheet of graphene. *Physical Review Letters*, 100(12):125504–4, 2008. 8, 14, 15, 75, 89, 112, 130, 133, 247

[51] K. S. Novoselov, A. K. Geim, S. V. Morozov, D. Jiang, M. I. Katsnelson, I. V. Grigorieva, S. V. Dubonos, and A. A. Firsov. Two-dimensional gas of massless dirac fermions in graphene. *Nature*, 438(7065):197–200, 2005. 9, 10, 11, 21

[52] Yuanbo Zhang, Yan-Wen Tan, Horst L. Stormer, and Philip Kim. Experimental observation of the quantum hall effect and berry's phase in graphene. *Nature*, 438(7065):201–204, 2005. 9, 10, 21

[53] V. A. Yampol'skii, S. Savel'ev, and Franco Nori. Voltage-driven quantum oscillations in graphene. *New Journal of Physics*, 10(5):053024, 2008. 9

[54] K. v. Klitzing, G. Dorda, and M. Pepper. New method for High-Accuracy determination of the Fine-Structure constant based on quantized hall resistance. *Physical Review Letters*, 45(6):494, 1980. 9

[55] D. C. Tsui, H. L. Stormer, and A. C. Gossard. Two-Dimensional magnetotransport in the extreme quantum limit. *Physical Review Letters*, 48(22):1559, 1982. 9

[56] R. B. Laughlin. Anomalous quantum hall effect: An incompressible quantum fluid with fractionally charged excitations. *Physical Review Letters*, 50(18):1395, 1983. Copyright (C) 2009 The American Physical Society; Please report any problems to prola@aps.org. 9

[57] R. B. Laughlin. Quantized hall conductivity in two dimensions. *Physical Review B*, 23(10):5632, 1981. Copyright (C) 2009 The American Physical Society; Please report any problems to prola@aps.org. 10

[58] Johannes Jobst, Daniel Waldmann, Florian Speck, Roland Hirner, Duncan K. Maude, Thomas Seyller, and Heiko B. Weber. Quantum oscillations and quantum hall effect in epitaxial graphene. *Physical Review B*, 81(19):195434, 2010. 10, 18

[59] Alexander Tzalenchuk, Samuel Lara-Avila, Alexei Kalaboukhov, Sara Paolillo, Mikael Syvajarvi, Rositza Yakimova, Olga Kazakova, JanssenT. J. B. M., Vladimir Fal'ko, and Sergey Kubatkin. Towards a quantum resistance standard based on epitaxial graphene. *Nat Nano*, 5(3):186–189, 2010. 10, 18, 19, 20, 21

[60] J.-C. Charlier, P. C. Eklund, J. Zhu, and A. C. Ferrari. Electron and phonon properties of graphene: Their relationship with carbon nanotubes. In *Carbon Nanotubes*, volume 111, pages 673–709. Springer Berlin Heidelberg, Berlin, Heidelberg, 2008. 10, 30, 40, 162

[61] Melinda Y. Han, Barbaros Ozyilmaz, Yuanbo Zhang, and Philip Kim. Energy Band-Gap engineering of graphene nanoribbons. *Physical Review Letters*, 98(20):206805–4, 2007. 10, 12, 30

[62] Xiaolin Li, Xinran Wang, Li Zhang, Sangwon Lee, and Hongjie Dai. Chemically derived, ultrasmooth graphene nanoribbon semiconductors. *Science*, 319(5867):1229–1232, 2008. 10, 12, 30

[63] Leonardo C. Campos, Vitor R. Manfrinato, Javier D. Sanchez-Yamagishi, Jing Kong, and Pablo Jarillo-Herrero. Anisotropic etching and nanoribbon formation in Single-Layer graphene. *Nano Letters*, 9(7):26002604, 2009. 12, 35, 213

[64] Lijie Ci, Zhiping Xu, Lili Wang, Wei Gao, Feng Ding, Kevin Kelly, Boris Yakobson, and Pulickel Ajayan. Controlled nanocutting of graphene. *Nano Research*, 1(2):116–122, 2008. 12

[65] Sujit S Datta, Douglas R Strachan, Samuel M Khamis, and A. T. Charlie Johnson. Crystallographic etching of Few-Layer graphene. *Nano Lett.*, 8(7):19121915, 2008. 12, 35

[66] Franziska Schaffel, Jamie H Warner, Alicja Bachmatiuk, Bernd Rellinghaus, Bernd Buchner, Ludwig Schultz, and Mark H Rummeli. On the catalytic hydrogenation of graphite for graphene nanoribbon fabrication. *physica status solidi (b)*, 246(11-12):2540–2544, 2009. 12

[67] Sprinkle M., Ruan M., Hu Y., Hankinson J., Rubio-Roy M., Zhang B., Wu X., Berger C., and de Heer W. A. Scalable templated growth of graphene nanoribbons on SiC. *Nat Nano*, 5(10):727–731, 2010. 12

[68] Jinming Cai, Pascal Ruffieux, Rached Jaafar, Marco Bieri, Thomas Braun, Stephan Blankenburg, Matthias Muoth, Ari P. Seitsonen, Moussa Saleh, Xinliang Feng, Klaus Mullen, and Roman Fasel. Atomically precise bottom-up fabrication of graphene nanoribbons. *Nature*, 466(7305):470–473, 2010. 12

[69] Dmitry V. Kosynkin, Amanda L. Higginbotham, Alexander Sinitskii, Jay R. Lomeda, Ayrat Dimiev, B. Katherine Price, and James M. Tour. Longitudinal unzipping of carbon nanotubes to form graphene nanoribbons. *Nature*, 458(7240):872–876, 2009. 12, 24

[70] M. Bhatnagar and B.J. Baliga. Comparison of 6H-SiC, 3C-SiC, and Si for power devices. *Electron Devices, IEEE Transactions on*, 40(3):645 –655, 1993. 12

[71] Inc. Cree. 4600 Silicon Drive Durham, NC 27703, USA. 12, 136, 152

[72] Xuebin Li. *Epitaxial graphene films on SiC: growth, characterization, and devices*. Dissertation, Georgia Institute of Technology, 2008. 13

[73] H Hibino, H Kageshima, and M Nagase. Epitaxial few-layer graphene: towards single crystal growth. *Journal of Physics D: Applied Physics*, 43:374005, 2010. 13, 56, 57, 64, 140, 146, 148, 184

[74] J. Penuelas, A. Ouerghi, D. Lucot, C. David, J. Gierak, H. Estrade-Szwarckopf, and C. Andreazza-Vignolle. Surface morphology and characterization of thin graphene films on SiC vicinal substrate. *Physical Review B*, 79(3):033408, 2009. 13

[75] Claire Berger, Zhimin Song, Xuebin Li, Xiaosong Wu, Nate Brown, Cecile Naud, Didier Mayou, Tianbo Li, Joanna Hass, Alexei N. Marchenkov, Edward H. Conrad, Phillip N. First, and Walt A. de Heer. Electronic confinement and coherence in patterned epitaxial graphene. *Science*, 312(5777):1191–1196, 2006. 13

[76] Claire Berger, Zhimin Song, Xuebin Li, Xiaosong Wu, Nate Brown, Duncan Maud, Cécile Naud, and Walt A. de Heer. Magnetotransport in high mobility epitaxial graphene. *physica status solidi (a)*, 204(6):1746–1750, 2007. 13

[77] Walt A. de Heer, Claire Berger, Xiaosong Wu, Phillip N. First, Edward H. Conrad, Xuebin Li, Tianbo Li, Michael Sprinkle, Joanna Hass, Marcin L. Sadowski, Marek Potemski, and Gérard Martinez. Epitaxial graphene. *Solid State Communications*, 143(1-2):92–100, 2007. 13, 14, 15

[78] I Forbeaux, J.-M Themlin, A Charrier, F Thibaudau, and J.-M Debever. Solid-state graphitization mechanisms of silicon carbide 6H-SiC polar faces. *Applied Surface Science*, 162-163(0):406–412, 2000. 13, 14, 15, 65, 74, 88, 145, 211

[79] Peter Sutter. Epitaxial graphene: How silicon leaves the scene. *Nat Mater*, 8(3):171–172, 2009. 13

[80] Joshua Robinson, Xiaojun Weng, Kathleen Trumbull, Randall Cavalero, Maxwell Wetherington, Eric Frantz, Michael LaBella, Zachary Hughes, Mark Fanton, and David Snyder. Nucleation of epitaxial graphene on SiC(0001). *ACS Nano*, 4(1):153–158, 2010. 13, 184

[81] Th. Seyller, K.V. Emtsev, K. Gao, F. Speck, L. Ley, A. Tadich, L. Broekman, J.D. Riley, R.C.G. Leckey, O. Rader, A. Varykhalov, and A.M. Shikin. Structural and electronic properties of graphite layers grown on SiC(0001). *Surface Science*, 600(18):3906–3911, 2006. 14

[82] F J Ferrer, E Moreau, D Vignaud, S Godey, and X Wallart. Atomic scale flattening, step formation and graphitization blocking on 6H- and 4H-SiC(0001) surfaces under si flux. *Semiconductor Science and Technology*, 24(12):125014, 2009. 14, 15, 140, 148, 150

[83] A.J. Van Bommel, J.E. Crombeen, and A. Van Tooren. LEED and auger electron observations of the SiC(0001) surface. *Surface Science*, 48(2):463–472, 1975. 14, 15

[84] J. Hass, W. A. de Heer, and E. H. Conrad. The growth and morphology of epitaxial multilayer graphene. *Journal of Physics: Condensed Matter*, 20(32):323202, 2008. 14

[85] A. Al-Temimy, C. Riedl, and U. Starke. Low temperature growth of epitaxial graphene on SiC induced by carbon evaporation. *Applied Physics Letters*, 95(23):231907–231907–3, 2009. 15

[86] Nicolas Camara, Jean-Roch Huntzinger, Gemma Rius, Antoine Tiberj, Narcis Mestres, Francesc Pérez-Murano, Philippe Godignon, and Jean Camassel. Anisotropic growth of long isolated graphene ribbons on the c face of graphite-capped 6H-SiC. *Physical Review B*, 80(12):125410, 2009. 16, 198, 199

[87] M. Orlita, C. Faugeras, P. Plochocka, P. Neugebauer, G. Martinez, D. K. Maude, A.-L. Barra, M. Sprinkle, C. Berger, W. A. de Heer, and M. Potemski. Approaching the dirac point in High-Mobility multilayer epitaxial graphene. *Physical Review Letters*, 101(26):267601–4, 2008. 16

[88] David W. Allan. Should the classical variance be used as a basic measure in standards metrology? *IEEE Transactions on Instrumentation Measurement*, 36:646–654, June 1987. 18

[89] Peter W. Sutter, Jan-Ingo Flege, and Eli A. Sutter. Epitaxial graphene on ruthenium. *Nat Mater*, 7(5):406–411, 2008. 21

[90] Xuesong Li, Weiwei Cai, Jinho An, Seyoung Kim, Junghyo Nah, Dongxing Yang, Richard Piner, Aruna Velamakanni, Inhwa Jung, Emanuel Tutuc, Sanjay K. Banerjee, Luigi Colombo, and Rodney S. Ruoff. Large-Area synthesis of High-Quality and uniform graphene films on copper foils. *Science*, 324(5932):1312–1314, 2009. 22, 30

[91] Yenny Hernandez, Valeria Nicolosi, Mustafa Lotya, Fiona M. Blighe, Zhenyu Sun, Sukanta De, I. T. McGovern, Brendan Holland, Michele Byrne, Yurii K. Gun'Ko, John J. Boland, Peter Niraj, Georg Duesberg, Satheesh Krishnamurthy, Robbie Goodhue, John Hutchison, Vittorio Scardaci, Andrea C. Ferrari, and Jonathan N. Coleman. High-yield production of graphene by liquid-phase exfoliation of graphite. *Nature Nanotechnology*, 3(9):563–568, 2008. 24, 31

[92] S. Stankovich. Graphene-based composite materials. *Nature*, 442:282–286, 2006. 24, 31

[93] J. N. Coleman, M. Lotya, A. O'Neill, S. D. Bergin, P. J. King, U. Khan, K. Young, A. Gaucher, S. De, R. J. Smith, I. V. Shvets, S. K. Arora, G. Stanton, H.-Y. Kim, K. Lee, G. T. Kim, G. S. Duesberg, T. Hallam, J. J. Boland, J. J. Wang, J. F. Donegan, J. C. Grunlan, G. Moriarty, A. Shmeliov, R. J. Nicholls, J. M. Perkins, E. M. Grieveson, K. Theuwissen, D. W. McComb, P. D. Nellist, and V. Nicolosi. Two-Dimensional nanosheets produced by liquid exfoliation of layered materials. *Science*, 331:568–571, 2011. 24

[94] K S Novoselov and A H Castro Neto. Two-dimensional crystals-based heterostructures: materials with tailored properties. *Physica Scripta*, T146:014006, 2012. 24

[95] Gedeng Ruan, Zhengzong Sun, Zhiwei Peng, and James M. Tour. Growth of graphene from food, insects, and waste. *ACS Nano*, 5(9):7601–7607, 2011. 24

[96] Zhen Hua Ni, Ting Yu, Yun Hao Lu, Ying Ying Wang, Yuan Ping Feng, and Ze Xiang Shen. Uniaxial strain on graphene: Raman spectroscopy study and Band-Gap opening. *ACS Nano*, 2(11):2301–2305, 2008. 24, 26, 27, 28, 30, 124, 133, 134

[97] Alpha T N'Diaye, Raoul van Gastel, Antonio J Martínez-Galera, Johann Coraux, Hichem Hattab, Dirk Wall, Frank-J Meyer zu Heringdorf, Michael Horn von Hoegen, José M Gómez-Rodríguez, Bene Poelsema, Carsten Busse, and Thomas Michely. in situ observation of stress relaxation in epitaxial graphene. *New Journal of Physics*, 11(11):113056, 2009. 24, 25, 26, 190

[98] Awnish K Gupta, Cristiano Nisoli, Paul E Lammert, Vincent H Crespi, and Peter C Eklund. Curvature-induced d-band raman scattering in folded graphene. *Journal of Physics: Condensed Matter*, 22(33):334205, 2010. 24, 157

[99] Otakar Frank, Georgia Tsoukleri, John Parthenios, Konstantinos Papagelis, Ibtsam Riaz, Rashid Jalil, Kostya S. Novoselov, and Costas Galiotis. Compression behavior of Single-Layer graphenes. *ACS Nano*, 4(6):3131–3138, 2010. 24, 25, 48, 158, 160

[100] T. M. G. Mohiuddin, A. Lombardo, R. R. Nair, A. Bonetti, G. Savini, R. Jalil, N. Bonini, D. M. Basko, C. Galiotis, N. Marzari, K. S. Novoselov, A. K. Geim, and A. C. Ferrari. Uniaxial strain in graphene by raman spectroscopy: G peak splitting, gruneisen parameters, and sample orientation. *Physical Review B (Condensed Matter and Materials Physics)*, 79(20):205433–8, 2009. 24, 25, 48, 125, 158, 160

[101] Nicola Ferralis. Probing mechanical properties of graphene with raman spectroscopy. *Journal of Materials Science*, 45(19):5135–5149, 2010. 24, 25, 40, 43, 46, 125

[102] Irene Calizo, Wenzhong Bao, Feng Miao, Chun Ning Lau, and Alexander A. Balandin. The effect of substrates on the raman spectrum of graphene: Graphene- on-sapphire and graphene-on-glass. *Applied Physics Letters*, 91(20):201904–3, 2007. 25

[103] Nicolas Mounet and Nicola Marzari. First-principles determination of the structural, vibrational and thermodynamic properties of diamond, graphite, and derivatives. *Physical Review B*, 71(20):205214, 2005. 25, 124, 125, 126, 129

[104] Glen A. Slack and S. F. Bartram. Thermal expansion of some diamondlike crystals. *Journal of Applied Physics*, 46(1):89, 1975. 25, 124, 125, 129

[105] V. Derycke, R. Martel, M. Radosavljević, F. M. Ross, and Ph. Avouris. Catalyst-Free growth of ordered Single-Walled carbon nanotube networks. *Nano Lett.*, 2(10):1043–1046, 2002. 25

[106] Z. Goknur Cambaz, Gleb Yushin, Sebastian Osswald, Vadym Mochalin, and Yury Gogotsi. Noncatalytic synthesis of carbon nanotubes, graphene and graphite on SiC. *Carbon*, 46(6):841–849, 2008. 25, 26, 129

[107] Joshua A. Robinson, Maxwell Wetherington, Joseph L. Tedesco, Paul M. Campbell, Xiaojun Weng, Joseph Stitt, Mark A. Fanton, Eric Frantz, David Snyder, Brenda L. VanMil, Glenn G. Jernigan, Rachael L. Myers-Ward, Charles R. Eddy, and D. Kurt Gaskill. Correlating raman spectral signatures with carrier mobility in epitaxial graphene: A guide to achieving high mobility on the wafer scale. *Nano Letters*, 9(8):2873–2876, 2009. 26, 119, 125, 134, 165, 243

[108] N. Levy, S. A. Burke, K. L. Meaker, M. Panlasigui, A. Zettl, F. Guinea, A. H. C. Neto, and M. F. Crommie. Strain-Induced Pseudo-Magnetic fields greater than 300 tesla in graphene nanobubbles. *Science*, 329(5991):544–547, 2010. 29, 124, 134

[109] F. Guinea, Baruch Horovitz, and P. Le Doussal. Gauge fields, ripples and wrinkles in graphene layers. *Solid State Communications*, 149(27-28):1140–1143, 2009. 29, 124, 134

[110] Y.-M. Lin, C. Dimitrakopoulos, K. A. Jenkins, D. B. Farmer, H.-Y. Chiu, A. Grill, and Ph. Avouris. 100-GHz transistors from Wafer-Scale epitaxial graphene. *Science*, 327(5966):662, 2010. 30

[111] Yu-Ming Lin, Keith A. Jenkins, Alberto Valdes-Garcia, Joshua P. Small, Damon B. Farmer, and Phaedon Avouris. Operation of graphene transistors at gigahertz frequencies. *Nano Letters*, 9(1):422–426, 2009. 30

[112] Yu-Ming Lin, Hsin-Ying Chiu, Keith A Jenkins, Damon B Farmer, Phaedon Avouris, and Alberto Valdes-Garcia. Dual gate graphene FETs with fT of 50 GHz. *IEEE Electron Device Letters*, 31:68–70, 2010. 30

[113] M. Sprinkle, M. Ruan, X. Wu, Y. Hu, M. Rubio-Roy, J. Hankinson, N. K Madiomanana, C. Berger, and W. A de Heer. Directed self-organization of graphene nanoribbons on SiC. *Nature Nanotechnology*, 5:727, 2010. 31

[114] Yanqing Wu, Yu-ming Lin, Ageeth A. Bol, Keith A. Jenkins, Fengnian Xia, Damon B. Farmer, Yu Zhu, and Phaedon Avouris. High-frequency, scaled graphene transistors on diamond-like carbon. *Nature*, 472(7341):74–78, 2011. 31

[115] Frank Schwierz. Electronics: Industry-compatible graphene transistors. *Nature*, 472(7341):41–42, 2011. 31

[116] Xuan Wang, Linjie Zhi, Nok Tsao, eljko Tomovic, Jiaoli Li, and Klaus Mllen. Transparent carbon films as electrodes in organic solar cells. *Angewandte Chemie International Edition*, 47(16):2990–2992, 2008. 31

[117] Junbo Wu, Mukul Agrawal, Hector A. Becerril, Zhenan Bao, Zunfeng Liu, Yongsheng Chen, and Peter Peumans. Organic Light-Emitting diodes on Solution-Processed graphene transparent electrodes. *ACS Nano*, 4(1):43–48, 2009. 31

[118] A. Fert, J.-M. George, H. Jaffres, and R. Mattana. Semiconductors between Spin-Polarized sources and drains. *Electron Devices, IEEE Transactions on*, 54(5):921 –932, 2007. 33

[119] Luis E. Hueso, Jose M. Pruneda, Valeria Ferrari, Gavin Burnell, Jose P. Valdes-Herrera, Benjamin D. Simons, Peter B. Littlewood, Emilio Artacho, Albert Fert, and Neil D. Mathur. Transformation of spin information into large electrical signals using carbon nanotubes. *Nature*, 445(7126):410–413, 2007. 33

[120] H. Jaffres, J.-M. George, and A. Fert. Spin transport in multiterminal devices: Large spin signals in devices with confined geometry. *Physical Review B*, 82(14):140408, 2010. 33

[121] Wei Han, W. H. Wang, K. Pi, K. M. McCreary, W. Bao, Yan Li, F. Miao, C. N. Lau, and R. K. Kawakami. Electron-Hole asymmetry of spin injection and transport in Single-Layer graphene. *Physical Review Letters*, 102(13):137205–4, 2009. 33

[122] Wei Han, K. Pi, K. M McCreary, Yan Li, Jared J. I Wong, A. G Swartz, and R. K Kawakami. Tunneling spin injection into single layer graphene. *Phys*, 105:167202, 2010. 33

[123] C. Józsa, M. Popinciuc, N. Tombros, H. T. Jonkman, and B. J. van Wees. Controlling the efficiency of spin injection into graphene by carrier drift. *Physical Review B*, 79(8):081402, 2009. 33

[124] Nikolaos Tombros, Csaba Jozsa, Mihaita Popinciuc, Harry T. Jonkman, and Bart J. van Wees. Electronic spin transport and spin precession in single graphene layers at room temperature. *Nature*, 448(7153):571–574, 2007. 33

[125] Wei Han and R. K. Kawakami. Spin relaxation in Single-Layer and bilayer graphene. *Physical Review Letters*, 107(4):047207, 2011. 33

[126] T. Maassen, F. K. Dejene, M. H. D. Guimares, C. Jzsa, and B. J. van Wees. Comparison between charge and spin transport in few-layer graphene. *Physical Review B*, 83(11):115410, 2011. 33

[127] T.-Y. Yang, J. Balakrishnan, F. Volmer, A. Avsar, M. Jaiswal, J. Samm, S. R. Ali, A. Pachoud, M. Zeng, M. Popinciuc, G. Gntherodt, B. Beschoten, and B. zyilmaz. Observation of long Spin-Relaxation times in bilayer graphene at room temperature. *Physical Review Letters*, 107(4):047206, 2011. 33

[128] Masashi Kumagawa, Hiroshi Kuwabara, and Shoji Yamada. Hydrogen etching of silicon carbide. *Japanese Journal of Applied Physics*, 8:421–428, 1969. 35

[129] D. J. Rearick, O. Maksimov, and V. D. Heydemann. Design of a hydrogen etching system for surface preparation of SiC wafers. *Journal of Vacuum Science & Technology A: Vacuum, Surfaces, and Films*, 24(5):1970–1971, 2006. 35

[130] MTI Corporation. 860 South 19th Street, Richmond, CA 94804, USA. 37

[131] S.A. Surma M. Grodzicki, R. Wasielewski and A. Ciszewski. Formation of excess silicon on 6h-sic(0001) during hydrogen etching. *ACTA Physica Polonica A*, 116:S–82, 2009. 37

[132] Stefano Piscanec, Michele Lazzeri, J. Robertson, Andrea C. Ferrari, and Francesco Mauri. Optical phonons in carbon nanotubes: Kohn anomalies, peierls distortions, and dynamic effects. *Phys. Rev. B*, 75:035427, 2007. 40, 48, 160, 162

[133] Stephanie Reich and Christian Thomsen. Raman spectroscopy of graphite. *Philosophical Transactions. Series A, Mathematical, Physical, and Engineering Sciences*, 362(1824):2271–2288, 2004. PMID: 15482979. 40

[134] F. Tuinstra and J. L Koenig. Raman spectrum of graphite. *The Journal of Chemical Physics*, 53(3):1126–1130, 1970. 40, 44, 47, 64, 102, 103, 152, 155, 157, 213, 248

[135] A. C. Ferrari, J. C. Meyer, V. Scardaci, C. Casiraghi, M. Lazzeri, F. Mauri, S. Piscanec, D. Jiang, K. S. Novoselov, S. Roth, and A. K. Geim. Raman spectrum of graphene and graphene layers. *Physical Review Letters*, 97(18):187401–4, 2006. 40, 42, 44, 50, 119, 120, 126, 155, 213, 248

[136] Andrea C. Ferrari. Raman spectroscopy of graphene and graphite: Disorder, electron-phonon coupling, doping and nonadiabatic effects. *Solid State Communications*, 143(1-2):47–57, 2007. 40, 42, 44, 64, 102, 160, 163

[137] Ewen Smith and Geoffrey Dent. *Modern Raman Spectroscopy: A Practical Approach*. Wiley-Blackwell, 2004. 41, 42, 43, 44

[138] N. Camara, G. Rius, J. -R Huntzinger, A. Tiberj, N. Mestres, P. Godignon, and J. Camassel. Selective epitaxial growth of graphene on SiC. *Applied Physics Letters*, 93:123503, 2008. 47, 102, 105

[139] L. G. Cancado, K. Takai, T. Enoki, M. Endo, Y. A. Kim, H. Mizusaki, A. Jorio, L. N. Coelho, R. Magalhaes-Paniago, and M. A. Pimenta. General equation for the determination of the crystallite size $l_\alpha$ of nanographite by raman spectroscopy. *Applied Physics Letters*, 88(16):163106–3, 2006. 47, 102, 105, 155, 213

[140] Shriram Shivaraman, M. V. S Chandrashekhar, John J Boeckl, and Michael G Spencer. Thickness estimation of epitaxial graphene on SiC using attenuation of substrate raman intensity. *Journal of Electronic Materials*, 38(6):725–730, 2008. 49, 50, 116, 117, 118, 171

[141] Ricardo Garcia. *Amplitude Modulation Atomic Force Microscopy*. Wiley-VCH, 1 edition, 2010. 51, 52, 53, 54, 55, 56, 59, 60, 61, 62, 63

[142] A. D. L Humphris, M. J Miles, and J. K Hobbs. A mechanical microscope: High-speed atomic force microscopy. *Applied Physics Letters*, 86(3):034106–034106–3, 2005. 53

[143] Garcia R and Perez R. Dynamic atomic force microscopy methods. *Surface Science Reports*, 47:197–301, 2002. 54, 55, 56

[144] Carlos Bustamante and David Keller. Scanning force microscopy in biology. *Physics Today*, 48(12):32–38, 1995. 60

[145] A. C. Ferrari and J. Robertson. Resonant raman spectroscopy of disordered, amorphous, and diamondlike carbon. *Physical Review B*, 64(7):075414, 2001. 64, 155, 213, 248

[146] C. Riedl, U. Starke, J. Bernhardt, M. Franke, and K. Heinz. Structural properties of the graphene-SiC(0001) interface as a key for the preparation of homogeneous large-terrace graphene surfaces. *Physical Review B (Condensed Matter and Materials Physics)*, 76(24):245406–8, 2007. 65, 74, 88, 145, 211

[147] J. B. Pendry. *Low Energy Electron Diffraction*. Academic Press, 1974. 65, 68, 69, 70, 71, 72, 73, 75, 112

[148] C. Riedl, A. A. Zakharov, and U. Starke. Precise in situ thickness analysis of epitaxial graphene layers on SiC(0001) using low-energy electron diffraction and angle resolved ultraviolet photoelectron spectroscopy. *Applied Physics Letters*, 93(3):033106–3, 2008. 75, 76, 77, 120

[149] P. J. Fisher, Luxmi, N. Srivastava, S. Nie, and R. M. Feenstra. Thickness monitoring of graphene on SiC using low-energy electron diffraction. *Journal of Vacuum Science & Technology A: Vacuum, Surfaces, and Films*, 28:958, 2010. 76

[150] H. Hibino, H. Kageshima, F. Maeda, M. Nagase, Y. Kobayashi, and H. Yamaguchi. Microscopic thickness determination of thin graphite films formed on SiC from quantized oscillation in reflectivity of low-energy electrons. *Physical Review B*, 77(7):075413, 2008. 78, 81

[151] E Bauer. Low energy electron microscopy. *Reports on Progress in Physics*, 57(9):895–938, 1994. 79, 80

[152] W. Telieps. Surface imaging with LEEM. *Applied Physics A Solids and Surfaces*, 44(1):55–61, 1987. 79, 80, 81

[153] R. M. Tromp. Low-energy electron microscopy. *IBM J. Res. Dev.*, 44(4):503–516, 2000. 79, 80

[154] N. Srivastava, Guowei He, Luxmi, and R. M. Feenstra. Interface structure of graphene on SiC(000-1). *Physical Review B*, 85(4):041404, 2012. 90, 113, 121, 132, 147, 177, 206

[155] Somnath Bhattacharyya. Observation of delocalized transport and low-dimensionality effects in disordered carbon thin films. *Applied Physics Letters*, 91(14):142116–142116–3, October 2007. 96

[156] A. C. Ferrari and J. Robertson. Interpretation of raman spectra of disordered and amorphous carbon. *Physical Review B*, 61(20):14095, 2000. 103, 104, 105, 152, 155, 157, 213, 248

[157] K. V. Emtsev, F. Speck, Th. Seyller, L. Ley, and J. D. Riley. Interaction, growth, and ordering of epitaxial graphene on SiC(0001) surfaces: A comparative photoelectron spectroscopy study. *Physical Review B*, 77(15):155303, 2008. 108

[158] Gerd Bergmann. Physical interpretation of weak localization: A time-of-flight experiment with conduction electrons. *Physical Review B*, 28(6):2914–2920, 1983. 110

[159] E. McCann, K. Kechedzhi, Vladimir Falko, H. Suzuura, T. Ando, and B. Altshuler. Weak-Localization magnetoresistance and valley symmetry in graphene. *Physical Review Letters*, 97(14), 2006. 110

[160] Christopher Barsby. Mphys report. Master's thesis, Condensed Matter Physics, University of Leeds, 2010. 116

[161] J. A Robinson, C. P Puls, N. E Staley, J. Stitt, M. A Fanton, K. V Emtsev, T. Seyller, and Y. Liu. Raman topography and strain uniformity of Large-Area epitaxial graphene. *Nano Lett.*, 9 (3):964–968, 2009. 119, 125, 126, 165

[162] C. Faugeras, A. Nerriére, M. Potemski, A. Mahmood, E. Dujardin, C. Berger, and W. A. de Heer. Few-layer graphene on SiC, pyrolitic graphite, and graphene: A raman scattering study. *Applied Physics Letters*, 92(1):011914, 2008. 120

[163] Benjamin Krauss, Pezter Nemes-Incze, Viera Skakalova, Laszlo P. Biro, Klaus von Klitzing, and Jurgen H. Smet. Raman scattering at pure graphene zigzag edges. *Nano Lett.*, 10(11):4544–4548, 2010. 122

[164] Nicola Ferralis, Jason Kawasaki, Roya Maboudian, and Carlo Carraro. Evolution in surface morphology of epitaxial graphene layers on SiC induced by controlled structural strain. *Applied Physics Letters*, 93(19):191916, 2008. 125

[165] J. Rohrl, M. Hundhausen, K. V. Emtsev, Th. Seyller, R. Graupner, and L. Ley. Raman spectra of epitaxial graphene on SiC(0001). *Applied Physics Letters*, 92(20):201918–3, 2008. 126

[166] David L. Miller, Kevin D. Kubista, Gregory M. Rutter, Ming Ruan, Walt A. de Heer, Phillip N. First, and Joseph A. Stroscio. Structural analysis of multilayer graphene via atomic moiré interferometry. *Physical Review B*, 81(12):125427, 2010. 129

[167] Giulio Cocco, Emiliano Cadelano, and Luciano Colombo. Gap opening in graphene by shear strain. *Physical Review B*, 81(24):241412, 2010. 133, 134

[168] Joseph L Tedesco, Brenda L VanMil, Rachael L Myers-Ward, James C Culbertson, Glenn G Jernigan, Paul M Campbell, Joseph M McCrate, Stephen A Kitt, Charles R Eddy, Jr, and D. Kurt Gaskill. Improvement of morphology and free carrier mobility through Argon-Assisted growth of epitaxial graphene on silicon carbide. *ECS Trans*, 19:137, 2009. ECS Trans. 19, 137 (2009). 142

[169] C. Virojanadara, R. Yakimova, J.R. Osiecki, M. Syväjärvi, R.I.G. Uhrberg, L.I. Johansson, and A.A. Zakharov. Substrate orientation: A way towards higher quality monolayer graphene growth on 6H-SiC(0001). *Surface Science*, 603(15):L87–L90, 2009. 149, 198

[170] Michael W Sprinkle. Epitaxial graphene on silicon carbide: low-vacuum growth, characterization, and device fabrication. http://smartech.gatech.edu/handle/1853/34735. Ph.D. 150

[171] Rong Yang, Zhiwen Shi, Lianchang Zhang, Dongxia Shi, and Guangyu Zhang. Observation of raman G-Peak split for graphene nanoribbons with Hydrogen-Terminated zigzag edges. *Nano Lett.*, 11(10):4083–4088, 2011. 162

[172] C Virojanadara, R Yakimova, A A Zakharov, and L I Johansson. Large homogeneous mono-/bi-layer graphene on 6H-SiC(0001) and buffer layer elimination. *Journal of Physics D: Applied Physics*, 43(37):374010, 2010. 175

[173] C. Riedl, C. Coletti, T. Iwasaki, A. A. Zakharov, and U. Starke. Quasi-Free-Standing epitaxial graphene on SiC obtained by hydrogen intercalation. *Physical Review Letters*, 103(24):246804, 2009. 175, 206

[174] Konstantin V. Emtsev, Alexei A. Zakharov, Camilla Coletti, Stiven Forti, and Ulrich Starke. Ambipolar doping in quasifree epitaxial graphene on SiC(0001) controlled by ge intercalation. *Physical Review B*, 84(12):125423, 2011. 175

[175] C. Virojanadara, S. Watcharinyanon, A. A. Zakharov, and L. I. Johansson. Epitaxial graphene on 6H-SiC and li intercalation. *Physical Review B*, 82(20):205402, 2010. 175

[176] S. Oida, F. R. McFeely, J. B. Hannon, R. M. Tromp, M. Copel, Z. Chen, Y. Sun, D. B. Farmer, and J. Yurkas. Decoupling graphene from SiC(0001) via oxidation. *Physical Review B*, 82(4):041411, 2010. 176, 206

[177] G F Sun, J F Jia, Q K Xue, and L Li. Atomic-scale imaging and manipulation of ridges on epitaxial graphene on 6H-SiC(0001). *Nanotechnology*, 20(35):355701, 2009. 192

[178] Alex Walton. *Fabrication and electrical characterisation of nanowires*. University of Leeds (Department of Physics and Astronomy), 2009. 216

[179] Taizo Kanagawa, Rei Hobara, Iwao Matsuda, Takehiro Tanikawa, Akiko Natori, and Shuji Hasegawa. Anisotropy in conductance of a Quasi-One-Dimensional metallic surface state measured by a square Micro-Four-Point probe method. *Physical Review Letters*, 91(3):036805, 2003. 218

[180] Iwao Matsuda, Masashi Ueno, Toru Hirahara, Rei Hobara, Harumo Morikawa, Canhua Liu, and Shuji Hasegawa. Electrical resistance of a monatomic step on a crystal surface. *Physical Review Letters*, 93(23):236801, 2004. 218

[181] J.W. Wells, J.F. Kallehauge, and Ph. Hofmann. Surface-sensitive conductance measurements on clean and stepped semiconductor surfaces: Numerical simulations of four point probe measurements. *Surface Science*, 602(10):1742–1749, 2008. 227, 244